On the Symmetry of Nuclear Identity between Relativistic Primary and Secondary Nuclei

Dissertation
zur
Erlangung des Doktorgrades
der Naturwissenschaften
(Dr. rer. Nat.)

dem
Fachbereich Chemie
der Philipps-Universität Marburg

vorgelegt
von
Louis Lerman
aus
Washington, D.C.

Marburg/Lahn 2002

Vom Fachbereich Chemie der Philipps-Universität Marburg/Lahn
als

Dissertation am angenommen: 5/31/02
Tag der mündlichen Prüfung am: 6/18/02

Erstgutachter: Herr Prof. Dr. R. Brandt
Zweitgutachterin: Frau Dr. M. Haiduc und Herr Prof. Dr. Jungclas

RHIP

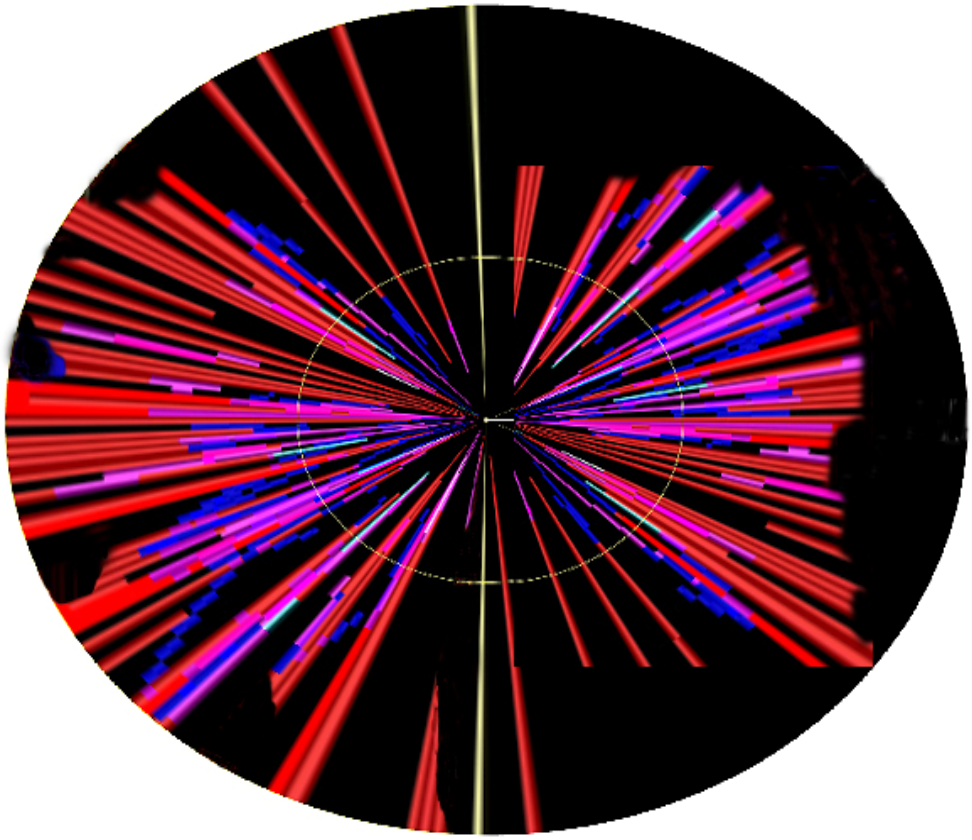

Relativistic Heavy Ion Phenomenology

We shall not cease from exploration
And the end of all our exploring
Will be to arrive where we started
And know the place for the first time.

T.S. Eliot (Four Quartets)

Über die Symmetrie der Identität von Atomkernen, untersucht am Beispiel relativistischer Primärteilchen und den daraus gebildeten Sekundärteilchen

Dissertation von Louis Lerman

(Kurzfassung in deutscher Sprache)

Es wird die Frage untersucht, ob hadronische Sekundärteilchen die gleichen fundamentalen Eigenschaften wie die primären relativistischen Teilchen besitzen, aus denen sie durch Kernwechselwirkungen hervorgegangen sind. Es werden zwei sich ergänzende Experimente beschrieben. Das erste Experiment bestand aus der Bestrahlung einer Kernspuremulsion mit den 1.8 AGeV ^{40}Ar-Ionen des BEVATRONS am Lawrence Berkeley Laboratory in Kalifornien und der anschließenden gründlichen Auswertung der Kernspuren im Emulsionsstack. Die vollständige Analyse dieser Art von Bestrahlung ist die erste in ihrer Art, und es wurden 1418 „Sterne" (der Wechselwirkung der ^{40}Ar-Ionen als Primärteilchen mit den Bestandteilen der Kernspuremulsion) am Mikroskop genau ausgemessen, dazu 1850 „Sterne", die von Sekundärteilchen induziert wurden und außerdem über 10.000 „Schauerteilchen" und „langsame, stark ionisierende Teilchen". Diese Ergebnisse bilden die experimentelle Datenbasis zur Untersuchung der Symmetrie zwischen Primärteilchen und den daraus gebildeten Sekundärteilchen. Ein Ergebnis dieser Untersuchungen ist die gesicherte Feststellung, daß der totale Wechselwirkungsquerschnitt von α-Teilchen sich nicht mit der Generationsfolge ändert.

Das zweite „Experiment" ist *virtueller* Natur und besteht aus Monte Carlo Simulations-Rechnungen, die auf den Emulsionsexperimenten aufbauen. Zuerst wird ein allgemeines Progamm, RHIP, entwickelt. Dieses ermöglicht die Untersuchung einer Reihe von Problemen aus der Teilchenphysik bis hin zu Anwendungen bei der NASA, um den Einfluß der galaktischen, kosmischen Strahlung während bemannter Raumflüge zu simulieren. Der Hauptteil dieser Arbeit besteht aber in der Entwicklung eines spezielleren Programmes, BFHL, das eine sehr detailierte Analyse der kernchemischen Untersuchungen („Kupfer Kalorimeter Experiment") an Kupfer-Targets ermöglicht, die ebenfalls mit den schon erwähnten 1.8 AGeV ^{40}Ar-Ionen bestrahlt wurden. Die sehr bis ins Einzelne gehenden analytischen Simulationsrechnungen zeigen, daß die experimentellen Meßergebnisse für das wichtigste Reaktionsprodukt dieser Kernreaktion - es ist das Nuklid ^{24}Na - nur erklärt werden können, wenn man einen drastisch angewachsenen *partiellen Wirkungsquerschnitt für die Bildung von ^{24}Na* postuliert. Es muß weiter angenommen werden, daß dieses insbesondere für solche Reaktionen gilt, die von schweren Sekundärfragmente ($Z \geq 2$) in einer Zeit von ca. 10^{-9} Sekunden nach ihrer Entstehung induziert werden. Zusätzliche Untersuchungen an den relativistischen „Schauerteilchen" unter Verwendung gleichartig erhöhter partieller Bildungsquerschnitte für ^{24}Na ergeben keine Anpassung an die experimentellen Meßbefunde. Es ist sehr interessant darauf hinzuweisen, daß ähnliche experimentelle Resultate bezüglich Lebensdauer, Energieschwelle und der Produktionsrate für kollektive „seltsame" („strange") Kernmaterie beobachtet wurden.

Was immer die endgültig akzeptierbare Interpretation dieser Phänomene in der Zukunft ergeben möge, die vorgelegte Arbeit weist sehr deutlich in die Richtung, daß hier ein bisher unvermutetes *nicht lineares Verhalten* in einer Teilmenge der Reaktionsprodukte bei den hier untersuchten relativistischen Kernreaktionen vorliegt. Es scheint eine Asymmetrie in den Kernwechselwirkungseigenschaften zwischen den Primärteilchen und den von ihnen nach Kernwechselwirkungen ausgehenden Sekundärteilchen vorzuliegen.

On the Exploration of the Symmetry of Nuclear Identity between Relativistic Primary and Secondary Nuclei

Dissertation by Louis Lerman

Do secondary hadrons, freshly created in the collision of a relativistic heavy ion nucleus, have the same properties of nuclear interaction as those of an otherwise identical primary?

To explore this question two types of experiments were performed, one in fact and one in fiction. The first was the scanning and measurement of an emulsion stack exposed to a 1.8 A GeV ^{40}Ar beam from Lawrence Berkeley Laboratory's Bevatron. This emulsion experiment is the first full-stack scan of a major exposure ever performed and includes 1418 stars of primary interactions, 1850 secondary stars, and tens of thousands of shower and slow heavily ionizing particles. As such it constitutes a dataset uniquely powerful in exploring questions of symmetry between primary and secondary populations. One of the emulsion results is the experimental determination (and to a particularly high accuracy for Z=2) that total (geometric) cross-section does not change with generation for the secondaries under study.

The 'fictional' experiments are a set of Monte-Carlo simulations based on the transport code *RHIP*, itself built upon the results of the emulsions experiment. *RHIP* is designed to attack a number of problems ranging from particle physics to NASA's need to model the nuclear cascades induced by Galactic Cosmic Rays impinging on manned spacecraft. The major version of *RHIP* dealt with here is *BFHL*, a detailed modeling of a 1.8 A GeV ^{40}Ar beam on cylindrically symmetric sets of Cu targets.

BFHL was then applied to the Copper Calorimetry Experiments also performed at Lawrence Berkeley Laboratory. The exhaustive simulation and analysis presented here shows that all but one of the variables considered can neither quantitatively nor qualitatively explain the results of the Copper Calorimetry Experiments. Amongst many others these failures of fit include all transport variables, the total cross-section (i.e. short mean free path), and a higher than normal P_t for shower particles.

Instead, the Copper Calorimetry Experiments can only be explained by a significantly enhanced partial cross-section for the production of the isotope measured (^{24}Na). This enhancement appears to have a lifetime of 10^{-9} or 10^{-10} seconds and to be carried by a subpopulation of secondary ($Z \geq 2$) fragments. (Simulations of shower particles having enhanced production cross-sections do not fit the experimental data as well.) Most intriguing is a congruence of energy thresholds, lifetimes, and production efficiencies between the inferred carrier of this enhanced production (partial) cross-section and collective strange matter.

Whatever the actual explanation, the results of this work strongly suggests that in a subset of relativistic ion collisions… asymmetries in nuclear interaction properties exist between primary and secondary populations, and that some form of previously unsuspected non-linear behavior exists in the involved collisions.

CONTENTS

Prologue

All of physics can be looked at as the study of nature's symmetries, asymmetries, and the breaking of these symmetries. By Noether's Theorem* this is equivalent to saying that physics studies those things conserved in physical processes, those that are not, and the mechanisms by which particular conservation laws are made and broken. This approach is fundamental to contemporary high-energy physics, and its universality illustrated below by application to the classical laws of mechanics and thermodynamics.

Newton's Laws of Motion

1) *A body in motion tends to stay in motion, and a body at rest tends to stay at rest.* Or more usefully… *a body in uniform motion tends continues to do so unless acted upon by an external force F* (as defined in the second law)
2) $F = ma$
3) *To every action there is an equal and opposite reaction.*

The first law states the symmetry (or invariance) of spatial translation and equivalently proclaims the homogeneity of space. The conserved quantity is of course that of momentum. The second law parameterizes any symmetry-breaking of an object's motion through the manifestation of a force that is itself a measure of the non-conservation of momentum. And the symmetries inherent in Newton's third law lead to the explicit law of the conservation of momentum.

In thermodynamics, by analogy, the first law deals with the time symmetries of processes; equivalently stated as the conservation of energy. And the second law of thermodynamics, in similar analogy, deals with the breaking of this symmetry in time and its equivalent non-conservation of energy.

---

* Produced in 1905 by Emma Noether, a student of Hilbert, it demonstrates that for every continuous symmetry there is a corresponding conserved quantity and for every conserved quantity (or 'law' of conservation) there exists a continuous symmetry.

But there is an even more fundamental symmetry implicit in the first laws of both mechanics and thermodynamics: the symmetry of identity …." a rose is a rose is a rose" or more abstractly X=X=X. This is non-trivial for when the symmetry of identity is itself broken, by definition new structures and processes come into being. And when dealing with collective phenomena the breaking of this symmetry of identity invariably involves phase transitions of one form or another. Indeed, in the study of the self-organization of nature, the forces and principles underlying this particular symmetry and its breaking are often the most fundamental.

The present work is an exploration of this latter symmetry, the symmetry of identity, in the regime of relativistic heavy ions. In particular it examines whether relativistic primaries and newly-created secondaries of the same (Z,A) sustain identical nuclear interactions: for example, will a newly created (i.e. secondary) ^{12}C nucleus behave identically the same in a nuclear collision as a ^{12}C nucleus from a primary beam. This is not an easy experimental problem, for it forces one to look down the center of relativistic beams of heavy ions…

Figure 1.1 Simulation of a Relativistic Heavy Ion Beam

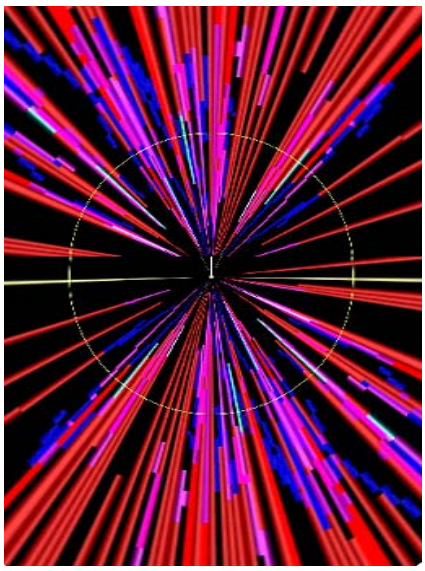

and to distinguish the collisions of secondary nuclei in a target from those of primaries.

1.1 The Experiment and its Conceptual Underpinnings

Aleklett et al (1987, 1988a,b) pioneered an experimental approach that can be used to explore this unusually reticent part of phase-space; attempting to differentiate the effects and properties of secondary projectiles from the presumed identical ones due to primaries. Their approach is in essence a "classical" beam transport experiment with relativistic heavy ions directed against thick metal targets. Thick targets are necessary due to the secondary nuclei's centimeter-scale mean free path. The chosen targets are cylindrically symmetrical copper blocks taken two at a time (Figure 1.2a) and N at a time (Figure 1.2b).

Figure 1.2 Basic Experimental Setups

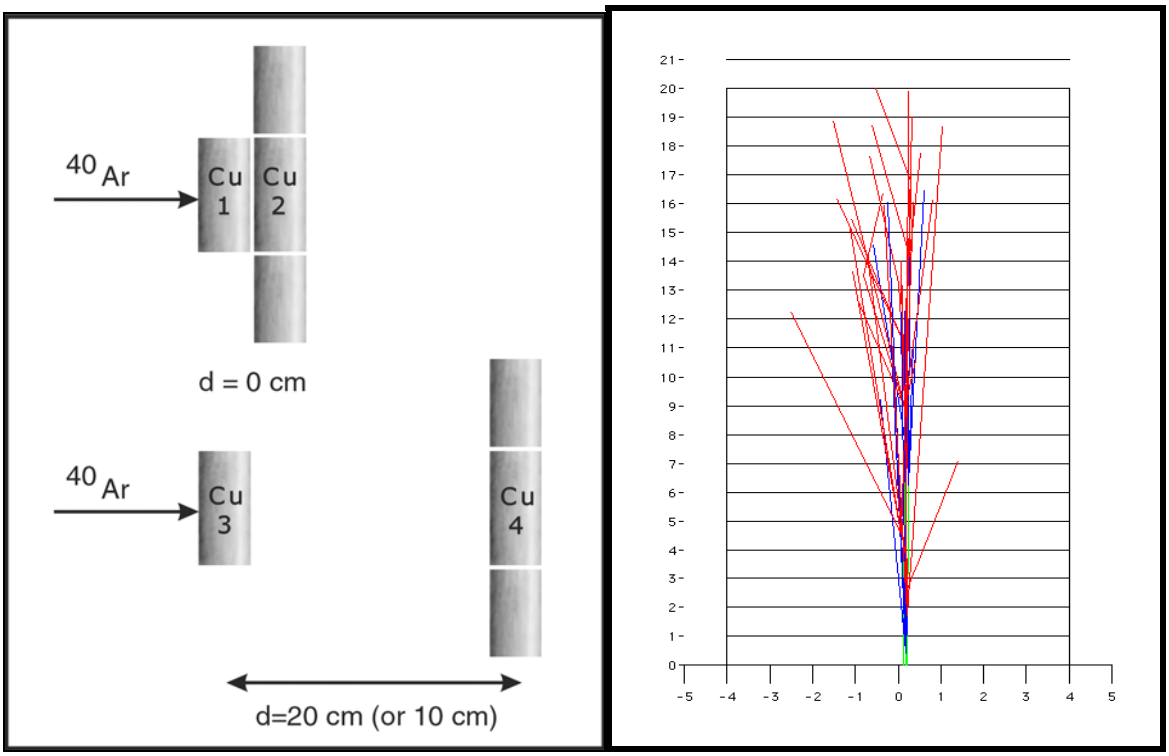

(a) (b)

Ordinarily, due to the non-separable mixing of generations, experiments using thick targets can only look at averaged quantities (as in calorimetry) or at variables representing a collective flow. Hence implicit in conventional thick target experiments is the assumption of a symmetry of identity between generations vis-à-vis their behavior in a cascade of nuclear collisions. (The resolution of generations is one of the reasons thin targets are used in the majority of experiments examining the characteristics of individual nuclear species.)

But the experimental approach of Aleklett et al actually takes advantage of the mixing inherent in thick targets and incorporates an elegant phenomenological twist (illustrated in Figure 1.3) to break the symmetry of the collision populations, primary vs. secondary.

Figure 1.3 Metalogical Setup

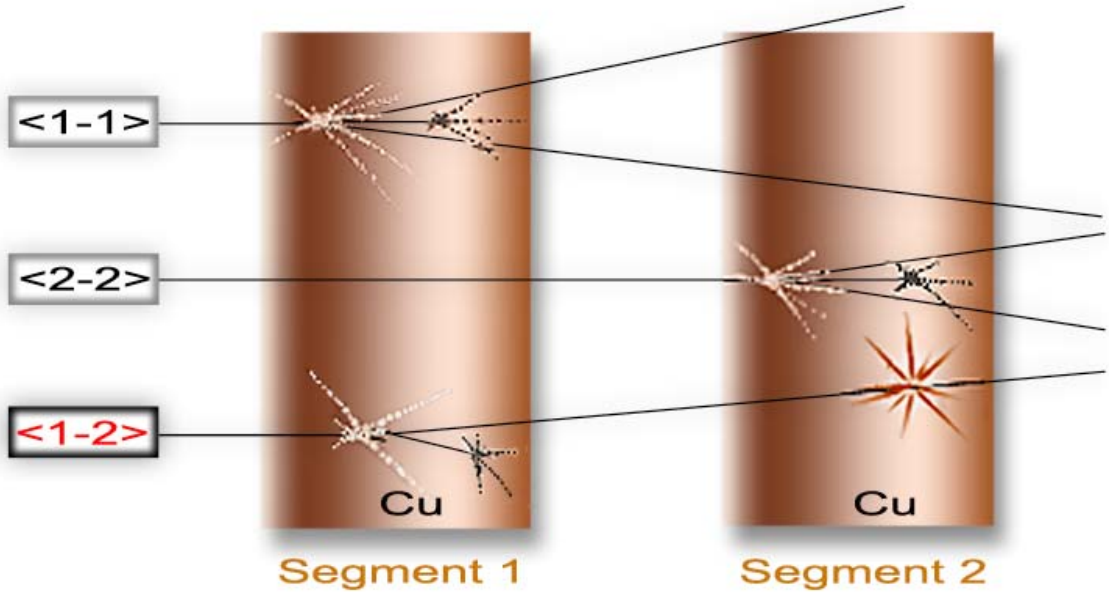

Without loss of generality, possible interactions fall into three classes:

< 1-1 > A primary interacts in Segment 1 (the front)
and produces a secondary which also interacts in Segment 1.

< 2-2 > A primary interacts in Segment 2 (the rear)
and produces a secondary which also interacts in Segment 2.

< 1 – 2 > A primary interacts in Segment 1 (the front)
and produces a secondary which interacts in Segment 2.

It is obvious that in the first two classes, <1-1> and <2-2>, the basic nuclear processes involved are identical and the amount of identical processes in Segment 2 should be reduced only in proportion to the amount of primary beam (exponentially) absorbed in Segment 1. If one then measures in each of the target blocks the activities of any target residues, the *ratio of activities* in these two segments should follow this exponential decrease; being one minus the amount of the primary beam absorbed in Segment 1 on the way to Segment 2. *For these first two classes any anomalous or unexpected secondary behavior will simply scale with the numbers of primary interactions.*

Instead it is the third class of interactions <1-2> that will make apparent any difference in the secondaries' behavior that is manifested in the absolute activity. *For this third class breaks the symmetry in an unscalable way*. For example, in class <1-2> any unusual secondary phenomena which might enhance absolute activity will enhance Segment 2's activity due to the increased number of secondaries born in Segment 1 that then interact in Segment 2. Thus relative to the otherwise expected values, there will be an enhancement of the activity ratio

$$R = \frac{Activity_{Segment2}}{Activity_{Segment1}} \qquad \textbf{(1.1)}$$

If one knows or can simulate the expected number and effect of such "normally" behaving secondaries (born in 1, interacting in 2) *then any greater activity in Segment 2 (i.e. an enhanced R) must be due to other processes that somehow enhance the production of whatever one is measuring.*

1.2 Experimental Applications of Activity Ratios

The application of this concept for a two block configuration was first performed by Aleklett et al (1987), while that for a 20-block cylinder was done by Haase (1990). Both sets of experiments were performed at Lawrence Berkeley Laboratory's (LBL) Bevatron, and confirmatory experiments were subsequently performed at a number of other institutions (see Section 5.2). Both LBL experiments utilized a 1.8 A GeV ^{40}Ar beam on a native copper target and are more fully described in Chapters 5 and 10.

What was measured, using Ge(Li)'s, was the ^{24}Na residue of the Cu target nuclei. This particular isotope was chosen both because of its clean, easy to detect, γ-lines and because the production cross-section curve for ^{24}Na in Cu is almost a step-function with a threshold beginning ~1 A GeV and which flattens out ~ 2 A GeV (Figure 1.4).

^{24}Na-production thus acts as a threshold counter for relativistic phenomena. Only (relativistic) projectile fragments will be able to produce ^{24}Na from interactions with the Cu target nuclei. This is the first of two particularly elegant aspects of the experimental design. In essence then ^{24}Na-production provides an unusual and extremely useful form of calorimetery where the total amount of ^{24}Na produced in a target segment is a direct function of the cumulative (target) interactions with relativistic (projectile) primaries and secondaries. Consequently we shall name this class of experiments *Copper Calorimetry Experiments*.

Figure 1.4 ^{24}Na Production Cross-Section in Copper[1]

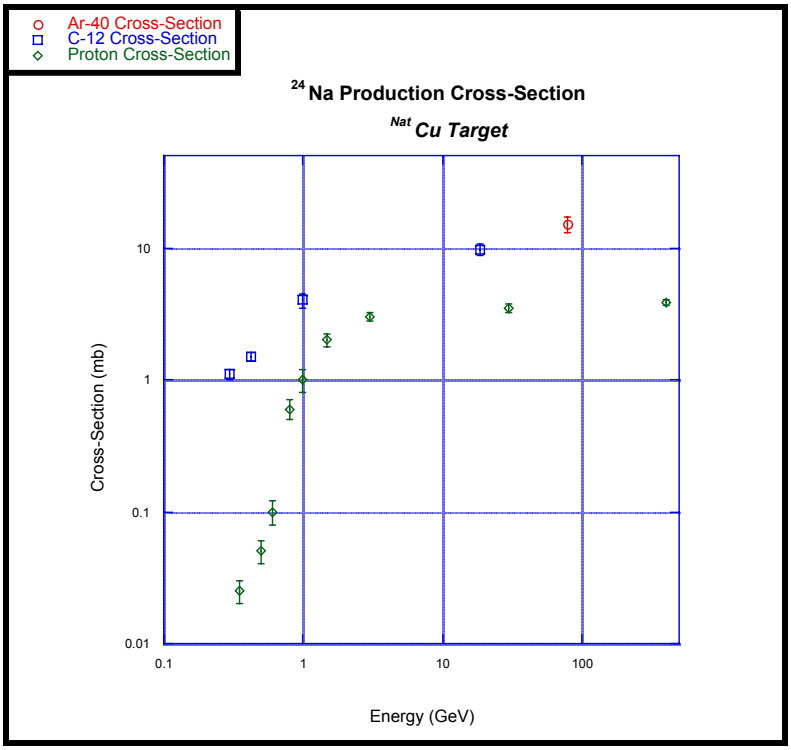

As an additional touch of experimental elegance the authors utilized not just the absolute activity of the isotopes under investigation, but the activity ratio R_d: the ratio of the activity of the downstream disk (at a distance *d)* to the activity of the front disk. This was done in order to finesse as much as possible systematic and experimental uncertainties: for each pair of disks shared identical histories, they were exposed to the same beam for the same amount of time, and they were measured in the same Ge(Li)'s. To quote the authors of the experiment

> *"...this activity ratio for a specific nuclide can be determined to a high degree of precision. All uncertainties due to particle fluxes, counting efficiencies, uncertainties in the decay scheme for a specific radioactive nuclide, etc. cancel out in the activity ratios R.*

[1] Section 7.1 contains a more complete discussion.

Essentially, the only experimental uncertainty in this ratio comes from counting statistics. As the number of counts is typically $>10^4$ our activity ratio R can be determined within ±1%. Such a precision is comparable only to that of large counter experiments or of high statistics bubble chamber experiments…"[1]

It's worthwhile noting that 15 years earlier a similar use of experimental ratios to decrease systematic errors was fundamental to the demonstration of the existence of neutral currents[2], allowing experimenters the necessary luxury of ignoring the absolute flux of neutrinos involved. The activity ratio R in the Copper Calorimetry Experiments offered a similar benefit, but also an additional one… that by itself justified the entire experimental effort**: any "new" physics that might be found in the secondaries will manifest itself in R_d.** And as this work shows, this seems to be the case.

1.3 The Approach to Monte Carlo

As concluded in Section 1.1 in order to establish the existence of something new or different it is necessary to know or simulate the expected number and effect of all "normally" behaving secondaries. Hence the creation of truly accurate simulations is fundamental to our approach. In particular Monte Carlo is used, itself invented to model a similar problem: the transport of neutrons in a fissionable 'target' of complex geometry. Indeed, the use of carefully crafted Monte Carlo simulations to accurately establish the denominator of the ratio

$$\frac{\textit{Observed Events}}{\textit{Events Expected by Conventional Assumptions}} \qquad \textbf{(1.2)}$$

is fundamental to contemporary high-energy physics.

---

[1] Aleklett et al. (1988a)
[2] Galison (1987), p.190

Monte Carlo simulation of potential background and interference effects has become the necessary gold-standard against which alternative explanations of new 'phenomena' are assiduously tested. This is especially so when dealing with low-probability or low-incidence phenomena in complex detector scenarios. For example, experiments to establish the existence of neutral-currents used this phenomenological approach; and in the past year it was used to demonstrate the reality of the tau-neutrinos in emulsion.

In the early years of its development there was a great debate as to whether Monte Carlo-based simulations were a poor man's approach to non-analytically treatable problems or were in fact *closer* to the stochastic reality of nature than analytic methods (which in essence deal with the average behavior of the system being analytically treated).
For problems of the sort dealt with in this study, we follow the latter interpretation: believing that an exhaustively explored set of Monte Carlo simulations built upon a solid database of physical fact is in essence an accelerator on a desktop; and of particular use in the search for phenomena whose existence is only hinted at, much less understood.
But this requires the database to be physically accurate and statistically meaningful.

The creation of a database capable of supporting such realistic simulations necessitated an additional set of experiments: a thorough scanning of an emulsion stack exposed to a 1.8 A GeV Argon beam as were the Cu targets. The stack was exposed and developed at LBL and then scanned and measured (see Chapter 3 in this study) at the Institute of Space Research (Bucharest, Romania). The multiplicities and angles of the nuclear cascades were exhaustively followed through five generations and a database was constructed (see Chapter 4). In fact this enormous effort became the first full-stack scan ever performed. The database was then used to construct a Monte Carlo simulation of cascade phenomena that is as independent as possible of theoretical models (see Chapter 6) and then applied to the interpretation of the experiments of Aleklett et al and Haase (see Chapters 7-9 and Chapter 10 respectively).

The ability to apply the emulsion-derived data to the copper simulation is due to an enormous simplification that follows the application of two underlying concepts: *factorization* and *limiting fragmentation*. The next section shows how these two concepts,

derived from Bohr's Hypothesis of (Nuclear) Independence, allow a complete separation of the origins of our input data for the beam and for the target. Consequently, as will be seen, we are justified in applying to our analysis and simulation of a 1.8 A GeV ^{40}Ar beam on Cu the detailed information derivable from the study of a 1.8 A GeV ^{40}Ar beam on emulsion (Ag and Br). Similarly the target production cross-sections will be shown to require studies that are independent of the beam, this simplification making them experimentally much more tractable.

1.4 Factorization & Limiting Fragmentation: Bohr's Declaration of Independence

Bohr's 'independence hypothesis' postulates independence between the processes of nuclear collision and emission. The cause is a short mean free path for intranuclear collisions of the participating nucleons, and the subsequent sharing of energy and potential excitation states over time-scales *shorter* than that of the emission of collision products. In the words of Bohr himself:

> *"The phenomena of neutron capture thus forces us to assume that a collision between a high speed neutron and a heavy nucleus will in the first place result in the formation of a compound system of remarkable stability. The possible later breaking up of this intermediate system by the ejection of a material particle or its passing with emission of radiation to a stable final state must in fact be considered as separate competing processes which have no immediate connection with the first stage of the encounter."* [1]

Hence there is a loss of 'memory' of the incident collision, and the subsequent evolution of the system proceeds independently of these initial conditions subject only to the applicable conservation principles.

[1] Bohr (1936); This was first experimentally proven by Goshal (1950) at LBL.

From this dissociation between the collisional excitation of a compound nucleus and its emitting decay come two of the most fundamental and simplifying properties of high-energy nuclear collisions[1, 2]: *limiting fragmentation* and *factorization*.

Limiting fragmentation says that above a given threshold of projectile kinetic energy the distribution of reaction products (the channels) will vary very little with energy. Also introduced by Feynman as 'scaling'[3], it manifests itself as an asymptotic behavior of the distribution of products (or reaction cross-sections) in the rest frame of the projectile or target. Following Friedlander and Heckman (1982) this can be expressed as follows: given an inclusive reaction

$$\mathbf{B}(\text{eam}) + \mathbf{T}(\text{arget}) = \mathbf{F}(\text{ragment}) + \mathbf{X}(\text{everything else}) \qquad \textbf{(1.3)}$$

with an invariant cross-section

$$E\frac{d^3\sigma_{BT}^{F}(s,p_{L,}p_T)}{d^3p} = f(s,p_{L,}p_T) \qquad \textbf{(1.4)}$$

where $s = (p_B + p_T)^2$; P_L and P_T are the conventional longitudinal and transverse momenta; and B,T, and F are the Beam, Target, and Fragments respectively. Then in the limit as the energy **E** goes to ∞

$$\lim_{p\to\infty} f(s,p_{L,}p_T) = f(p_{ll},p_{\perp}) \qquad \textbf{(1.5)}$$

the single-particle inclusive spectrum and cross-sections asymptotically become energy independent. Hence the asymptotic value above 2 GeV seen in Figure 1.4. (See Section 7.1)

---

[1] Feshbach and Huang (1973) and Goldhaber and Heckman (1978)

[2] Historically, both concepts came to relativistic heavy ion physics from particle physics.

[3] Feynman (1969) Feynman's introduction to the paper offers a fascinating look at both the concept's origins as well as his scientific approach: *"I have difficulty in writing this note because it is not in the nature of a deductive paper, but is the result of an induction. I am more sure of the conclusions than of any single argument which suggested them to me for they have an internal consistency which surprises me and exceeds the consistency of my deductive arguments which (only) hinted at their existence."*

The other simplifying concept, factorization, breaks the production cross-section for a secondary fragment into two separable terms. One depends only on the beam and fragment under consideration, and the other is a scaling factor that is a function only of the target. Using the same nomenclature as above:

$$\sigma_{BT}^{F} = \sigma_{B}^{F} \gamma_{T} \qquad \textbf{(1.6)}$$

where the cross-section depends only on a component σ_{B}^{F} involving the beam and fragment to be measured; along with a scaling factor γ_{T} depending only on the target. Needless to say, beam and target designations may be reversed in this formulation.

Those regions of phase-space where limiting fragmentation and factorization hold can only be established by experiment. But an astonishing simplification occurs in such regions: fragmentation channels of the projectile and target nuclei are independent of each other! This means that for a given projectile beam the fragmentation cross-sections are essentially independent of the mass of the target. In the words of Friedlander and Heckman[1],

> *" The practical consequence of...Limiting Fragmentation and Factorization is enormous, because the unlimited number of energy/target combinations one might conceivably measure for fragment production cross-sections is now reduced to only <u>one</u> – once the asymptotic energy region is established."*

Friedlander and Heckman present an extensive discussion of the early experiments establishing the regions where such fortuitous combinations of limiting fragmentation and factorization hold. This sweet zone of simplification turns out to be in the 1-2 A GeV range of beam energies. The experiments discussed (with experimental errors of ~1%) include Cu targets in this same energy range, establishing our ability to make use of these simplifications in our own work. Compare, for example, the ^{24}Na production cross-section of protons on Ag (Figure 1.5) to that of protons on Cu (Figure 1.4).

[1] Friedlander and Heckman (1982)

Figure 1.5 ^{24}Na Production Cross-section[1]

[p + Ag→ ^{24}Na]

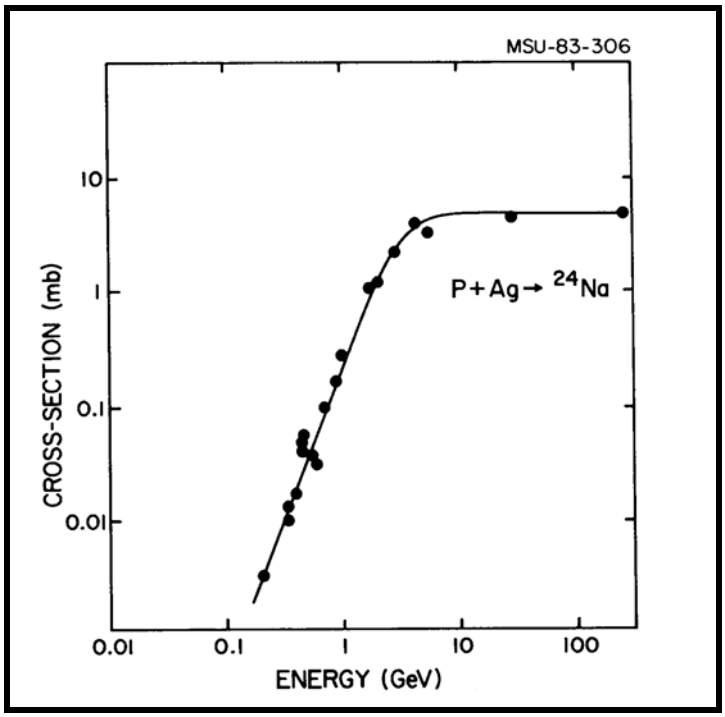

Hence our approach rests on a strong empirical foundation. Because of factorization and limiting fragmentation we can legitimately separate beam and target. In particular, the richly detailed information about a 1.8 A GeV ^{40}Ar beam's interactions in emulsion is realistically applied to a 1.8 A GeV ^{40}Ar beam on Cu. The target production (partial) cross-sections for ^{24}Na are independent of all this, and can correctly be interpolated from Cu data sets as well as those on other metal targets. (See for example Figure 7.1c, "^{24}Na Production Cross-section on a Au target".) Additionally the mean free path of protons in emulsion is ~133 gm/cm^2, while that of copper is ~135 gm/cm^2. This means that 'on average' the mean free paths and the average geometric cross-sections of the two media are virtually identical, further establishing the validity of comparing processes that depend on the total cross-section.

[1] Scott (1983)

1.5 Simulation and Phenomenology: Results and Discussion

Applying all of this to the Copper Calorimetry Experiments required extensive simulation as reported in Chapters (7-11). All but one class of models failed to qualitatively match the experimental data, and this included variations of all model variables representing the real-world variables of total cross-section, kinematics, and geometric transport.

The *only* variable class which offered a ubiquity and robustness of fit was a simple model that included an enhanced partial ^{24}Na production cross-section for subpopulations of secondary heavy ion fragments. *In other words, the assumed symmetry of identity between generations is broken for the nuclear interactions studied.* It was the only model, within the context of our simulations, that fit the two-block data (see Chapter 9). And when applied to the entire n-component cylinder, it offers a visibly superior fit as well (see Chapter 10). Figure 1.6 shows a representative fit, explanatory details being found in Chapters (7-11). Note that secondary shower particles with enhanced production cross-sections were also explored (See Chapter 11), but within the limitations of our current models they do not offer as good a fit as do the ones involving heavy ions.

The Monte Carlo approach used in the present work closely resembles those used in the search for neutral currents, as well as a variety of more contemporary neutrino problems. In our case and these others an initially unseen hypothetical phenomenology is sought to be established as physical fact through a complex warren of simulated models and backgrounds. When 'nothing else works'… the phenomena is taken for 'virtual' fact, and moves even closer to 'reality' when these virtual facts can accurately predict results from other more complex sets of experiments (as ours will be shown to do when going from the two component target to the n-component one).

This underlines our use of one of the most important approaches developed in the exploration of the hidden jungles of particle physics: *phenomenology*. The phenomenological approach is a time-honored and powerful one in particle physics; especially useful when doing initial forays into previously unexplored territories of physical phase-space.

Figure 1.6 Comparison of R-values between Model Classes and Experiment[1]

(1.8 A GeV ^{40}Ar on a Copper Cylinder)

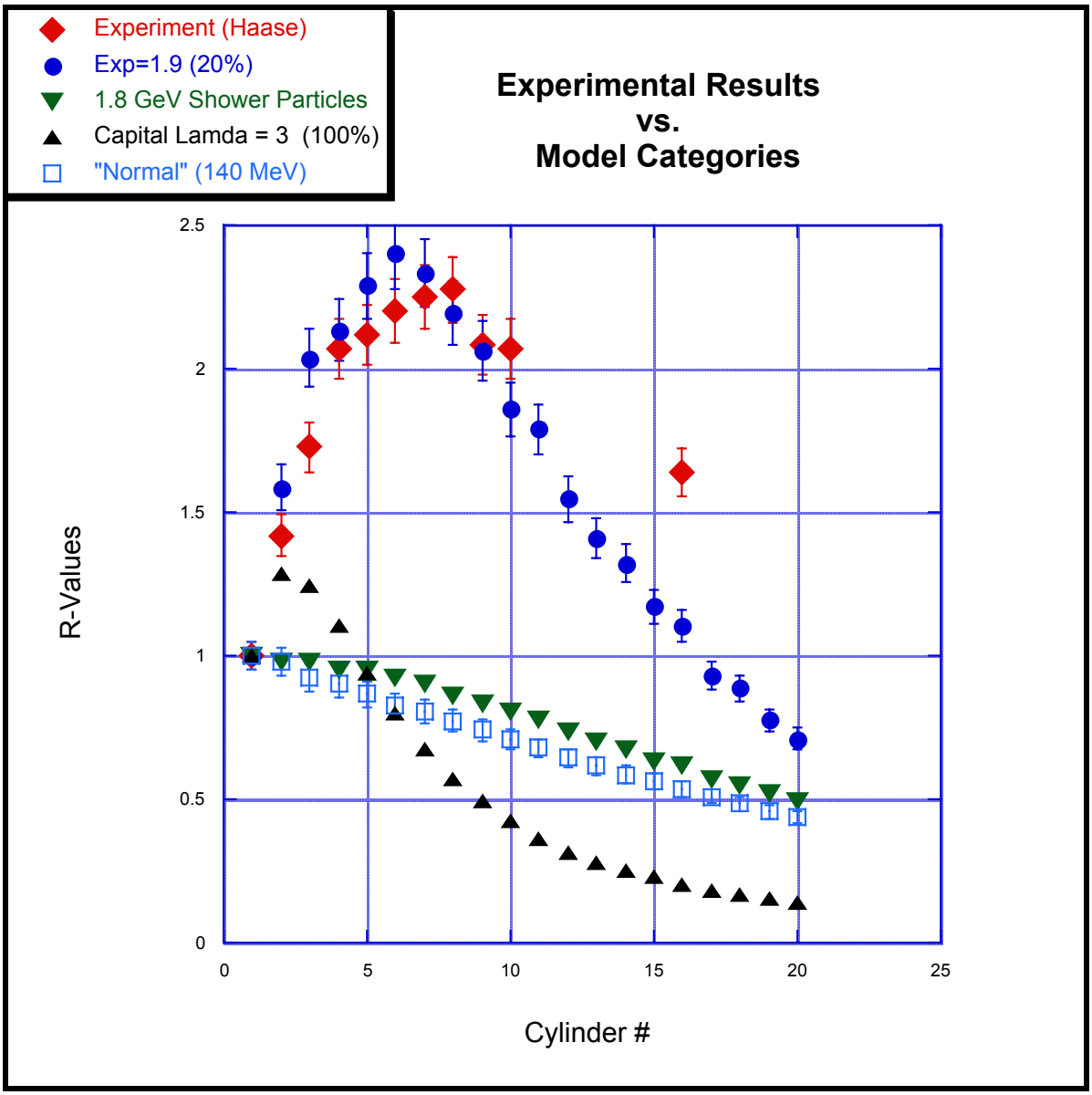

[1] This is Figure 10.12c , with the different model categories being explained in Chapters (7–10). The red diamonds are the experimental results of a 20-unit cylinder [Haase,1990], and the blue circles are the predictions of a model incorporating an enhanced production cross-section.

In sum then our collective approach to the problem under study is most classical: experimentally, computationally, phenomenologically. And each of these components has been approached with decimal-point rigor:

- ❖ It is extremely difficult to find fundamental flaws in the experiments as performed. The initial Copper Calorimetry experiments were performed three times and for each the subsequent measurements were performed at multiple laboratories around the world. The results were then averaged. The claimed experimental errors are ~ 1%.

- ❖ The emulsion scanning and measuring were exhaustively checked and rechecked to an accuracy of ≤ 0.1%.

- ❖ Like all programming efforts, ours could conceivably have bugs in them that are so well hidden as to be virtually 'immortal', but the consistency of the results after countless rounds of checking and cross-checking from every conceivable angle suggest that the fundamentals of our simulation programs work.

- ❖ The phenomenology is based on a set of a few basic assumptions. At the lowest level these include the gaussian distributions of beam profiles and the exponential absorption rates of relativistic nuclei going through matter; while the next level up includes the assumptions of limiting fragmentation and factorization.

Still, our phenomenological explanation may turn out not to be "real". The phenomenological approach adopted was developed with this possibility in mind, and this case then becomes interesting in a very different way. Because only a few basic assumptions are used, and very classical ones at that, a failure of the phenomenological approach would mean that at some level the basic assumptions of the approach need to be questioned: in our case the assumptions of linearity and separability, including those of factorization and limiting fragmentation.

As will be discussed more fully in Section 10.5 the assumed applicability of both factorization and limiting fragmentation to some of the secondary population must then be questioned. This in turn suggests the occurrence of non-linear collective interactions, quite possibly related to strange hypermatter or even the still unseen border of the quark-gluon plasma phase transition.

Regardless of whether this is the correct interpretation, what seems evident is that some nuclear interactive properties of freshly-created secondaries are, for a short time $\leq 10^{-9}$ *seconds, different than those of the same (A,Z) nucleus that has been 'sitting on the shelf'.*

The symmetry of identity between primary and secondary appears to be broken, and like all other broken symmetry problems in physics is likely to be related to some form of critical phenomena or self-organizing system. In this particular context, if the effect is found to be 'real' and representative of what is to be found in other interactions, our findings could be of fundamental importance.

1.6 Other Potential Applications of this Work

The work presented here straddles the border between several regimes of study. It seeks to use high-energy nuclei as macro-laboratories to study particle physics phenomena, while utilizing the techniques and approaches of particle physics to better understand relativistic heavy ion interactions. It also uses standard radiochemical techniques to produce what is in essence a radiochemically based calorimeter for high-energy physics interactions. In so doing, this radiochemical approach finesses the otherwise small statistics of conventional nuclear physics experiments that utilize visually-scanned targets such as nuclear emulsions or bubble chambers. Yet it uses the extraordinary resolution of emulsions to establish a database for the Monte Carlo simulations necessary to establish both background and inferred effect.

In the pursuit of our scientific goals we have taken advantage of this multi-scale approach and the consequent breadth of tools utilized. Each step of our investigation, in and of

itself, was designed to provide the basis for applications to other, quite different, scientific problems. These include the following:

1) The emulsion experiments were meant to be a significant contribution in and of themselves. The careful and exhaustive measurements performed coupled with the exploratory tools developed allow many other explorations of the interaction of relativistic heavy ions and emulsion nuclei.

2) Because of the strong experimental underpinnings (Chapters 2, 3) of our interpretative approach and the minimalist use of assumptions, it is expected that our own results can help to ground (in the narrow regions studied) other more theoretically based relativistic heavy ion transport codes.

3) Independent of the ultimate conclusions regarding the interpretation of the copper calorimetry experiments, the database and transport code should be of turn-key use to NASA. Since the base of emulsion is made from the bones of bovines the response of nuclear emulsion to high-energy nuclei is considered to be within 20% of that of a living creature's. Additionally, copper is often the substance used to model the shielding of spacecraft. Thus for long-duration manned space-flight missions (International Space Station and missions to Mars) the database and code seem directly applicable to modeling shielding concerns from high-energy galactic cosmic rays (GCR).

   The National Academy of Sciences estimates that the differential cost between different solutions to this still unresolved GCR shielding problem is in the tens of billions of dollars[1]. The applicability of our database and simulation model of 1.8 A GeV ^{40}Ar seems particularly apt since the energy distribution of GCR peaks ~1 A GeV (Figure 1.6a) and the majority of the mass spectrum lies below Ar (Figure 1.6b).

[1] National Academy of Sciences (1996) *"Radiation Hazards to Crews of Interplanetary Missions"*

Figure 1.6a Energy Spectrum of Galactic Cosmic Rays[2]

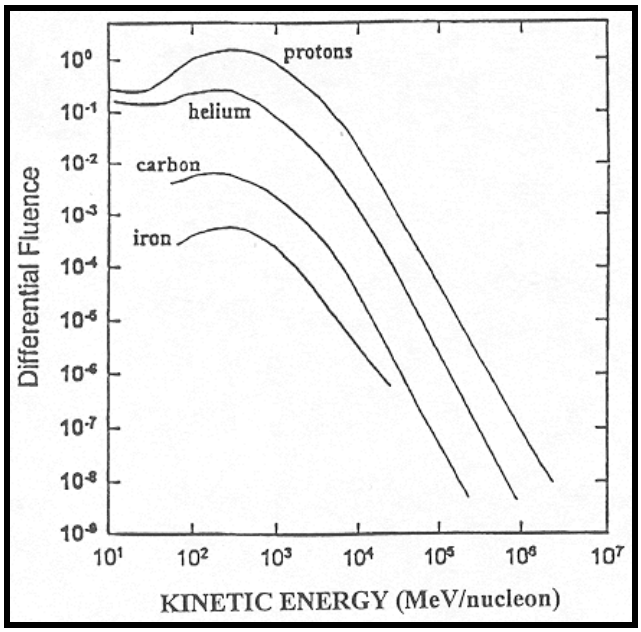

Figure 1.6b Mass Spectrum of Galactic Cosmic Rays

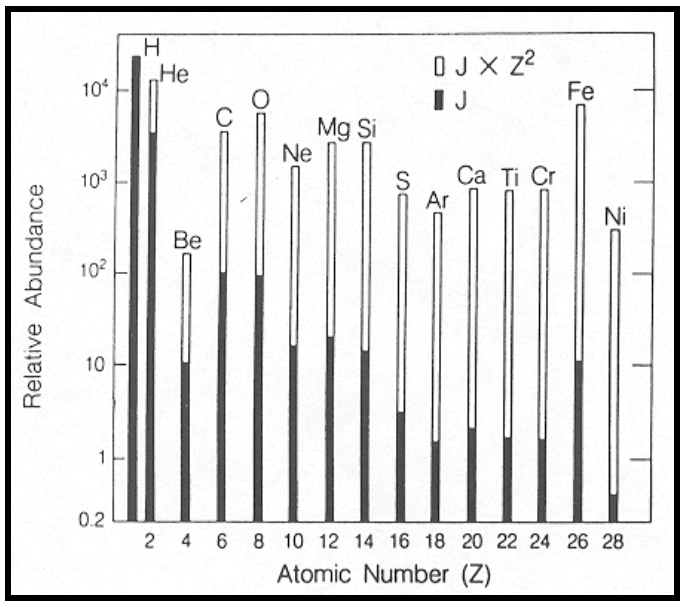

[2] Figures 1.6a,b both come from the National Academy of Sciences (1996) report.

3) If the phenomenological results unearthed in this work turn out to be physically real, then the unusual production cross-section phenomena of the secondaries of relativistic heavy ions (Chapters 9 and 10) could have a considerable impact on the modeling of relativistic heavy ions in astrophysical phenomena.

4) And if indeed this enhanced production due to secondaries turns out to be real and generalizable, potential applications may exist with respect to the accelerator-based transmutation of nuclear waste[1]. Depending on the actual physical processes underlying the production of ^{24}Na in relativistic argon-copper interactions, a more general enhancement of induced fission could play an important role in enhancing the ultimate technological feasibility of nuclear waste disposal through transmutation by relativistic heavy ions[2]. In particular, this phenomena may complement the other distinct advantages of heavy ions in inducing such transmutations. *But this very much depends on whether the underlying causes are local to the relativistic Ar-Cu interaction, or have a more general applicability*.

Chapter 2 that follows presents the background (physical, chemical and historical) for our use of nuclear emulsion; for the validity and advantage of our entire approach rests upon the precision of vision inherent in emulsion.

[1] This will be more than welcome by many parties, including most of the citizens of my home state Nevada… planned home of the United States' Nuclear Waste Repository.
[2] Bowman (1994)

II Nuclear Emulsions

2.1 Nuclear Emulsions: An Introduction

Nuclear emulsion is an amazing substance: silver halide crystals suspended in a gelatin of animal-based collagen. In spite of these seemingly 'low-tech' origins emulsions remain the most sensitive of detectors: making visible charged particles and nuclei through a chemical amplification of the atomic-scale disturbances caused by the passage of these charged particles. Simultaneous with its role as detector, nuclear emulsion is capable of acting as target. In so doing the use of nuclear emulsions subsumes a ladder of processes covering more than 10^{16} orders of magnitude.

As a matter of chemical fact nuclear emulsion is little different from conventional black and white photographic films, differing principally in the size and density of the silver-halide (mostly Ag-Br) crystals. Invented in 1871 by the physician Richard Lee Maddox, the gelatin-suspension of light-sensitive silver halide crystals was the first 'dry' photographic medium and rapidly superseded the "wet" colloidon (nitro-cellulose) process of photography[1]. The crucial difference between gelatin and colloidon (its "decisive advantage" in the words of C.F. Powell) is that gelatin is permeable to water. Hence after preparation it can be dried for easy transport and use; but after exposure it can be re-wetted, allowing the developing solution and subsequent chemistries access to the interior atoms of the emulsion. But inherent in this critical capability is a tendency towards geometric distortion of the emulsion sheet, a problem which must be finessed with great care in the laboratory.

The experimental physicist R.J. Wilkes adds that in the 130 years since its invention, no artificial substitute has displaced animal-based gelatin as the matrix material of choice;

[1] Maddox (1871) This, one of the great industrial revolutions of the 19th century, was announced in only 10 short paragraphs and heralded in these modest words: *"…a few remarks of another medium may perhaps not be uninteresting to the readers of this Journal, though little more can be stated than the result of somewhat careless experiments tried at first on an exceedingly dull afternoon. It is not for a moment supposed to be new, for the chances of novelty in photography are small (sic!)…"*

its superiority depending on "cattle's taste for an occasional bit of spicy greenery, since the trace amounts of sulfur in gelatin are crucial in the solid-state physics of trapping photoelectrons in the halide crystals" [1].

Whereas photographic film is by definition photon-sensitive, grains of nuclear emulsions are made developable by *virtual* photons, waves of ionization emanating from a charged particle's electric field as it moves through the emulsion. But like photographic film, nuclear emulsion is chemically developed and stabilized after its 'exposure' to charged particles. And like photographic film, under chemical development the initially opaque gelatin of the nuclear emulsion "magically" turns transparent: revealing to a trained eye the path of the charged particle…. suspended in the line of its history in space…. traced along a trail of shimmering black grains of silver.

Science may well understand the majority of solid-state processes involved, but as one who has worked extensively with photographic emulsions… one never tires of watching this transformation: that magical moment when translucence and form are together sculpted from opacity.

In spite of, partially because of, the complexity and inhomogeneity of the medium and process, nuclear emulsions offer the greatest of spatial and temporal resolutions (1μ and 10^{-12} sec). Comparisons with other detector technologies are seen in Figure 2.1. And after solid-state etchable plastics they are the most stable of all particle and nuclear detectors. It is hardly surprising then that emulsions have played an extensive and fundamental role in the history of experimental nuclear and particle physics. For as Barkas pointed out in his 1963 classic on nuclear research emulsion:

> *"....emulsion has no great advantage when one is looking for a particle of predicted properties. It is of greatest use [however] for discovering utterly new things, the anomalous behavior of which often can be recognized unambiguously from a single event. Thus for example, the tau meson was established firmly by a single event, despite the fact that it took a long time to find another example of this decay mode."* [2]

[1] Wilkes (1997)
[2] Barkas (1963), p.5 [All references to Barkas are from this volume]

Figure 2.1 Space-Time Resolutions of Detector Technologies[1]

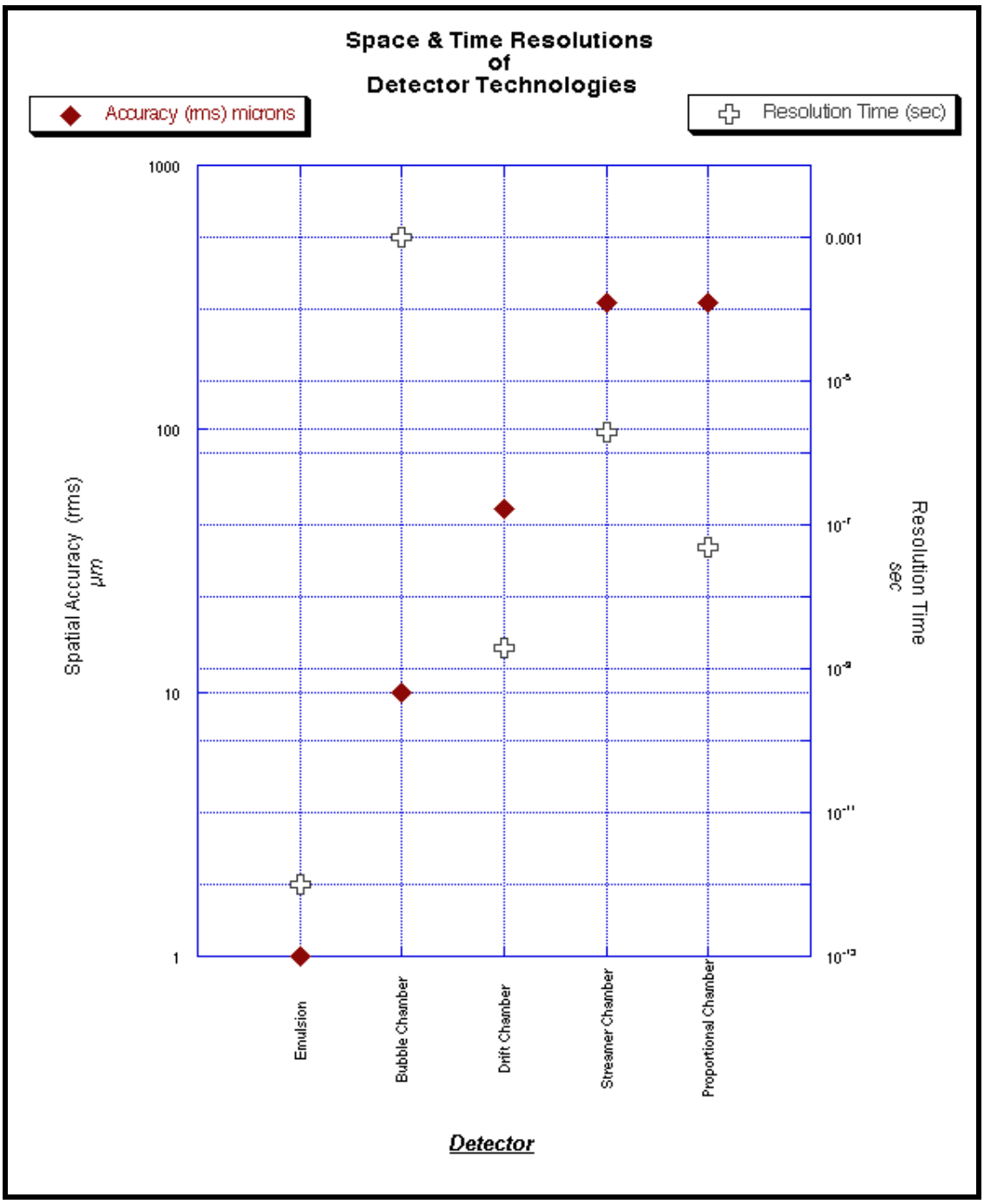

[1] Particle Data Group (1996), p. 132

Fermilab's extensive use of emulsions over the past few years leading to its discovery of the tau neutrino is a recent example. This broader point is well demonstrated in a list of fundamental discoveries and their means:

Table 2.1 Discoveries and their Means[1]

Discovery	Instrument
X-rays	*Fluorescent Screen & Emulsion*
Radioactivity	*Emulsion (Becquerel)*
γ–rays	*Emulsion (Villard)*
α	*Electroscope and Emulsion*
β^-	*Electroscope and Emulsion*
Π^+	*Emulsion*
Π^-	*Emulsion*
Π^o	*Counters and Emulsion*
Λ	Cloud chamber
K^+	*Emulsion*
K^-	*Emulsion*
K^o	Cloud chamber
Σ^+	*Emulsion*
Σ^-	Cloud chamber
Σ^o	Bubble chamber
Ξ^-	Cloud chamber
Ξ^o	Bubble chamber
$\bar{p}$	Counters
$\bar{n}$	Counters
Λ^-	*Emulsion*
ν_τ	*Emulsion*
Doubly Strange Nuclei	*Emulsion*

[1] The core of this list is taken from tables compiled by Powell (1959) and Barkas (1963). Not surprisingly they could not include the ν_τ or the doubly strange nuclei.

Surprisingly missing from the lists of both, however, was *the discovery of radioactivity itself* in 1896. For it was the chance juxtaposition of uranium and photographic paper (emulsion) that the fields of radiochemistry, atomic, and nuclear physics were initiated by Becquerel (Becquerel 1896a,b).

Indeed a reading of the earliest papers of radiochemistry and atomic physics shows that the first researchers, from Madame Curie* onward continued to rely on emulsions as a principal detector; especially for the qualitative authentification of the radioactive property itself. And little recognized is the role played by emulsions in Rutherford's discovery of alpha and beta radiation (then known as a and b radiation).

(from the "The Collected Works of Lord Rutherford of Nelson," vol. I, p. 169)

Uranium Radiation and the Electrical Conduction Produced by It

by E. RUTHERFORD, M.A., B.SC.
formerly 1851 Science Scholar,
Coutts Trotter Student, Trinity College, Cambridge;
McDonald Professor of Physics, McGill University, Montreal.

From the Philosophical Magazine for January 1899, ser. 5, xlvii, pp. 109-163
Communicated by Professor J. J. Thomson, F.R.S.

§ 1. *Comparison of Methods of Investigation*

The properties of uranium radiation may be investigated by two methods, one depending on the action on a photographic plate and the other on the discharge of electrification. The photographic method is very slow and tedious, and admits of only the roughest measurements. On the other hand, the method of testing the electrical discharge caused by the radiation is much more rapid than the photographic method, and also admits of fairly accurate quantitative determinations.

The question of polarization and refraction of the radiation can, however, **only** be tested by the photographic method. The electrical experiment (explained in §2) to test refraction is not very satisfactory.

(emphasis LL)

---

* See for example *"Rays Emitted by Compounds of Uranium and of Thorium"*
A Note by Mme Sklodowska Curie presented by M. Lippmann, Comptes Rendus 126, 1101-3 (1898)

Rutherford's paper is remarkable in another less recognized way. It is the earliest discussion of what has become the divergence between solid-state detectors (emulsions and plastics) and electronics-based digital detectors[1]. In so doing it presages the critical point made above by Barkas, and which is fundamental to the present work:

> *For a critical class of measurements, especially when being used to explore phenomena whose properties and parameter remain unknown… there is often no satisfactory alternative to (nuclear) emulsions.*

2.2 The Birth of the Modern[2]

The emulsions used above were of course the black and white photographic emulsions of the time. A fascinating overview of the history of the photographic emulsion is found in C.F. Powell's classic "The Study of Elementary Particles by the Photographic Method" [Powell, 1959]. Within the field of nuclear emulsions it is simply referred to as 'The Bible'. The following "pre-history" of nuclear emulsions owes much to this source, as well as to Peter Galison's tour-de-force, "Image and Logic" (1997).

Powell points out that one of the pioneers of photography, Niepce (who first made emulsions of silver halides, but with a water soluble matrix of starch and albumen), actually observed as early as 1867 "that photographic plates were fogged by salts of uranium even when sheets of paper were interposed between them'. Yagoda (1949) has remarked that had this observation been attended to… radioactivity is likely to have been discovered thirty years before it actually was.

Most curieously Powell, like Barkas, overlooks the first two decades of emulsion's contributions to atomic physics (Rutherford, Curie, and others); but starting with the work of Mugge (1909) and Kinoshita (1910, 1915) he presents an extensive discussion of its "development" and uses in nuclear physics. Emulsions explicitly designed to be

[1] This is also the beginning of the divergence between detectors based on visual images and those based purely on numerical outputs; i.e. between *Image and Logic*…see [Galison 1997]

[2] With thanks to the author Paul Johnson for the expression

sensitive to charged nuclear particles began to be developed in 1927 by Myssowsky and Tschishow who also made stereo-photographs of alpha-particle tracks, thus anticipating by decades the use of stereographic images in bubble chambers. But the first major breakthroughs began in 1935 (Zhdanov and Ilford Limited), followed in 1945 by the creation of new more concentrated emulsions (Demers and Ilford). Then in 1948 Kodak developed an emulsion sensitive to (an electron's) minimum ionizing radiation.

The stage was thus set for nuclear emulsions to relinquish their coarse imprecise characteristics ("admitting only the roughest of measurements" as Rutherford characterized them in 1890) to become the most sensitive of particle detectors. Whereas in the decades prior to 1945, emulsions were used primarily to confirm phenomena or particles discovered by other means (Marietta Blau's work[1], nothwithstanding), these new modern emulsions rapidly proved their worth in the hands of Cecil Powell and his collaborators at Bristol. Within weeks came the discovery of the π-meson by Cesar Lattes (1947), followed shortly by the discovery of heavy nuclei in cosmic rays by Phyllis Freier (1948)[2].

Powell later described the first examination of the new emulsions exposed at high-altitude as

> *" a whole new world. It was as if, suddenly, we had broken into a walled orchard, where protected trees flourished and all kinds of exotic fruits had ripened in great profusion".*[3]

Occhialini's description of the atmosphere at Bristol is more personal:

> *" Unshaved, sometimes I fear unwashed, working seven days of the week till two, sometimes four in the morning, brewing inordinately strong coffee at all hours, running, shouting, quarrelling and laughing, we were watched with humorous sympathy by the war-worn native denizens of the Royal Fort. . . . It was a reality of intense, arduous and continuous work, of deep excitement and incredibly fulfilled dreams. It was the reality of discovery…".*[4]

[1] Galison (1997) pp. 146 – 160
[2] Both Lattes and Freier were graduate students at the time.
[3] Owen Lock, CERN Courier, June 1997
[4] Owen Lock, CERN Courier, June 1997

A necessary counterpoint is offered by Peter Galison[1]:

> " These "fruits' (pions, kaons, the anti-lamda-zero, the sigma plus, a myriad of new decay patterns) helped seed the new field of elementary particle physics, and because film was cheap and transportable, it offered the Europeans a chance to use mountaintop cosmic rays to compete with American accelerators. At the same time, both in the United States and in Europe, emulsion physicists stood on precarious ground…
>
> …..new particles burst on the scene. Some, like the pion, dramatically altered physicists' notions not only about what kind of entities populated the world, but also about underlying conceptions of the forces that bind matter together — **though some of these new stars of the submicroscopic stage exited just as quickly. For the clumps of darkened silver were rife with instabilities, immersed in visual noise. Tracks faded over time, while new, spurious tracks could conflate with "genuine" ones at any time during the film's lifetime. During development and drying, emulsion and paper backings bent, distorting tracks and making one kind of event look like another. Physicists fretted in their notebooks, letters and meetings that scanners might only see what was expected in the events. And all this became even more complex as physicists joined in ever larger collaborations where conclusions had to be negotiated at far-flung distances."** *(emphasis LL)*

Nonetheless the development of these " modern" nuclear emulsions has led to a cornucopia of applications well beyond the domains of nuclear and particle physics. Biological and in-vitro biochemical autoradiography is but one notable example. Some are described in Powell, but many others have been developed only more recently. An excellent chronicling of these developments is in successive volumes of the *International Conferences on Solid State Detectors* along with those of *Nuclear Tracks in Solids.* It is to be hoped that our present use of emulsions will only honor this tradition of novel exploration and unanticipated discoveries. But if we hope to do so, we must take sufficient care to understand and compensate for the difficulties inherent in this technology; for its complexity is commensurate with its capabilities. We focus now on those aspects of nuclear emulsions integral to our own experiments.

[1] Peter Galison in "How Do You Track a Cosmic Ray?" <www.hrc.wmin.ac.uk/noise/content/materialtracks/texts.html>

2.3 Properties of the Modern Nuclear Emulsion

Emulsions share with bubble-chambers a significant experimental capability: to be simultaneously both target and detector. But nuclear emulsions go a remarkable step further…they essentially ”take their own picture”.

Each of these three functionalities in emulsions (target, detector, recorder) is due to different scales of phenomena acting upon the same atomic ingredients. Because our present work makes use of all three functionalities, they recommend themselves as the axes around which to outline the physical/chemical properties of nuclear emulsions. For in the end (and especially at the beginning!), the most natural way to deal with our experimental design has been to pay attention to emulsion’s basic functionalities and the bridges between them. By bridges we mean the self-organizing bootstrapping of functionality between scales. The ‘bridge’ from target to detector is via the target-like attribute of the collective electron density (mediated through ionization effects). The bridge of detector capability to self-recording is provided by the solid-state properties of the gelatin matrix which allow the finely tuned balancing acts of silver ion stabilization vs. migration to occur. Ultimately, this 'separation by function' is implicit in our collective experimental and theoretical actions.

To make the results of a computer simulation of a beam of particles traveling through a stack of nuclear emulsion meaningfully congruent to a similar beam going through a stack of copper cylinders… we must deal only with the target-like properties of each. Then we must transform the results of scanning and measurement into a sense of the local physics that has occurred. For it is only the detection of the local physics derived and inferred from the measurements, and not the measurements themselves, which provides a realistic base of our Monte Carlo simulation. In so doing we must balance emulsion's capabilities as a detector against the limitations, errors, and noise induced by emulsion's self-recording process, its chemical development.

2.4 Nuclear emulsion as 'Target'

All of the above is applicable to nuclear emulsions in general. Because Ilford's G5 emulsion has been used exclusively in this work, only the specifics of G5 emulsion will be presented in any detail. Table 2.1 shows a number of compositional properties of Ilford's G5 emulsion.

Table 2.2 Compositional Properties of Ilford G5 Emulsion[1]

Z	Atomic Weight	Concentration	N	n_e=NZ	σ_1	Nσ_1	σ_2	Nσ_2
		g/cm^3	atoms/cm^3 X 10^{-22}	e$^-$/cm^3 X 10^{-22}	barns	cm^2 x 100	barns	cm^2 x 100
Ag	107.880	1.8170 ± 0.0290	1.0150	47.69	1.395	1.4160	1.1025	1.0400
Br	79.916	1.3380 ± 0.0200	1.0090	35.31	1.144	1.1540	0.8410	0.8480
I	126.920	0.0120 ± 0.0002	0.0057	0.30	1.558	0.0089	1.1440	0.0065
C	12.010	0.2770 ± 0.0060	1.3890	8.34	0.323	0.4490	0.2370	0.3300
H	1.008	0.0534 ± 0.0012	3.1920	3.19	0.062	0.1980	0.0455	0.1450
O	16.000	0.2490 ± 0.0050	0.9370	7.50	0.391	0.3670	0.2870	0.2690
N	14.008	0.0740 ± 0.0002	0.3180	2.23	0.358	0.1140	0.2630	0.0840
S	32.066	0.0072 ± 0.0002	0.0136	0.22	0.623	0.0084	0.4570	0.0062

The mean atomic number is 13.30 (close to Al), while the mean atomic number minus hydrogen is 21.67 (between the metals Sc and Ti). According to Shapiro (and Barkas) the total geometric cross section of G5 emulsion, including hydrogen, is equivalent to a mean free path of 26.9 cm or 103.0 g/cm^2 (multiplied by the density 3.8 g/cm^3**).** But this figure is a theoretical one based on the simplistic geometric notion that a nuclear radius $R= r_o A^{1/3}$, where A is the atomic mass number and r_o is the Compton wavelength of the pion (~ 1.4 x 10^{-13} cm). The more accurate experimental figure[2] for the mean free path of protons in G5 emulsion is ~35 cm or 133 g/cm^2. (That this value is close to that of copper, 135 gm/cm^2, will be useful when applying emulsion results to our simulations in copper.)

[1] Shapiro (1956), p. 382.
[2] Particle Data Group (1978); Otterlund (1975)

2.5 The Geometric Interpretation of Nuclear Cross-Section (Bradt-Peters Formalism)

We can further divide the component atoms of nuclear emulsion into heavy and light elements (along with hydrogen). These groupings will be critical in our scanning, analysis, interpretation, and simulation.

Table 2.3 Relative Weights and Cross-Sections of Emulsion Atoms[1]

	Including Hydrogen		Excluding Hydrogen	
	Relative weight (%)	*Relative* Σ_t ($N_i\sigma_i$) (%)	*Relative weight (%)*	*Relative* Σ_t ($N_i\sigma_i$) (%)
Ag, Br, I	82.7	69.4	83.9	73.3
C, N, O, S	15.9	25	16.1	26.6
H	1.4	5.3		

Due to a saturation of nuclear densities with increasing mass, nuclei larger than alphas (especially for Z>5) tend to have a constant volume per nucleon. This argues for a geometric consideration of nuclear cross-sections (above a few hundred MeV). In such a geometric approximation nuclei are spherical and interaction will occur if their impact parameter (i.e. spatial separation) is less than the sum of their radii. Bradt and Peters [Bradt 1950] first worked out a formalism for this empirical approach, and which has subsequently been applied to both charge-changing and non-charge-changing interactions.

One of many formulations of the Bradt-Peters relationship for the interaction cross-section of a projectile nucleus of radius R_p and a target nucleus R_t is

$$\sigma = \pi (R_t + R_p - R)^2 \qquad (2.1)$$

where $R_{t,p} = R_o (A_{t,p})^{1/3}$ and a single nucleon radius is taken to be $R_o = 1.45 \times 10^{-13}$.

The latter term, R, has to do with nuclear surface transparency, but is experimentally determined and here taken to be $R = 1.17\ R_o$.

Particularly useful is the fact that the Bradt-Peters approach predicts the *mean free path* (mfp) as the experimentally measurable quantity as opposed to the cross-section. In particular, for a composite medium such as emulsion made up of different atomic species, but with bulk density ρ, the mean free path denoted by λ is

$$\lambda = (\langle A \rangle / N\rho)(\Sigma c_i \sigma_i)^{-1} \qquad (2.2)$$

where $\langle A \rangle$ is the average atomic number

$$\langle A \rangle = (\Sigma c_i A_{Ti}) / \Sigma c_i \qquad (2.3)$$

N is Avogadro's number, the cross-section for the *i*-th atomic species is σ_i , and c_i is the atomic fraction of the target species *i*. Applying this to G5 emulsion yields the following relative frequencies of collisions with the three constituent classes of emulsion (by mass) along with the corresponding interaction lengths.

Table 2.4 Corresponding Interaction Lengths and the Relative Frequencies of Collisions of Nuclei Classes as deduced from the Bradt-Peters Formula[1]

G5 Emulsion	Incident nuclei					
Target nuclei	H	He	Be	N	Si	Fe
H	4	8	11	14	17	20
CNO(S)	24	28	29	30	31	31
AgBr(I)	72	64	60	56	52	49
Interaction Length (cm)	28	20	15	13	9.7	7.1
Interaction Length in Air (g/cm^2)	72	45	33	28	20	14

[1] Shapiro (1956), p. 383
[1] Powell (1959), p. 606

The Bradt-Peters formula is considered in this case to be accurate to ~15%. Anticipating some of our measured results in Chapter 4 we found the average mean free path of He in our emulsions to be 22.53 ± 0.91 cm. This is consistent with a host of other measurements of relativistic alphas in emulsions and discussed more fully in Chapter 4. Hence, for nuclei in the regime that we are considering, this experimental agreement offers necessary (though hardly sufficient) support for a straightforward interpretation of nuclear cross-sections as geometrically-based. *An excellent up-to-date review of both the theoretical and experimental approaches to the geometric modeling of nuclear cross-sections is found in Nilsen (1995).*

2.6 The *Question* of the Constancy of Emulsion Compositions

The compositional table (Table 2.2) has been the accepted standard for G5 for almost a half-century, and is based upon two communications from C. Waller of Ilford's Research Laboratory[1]. Ostensibly at the request of Occhialini, Waller was the actual designer of the first modern nuclear emulsions (those used to find the π-meson). Peter Galison has a slightly different, though not inconsistent, take on the origins of these modern nuclear emulsions[2]:

> " Ever since Marietta Blau began using dental x-ray film to track cosmic rays in 1930s Vienna, the making of nuclear emulsions was a delicate, even black art somewhere between physics and chemistry. Sensitivity and instability went hand in hand as physicists signed a remarkable concord with the industrial chemists. Just after World War II, flush with successful production of emulsions for the atomic bomb project, Kodak and Ilford made an offer that the physicists could hardly refuse. Roughly:
>
> *"If you physicists agree, we will produce for you an emulsion so extraordinarily sensitive that it will register every possible charged particle. You will have a nuclear physics instrument more powerful than anything anywhere. Nonetheless — and you must pay this heed — emulsion manufacture is a highly secretive and proprietary business. Neither now nor in the future will you ever know precisely what is in these emulsions nor how we prepare them."*
>
> The physicists signed*."*

[1] My own inquiries to Ilford resulted in claims virtually identical to those listed above.
[2] Peter Galison in "How Do You Track a Cosmic Ray?" <www.hrc.wmin.ac.uk/noise/content/materialtracks/texts.html>

The above underlines a curiosity about commercially available nuclear emulsions. Unlike the overwhelming majority of scientific instrumentation (which are typically built and understood 'to spec' by the scientific community at all levels of construction) the actual content and manufacture of nuclear emulsions has remained a trade secret. This is true for all the companies that manufacture them (Ilford, Kodak, Fuji), and is hardly an isolated perspective.

Barkas puts it thus[1],

> *"…one cannot assume blindly that the behavior of emulsion gel is the same as that of gelatin. There are many reasons to believe that manufacturers of nuclear research emulsions may alter the gel so that it no longer has the properties of natural gelatin."*

Proving the larger point here is the relative availability of manufacturing details for the ultra-fine-grained emulsions of one of the scientific pioneers of the field, Demers. In practice of course there is no reason to consider this ignorance a problem; especially with the typical consistency of mean free paths measured in these emulsions. But consideration of this matter goes beyond a socio-economic curiosity when one must consider all of the variables that could *potentially* effect emulsion-based experiments purporting to show mfp's substantially different than the otherwise accepted norms.

Or as Powell is quoted as saying[2],

> *'In all our work we rely on the Principle of Uniformity of Nature; that is, we believe that if the same experiment is performed several times in exactly the same way, then the results will be the same. However I do not believe that there is also a Principle of Uniformity of Nuclear Emulsion, except by the grace of the manufacturers.'*

---

[1] Barkas (1963), p. 65
[2] Galison (1997), p. 225

Additional information from Mr. Waller's early measurements of G5 showed a variation in density with a sample of 40 batches, and at various relative humidities:

Table 2.5 Effects of Relative Humidity on Density for G5 Emulsion[1]

Relative Humidity	*Density (g/cm^3)*		
	Lowest Batch	*Mean*	*Highest Batch*
Dry (HSO)	4.033	4.062	4.113
32%	3.922	3.962	4.002
58%	3.811	3.852	3.892
84%	3.592	3.63	3.671

A 10% variation is evident. That this has a potential import can be seen in the electron density $\mathbf{n_e}$ for emulsions as a function of density ρ (where the density variations are due solely to the relative humidity). Shapiro derives the following expression[2]:

$$\mathbf{n_e = (0.1037 + 0.2468\ \rho)\ x\ 10^{24}\ \ electrons/cm^3} \qquad \mathbf{(2.4)}$$

which he claims to be good to ~0.1% for most nuclear emulsions. The importance of the electron density for what is essentially a multi-scale set of ionization processes is obvious.

Peter Galison, again[3]:

> *"The other day I was talking to [Ilford],"* one American physicist confided, *"and I told him that we take great care to keep the emulsion packages well sealed, so that we can be sure that the water content is always that which corresponds to the relative humidity of 50% at which the emulsions are dried and packed at Ilford's".*
>
> Oh, responded the Ilford chemist, *"but we don't have the time to let the emulsions reach equilibrium*." Suddenly the physicist's interpretations were thrown into doubt: the emulsions might vary from batch to batch, package to package, or even pellicle to pellicle. Measuring Nature's consistency would depend on that of the Manufacturer."

---

[1] Shapiro (1956), p.383
[2] Shapiro (1956), p.386
[3] Galison (1997), p. 224

In reality all of this merely requires that which is required by the rigorous methodology of science in the first place: sufficiently large error bars to cover potential systematic effects and most importantly… alternative checks for any new effect claimed. The "problem" here, of course, is that emulsions have sensitivity limits not easily replicated by other technologies: in particular their ability to resolve trajectory information at a length-scale of a micron, and a time-scale as fine as 10^{-12} seconds. For ultra-short lived phenomena involving charged particles, emulsions are unique.

2.7 Nuclear Emulsion as Detector-Recorder

Essentially all charged particle detectors function as a consequence of ionization phenomena. The reaction of an emulsion to the passage of a charged ionizing particle depends (somewhat simplistically) on the following emulsion characteristics:

1) The distributions of size, density, and spatial packing of silver halide crystals in the gelatin matrix

2) The probability of a given ionizing particle to create a *latent image* due to its activation of a silver halide crystal

3) The development and stabilization processes of the post-exposure emulsion

The most important difference between nuclear and photographic emulsions is the silver halide content. As in standard photographic imaging, nuclear emulsions' role as a detector rests upon the sensitivity of silver halide crystals; in particular their capacity to become *developable* by the addition of only a small amount of energy.

A silver halide crystal which has absorbed sufficient energy to be *activated* is said to have a *latent image*. Functionally, activation of a silver halide crystal means that under development it is more readily convertible to metallic silver. Atomically, this is understood to occur in the AgBr crystal through the creation of small nucleation sites of at least four atoms of silver. But only through the application of a development process, still something of a 'black art', does latency become reality and activated crystals grow into silver grains 2-3 times their original size.

Developers can be either chemical or physical. Chemical developers are typically reducing agents with sulfur compounds being especially important. But physical development by itself is also possible. Physical developers contain silver (or other metal ions such as gold) and deposit them directly onto the activated latent image centers. However, latent image centers susceptible to physical development alone need several times the initial exposure or activation energy than those developable by chemical agents. Complicated beasts that they are, nuclear research emulsions generally use a combination of both chemical and physical development processes[1].

In reality, a number of secondary environmental variables can also affect an emulsion's response to an experimental exposure. These include pre-exposure mechanical handling, temperature and humidity variations, exposure to light, and a host of subtle chemical treatments (intentional and otherwise). We will have to come back to these secondary variables when discussing possible errors in the measurement process. But because the work being presented here uses emulsions acquired post-exposure and development we will not go into detail on these matters, referring the interested reader once again to the classic texts by Powell and Barkas.

The above clearly shows that nuclear emulsion's functional capabilities as detector and recorder are intimately connected. In practice, one does not exist without the other. That is, we do not ordinarily expose emulsions, and then read the history of the events without development. Nor does one normally develop and record tracks without an exposure.

But in the interest of better distinguishing the physics from the chemistry of emulsions, and of our subsequent use of each, we shall first treat independently the "detector" aspect. We'll do this by first considering only the primary response of emulsions to the passage of ionizing particles. The advantage to us is that the first two sets of processes more closely follow from the physics of the interactions of primary and secondary particles with the emulsion. For it is the delineating of *this* physics that is the true focus of all our emulsion scanning efforts, being the experimental core of the Monte Carlo simulations to be described in Chapter 6.

[1] see Barkas (1963), p.41

Development can then be looked at as a chemistry-based amplification of the physics signal. The *recording* functionality of emulsions is of course dependent on this development process, which is in fact the intermediary step (the *bridge* in previous terminology) from the actual physics to our measurements and inferences about the 'actual' physics. Hence our focus in the next chapter, on the methodology of the scanning experiment, will in large part be dependent on the visual effects, limitations, and artifacts of this development process.

2.7.1 Nuclear Emulsion as *Detector*

An important experimental justification for this separation by functionality is the fact that development of conventional photographic emulsions can drastically change the ultimate contrast, itself highly dependent on differences of the exposure to light. But in nuclear emulsions the contrast (hence the ease in distinguishing tracks) is relatively insensitive to such differences of development. This directly follows from the way in which grains are activated in the first place: not by the continuous loss of energy *(dE/dx)* that a charged particle undergoes when moving through a 'sea' of stationary charges….but instead by the local emission of individual energetic delta-rays ('knock-on' electrons by any other name).

Details of this process will be discussed much more fully in the next chapter, but for our present concern this is a clear demonstration of the *local* and *target-like* nature of the detection process. The activation of each silver halide crystal is thus an "undeveloped snapshot" of the very local energy emission of the projectile particle moving through the emulsion, and with a resolution of the scale of the individual crystals.

In other words, the physics stays local.

In G5 emulsion this means that one has spherically symmetrical detectors, each considerably less than 1 μ in diameter. This is nicely seen in the following pictures of undeveloped G5 emulsion, the spherical objects in both images being undeveloped silver halide crystals.

Notice especially the uniformity of its crystal size (Figure 2.2a). This is not true for all nuclear emulsions, G5 being known especially for this property, with its size distribution being characterized by[1]:

Mean Diameter $\langle D \rangle = 0.275\ \mu$

Variance of diameter, $\sigma^2 = 0.0022\ \mu^2$

Asymmetry of Distribution $\langle (D - \langle D \rangle)^3 \rangle = -1.7 \times 10^{-5}\ \mu^3$

Note also in Figure (2.2b) the uniformity of the area distribution of the silver halide grains.

Figure 2.2.a Electron Microscope Image of Undeveloped G5 Emulsion Grains[2]

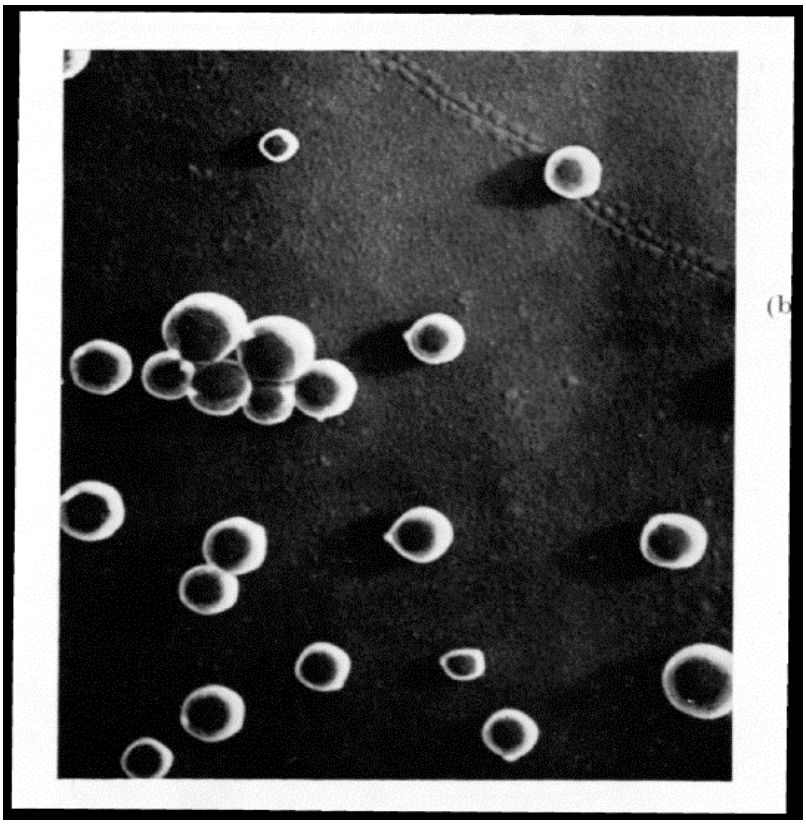

[1] Grain statistics from Barkas (1963), p. 62

[2] Both Figures (2.2a,b) are from Powell (1959), each at 20K X magnification

Figure 2.2.b Electron Microscope Image of Undeveloped G5 Emulsion Grains

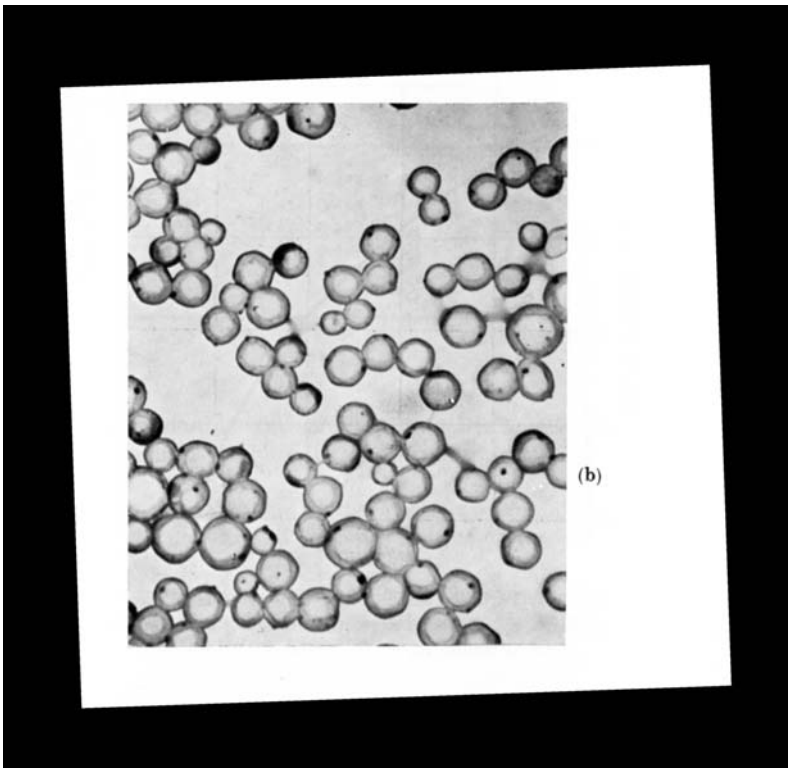

That this inherent spatial resolution far surpasses any other detector technology is well known. What is rarely recognized however is that this is at the very limit of optically-based visualization. For in Powell's words[1]…

> *" in its present stage of development, the average grain-size in emulsions able to record the tracks of particles of charge **e** at minimum ionization (between 0.1 and 0.4) corresponds approximately to the smallest size of grain that can be resolved with optical equipment of the highest quality."*

[1] Powell (1959), p. 52

2.7.2 Nuclear Emulsion as Recorder

Upon development, what we see is opacity. When properly developed (and thin enough) the matrix of the emulsion turns transparent. Unactivated silver halide crystals are washed out of the emulsion, leaving in principle only the activated crystals… now grains of silver. The geometries, topologies, and noises of these remaining grains is the topic of the next chapter, but a summary of key track characteristics is of use:

> Tracks themselves are microscopic rows of developed silver grains ~0.5 – 0.8 microns in diameter. Tracks may be called black, grey, or thin depending on the rate of ionization loss of the moving charged particle and the sensitivity of the emulsion. The geometry is straight if made by a fast particle, crooked if made by a slow one. Large deflections are due to nuclear encounters and small-scale deflections result from multiple Coulomb scattering. [Shapiro 1956]

All of this suggests to us that classical linear geometry plays a fundamental role. This is a non-trivial conclusion, for it is fundamental to the accuracy of our scanning, a correct interpretation of measurements taken, and our construction of a physically meaningful geometrically-based simulation.

The length of a track may range from 1 or 2 microns to centimeters, but accompanying the idealization just described is an assortment of physical distortions randomly distributed throughout the emulsion. Depending on the emulsion sensitivity, these include a fringe of delta rays (secondary electron tracks) clotted about the trajectory. Additionally, the emulsion itself will have undergone a serious contraction in the z-direction, necessitating appropriate corrections. Meanwhile, diffusion-limitations of the development chemistry insures that the development process itself will be uneven throughout the emulsion. This too must be 'corrected' for.

Other problems resulting from the development will be treated in the next chapter on the measurement process, but the bottom line is this: *The development process, necessary as it is to the very function of emulsions, also adds a considerable amount of noise to the signal of the passage of the charged particle.*

2.8 Limitations of Nuclear Emulsions

Other limitations exist as well, the biggest being an economic one. The experimental use of emulsions requires an **ENORMOUS** amount of backbreaking, eye-irritating work …. all of which must be done by well-trained and experienced workers in a obsessively-careful and disciplined manner. And like any other experimental technique it has its own set of measurement problems. Details will be treated in the next chapter (*Methodologies of Scanning and Measurement*) so the principal sources of error and inherent limitations will only be mentioned here by name.

The Physical Emulsion

Sensitivity issues:

- Detection efficiency
- Intrinsic signal/noise
- Environmentally induced noise

Stability:

- Fading of latent image
- Stability after processing

Geometry:

- Environmental effects (of humidity)
- Expansion/Contraction of the gel as a function of processing

Human/Mechanical Factors

Scanning

- Efficiency
- Economics

Measurement Errors:

- Limitations of equipment *(such as the mechanical controls of scanning microscopes)*
- Limitations of technique *(such as the measurement of charge for Z>6)*

2.9 Advantages of Nuclear Emulsions

Along with Figure 2.1 the following qualitative outline clearly shows why nuclear emulsions are still so often resorted to for exploratory and authenticating purposes – even in experiments designed around other types of detectors.

1) Stopping power → Resolution in time
   (resolution in space when coupled with #2)

2) Microscopic size of grains →
   a) Resolution in space
   b) Resolution in time
      (time resolution also due to high ionization rate → observation of short-lived phenomena)
   c) High angular resolution
   d) High information density

3) Continuous sensitivity

4) Stabilization
   (#4 with #3 yields ability to integrate over time… and space if the emulsion is moving)

5) Direct observability of the action and path of a charged-particle

6) 3-dimensional 4-π recording geometry
   (Unlike bubble and cloud condensation chambers the 3-D perspective of emulsions is continuous and not 'reconstructed)

These properties, taken together, are little short of amazing for this earliest of all particle detectors. Proper use requires a substantial effort, but offers potentially great rewards. For as Barkas has said with such eloquence,

"(Though) emulsion has no great advantage when one is looking for a particle of predicted properties... it is of greatest use for discovering utterly new things. "

III. Methodology of Scanning and Measurement

In the previous chapter we introduced both the general and the functional properties of nuclear emulsions. We continue now with a description of how our particular emulsion experiments were done.

A stack of nuclear emulsions was exposed by Dr. Harry Heckman of Lawrence Berkeley Laboratory (LBL) 1.8 A GeV argon nuclei at Berkeley's Bevalac. Our stack components were identical to those used in Aleklett et al, being Ilford G-5 emulsions (10 x 20 x 0.06 cm each). After processing and development at LBL we were provided with the interior plates.

In the work described here we have used this stack to perform two different but complementary emulsion experiments. The first was to create a database of stars to act as the core of a set of Monte Carlo simulations of a relativistic argon beam directed against both emulsion and Cu targets. The second experiment took advantage of the large number of stars being measured in the "first" experiment to examine the mean free paths of various secondaries.

Although functionally interdependent, it should be obvious that scanning and measurement are not at all the same thing. *Scanning* embodies an approach to the finding of tracks and stars in the first place. *Measurements* are then performed upon the discovered stars and tracks. Because work with emulsions is so time consuming we needed to make a priori decisions as to what was to be measured and how. These initial decisions were in turn guided by the information needed for the primary job of the scanning team: creation of the Monte Carlo database focusing on the exploration of the relativistic components of the relativistic heavy ion interactions.

For example: one of its principle foci was a simulation of the Copper Calorimetry Experiments performed at LBL by Friedlander, Brandt, Seaborg, Hoffman, and colleagues [Aleklett et al 1987, 1988]. Because the production of ^{24}Na has a fairly steep threshold for production around 1 GeV (see Chapter 7) these experiments used the

production of ^{24}Na as a novel form of threshold counter for relativistic interactions. Detailed information on the high-energy components (> 1 GeV) is therefore essential, but lower energy particles can essentially be ignored. This allowed us to seriously limit the extent to which the low-energy end of the particle spectrum needed to be examined and measured. Hence, along with a discussion of the scanning and measurement processes themselves, this chapter will also discuss more completely those properties of emulsions relevant to these initial decisions.

3.1 ***What can we observe….What do we observe?***

Observation is the common thread linking scanning and measurement. So let us back-track for a moment and ask of emulsions as to what in principle can we observe?

The answer is deceptively simple: after development *all that we see is opacity*….
the opacity of the silver grains, sole survivors of the emulsion's pre-exposure crystal population. All that we observe and measure in emulsions, extrapolate from, simulate and infer are based upon simple patterns of opacity -- grain densities, grain topologies, and grain geometries. Indeed, these patterns are so deceptively simple that in essence there are only two basic designs… stars and tracks.

This is best illustrated in a style of physics presentation also pioneered by Powell: the visual atlas. Let us examine at successively finer scales a relativistic argon nucleus undergoing a central collision with 5 alphas as secondaries*.

* Image from LBL (XBB 771-32)

Figure 3.1 Relativistic Argon Track in Emulsion

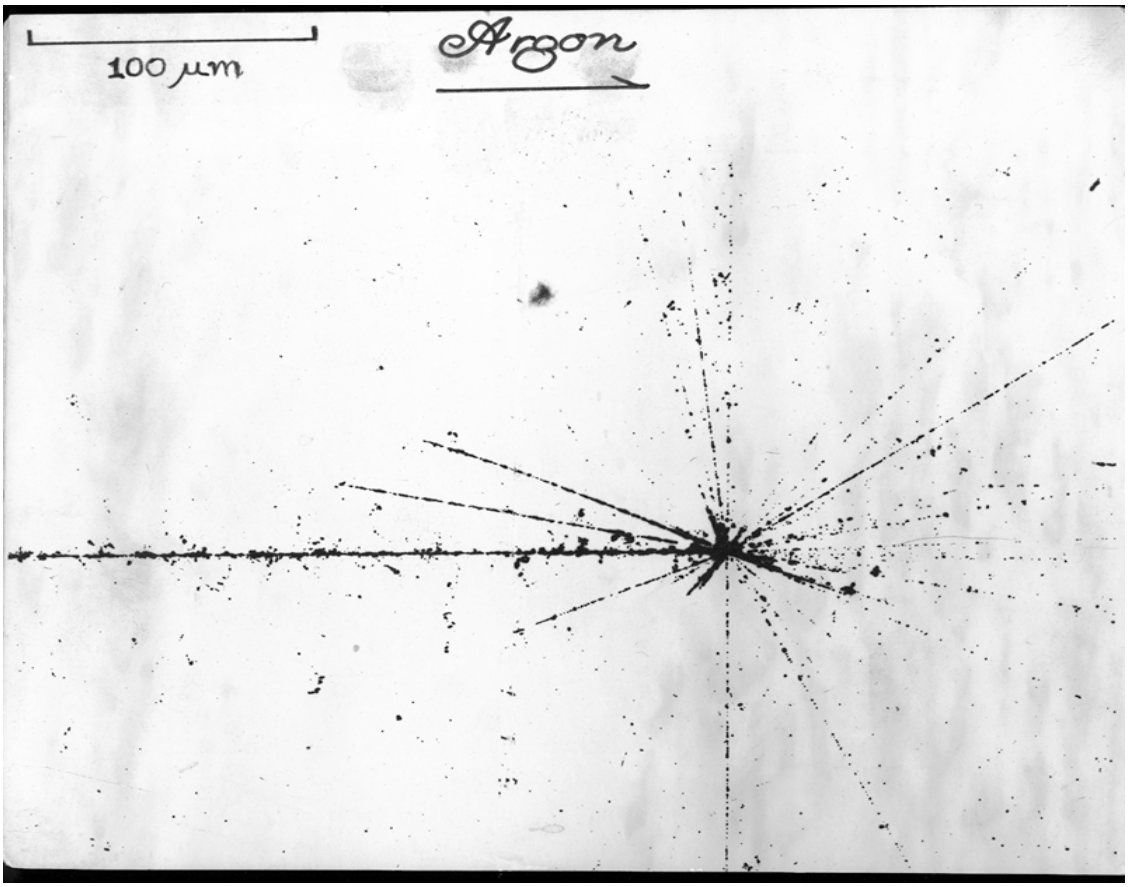

Evident at first glance in Figure 3.1 are the tracks, clean geometric lines, emanating from a topologically distinct central star. The topological description of stars… singly-connected 'hairy' cores embedded within the multiply-connected family of tracks … becomes important when one tries to automate the scanning process. A human being's ability to easily see such patterns as patterns is biologically hard-wired into us. Replacing a human scanner by a computer is still limited to the act of finding unique and simple, but rare, patterns in a large sea of tracks. The CERN projects Chorus and Opera helped to pioneer this approach, as have continuing efforts by the Japanese physics community. Indeed, Fermilab's discovery of the tau neutrino was done in conjunction with Japanese teams and their automated scanning technologies. But it still took more than three years of scanning!

In contrast to this comparatively 'easy' finding of topologically unique vertices, the mapping and quantitative measurement of every track in relativistic cascades is an arduous, unbelievably difficult task. It requires enormous patience coupled to considerable skill and experience. Stamina and judgement are paramount, along with *lots of quality control and checks for internal consistency*. Increasing the resolution of observation in the argon collision pictured above hints at these challenges (Figure 3.2).

Figure 3.2 Relativistic Argon Track in Emulsion

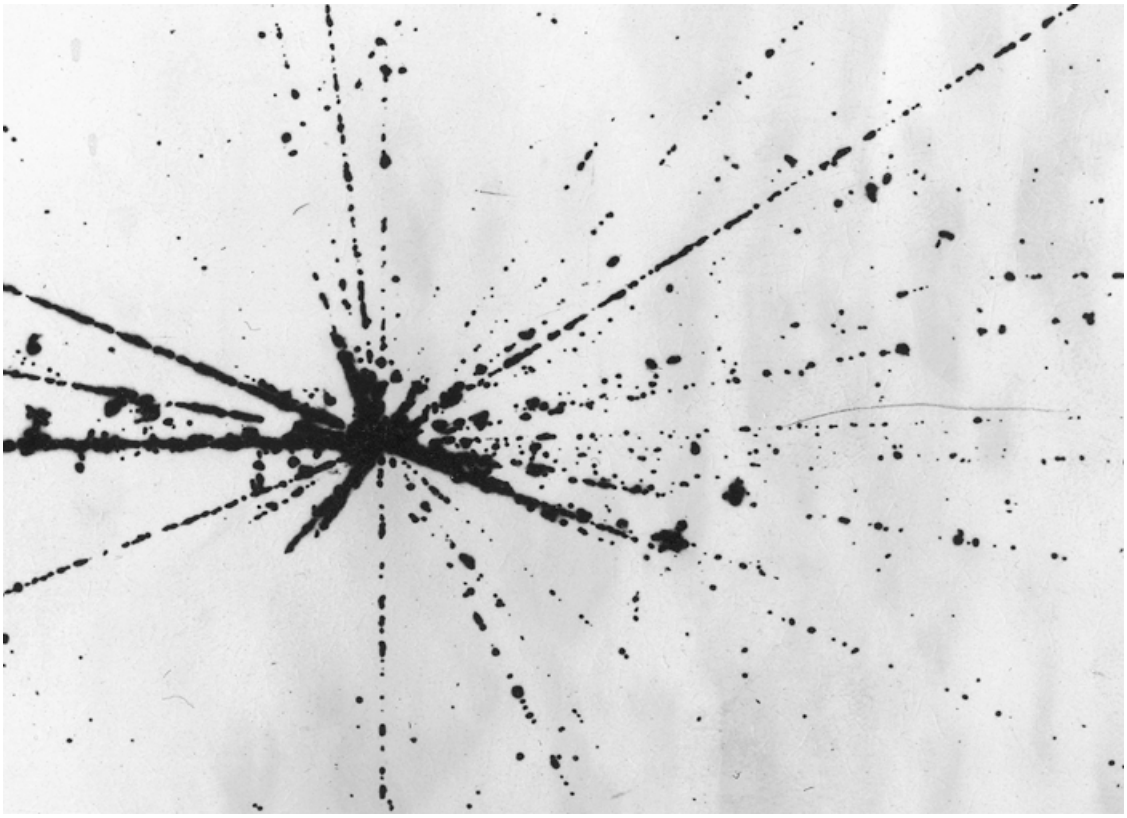

At the previous two scales the individual grains making up the figure are less easily seen; but upon further enlargement the 'pointillist' composition of the lines becomes evident (Figure 3.3).

Figure 3.3 Relativistic Argon Track in Emulsion

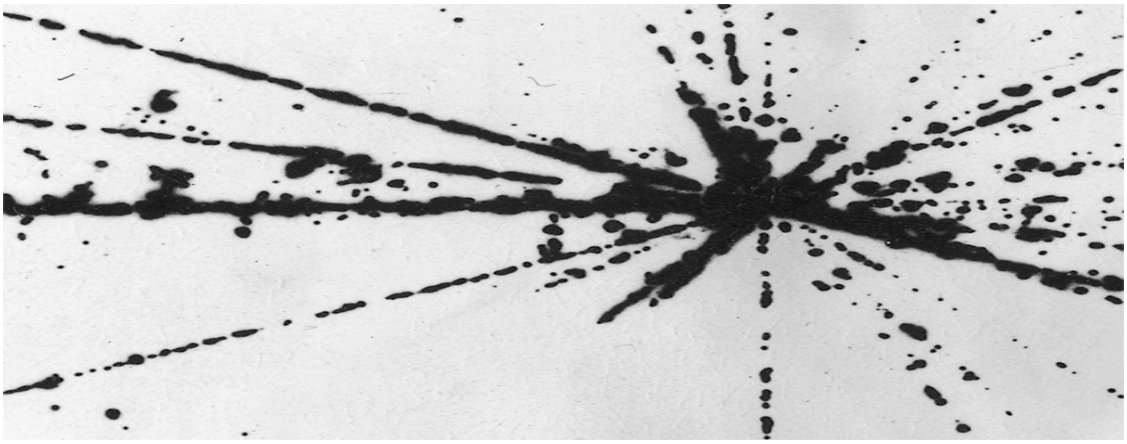

This is a little larger than the visual scale of scanning. But quantitative measurements require a further enlargement still (Figure 3.4). At the *scale of quantitative measurements* individual grains have become geometric "points".

Figure 3.4 Relativistic Argon Track in Emulsion

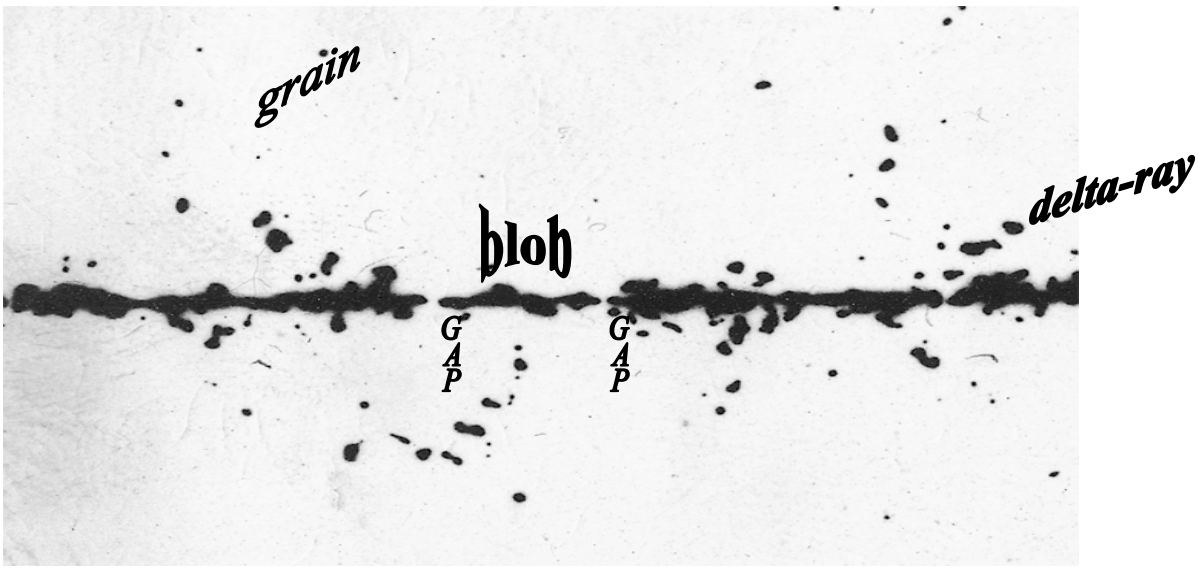

In Figure 3.4 the 'dot' on the letter *i* in *grain* is an individual grain. Also seen in the image are clumps of individually indistinguishable grains, which have been given the scientifically ordained and technically accurate name of *blobs*. And the spaces between blobs, or individual grains, are termed *gaps*. These, along with delta-rays, are the stuff of quantitative measurements.

Even in this single image it is apparent that the blobs, gaps, and delta-rays along a single track encompass considerable statistical variability. Hence, measurements of these characteristics is quite unlike the search for specific visual characteristics. Instead of the comparatively easy search for the overall topology of a star's vertex we are forced from the beginning to be very careful in our statistical and probabilistic reasoning. The transition from geometric points to numerical ones will be discussed later in this chapter.

3.2 The Emulsion Stack: Prelude to Scanning

The exposed stack consisted of about 40 stripped Ilford G-5 emulsions (10 x 20 x 0.06 cm each).

Figure 3.5 Star Formation from a Beam Particle Going through an Emulsion Stack

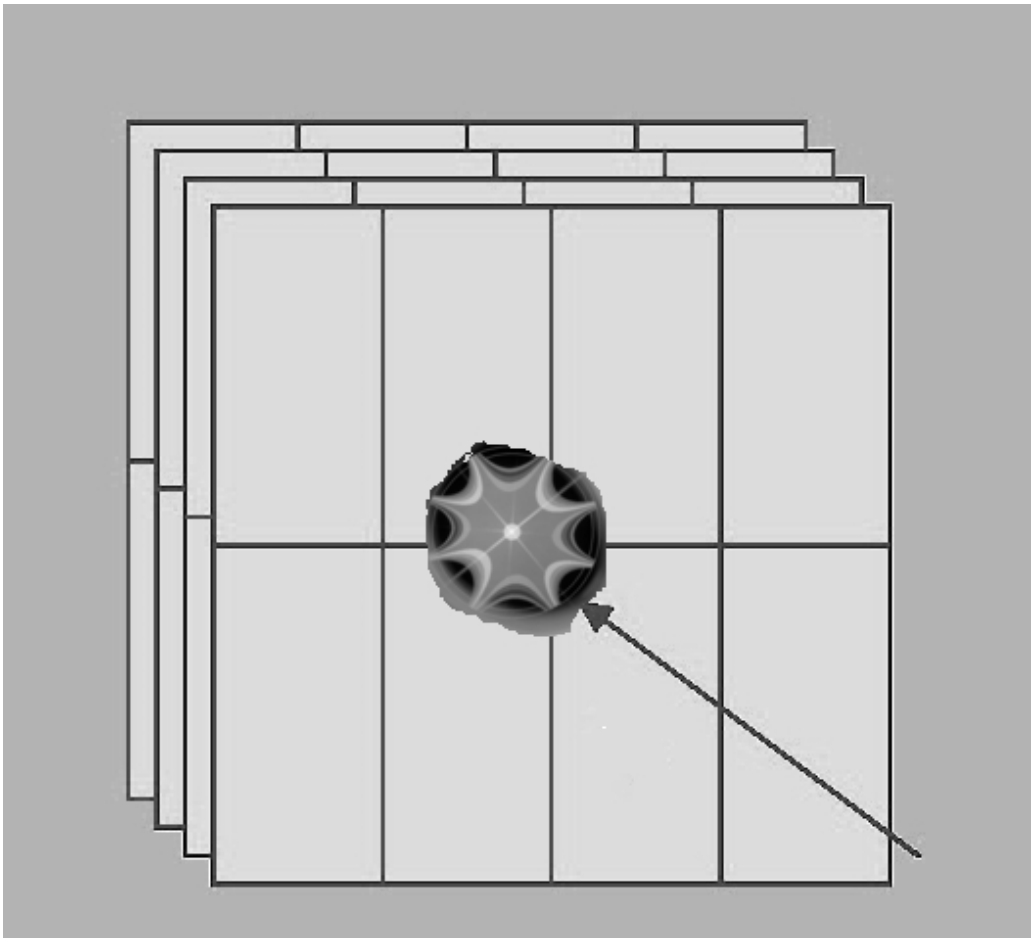

The stack was exposed to a beam of 1.8 A GeV argon nuclei at Berkeley's Bevatron, under the direction of Dr. Harry Heckman (LBL). Processing and development was performed on-site, and we were provided with 32 of the interior plates (no. 4 - 36).

The surface plates of a stack are susceptible to a number of extraneous environmental variables, hence it is standard practice to discard from the measurement set a number of the outer emulsion plates on both ends. For a similar concern of boundary effects and distortions, when scanning individual emulsion plates the first 2mm from the edges in the X-Y plane are ignored.

The act of scanning itself proceeds along two different methods*: along-the-track* scanning and *area* scanning. The former is an 'unbiased' approach where an incoming primary track is followed until it has an interaction. The latter is a less formal, somewhat opportunistic "eyeballing" of the emulsion in the search for 'stars'. It is obvious that area-scanning will be biased towards the finding of the more spectacular central collisions such as the one pictured above.

Single emulsion plates must necessarily be thin, no more than a millimeter (1000μ). This is due to the critical need for the diffusion of developing chemistry to be uniform throughout the strip, the need to minimize mechanical deformations of the emulsion itself, and most importantly the ability to optically follow the track of an individual charged particle through the entire depth of the emulsion. For when emulsions are scanned, they are viewed in a transmitted light that backlights the developed grains of silver. To insure sufficient contrast for seeing, these grains must have a high relative opacity to that of the surrounding gelatin. The thickness of a single emulsion plate is thus limited by the integrated opacity of the gelatin matrix, and by the cumulative scattering of light which increases with emulsion thickness.

With these functional concerns in mind, emulsions have become standardized at pre-exposure thicknesses of 600μ and 1000μ. Exposure, development, and drying shrink their depth by ~50%. In our experiment the dried emulsion strips were about 250-270μ thick. But the mean free paths of relativistic nuclei in emulsion is measured in tens of centimeters (see Tables 4.5 and 4.6). To increase both the probability of nuclear collisions and the stopping power of the emulsion itself (due to cumulative ionization effects) stacks of "stripped" emulsions were developed:

After initial manufacture, emulsions are stripped from their mechanical support base (glass), and compressed together to make a solid uniform target. After exposure, the individual emulsion 'strips' are separated by chemical and mechanical means and remounted on glass supports.

A complete tracking of individual relativistic particles will therefore necessitate scanning across many individual emulsion plates.

Figure 3.6*

Exploded View of a Particle's Trajectory through Successive Emulsions in a Stack

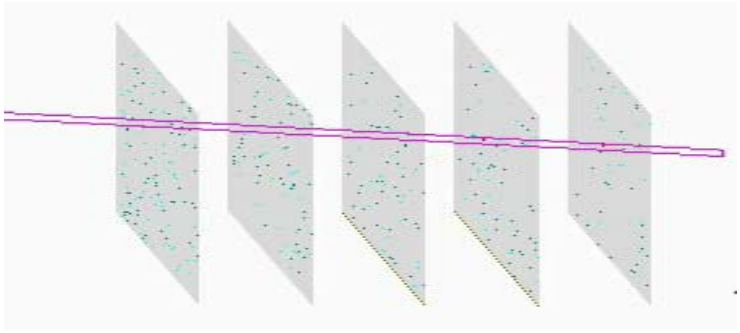

The complete mapping and measurement of even a single cascade family (of up to several hundred individual particles) therefore requires the scanner to work back and forth across successive emulsion plates. And to get a reasonable statistical sample the integrated path length of tracks scanned must be in the thousands of centimeters. Registration of position, both relative and absolute, becomes critical.

Additional needs for precision in (and coherence of) the measurement process comes from the fundamental optical properties of a microscope capable of scanning nuclear emulsion. As discussed in Chapter 1, there is a happy convergence of the optical and emulsion phenomenological scales. The average grain size of commercial emulsions sensitive to minimum-ionizing Z=1 particles is [0.1-0.4] μ. This is also the scale of

* Adapted from a Fermilab image

maximum resolution in optical microscopes. As a consequence of the necessary objective strengths to reach this resolution, the depth of field Δ about the point of focus is at the scale of microns. In particular, if

$$\Delta = \frac{\lambda}{4n\sin^2(\alpha/2)} \qquad \textbf{(3.1)}$$

for air the depth of field of blue-green light is ~ 8μ, but it is only ~0.5μ in an immersion microscope (Barkas p224).

Hence, to follow the trajectory of individual charged particles through a single emulsion plate the scanning and measuring must be performed at successive depths of differential focus as illustrated in Figure 3.7*.

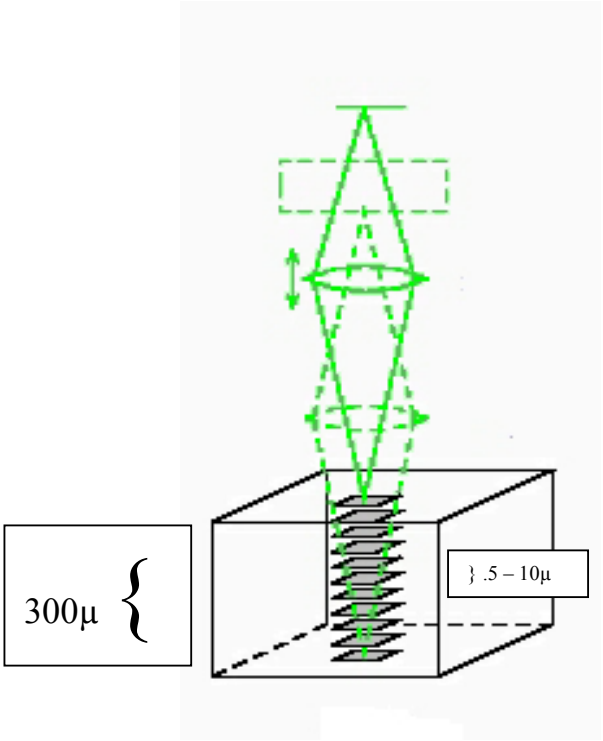

Figure 3.7

Optical stages at successive points of focus in a single emulsion plate.

Although the act of scanning is in reality a continuous change of mechanical focus, a standard 0.06 cm thickness of emulsion (one strip) would in principle require hundreds of separate focusings to view the entire depth.

* *Image adapted from Fermilab*

Absolute integrity in the X-Y plane utilizes reference to a rectangular grid imprinted photographically on the base of each emulsion strip. Relative and local planar measurements as well as measurements of depth were kept coherent through the calibration of the semi-automatic (Jena) KSM microscope used for the measurements.

It must be noted that there is an anisotropy in the mechanical and thermal errors associated with the KSM microscope. In the Y-axis, the error is practically at the optical limit, ~ 0.1μ. In the X-axis, due to the mechanical construction of the mechanical arm, the errors have an order of magnitude ~ 1μ. And in the Z-axis, due to the mechanical effects of gravity the precision ~1-2 μ.

3.3 Patterns of Opacity…… … .. . origins

In the emulsion's world of transparency, all that we see is opacity. The unit of this opacity is a developed silver halide grain, and it is the local density of these developed grains (dots, blobs, and stars) that tells of the past presence of a moving charged particle.

The key word here is *local*, for the formation of the latent image of a grain is a local ionization effect due to the interaction of the emulsion's atoms with the Coulomb field of the moving charged particle. It is not however a direct function of the average energy loss per unit distance, but is instead due to the low-energy electrons (delta rays) that are thrown out of the emulsion's atoms in the wake of the passage of the projectile's electromagnetic field.

To illustrate this Powell (p.43) points out that a minimum ionizing particle of charge Z=1 has a continuous energy loss of ~ 700 KeV/mm. For a 0.3 μ diameter grain this would lead to an energy deposit of only ~300 eV. Considerably more energy is available from low-energy electrons that are liberated in the wake of the passage of the projectile's (nuclear) electric field, but whose mean free path is less than the grain diameter. Electrons ≤ 5 KeV satisfy this condition and are termed delta rays (δ rays).

Electrons above 5 KeV typically escape from the grain and do not contribute to grain formation. Hence the importance of the energy spectrum of the electrons liberated in a material due to the actions of a moving charged particle (Figure 3.8*).

Figure 3.8 Approximate Energy Distribution of δ-Rays

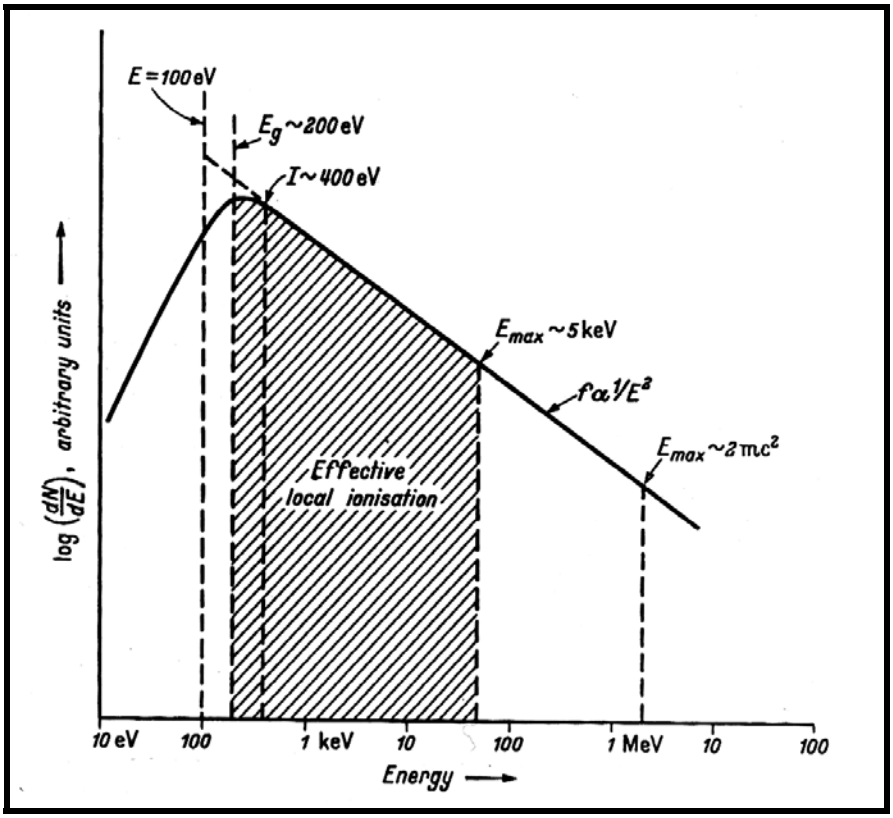

All usefulness is not lost, however, for those electrons with energies significantly greater than the nominal 5 KeV limit for 'exposing' individual grains. Single δ–rays with energies greater than 10 KeV can produce the 'whiskers' of exposed grains which emanate from the saturated core of the track of a higher-Z relativistic particle. These whiskers can in turn be 'counted', helping to determine the Z of the particle producing the core track. (See section 3.8)

* Powell (1959), p. 48

3.4 Bethe-Bloch Equation

For a relativistic charged particle, with a mass much greater than that of an electron, the energy through collisions with bound electrons is described by the Bethe-Bloch equation*:

$$-\frac{dT}{dx} = nZz^2 \frac{4\pi\alpha^2 h^2}{m_e \beta^2}\left[\ln\frac{2m_e c^2\beta^2}{I(1-\beta^2)} - \beta^2\right] \qquad \textbf{(3.2)}$$

$\frac{dT}{dx}$ is the loss of kinetic energy/unit distance

Z_p is the charge of the projectile

Z_m is the charge of a homogeneous target material

n is the density of atoms of atomic number Z_m

I is the mean excitation potential and is experimentally determined
(I is approximated by $I = 16Z^{0.9} eV$ for Z > 2)

Several important relationships are immediately apparent.

1) The energy loss is proportional to Z_p^2, the square of the projectile's charge; but is independent of its mass. This will simplify things enormously.

2) For non-relativistic particles (such as target ejecta in the lab frame) there is a β^{-2} dependence. Hence, the slower the particle, the greater the energy loss per unit distance.

* Along with the formaluation used here, Williams (1991) points out that the Bethe-Bloch formula can be looked at as an extension of the Mott scattering formula which in turn is an extension of Rutherford's scattering formula, the founding formula of nuclear physics.

3) At relativistic velocities the energy loss becomes logarithmically asymptotic. However, density effects and shielding due to polarization effects decrease the actual rate of increase. Also, the local ionization effects of the δ–rays leads to a relativistic plateau.

Figure 3.9 Bethe-Bloch Ionization Curves

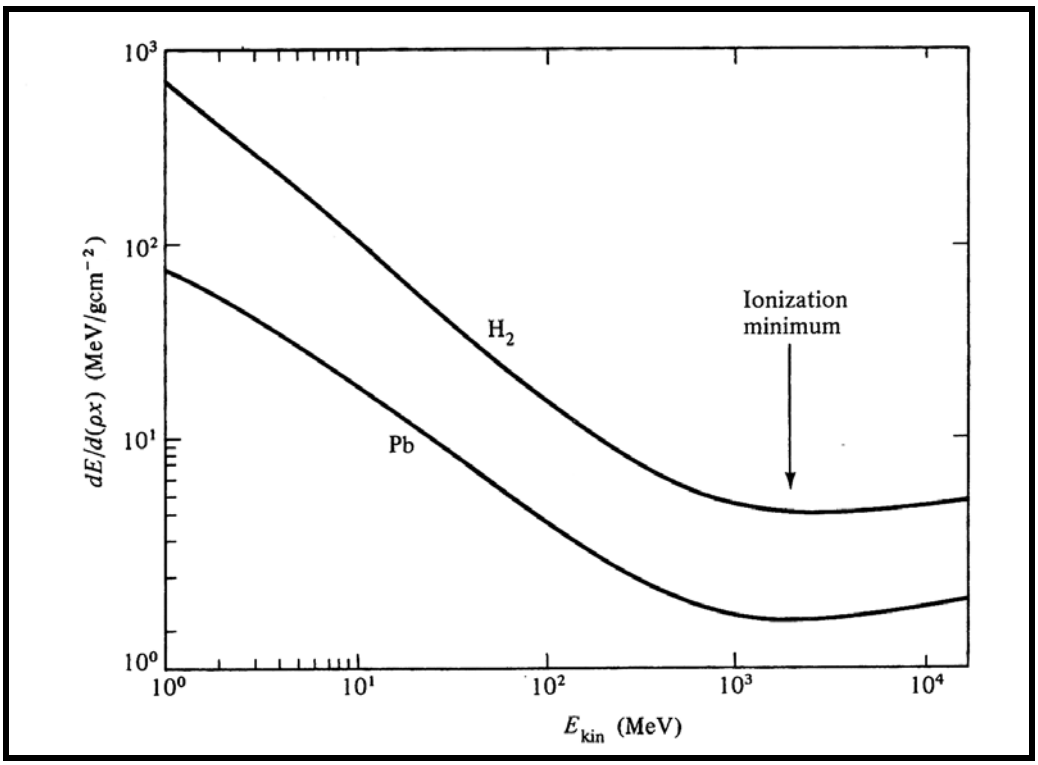

(Frauenfelder & Henley)

Tincknell (Tincknell, 1984) discusses the application of the Bethe-Bloch formalism specifically to Bevalac energy heavy ions traversing heterogeneous media such as nuclear emulsion and CR-39 (at the time he was a member of Buford Price's group). A summary of some of the background physics relevant to our own exposures is excerpted below:

"Nuclear projectiles passing through condensed matter are usually fully stripped of orbital electrons for projectile velocities of $\beta \geq Z_p/137$. Heuristically, this is a consequence of the Bohr criterion which states that electron pickup (loss) predominately occurs for projectile velocities below (above) the electron orbital velocities of the projectile atoms. Since the first Bohr orbital velocity is about $Z_{P\alpha}$, where α is the fine structure constant ~1/137, all but the heaviest projectiles (e.g. Uranium) are fully ionized at energies about 1 A GeV.

The effective charge of a projectile nucleus is approximately a function only of the charge Z_p and velocity

$$Z_P^* \approx Z_p(1 - e^{\frac{-180\beta}{Z_P^{2/3}}}) \qquad \textbf{(3.3)}$$

Due to the Coulomb interaction of this positive charge with the target atoms, projectile nuclei lose energy by creating electronic excitations in the target matter. The energy loss per unit distance is described by the Bethe energy loss formula:

$$\frac{dE}{dx} = \frac{4\pi N Z_P^{*2} e^4}{m_e v^2}[\ln 2m_e c^2\beta^2\gamma^2 - \ln I_{adj} - \beta^2] \qquad \textbf{(3.4)}$$

Where $N \equiv N_{Avog}\rho Z_T / A_T$ is the electron density of the medium, $Z_P^* e$ is the effective projectile charge, -e is the electron charge, m_e is the electron rest mass, $v = \beta c$ is the projectile velocity, $\gamma^2 = 1/(1-\beta^2)$, and I_{adj} is the logarithmic adjusted mean ionization potential of the absorbing medium. For compound media, this takes the form

$$\frac{dE}{dx} = \frac{4\pi N Z_P^{*2} e^4}{m_e v^2}\frac{\rho}{A_Z}[\ln 2m_e c^2\beta^2\gamma^2 - \ln < I_{adj} > -\beta^2] \qquad \textbf{(3.5)}$$

where $A_Z \equiv \frac{\sum_i c_i A_{\mathrm{T},i}}{\sum_i c_i Z_{\mathrm{T},i}}$ is the average nuclear mass per nuclear charge of the medium (A per Z), and $\ln< I_{adj}> \equiv \frac{\sum_i c_i Z_{\mathrm{T},i} \ln I_{adj,i}}{\sum_i c_i Z_{\mathrm{T},i}}$ is the average adjusted logarithmic ionization potential of the medium. This expression takes an approximate asymptotic value of $2Z_P^2$ MeV cm^2g^{-1} for nuclei with Bevalac energies. Energy losses of this magnitude are slight compared with kinetic energies of 1 to 2 *A* GeV….

For energies of ≥1 *A* GeV and media with an average atomic charge of ≤29 (nuclear emulsion or plastic), the projectile range is generally greater than the mfp for interaction.

$$\lambda = (\frac{< A >}{N_{Avog}\rho})(\sum_i c_i \sigma_i)^{-1} \qquad \textbf{(3.6)}$$

where N_{Avog} is Avogadro's number, ρ is the density, $< A > \equiv \frac{\sum_i c_i A_{\mathrm{T},i}}{\sum_i c_i}$ is the average atomic number of the medium, c_i is the atomic fraction of target species."

(Tincknell 1984)

One of the most important functional points of the above is the ability to assume a constant ionization for relativistic (projectile) tracks being followed through a stack. This tremendously simplified the measurement effort enabling, for example, the use of photometry for charge measurements. Details will be discussed in this chapter and the next.

3.5 Energy Loss and Grain Density…. a Linearity

Given the above one must then relate this energy loss to the actual grain densities. One finds for the same velocity, but differing Z, an excellent fit between grain density ***g*** (number of grains/mm) and Z_p^2 dependence (in G5 emulsion).

Figure 3.10 Grain Density vs. Z_p^2 in G5 Emulsion*

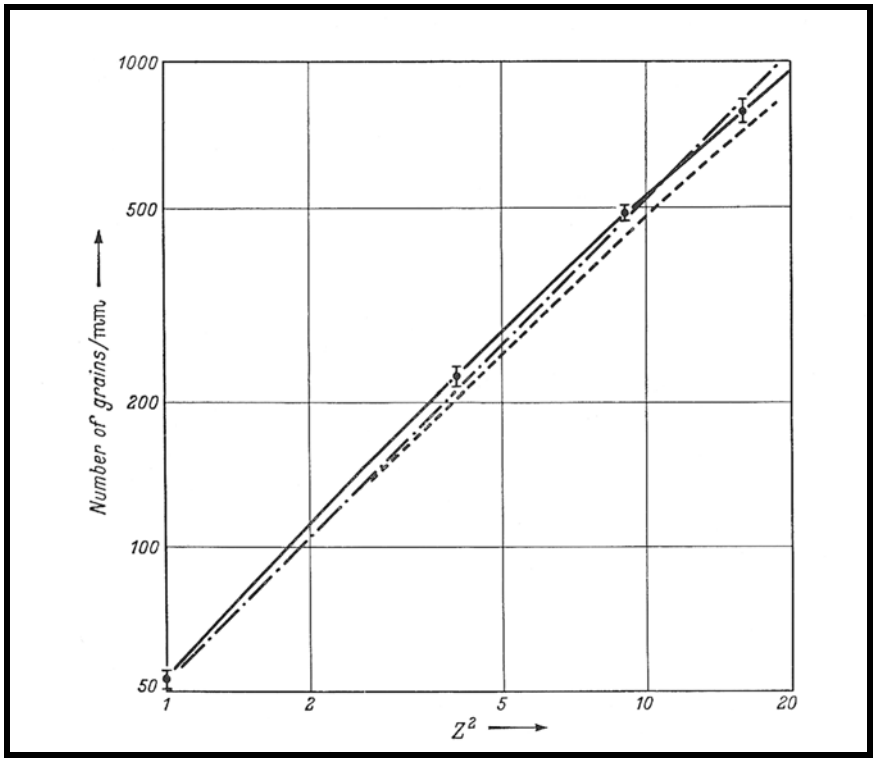

This near linearity is fundamental to the precision of measurement for which nuclear emulsions are known. Indeed, it is fundamental to their very use. For Powell strongly argues that this linearity directly implies that the overwhelming majority of individual seen grains are the creations of a single δ-ray, each exposed grain the "consequence of single acts":

* Powell (1959), p. 47

> "If an appreciable fraction of the grains were made to develop as a result of the joint action of two δ-rays, for them the relation between g and I would be of the form $g \propto I^2$; i.e. $g \propto Z^4$. The absence of such a group of grains in appreciable intensity is proved by the observed linear relation between g and Z_p^2." *

This isomorphism between grain density and local ionization explains why the response of nuclear emulsions to chemical development is so different from that of ordinary photographic emulsion. In the latter, image contrast is proportional to different exposures, and can be drastically modified by changes in chemical development. This is not the case for nuclear emulsions which have an extremely wide latitude; offering little change in contrast in response to comparatively large changes of chemical development. As Powell nicely puts it, " For low values of the specific ionization, since the blacking is proportional to the ionization, 'gamma' for the emulsion is equal to unity."

All of this means that our basic unit of opacity, a single developed grain, when analyzed and measured in the context of a distinct pattern of opacity (blobs, stars, and tracks) offers the careful observer a potential transparency of physical meaning.

* Powell (1959), p.46

Figure 3.11 offers an 'artistic' rendering of such a network of patterns.

Figure 3.11

Artistic Rerendering: Limiting Angles of Projectile Fragments and Relativistic Contraction

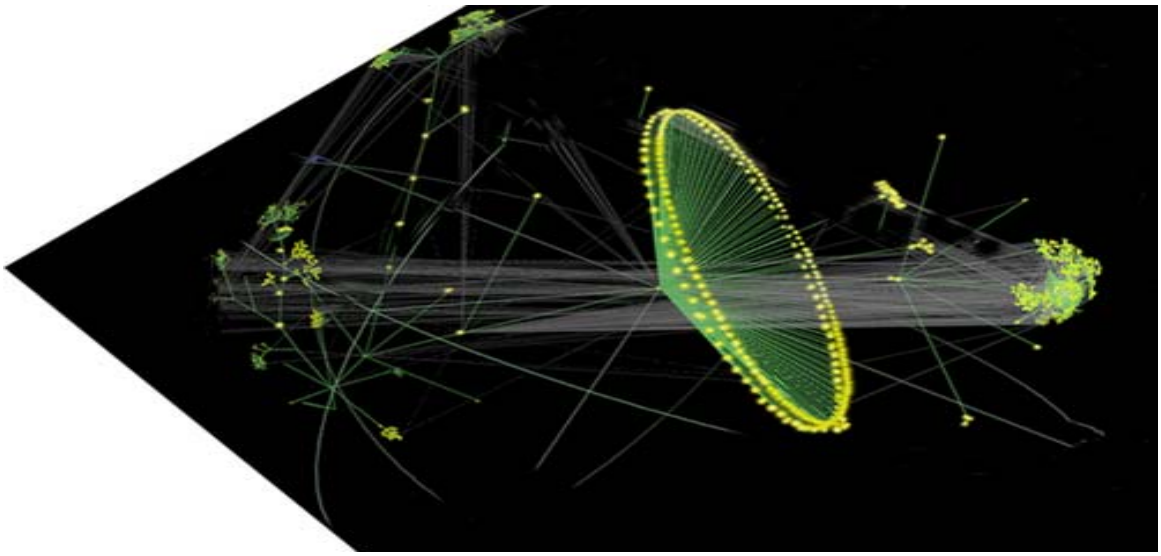

3.6 Scanning and Classification

In this section we follow, from the scanner's perspective, a relativistic argon primary nucleus as it enters and traverses G.5 nuclear emulsion. In so doing we will illustrate the track classifications and measurements that were made in the emulsion-scanning part of our work. Most of the techniques used are described in great detail in Powell's "bible" on nuclear emulsions (Powell 1959). The reader should refer to this volume and to Barkas (1963) for more of the technical details.

Starting from a scan line 2 mm from the edge of the emulsion plate beam particles were followed until they interacted inside the emulsion or until they exited from the plate being scanned. If the argon did not interact in that one plate, its length of track scanned was recorded, but it was not followed into the next plate.

For if one wants to determine mean free path one can follow a track until something happens or one can integrate all of the tracks followed (of a given Z) and divide by the number of interactions. In the latter case one uses the estimator

$$\lambda^* = \frac{\sum S_i}{N_Z} \qquad \textbf{(3.7)}$$

which includes the summation (S) over the total path length of both interacting and noninteracting tracks that lead to the N interactions. (For measured values see Table 4.5 in Section 4.3.)

In contrast to the primaries whose scanning ended at the boundary of the plate being scanned, all secondaries with $Z \geq 2$ were followed throughout the entire stack; as were all subsequent generations of interactions and produced particles. The angles and charges of secondary particles for *all interactions* were measured. *These efforts produced the first full-stack scan ever performed and as such offers a unique perspective on questions involving primary vs. secondary populations.*

All interactions having as their origin a beam particle were attributed to the same family; a family being abandoned only after all the tracks from all the stars were followed, and all the interactions inside the stack were found. And after any interaction was found, an additional backward scanning along the track was done in order to insure that no interaction was lost.

Each star was cataloged and then drawn by hand before any measurements began. Cataloging consisted of 2 numbers assigned to each star: a family number and the ordinal number of the star within the family. Stars were then organized according to family, generation, and primary track; and the following analyses and measurements performed:

1) the position of the star within its cascade family
2) geometric properties of the star's components
3) identification of the star's various components by Z and projectile/target origin

During the scanning process alone, all stars were examined, confirmed, and cross-checked by *at least* 4 different people, each concerned with only one of the following:

1) Scanning
2) Drawing
3) Assigning of Identification Numbers
4) Construction of the Geometry

A list of the 17-person team along with the responsibility of each is found in Appendix A. One of the many benefits of this "industrialized" cross-checking was the extraordinary accuracy and completeness of the scanning. Statistical support for this statement will be found in Chapter 4.

3.7 Geometry

Length

Distances > 3mm were evaluated using the grid photographically imprinted on the emulsion strip by Ilford. Distances < 3 mm were measured with the eyepiece under magnifications:

10 x 1.5 x 15 for distances > 1mm

15 x 1.5 x 100 for distances < 1mm

Corrections were of course made for dip angle.

Angle measurements

A semi-automatic microscope type KSM (Jena- Germany) was used. A star is aligned with the primary along the X-axis of the microscope. The particles emitted under a projected angle bigger then 10^0 were measured using the goniometer built into the microscope. Angles of all other tracks were measured through use of their coordinates. The depth in emulsion was evaluated relatively to the surface of the emulsion plate. The coordinates (x,y,z) and angles were then transferred to an on-line computer.

Geometrical reconstruction

A program was written to transform the readings into angles. Real emission angles are computed relative to the primary track

3.8 Charge Measurements

Charges were measured by some combination of the standard methods:

1) Counting Grains
2) Fowler – Perkins (counting blobs or gaps)
3) Delta rays
4) Integrated Width Photometry

These methods can be collectively looked at as the measurement of an emulsion's linear response to consecutively larger scales of opacity (grains, blobs, and tracks) up to the point of saturation for each. One counts grains until they begin to merge into blobs, after which one begins to count blobs (or equivalently… gaps).

A continuous track can validly be looked at as a coalescence of blobs, while the thickening of a track can correctly be considered a superposition and integration of small-scale (low-energy) delta rays. Hence, as continuity of a track begins to occur, one can still count delta-rays. And as the thickness and development 'shadow' of a relativistic heavy ion track increases, one can usefully measure and compare the total integrated opacity of the core of the track.

This is hardly a fortuitous coincidence, and seems a posteori (to this author at least) to follow from the fact that this sequence of methods is in essence sampling the energy spectrum of delta-rays (Figure 3.8) at increasingly energetic thresholds. Coupled to this is the linear response of grains across these many orders of magnitude of energy.

Furthermore, in each method what we are counting is the *boundary* of the opacity unit under consideration. Since each such unit, defined by its boundary, is made of these linearly responsive grains the local components of each boundary should grow linearly in the appropriate pre-saturation regime. This growth will be modulated by the 3-D geometries of delta-ray transport and the subtleties of the emulsion's composition, sensitivity, development, and secondary characteristics. (These secondary considerations range from the filamentary structure of developed grains to the anisotropy of grain orientations due to settling in a gravitational field).

Hence the actual macroscopic entities to be measured will not all be linear. Indeed, exponential distributions are frequently to be expected, due to the emulsion's absorption of the emitted delta-rays. But the linear response of the boundary in its local build-up would seem to be the taproot connecting each of these methods to the appropriate scattering formalisms (Rutherford, Mott, or Bethe-Bloch); and hence the ability to discriminate the charges responsible for the specific ionization of the tracks under investigation. A simple outline of these methods follows:

Grains

As was discussed in the previous sections of this chapter, the passage of a singly-charged particle at minimum ionization through an emulsion can expose individual grains which can then be visually discriminated and counted. The charge determination follows from the measured grain density g_o .

Blobs

As the local ionization increases, individual grains become unresolvable and multiple grains visually coalesce into 'blobs', separated from each other by 'gaps' of unexposed emulsion. It is obvious that the number of blobs is essentially equal to the number of gaps between them. Following O'Ceallaigh's discovery that these gap lengths have an exponential distribution, Fowler and Perkins developed the 'law of gap lengths' which can be summarized in the two relationships:

$$\mathbf{H}(l) = \mathbf{B}\, \mathbf{e}^{(-\Gamma l)}$$

$$\mathbf{B} = g\, \mathbf{e}^{(-\Gamma a)} \qquad \textbf{(3.8)}$$

where

H is the *density of gaps* greater than a length l

B is the *blob density*

Γ is the *gap length coefficient*

α is the reciprocal of the *developed grain diameter*

The gap length coefficient Γ is the reciprocal of the mean gap-length l_m, and is numerically equal to the slope of exponential distribution (on a log-plot) of the gap density vs. gap length.

Γ embodies a number of characteristics of critical importance to experimentalists. Γ has been shown to be more than just a function of the grain density, but is itself an estimate of the ionization and true grain density. For a specific ionization Γ is essentially independent of mean grain-size; and for the G5 emulsion used in our experiment, Fowler and Perkins have showed that the information derivable from Γ is *independent of development*. This independence of development is one of the great unifiers between different studies done on differently exposed and differently developed emulsions.

The Fowler-Perkins method of blob counting embodies one other advantage, making it the first choice of techniques when applicable: 55% of the information available within a track can be obtained without measurement.. … …. . … . .. … simply by counting the blob density of the track along with the number of gaps of length greater than ~2.5 l_m. It is this last point, of economic as well as systematic value, that makes the technique 'really work' in the real-world.

Delta rays

At still higher ionizations the core of the track becomes 'clogged' due to the visual saturation of the grains exposed and developed. At this point however, in addition to those lower-energy electrons that expose grains in the actual path of the traversing particle, the energy distribution of secondary electrons is such that higher-energy delta rays are ejected. As discussed earlier, single δ–rays with energies > 10 KeV will then produce 'whiskers' of exposed grains emanating from the saturated core of the track of a higher-Z relativistic particles. In actual fact, according to Powell, the observable (and countable) delta-rays are principally due to knock-on electrons having an energy between 15 and 75 KeV.

Following Barkas' formulation (Barkas p. 349), the differential delta-ray spectrum follows from the differential cross section for energy transfer to an unbound electron at rest from a point charge Ze:

$$\left(\frac{d\sigma}{dE}\right)dE = \frac{2\pi z^2 r_0^2 mc^2}{\beta^2}\left(1-\frac{\beta^2 E}{E_{\max}}\right)\frac{dE}{E^2}cm^2 \qquad \textbf{(3.9)}$$

E_{max} is the maximum value of these energetically kicked or 'knock-on' electrons. If E_{min} is the minimum energy for delta-ray production (from section 3.3), at relativistic energies (as $\beta \rightarrow 1$) then $E_{max} >> E_{min}$. Hence the number of delta-rays greater than E_{min} is:

$$n_\delta \approx (2\pi r_0^2)\frac{mc^2}{E_{\min}}z^2 = \text{constant} \times z^2 \qquad \textbf{(3.10)}$$

Empirical evaluation of the constant for particles of fixed charge (alphas for example) then leads to the ability to determine relativistic charges through delta-ray counts.

3.9 A Self-Organizing Systems Approach to the Evolution of Structures

If one integrates the differential density of gaps over the length of the track,

$$L = -\int_0^\infty l(\frac{dH}{dl})dl \qquad \textbf{(3.11)}$$

L, the lacunarity*, is that fraction of a track made up of gaps. It is clear that nothing useful will be seen at the two extrema, for if L = 1 then there is nothing but background emulsion and if L = 0 then the track is a continuous black band. It is easy to see that the track opacity can then formally, if a little too simply, be defined as

$$\boldsymbol{O} = (1 - L) \qquad \textbf{(3.12)}$$

As the local ionization increases, the lacunarity decreases, the opacity increases and the end result is a loss of distinguishable, and hence quantifiable, track structures.

But it is critical to recognize that this is only the *linear* portion of the track structure. As in the previous discussion on the boundaries of opacity (the more general meaning of the word again) saturation of information in a given dimension creates, by definition, a boundary that is in effect a structure seen in the next higher dimension accessible to the system. This need not be a spatial dimension but can be any spanning dimension of the system's phase space.

The author's (L2) work on self-organizing systems allows a more general perspective still. By definition, a boundary embodies more structure than a homogeneous interior. Yet this boundary will also by definition entail a lesser measure of symmetry than a homogeneous interior. Hence *almost* by definition

---

* The lacunarity integrated over the residual range is not only a measure of ionization, but a small piece of poetry as well: it was first named *"the integrated emptiness"* (Bowker et al, referenced in Barkas)

do structure-building and symmetry breaking occur together at a boundary. This can be further generalized to the idea that it is essentially (exclusively as can be shown by the author) at boundaries where self-organization of structure and dynamic process occurs.

Of course the boundaries are not limited to spatial ones, but can be dynamic processes as well. Applying this perspective to emulsions: *the hierarchical structures of grain, blob, gap, and track self-organize through the flow of energy and chemical potential that is the mass-transport of delta ray electrons.*

Going further, the organization of structure occurring at this boundary means that entropy will be decreasing in that locale and hence will embody a greater amount of information (This inverse relationship of entropy and information is due to Jaynes 1956, who first demonstrated the equivalence of statistical mechanics and information theory.) Information is 'conserved' in an additional sense of symmetry at this boundary: reflecting as it does the symmetry whereby a greater amount of information is needed to describe the boundary, but in the process yields that much more information to the observer through its description.

Admittedly all this "might" seem a bit too theoretical and abstract when actually in the midst of counting blobs and re-measuring gaps…but it is the very abstractness of this somewhat novel approach that offers a deeper understanding of the evolution of the different structures actually measured in, and in response to, the different ionization regimes.

For example, returning to the more empirical aspects of emulsions, Barkas (1963) describes the devolution of information-gathering ability thus:

> "When the ionization is low, most of the information content of the track granularity can be obtained by blob counting or measurement of the gaps. If the ionization is somewhat higher, however, the blob

> lengths become a source of information, and near the blob density maximum the blob lengths contain more information than the gap lengths. At still higher rates of energy loss, the mean blob length provides most of the information in the linear structure of the track, but the absolute quantity of information still tends to vanish when the lacunarity approaches zero."
>
> "Fortunately," he goes on to say, "…another measurement becomes available. The width of the track rises with increasing grain density just in the region where little information remains in the linear track structure."

As the previous discussions on self-organization of the boundaries of opacity make clear, it is hardly fortuitous! But obtaining a quantitative understanding of the 2-dimensional track-width is not a simple matter. In going from the zero and one-dimensional structures to two-dimensional ones all of the specific emulsion characteristics and particle variables play entangled roles. Nonetheless, depending on local calibrations, locally useful charge measurements can be made from a careful examination of track width. Indeed, as discussed next, photometric techniques have been expressly designed to do so.

3.10 Charge Measurement by Photometry

All photometeters share the basics of an emulsion-scanning microscope whose eye-piece image is transmitted to a photomultiplier device.

Figure 3.12 Photometry Scanning Set-up*

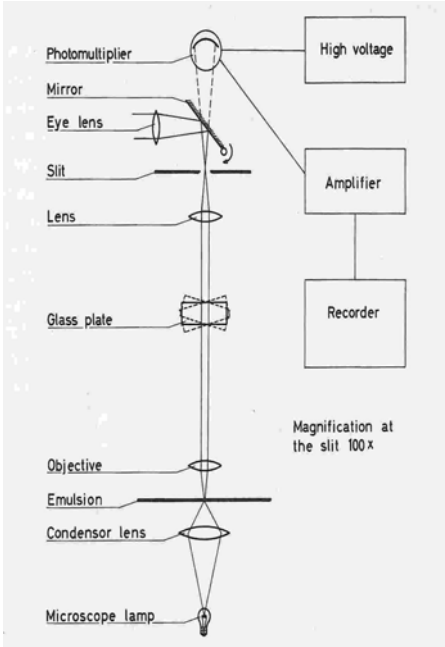

The output signal when amplified is in principle proportional to the light absorption through the track. In our charge measurement work integral photometry was used, the system being designed by Andrei Gheata (currently a CERN staff member). Although he did not perform the bulk of the measurements per se, over several years it was he who evaluated all of the photometric data to establish the fragment charges. The photometric approach as used by Project Cascade is described in the following three pages. The description, graphs, and empirical fits are all based on internal project reports written by Dr. Gheata.

* Powell (1959)

In essence the integral photometry method compares the integrated opacity of the central core of the track to the non-exposed background adjacent to the track itself. There are two principle methods of measurement that in turn depend on the relative width of the sampling slit.

For charges between 4 and 18 (those measured in Project Cascade) the charge estimate is defined as the light transmission through a track portion, divided by the mean light transmission through the corresponding left and right side regions. This is called the *integral photometry width* and is expressed in slit unit's due to its proportionality with the mean track width, if the slit width is properly chosen.

Because the track makes a shadow longer than its dimensions, the slit width must be greater than the shadow; background measurements being made well beyond this region. The slit length is also important. A long slit integrates a longer portion of a track, reducing the number of measurements. However, in this case we found it difficult to avoid observable emulsion irregularities or tracks passing nearby. So, a compromise was made by choosing a slit of 5 mm, corresponding to about 100 μm of a track.

A different method is used for charges greater than 18 where the track width is sufficiently broad that it can be scanned with a slit that is narrow compared to the track. In the Z >18 case the mean track width is then calculated directly from the track absorption profiles.

The two forms of measurements are not exactly the same, and are most useful when used individually in a given study to provide internally consistent relative charge measurements. In both methods,

a number of measurements along the track are necessary to obtain an accurate estimate of the charge. It is important to know how the mean track width depends on charge, energy, dip and depth in emulsion. Fortunately, the measured fragments are relativistic, which by the Bethe-Bloch formalism means the ionization has a weak dependence on energy. *It is this constancy of ionization throughout the fragments' range that allows photometry to be used at all.*

The particle charge is then calculated from the mean integral widths along the track. The standard error amounts up to 0.3 charge units in the interval $4 < Z < 18$ but it can increase dramatically if certain methodological cautions are not taken.

Since no relativistic particles in Project Cascade had Z>18 the integral photometry method was used. In integral photometry the *mean integral photometry width* $\langle IW \rangle$ is a function of charge, dip and depth of track in emulsion:

$$\langle IW \rangle = C\left(E, \overline{S}\right) f(Z)\, g(h) \cos \alpha \qquad (3.13)$$

$C\left(E, \overline{S}\right)$ has a negligible energy dependence, but includes those emulsion variables that are inherently unpredictable: sensitivity differences, distortions, emulsion shrinkage, causally unrelated tracks passing too close to the measured track. To reduce the unknowns embodied in $C\left(E, \overline{S}\right)$, measurements were made on both primary and secondary tracks of an interaction. By dividing the corresponding

integral widths, relative measurements of reasonable accuracy were possible*.

$$\frac{\langle IW \rangle_s}{\langle IW \rangle_p} = \frac{C(E,S)\, f(Z_s)\, g(h_s) \cos {}_p\alpha_s}{C\left(E,\overline{S}\right) f(Z_p)\, g(h_p) \cos \alpha} \qquad (3.14)$$

An additional benefit of this approach is an enhanced compatibility and internal consistency between measurements taken in different plates. *f(Z)* is empirically found, and graphed below.

Figure 3.13 ***f(Z) vs. Z***

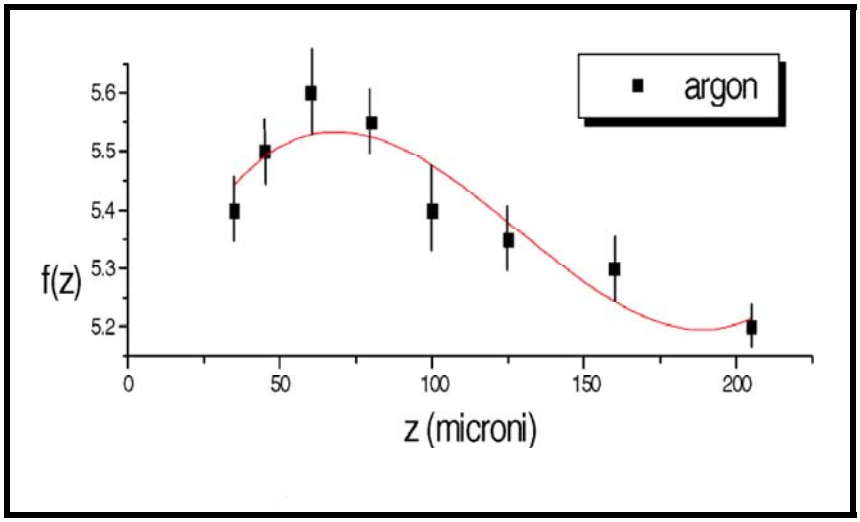

* This is of course analogous to what was done in the Copper Calorimetry Experiments in order to ratio out the complex uncertainties of unknown variables.

Depth Dependence

For all primary tracks the mean photometry width varies linearly with depth in the emulsion:

$$g(h) = A_1 + A_2\, h \qquad \textbf{(3.15)}$$

With this comparative method, we can find the integral width distribution for secondary fragments, the experimental resolution being about 0.3 charge units (for smaller Z). Along with the rest of the empirical fits to (the specifics of) our particular emulsion's exposure and development, this distribution yields a linear relationship between charge and photometric width.

Figure 3.14 Integral Photometric Width (DCIW) vs. Charge Z

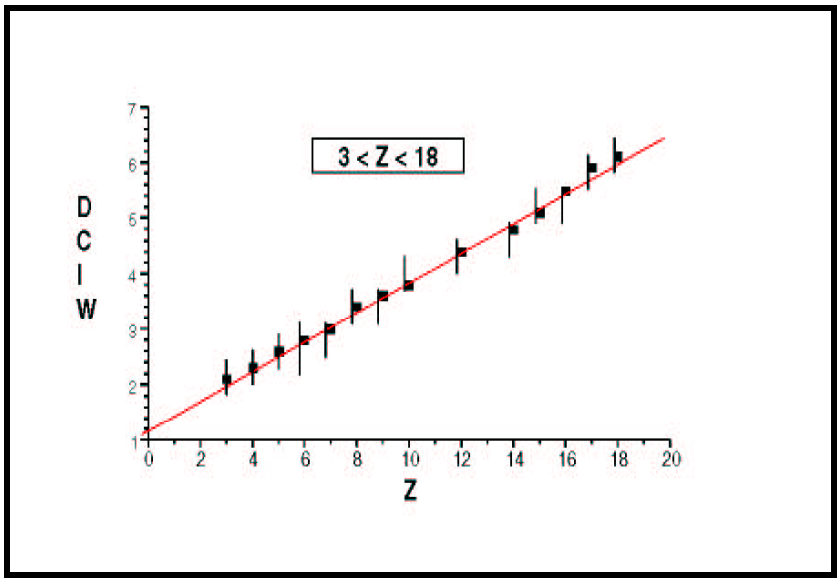

The charge measurements thus follow from the fact that the integral photometry width is indeed proportional to the mean track width which itself varies linearly with charge.

The above section on integral photometry is based on Project Cascade reports by A. Gheata

3.11 Charge Measurements in our Experiment: Trade-offs and Balancing Acts

Charges were determined at first solely by the counting of delta-rays. For Z=3,4,5 the use of delta-rays offers a clean discrimination of charge. Sufficient counts of delta-rays are necessary, but given enough measurements and re-measurements the result is an empirical peaking that falls into easily definable categories. Hence these charges were easy to distinguish.

But for larger Z the grain density of ~ (15 grains/100μm) suggested that the necessary number of delta ray counts to accurately measure all tracks (anywhere in the stack) would be difficult to acquire. An independent technique was then introduced, photometry, and all charges that were previously measured by delta rays were re-measured. The charge was re-measured yet again every time there was a discrepancy between the values obtained from the two independent methods. Because of the grain density an exact coincidence of charge values between the two methods was sometimes difficult to attain. But Fowler-Perkins to the rescue!

The Fowler-Perkins approach was more compatible with the overall state of tracks in the emulsion, and was therefore *much more* consistent with the independent values from photometry. Delta-ray counting was therefore abandoned for general use in favor of Fowler-Perkins for Z<7 and blob counting for Z>6. Subsequently all charges with Z< 7 were measured by Fowler-Perkins; as well as 50% of those with Z>7.

In this way every charge was measured at least 2 times and by at least two different methods. Typically,

Z< 5: Delta rays and Fowler-Perkins (using gap lengths of 1 and 2 μ)

Z >5: Photometry and Fowler-Perkins (gap lengths of 1 μ and 'all gaps')

In addition, many more measurements were made due to charge conservation requirements. The balance of charge was analyzed for all stars. All tracks in a star were re-measured using an alternative method any time there was a difference of more than 1 or 2 charge units between the incoming charge and the sum of the outgoing secondary charges (in the 12-degree inner cone).

The result of all of this was that for most of the secondaries any remaining differences in value were no bigger than 1 charge unit, and this only for the larger Z secondaries. For smaller Z, the error is more typically 0.3 charge units. This is probably the largest source of experimental error. It has been taken into account in the construction of the database (through the application of baryon conservation across stars and families) and through extra simulations in the Monte Carlo. The other major source of scanning/measurement error (at most a few percent) is the difficulty at small angles from the projectile path of distinguishing grey (slow target) tracks from those of relativistic (projectile) shower particles.

Both of these will be addressed more fully in Chapters 4 and 7 when discussing potential sources of errors, systematic and computational. And the results of these measurements will be found in the next chapter, *Scanning and Measurements*.

IV Scanning and Measurements

The very last run of Lawrence Berkeley Laboratory's Bevalac was a 1.8 A GeV ^{40}Ar beam directed at a stack of Ilford G5 emulsion. The 30 interior plates were then made available to Project Cascade by Dr. Harry Heckman of LBL. The subsequent scanning and measurements were performed by the professional scanners of the High Energy Astrophysics group of the Institute of Space Research (Bucharest, Romania). The 17-person team, along with their responsibilities, is listed in Appendix A. Dr. Maria Haiduc supervised and coordinated the on-site scanning efforts.

4.1 The Primaries Z=18

Scanning began 2 mm from the edge of each plate and beam particles were followed until they exited from the plate or until they interacted inside the emulsion. *All secondaries with $Z \geq 2$ were followed through the entire stack, as were all subsequent generations of interactions and produced particles.* The angles and charges of secondary particles from all the interactions were also measured. The total length of tracks scanned was 437.8 meters. 124 meters of primary argon track was followed, in which was found 1418 stars of primary interactions. Hence, the mean free path of the primary Argon is:

$$\lambda (^{40}\mathrm{Ar}) = (124 \text{ meters}/1418) = 87.51 \pm 2.3 \text{ mm} \qquad (4.1)$$

A comparison of this value with other studies (Table 4.1) offers a preliminary validation of the data. Note that the starred (*) studies were under the same conditions as our own work: Ilford G5 emulsions exposed to the Bevalac's 1.8 A GeV ^{40}Ar beam.

Table 4.1 Mean Free Path of ^{40}Ar Primaries•

Study	Mean Free Path (mm)	Error (mm)
Lerman et al [1] *	87.51	2.3
Friedlander et al [2] *	90.0	14
NRC (Canada) [3] *	83	14
Bhanja et al [3] *	89.7	1.6
Barbour et al [3]	92.0	15
Jain et al [3] *	96.0	11
Beri (1983) [4] *	92.1	1.6

From these 1418 primary interactions, the following particles were found and measured.

17261 slow heavily ionizing particles (black and grey tracks from the target)

13516 shower particles (fast Z=1 particles from the projectile)

1587 alpha particles (from the projectile)

938 relativistic heavy fragments with $Z \geq 3$ (from the projectile)

1 Current Study
2 Dr. Erwin Friedlander, private communication
3 Beri et al in 6th High Energy and Anomalon Conf (Pre-prints, p.9)
4 Beri et al in 6th High Energy and Anomalon Conf (Proceedings, p.27)

From these in turn came *1850 secondary stars*, whose distribution by charge follows:

Table 4.2 Secondary Stars

Charge	Number of Interactions
2	1043
3	31
4	46
5	38
6	51
7	53
8	60
9	34
10	51
11	48
12	56
13	46
14	48
15	54
16	65
17	37
18	89

As an essential quality control check on the scanning process: after the scanning was done and the charges evaluated we followed backwards *all* secondary tracks in *all* families and found *only 3* more interactions that were lost during the first scanning. *This yields a scanning accuracy of ~ 0.1%.*

4.2 Z=2

Of the secondary 2205 alphas followed through the stack (214.5 meters of track) there were 1043 subsequent interactions, resulting in a mean free path for these alphas of:

$$\lambda \text{ (alphas)} = 205.6358 \pm 6.367318 \text{ mm} \qquad (4.2)$$

These figures compare favorably with the study by Heckman et al. (1978) which found λ (^{4}He) = 218 ± 7 mm for a Bevatron beam of 2.1 A GeV ^{4}He. It also compares favorably with a study of Bhanja which found the mean free path of He to be λ (Z=2) = 195.2 ± 6.5 mm. Although Bhanja et al's exposure was under seemingly identical conditions it should be noted that the biased estimator $\lambda^* = \frac{S}{N+1}$ was used to derive their figure rather than the conventional unbiased $\lambda^* = \frac{S}{N}$ used by ourselves. This estimator

$$\lambda^* = \frac{\sum S_i}{N_Z} \qquad (4.3)$$

includes the summation (S) over the total path length of both interacting and noninteracting tracks that lead to the N interactions. Applying this estimator to the population of alphas as a function of distance from the parent star reveals a striking uniformity of estimated mean free path, especially at the closest distances (Figure 4.1).

And as a quality control check of the measurement process we rescanned and remeasured *all* Z=2 tracks. Only *one* revision was required. *This yields a measurement accuracy for our study of ≤ 0.1%.*

Figure 4.1

Mean Free Path of Z=2 Secondaries as a Function of Distance from Parent Star

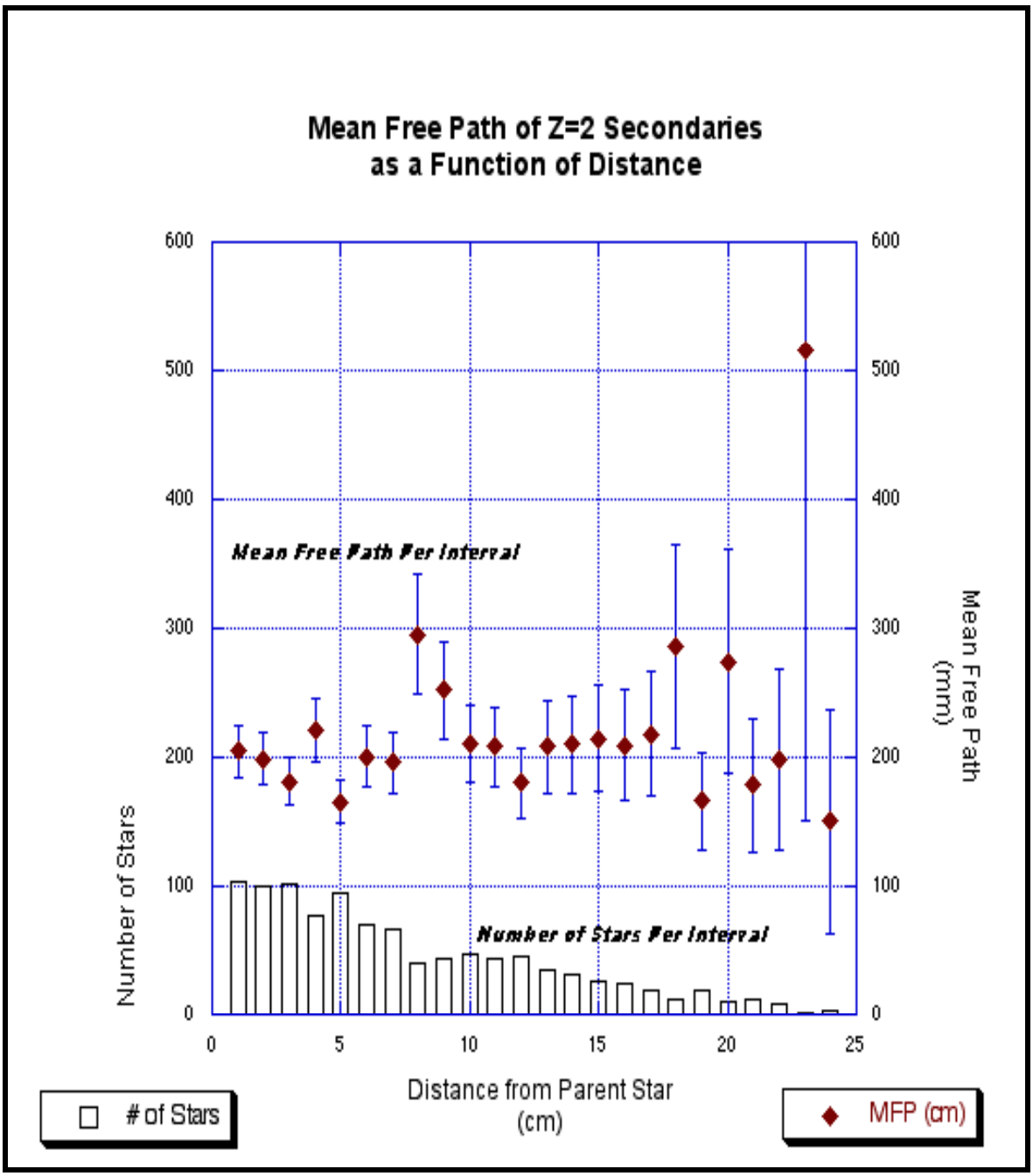

Looking more closely at the first cm reveals a value of $\lambda = 204.92 \pm 20.9$ mm

Table 4.3 and Figure 4.2

Mean Free Path of Z=2 Secondaries in First Centimeter from Parent Star

Distance from Parent Star (mm)	# Stars (Z=2)	Estimated MFP (mm)	Error MFP (mm)
0.00 – 1.00	10	219.47	69.40
1.00 - 2.00	8	272.89	96.48
2.00 - 3.00	7	310.71	117.44
3.00 - 4.00	4	539.68	269.84
4.00 - 5.00	13	164.67	45.67
5.00 - 6.00	15	141.5	36.54
6.00 - 7.00	13	161.98	44.92
7.00 – 8.00	16	130.51	32.63
8.00 - 9.00	9	230.91	76.97
9.00 - 10.00	9	229.47	76.49
0.00 -- 10.00	***104***	***204.92***	***20.09***
10.00 -- ∞	***939***	***205.71***	***6.71***

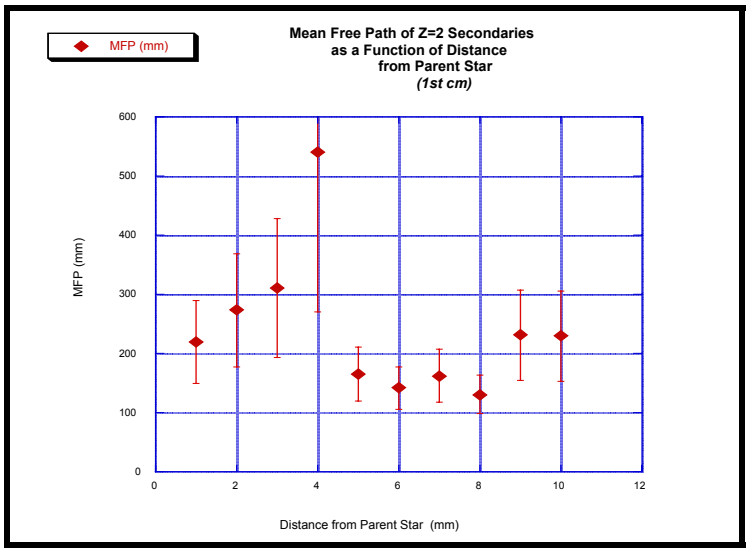

As seen in Table 4.4 below, the statistics are strongest for the first few centimeters, where any anomalous mean free path behavior (anomalons) would be expected to show up.

Table 4.4 Estimated Mean Free Path as a Function of Distance from Parent Star

Distance from Parent Star (mm)	# Stars (Z=2)	Estimated MFP (mm)	Error (MFP) (mm)
0 – 10	104	204.92	20.09
10 – 20	100	198.66	19.87
20 - 30	102	181.32	17.95
30 – 40	78	221.19	25.04
40 - 50	95	165.77	17.01
50 - 60	71	200.83	23.83
60 - 70	67	195.79	23.92
70 - 80	41	295.36	46.13
80 - 90	44	252.17	38.02
90 -100	48	210.64	30.4
100 -110	44	208.08	31.37
110 –120	45	180.42	26.9
120 –130	35	208.01	35.16
130 –140	31	210.22	37.76
140 –150	27	214.49	41.28
150 –160	24	209.57	42.78
160 -170	20	218.28	48.81
170 -180	13	285.78	79.26
180 -190	19	166.25	38.14
190 -200	10	274.61	86.84
200 -210	12	178.15	51.43
210 -220	8	197.75	69.91
220 -230	2	516.23	365.03
230 -240	3	150.4	86.83
240 -******	0	0	0

This constancy of mean free path with distance from the parent star offers a strong suggestion that in this study at least *no anomalous mean free paths are seen for Z=2 objects.* The 'conventionality' of the data set is thus reinforced, supporting its applicability as a basis for the created Monte Carlo programs.

An Aside on the "Classical" Emulsion-Based Anomalons

Note that our findings are in sharp contrast to the findings of Friedlander et al (1983), seen in Figure 4.3 , as well as other earlier studies such as those by Klein et al (1983).

Figure 4.3 Mean Free Path (Z=2) as Measured by Friedlander et al (1983)

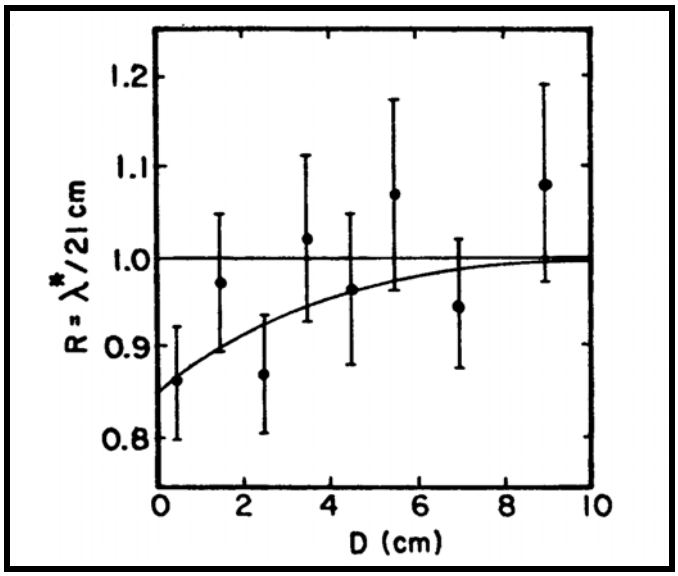

The large population of alphas in the current study, their high accuracy due to rescanning and remeasurement, and the industrialized set-up of the scanning team all suggest the primacy of this study over these earlier, smaller ones. If so, broader implication may well exist. For this consistency of mean free path at all distances from the parent star weighs against the likelihood of the existence of the emulsion-based anomalon (Karant 1983, El-Nadi 1983, Klein1983, Killinger 1983, Friedlander 1983). Bayman and Tang (1987) point out in their summary article on the anomalon phenomena that the existence, *or not,* of Z=2 anomalous mean free path particles is likely to be critical to any existence 'proof' of emulsion-based anomalons. Nonetheless, our Z=2 results may not be a definitive *nay* by themselves; for Bayman and Tang also suggest that (even if anomalons exist) only projectiles lighter than ^{22}Ne might be necessary to produce Z=2 anomalons.

4.2 **Z≥3**

For the heavy secondaries [Z≥3] encompassing 99274.95 mm of measured tracks the interaction parameters are:

Table 4.5 Measured Interaction Parameters of Heavy Secondaries

Charge	*Length Scanned (mm)*	*Interactions*	*Lambda (mm)*	*Sigma (mm)*
3	5927.992	31	191.22	34.34
4	8803.3	46	191.37	28.21
5	6392.414	38	168.22	27.28
6	7320.389	51	143.53	20.09
7	6330.116	53	119.43	16.40
8	8096.322	60	134.93	17.42
9	3763.832	34	110.70	18.98
10	6209.028	51	121.74	17.04
11	5491.813	48	114.41	16.51
12	6590.078	56	117.68	15.72
13	5386.611	46	117.10	17.26
14	5024.002	48	104.67	15.11
15	5065.949	54	93.81	12.77
16	6801.327	65	104.63	12.98
17	4391.663	37	118.69	19.51
18	7680.11	89	86.29	9.15

Similar studies to that shown in Figure 4.1 were done for all $Z \geq 3$ secondaries. No anomalous mean free path was observed at any scale. But due to the fragmentation distribution being heavily peaked at $Z \leq 2$, our statistics for $Z \geq 3$ offers a less definitive experimental answer to the broader question of whether anomalons exist or not. It should be noted however that our sample of $Z \geq 3$ nuclei is comparable in number to that utilized in the major study of emulsion-based anomalons (Friedlander et al, 1980, 1983), but a comparably rigorous statistical analysis to theirs has not been performed.

Nonetheless, comparisons of these measured mean-free-paths against predictions offers an initial clue. Shown below in Table 4.6 are the experimental values along with theoretical mean free paths derived from the fitted relationship in equation (4.4)**:**

$$\lambda = \Lambda Z^{-b} \tag{4.4}$$

where $\Lambda = \Lambda_{beam} = 30.14 \pm 1.6$ cm and $b = 0.44 \pm 0.02$

The origins of this fit are discussed by Friedlander et al (1983), who in turn utilized work by both Karol (the soft-transparency model) and Heckman (Bradt-Peters approach). For $Z \geq 3$ the fit for emulsion is seen to be quite good (exceptional even for all charges but Z=7) justifying the use of this formulation of $\lambda(Z)$ to establish the base mean free path values in our simulations. The initial values for Cu predicted by this formula, and used in our simulations, are also listed.

As to the predictive fit for Z=7, Heckman et al. (1978) studied Bevatron primary beams of Z=(6,7,8) at 2.1 A GeV. Due to the use of primary beams, their statistics were considerably greater than ours which came only from the fragmentation of ^{40}Ar primaries. Table 4.6b shows that our theoretical model fits almost perfectly their data in the regime of $Z = 7 \pm 1$. Recalling that the λ_{theory} is based on a ΛZ^{-b} fit to such past measurements it is apparent that the mean free paths of these stars appear quite normal and consistent with past measurements performed at LBL. Other matches with past LBL studies are found in Table 4.11.

Table 4.6a

Mean Free Path of Relativistic Heavy Ions in Emulsion

Theory vs. Experiment

(cm)

Charge	MFP Emulsion *(experiment)*	MFP Emulsion *(theory)*	MFP Cu *(theory)*
1		32.4	13.8
2	20.6±0.6	24.05	10.24
3	19.1±3.4	20.2	8.6
4	19.1±2.8	17.85	7.6
5	16.8±2.7	16.22	6.91
6	14.3±2.0	14.99	6.38
7	11.9±1.6	14.03	5.98
8	13.4±1.7	13.25	5.64
9	11.0±1.9	12.6	5.36
10	12.1±1.7	12.04	5.13
11	11.4±1.7	11.55	4.92
12	11.4±1.7	11.13	4.74
13	11.7±1.7	10.75	4.58
14	10.5±1.5	10.42	4.44
15	9.4±1.3	10.11	4.31
16	10.4±1.3	9.83	4.19
17	12.1±2.0	9.58	4.08
18	8.6±0.9	9.35	3.98

Table 4.6b

Mean Free Path of Relativistic Heavy Ions in Emulsion

Theory vs. Experiment (Z=6,7,8)

(cm)

Charge	MFP Emulsion *(Lerman)*	MFP Emulsion *(theory)*	MFP Emulsion *(Heckman)*
6	14.3 ± 2.0	14.99	13.8 ± 0.5
7	11.9 ± 1.6	14.03	13.7 ± 0.6
8	13.4 ± 1.7	13.25	13.0 ± 0.5

With regard to the "anomalon" hypothesis it should be noted that there is no indication in any of our studies of systematically lower mean-free-paths in the first few centimeters. This is important vis-à-vis the fact that this data set is the base of the Monte-Carlo to follow. Note that this contrasts with a data set with essentially the same order of magnitude of secondaries per charge bin as presented by Friedlander et al (1983). This is mentioned principally because it was a hunt for such objects that catalyzed what became the Copper Calorimetry Experiments, but is not addressed further in this chapter. *We shall briefly return to the question of these emulsion-based anomalons at the conclusion of Chapter 8, where we finish dissociating them (or any other short mean free path phenomena) from the results of the Copper Calorimetry Experiments under study.*

Note that Λ and **b** play a larger role than mere fitted constants. They are capable of acting as simulation variables, parameterizing a broad range of Z-dependent interaction cross-sections. Setting Z=1, Λ is seen to 'represent' the inverse of a single nucleon's geometric cross-section. And **b** roughly reflects the projection onto an interaction plane of the space packing of nucleons in a spherical nucleus. If the spherical nucleus were completely filled by nucleons, **b** would equal 2/3. Instead, the fit finds **b** to be ~ 2/5,

suggesting in our crude model that for purposes of geometric cross-sections, nucleons collectively fill only 60% of the available nuclear space.

4.4 Other Statistics of the Database

The charge distribution by generation is as follow, and where Charge=19 are Z=1 particles between {12 – 20} degrees and Charge = 20 are Z=1 particles between {20 - 45} degrees*:*

Table 4.7 Generations of Secondaries by Charge

Charge	*Generation 1*	*Generation 2*	*Generation 3*	*Generation 4*	*Generation 5*
1	0	83	0	0	0
2	0	490	178	37	7
3	0	20	4	3	1
4	0	17	11	1	1
5	0	20	12	3	0
6	0	30	11	3	0
7	0	33	6	3	0
8	0	25	13	4	0
9	0	15	9	1	0
10	0	31	8	2	0
11	0	22	7	3	0
12	0	31	9	2	1
13	0	34	9	1	0
14	0	26	7	1	0
15	0	37	6	2	0
16	0	37	8	0	0
17	0	26	2	0	0
18	817	63	7	1	0
19	0	27	0	0	0
20	0	0	0	0	0

Figure 4.4

STARS BY GENERATION AND CHARGE

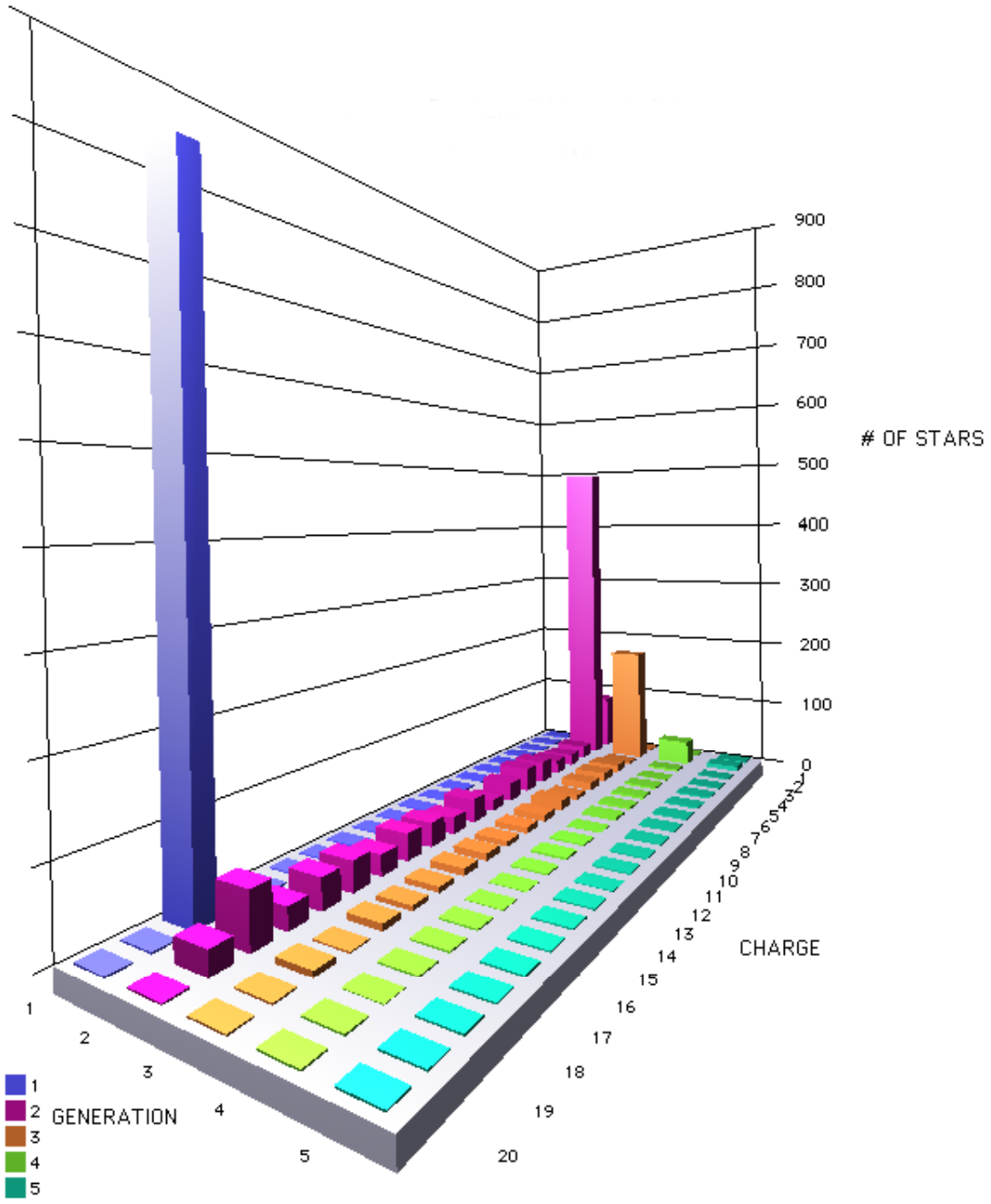

And the Fragmentation Matrix for Z>2 is:

Table 4.8 Fragmentation Matrix

CHARGE	3	4	5	6	7	8	9	10	11	12	13	14	15	16	17	18
3	3															
4	2	1														
5	1	4	3													
6	1	2	2	2												
7	1	4	6	2	2											
8	3	2	2	3	3	6										
9	1	1	1	2	3	3	1									
10	2	3	6	3	6	2	4	1								
11	0	1	1	3	4	2	2	1	3							
12	0	4	1	3	5	2	0	5	3	2						
13	3	0	3	4	1	3	1	4	2	2	3					
14	1	3	2	1	3	5	7	1	1	5	3	6				
15	1	2	1	1	2	3	2	2	6	7	5	1	3			
16	3	3	1	2	1	1	1	3	6	6	2	3	8	4		
17	0	0	2	1	0	1	2	3	0	0	1	1	2	3	5	
18	32	44	33	51	44	50	25	61	46	54	53	60	64	79	54	111

The vertical column of CHARGE represents the charge of the local primary, while the horizontal row of CHARGE is the charge distribution of the daughter products that have been measured. Hence the first matrix element has a value of 3 meaning that all local primaries of Z=3 had daughter products of charge Z=3; while the second row shows that local primaries of Z=4 split 2:1 into daughter products of Z=3 and Z=4. All Z=2 daughter products have been ignored in this version of the Fragmentation Matrix for beyond the values themselves one of the most important implications of the Fragmentation Matrix is its pure diagonal nature: i.e. a zero value for all matrix elements (i,j) where j>i. Also seen graphically below, this is an important quality control check on the scanning: for although it is physically impossible that fragments could have a charge greater than their parent, mistakes in scanning could indicate otherwise.

Figure 4.5

Fragmentation Matrix

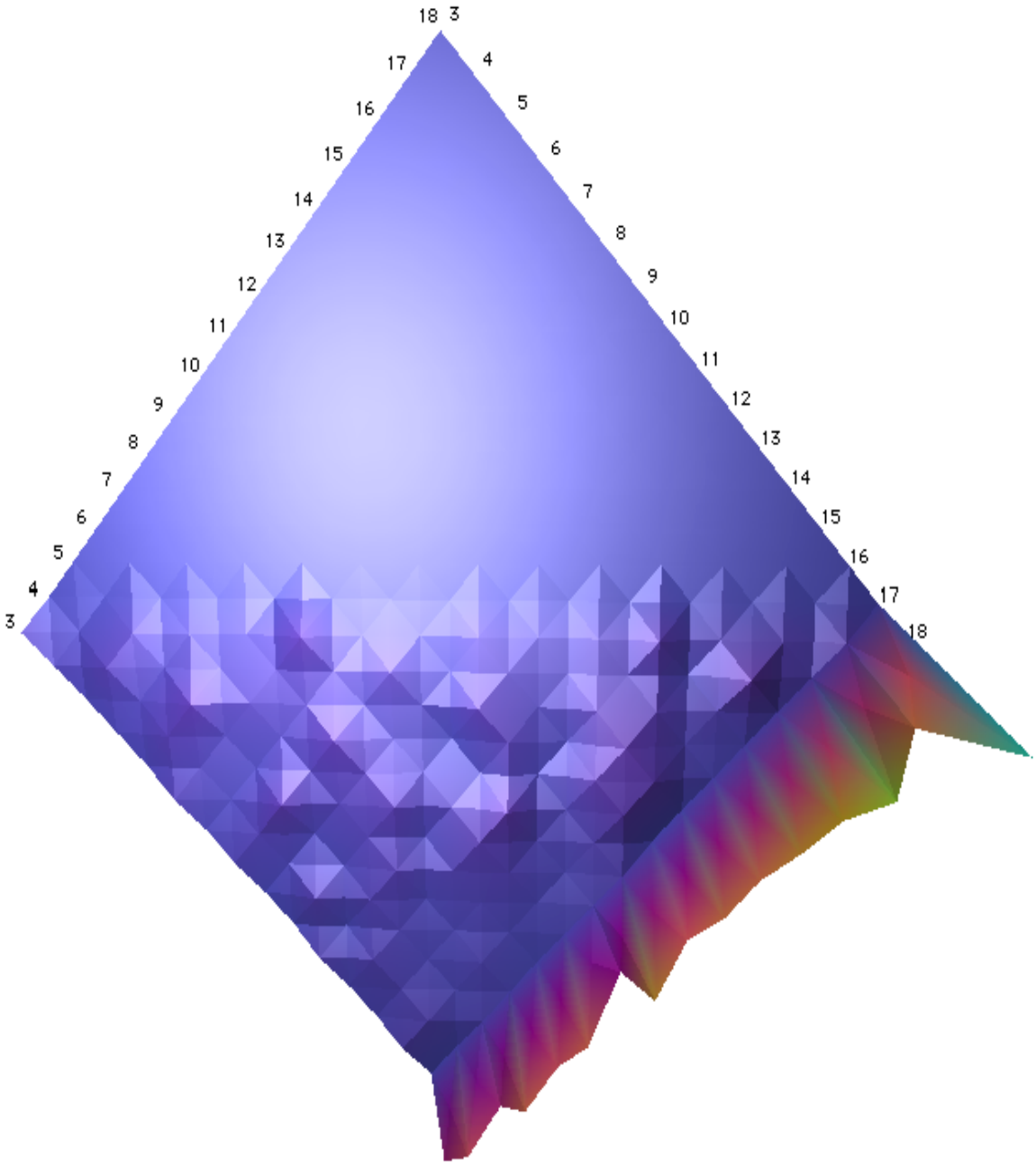

(Z-axis View)

4.5 The Analyzer

Other analyses of the emulsion results come from a suite of analytic tools (*The Analyzer*) created to mine the emulsion data set. It allows one to make cuts amongst a wide set of multivariable conditions. The first stage of (independent) variables includes:

Nz = Charge of the "local" primary
Nh = Number of 'heavy" tracks = $N_{black} + N_{grey}$
Ns = Number of relativistic shower particles (Z=1) = N_{shower}
Nalf = Number of alphas = N_{alpha}
Nf = Number of relativistic fragments with Z≥3
KZ = charge of the fragment
Thc = limit of the angle theta for the particles under consideration
Eta = rapidity
Theta = polar angle
Psi = azimuthal angle
Proj = progected angle

The second stage of conditional variables can be set to run between the limits of [0, 99], and include:

Nz = Charge of the "local" primary
Nh = $N_{black} + N_{grey}$
Ns = N_{shower}
Nalf = N_{alpha}
Nf = Number of relativistic fragments with Z≥3
Ntype = Phenomenological classification of tracks as indicated below

Black = 1	*Shower = 3*	*Fragments = 5*
Grey = 2	*Alphas = 4*	

As a useful example, the charge distribution of the local primaries on the interval [2,18]:

Figure 4.6 Charge Distribution of Local Primaries

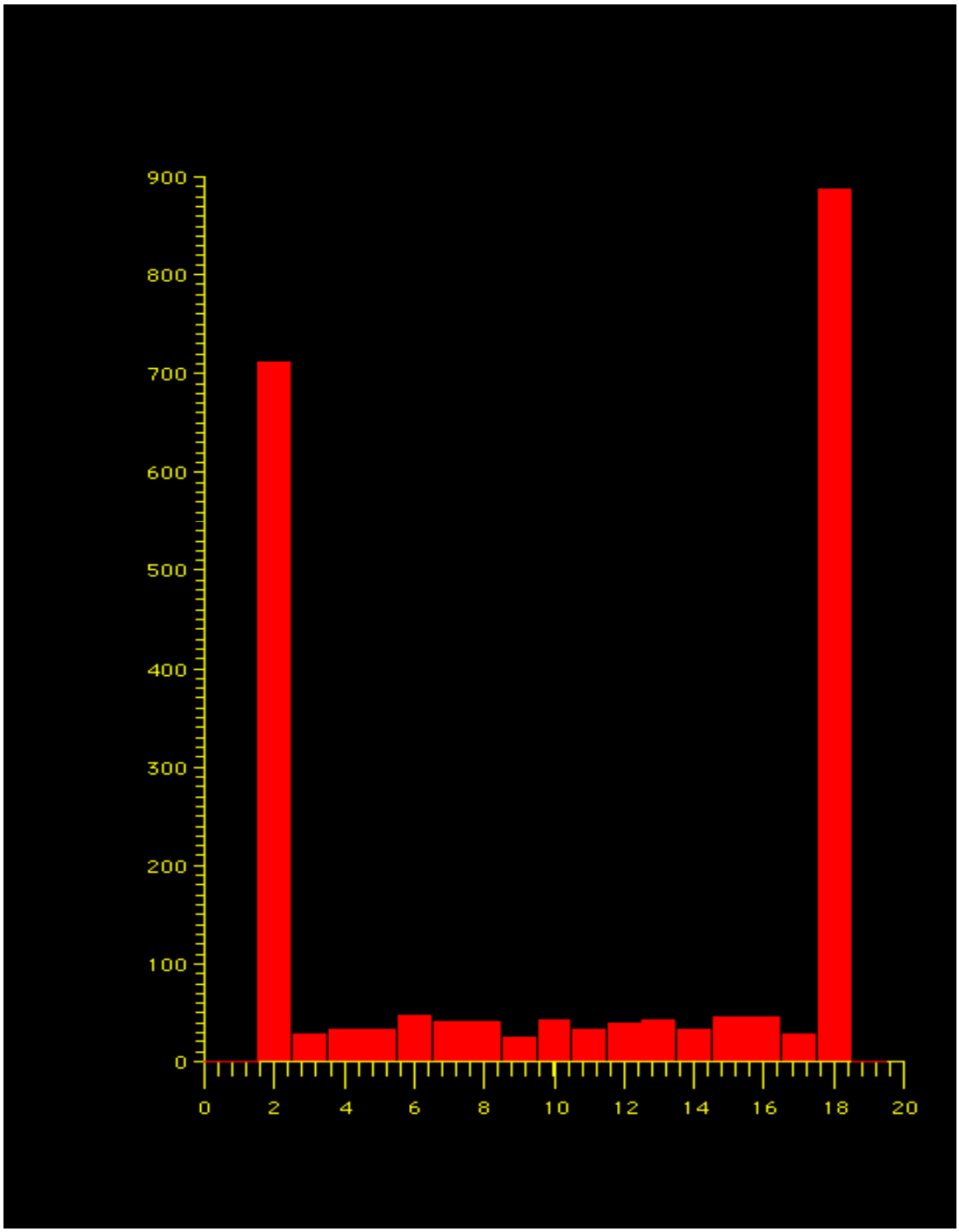

whose on-screen output presents the following statistics:

Table 4.9 Gross Statistics of Charge Distribution of Local Primaries

```
Analyzer #:  1          nz ,  0≤nz≤20


    2156 events




Mean       =     10.6999              ±    0.1547

Dispersion =      7.1828              ±    0.1094

Skewness   =     -0.1756              ±    0.0528

Excess     =     -1.7928              ±    0.1055
```

Looking more closely at the region Z=[3,17] reveals:

Figure 4.7 Charge Distribution of Local Primaries [3, 17]

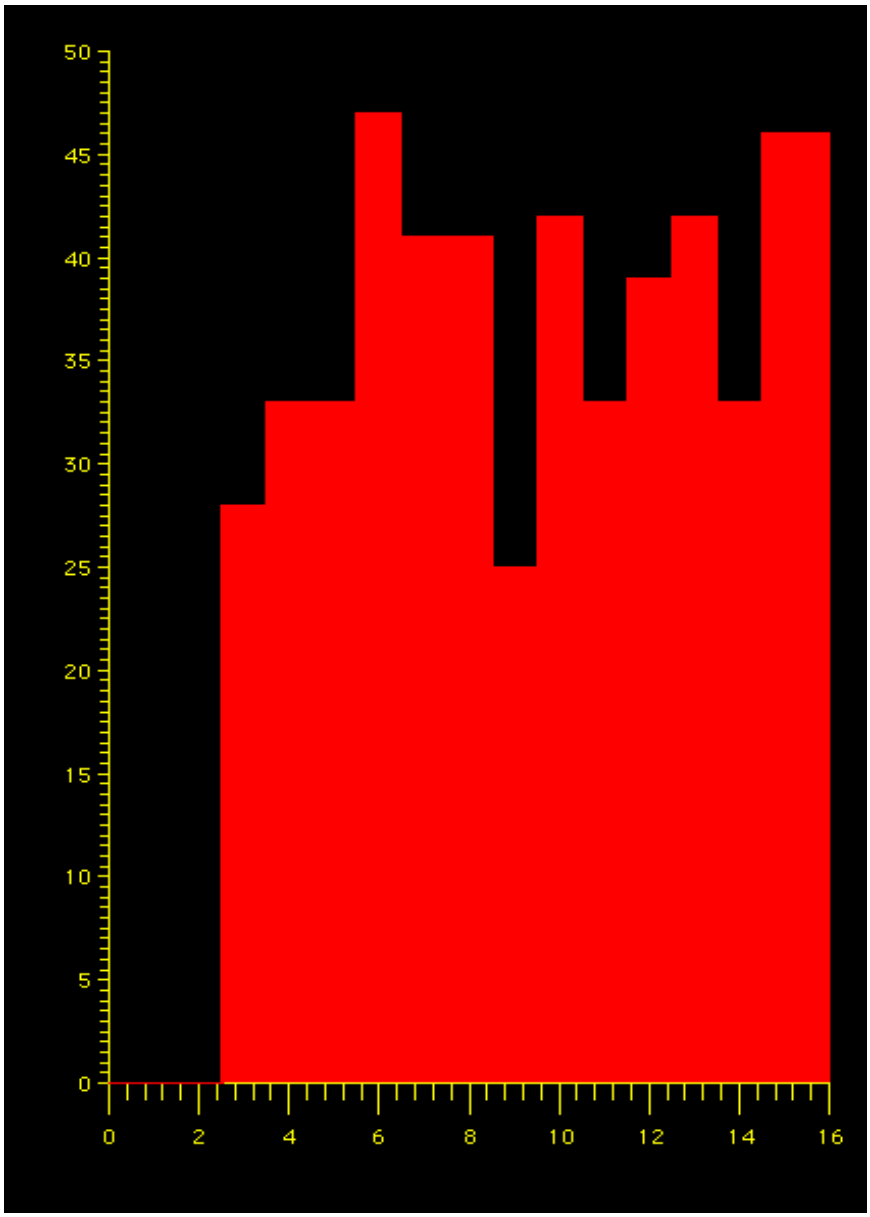

whose statistics are:

Table 4.10 Gross Statistics of Charge Distribution of Local Primaries

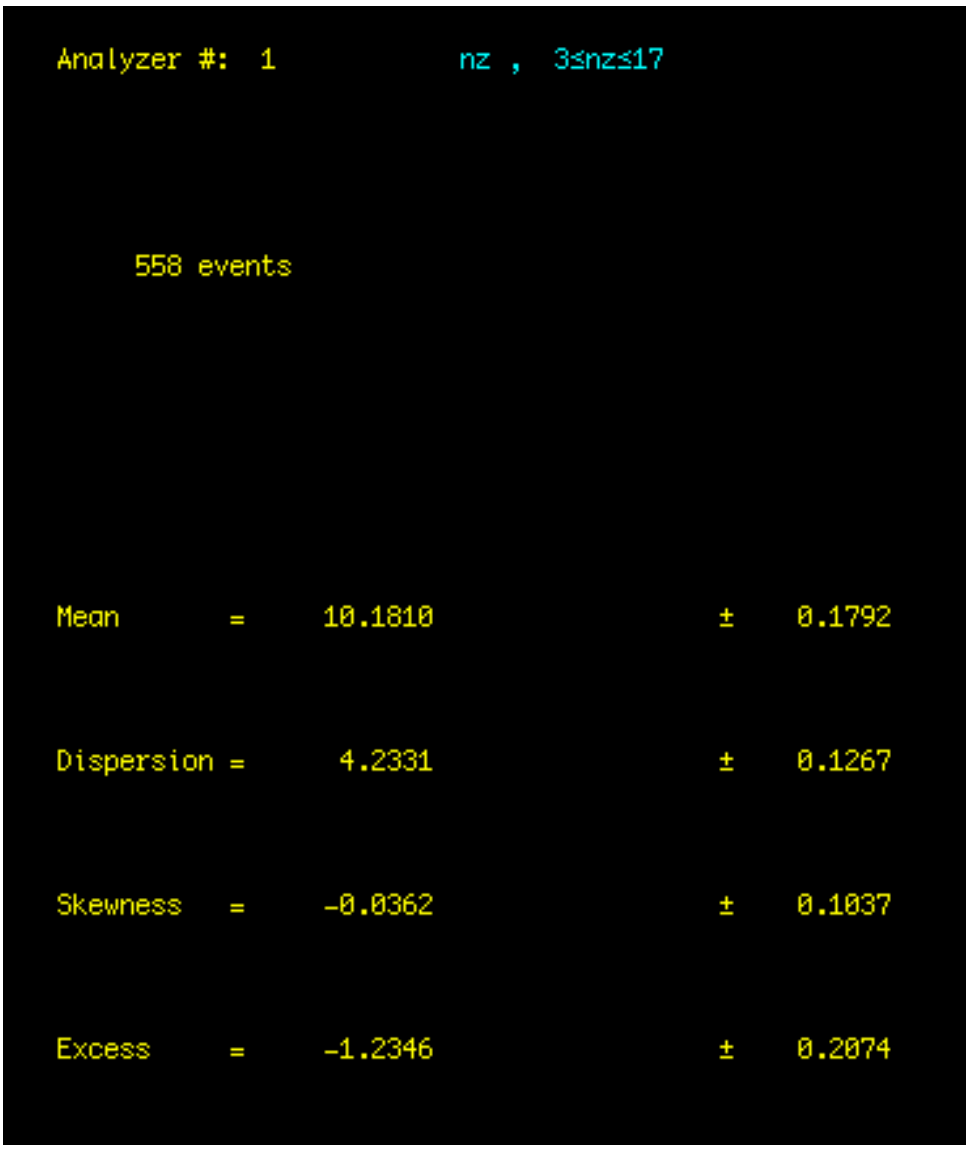

This tool, *The Analyzer*, was used to analyze and compare the critical statistics of our sample of over 2000 events to the much smaller sample (less than 100) utilized in the original Copper Calorimetry Experiments. Their results for a 1.8 A GeV ^{40}Ar beam on G.5 emulsion are summarized below, along with a comparison to our own. The detailed graphical analyses and statistics are in Appendix A.

Table 4.11

Mean Characteristics of Events

(1.8 A GeV ^{40}Ar Projectiles in Nuclear Emulsion)

	All events (Aleklett)	***All events* (Lerman)**	$N_h \leq 8$ *(Aleklett)*	$N_h \leq 8$ ***(Lerman)***	$N_h \leq 9$ *(Aleklett)*	$N_h \leq 9$ ***(Lerman)***
$\langle N_h \rangle$	9.8 ± 1.5	***8.9 ± 0.3***	3.0 ± 0.3	***2.9 ± 0.1***	22.6 ± 1.6	***21.79 ± 0.5***
$\langle N_s \rangle$	10.4 ± 1.0	***9.8 ± 0.3***	7.0 ± 1.0	***6.0 ± 0.2***	16.7 ± 1.6	***17.8 ± 0.6***
$\langle N_\alpha \rangle$	1.2 ± 0.2	***1.19 ± 0.04***	1.2 ± 0.2	***1.17 ± 0.05***	1.3 ± 0.3	***1.2 ± 0.05***
$\langle \theta_s^o \rangle$	16.7 ± 0.5	***19.8 ± 0.19***	14.0 ± 0.7	***14.5 ± 0.25***	18.8 ± 0.7	***23.6 ± 0.26***
$\langle \theta_\alpha^o \rangle$	1.9 ± 0.1	***1.9 ± 0.04***	1.7 ± 0.2	***1.8 ± 0.05***	2.2 ± 0.2	***2.1 ± 0.08***
$\langle Z_{F,Z>2} \rangle$	12	***11.49 ± 0.18***	13	***12.0 ± 0.2***	9	***8.7 ± 0.36***

As before

$\mathbf{N_h} = N_{black} + N_{grey}$

$\mathbf{N_s} = N_{shower}$

$\mathbf{N_\alpha} = N_{alpha}$

and from Aleklett et al (1988) θ_s^o and θ_α^o are the critical angles for shower particles and alphas respectively; while $Z_{F,Z>2}$ is the charge of projectile fragments with $Z > 2$.

It is apparent that there is an excellent agreement between all values, except for $< \theta_s{}^o >$ in the relativistic cone centered about the heavy secondaries. Although the values for $< \theta_s{}^o >$ in the peripheral regions is about the same ((14.0 ± 0.7 vs 14.5 ± 0.25) the value for 'All Events' is thrown off by the numerical discordance in the central region. This difference could be due to the possibility of our stack having a lower sensitivity so that some relativistic particles might have been lost at smaller angles.

We can't know for sure, since the original plates used by Aleklett et al are not available for comparison. Since everything else is essentially identical, we compensated for this possibility in one of the simulations by twinning all charge one particles with angles less than 12 degrees. These results are presented in the simulation results chapters, where it will be shown that this does not influence our results at all.

The otherwise near-identicallity of the mean characteristics of the scanned events in the two populations (Aleklett et al's and Lerman et al) has a critical implication. It means that the databases of our Monte-Carlo simulations are sufficiently comparable that any differences in simulation results will most likely be due to computational approaches and variables and not to the details of the scanning per se. This important point will be dealt with in Chapters 7 and 8 when discussing (computational) errors. It will be shown that the computational results and the resulting physical interpretation of Aleklett et al was likely due to a computational fluctuation due to having too small an initial database.

V The Argon–Copper Calorimetry Experiments

5.1 Experimental Setup*

The basics of these experiments are deceptively simple: two concentric copper disks are irradiated by a relativistic ^{40}Ar beam at varying distances apart. The natural copper disks are 1 cm thick cylindrical cross-sections with a 4 cm radius. The downstream disk was surrounded in turn by a "guard ring", a 7 cm torus with a 4 cm doughnut hole for the target disk. The setup is shown in side-view below.

Figure 5.1 Experimental Setup for Copper Calorimetry Experiments

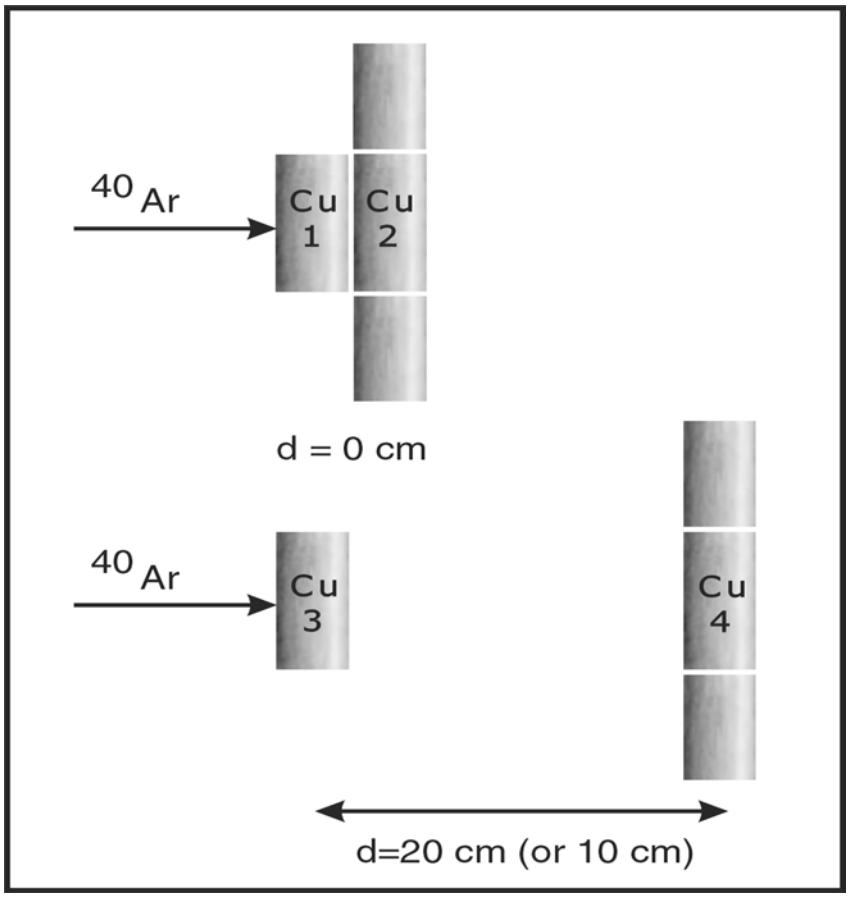

* Aleklett et al (1988a)

Separate experiments were performed at LBL's Bevalac for 3 different separations (0,10,20 cm) of the two target disks. A well-focused beam of $\sim 10^{12}$ argon ions passed through each disk during the 2-4 hour exposures. The beam was nominally focused to a diameter of 1 cm, and post-exposure autoradiography of the targets showed 99% of beam-transmuted nuclides to lie within a 2 cm radius. Following exposure, short-lived isotopes were allowed to decay for 12-24 hours after which the samples were measured by off-line γ-ray spectroscopy using Ge(Li) detectors with a resolution of 1.8 kev. Counting continued for several months.

To decrease systematic errors the results were averaged from three independent experiments performed at LBL and with the off-line measurements being performed at three separate institutions (LBL, Marburg, Purdue). Calibrations, counting efficiencies, and corrections for potential geometric inhomogeneities of both beam exposures and target geometries were measured through the use of ersatz aluminum targets undergoing the reaction $^{27}Al(n,\alpha)^{24}Na$. Potential errors were found to be 2 ±1 %.

With a 15.02 hour $t_{1/2}$ and an easily identifiable 1368.5 kev γ-ray peak ^{24}Na was particularly easy to measure. But of all the nuclides measured, ^{24}Na was critical for far more than its calibration abilities. As seen in Figure 5.2 below, its production cross-section has a step-function-like dependence on energy. In particular, production of ^{24}Na below 1 Gev per nucleon is minimal. And by 2 A Gev the production is essentially asymptotic.

^{24}Na-production thus acts as a threshold counter for relativistic phenomena.
Only projectile fragments will be able to produce ^{24}Na from interactions with the Cu target nuclei. This is the first of two particularly elegant aspects of the experimental design. In essence then ^{24}Na-production provides an unusual and extremely useful form of calorimetery, where the total amount of ^{24}Na produced in a target segment is a direct function of the cumulative (target) interactions with relativistic (projectile) primaries and secondaries.

Figure 5.2 ^{24}Na Production Cross-Section in Copper*

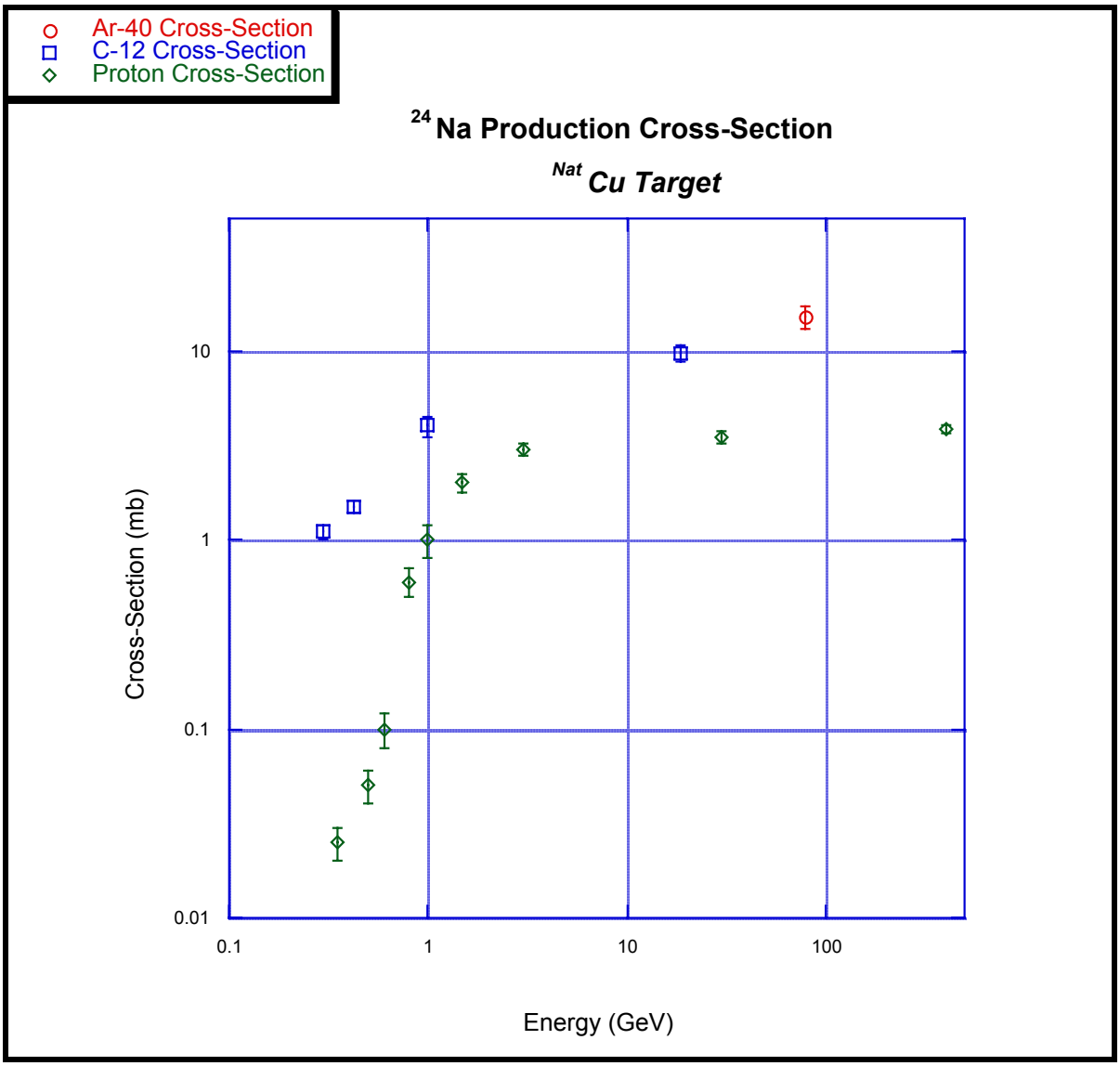

* Production cross-section values are courtesy of Professor Dr.'s Brandt and Friedlander; and were compiled by them from experimental work that included: Cumming (1974,1976,1978), Cole and Porile (1981,1982), Lund (1981), Hudis (1962,1968), Rudstam (1962), Barr (1957), and Friedlander (1954).

As an additional touch of experimental elegance the authors utilized not just the absolute activity of the isotopes under investigation, but the activity ratio R_d: the ratio of the activity of the downstream disk (at a distance *d)* to the activity of the front disk. This was done in order to finesse as much as possible systematic and experimental uncertainties: for each pair of disks shared identical histories, they were exposed to the same beam for the same amount of time, and they were measured in the same Ge(Li)'s. To quote the authors of the experiment[1]:

> *"...this activity ratio for a specific nuclide can be determined to a high degree of precision. All uncertainties due to particle fluxes, counting efficiencies, uncertainties in the decay scheme for a specific radioactive nuclide, etc. cancel out in the activity ratios R. Essentially, the only experimental uncertainty in this ratio comes from counting statistics. As the number of counts is typically $>10^4$ our activity ratio R can be determined within ±1%. Such a precision is comparable only to that of large counter experiments or of high statistics bubble chamber experiments..."*

It's worthwhile noting that 15 years earlier a similar use of experimental ratios to decrease systematic errors was fundamental to the demonstration of the existence of neutral currents[2], allowing experimenters the necessary luxury of ignoring the absolute flux (sic!) of neutrinos involved.

The activity ratio R in the Copper Calorimetry Experiments offered a similar benefit, but also an additional one… that by itself justified the entire experimental effort**: any "new" physics that might be found in the secondaries will manifest itself in R_d.** Indeed this will be seen to be the case! The underlying logic is easily seen by referring to the diagram below (Figure 5.3).

[1] Aleklett et al. (1988a)
[2] Galison (1987), p. 190

Figure 5.3 Metalogical Setup of Copper Calorimetry Experiments

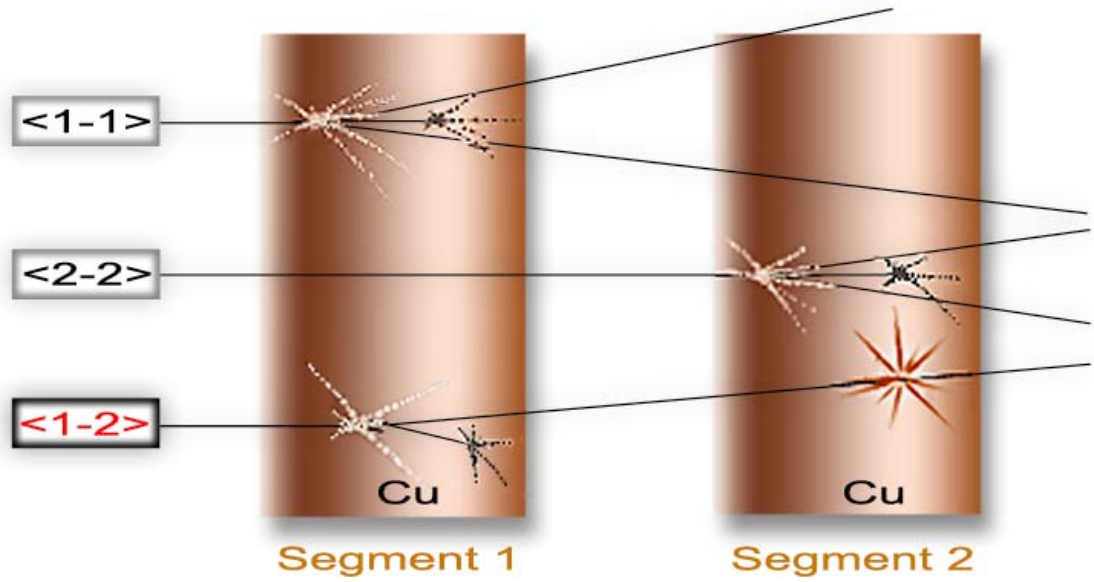

Possible interactions fall into three classes:

< 1-1 > A primary interacts in Segment 1 (the front)
and produces a secondary which also interacts in Segment 1.

< 2-2 > A primary interacts in Segment 2 (the rear)
and produces a secondary which also interacts in Segment 2.

< 1 – 2 > A primary interacts in Segment 1 (the front)
and produces a secondary which interacts in Segment 2.

It is obvious that in the first two classes, <1-1> and <2-2>, the basic nuclear processes involved are identical. Since the primary beam is exponentially absorbed in each segment the amount of identical processes in Segment 2 should be reduced only in proportion to the amount of primary beam absorbed in Segment 1. Hence the ratio of activities in these two segments should follow this decrease, being one minus the amount of the primary beam exponentially absorbed in Segment 1 on the way to Segment 2.

For these first two classes any anomalous or unexpected secondary behavior will simply scale with the numbers of primary interactions. This is the one disadvantage of the use of activity ratios to finesse the uncertainty of values and the ignorance of processes: any activity due to unusual secondary behavior will be lost in the ratio if the 3rd class of secondary interactions <1-2> is too small.

Indeed (as will become evident) it's the third class of interactions <1-2> that will make apparent any difference in the secondaries' behavior that is manifested in the absolute activity. *For this third class breaks the symmetry in an unscalable way*. For example, in class <1-2> any unusual secondary phenomena which might enhance absolute activity will enhance Segment 2's activity due to the increased number of secondaries born in Segment 1 that then interact in Segment 2. Thus relative to the otherwise expected values, there will be an enhancement of the activity ratio

$$R = \frac{Activity_{Segment2}}{Activity_{Segment1}} \qquad \textbf{(5.1)}$$

If one knows or can simulate the expected number and effect of such "normally" behaving secondaries (born in 1, interacting in 2) *then any greater activity in Segment 2 (i.e. an enhanced R) must be due to other processes that somehow enhance the production of whatever one is measuring.*

Hence the need to create truly accurate simulations!

Indeed, the use of carefully crafted Monte Carlo simulations to accurately establish the denominator of the ratio

$$\frac{\textit{Observed Events}}{\textit{Events Expected by Conventional Assumptions}} \qquad \textbf{(5.2)}$$

is fundamental to contemporary high-energy physics. This is especially so when dealing with low-probability or low-incidence phenomena in complex detector scenarios. The existence of neutral-currents was established in 1973 using this phenomenological approach; and in the past year it was used to demonstrate the reality of tau-neutrinos in emulsion.

5.2 The Copper Calorimetry Experiments: Results

The table and graph below summarize the results of the LBL experiments [Aleklett, 1987 and 1988]. The experimental set-up was the two-segment cylindrical target discussed above with the two segments at various distances R_d from each other. Extraordinary experimental care was taken: the experiments for R_0 were independently performed *three* times, and those for R_{20} performed *twice.* The results of each experiment were then averaged yielding total experimental errors at the 2±1 percent level. These averaged results are presented below in Table 5.1 and Figure 5.4. Other experiments of this type were subsequently performed, the most reliable results listed below in Table 5.2. Experimental errors for these other, confirming experiments, are also stated to be 1-2%.

Haase (1990), using the Bevatron's 1.8 A GeV ^{40}Ar beam, performed an identically designed experiment against a cylindrical target of 20 such segments. Chapter 10 is devoted to a discussion of Haase's experimental results, for they seem critical to our understanding of the actual physics involved.

Table 5.1 Experimental Values of R_0 (LBL 1987)

	0.9 A GeV ^{40}Ar	1.8 A GeV ^{40}Ar
R_0	1.167 ± 0.011	1.501 ± 0.008
$R_{ring,0}$	< 0.01	< 0.01
R_{10}	1.118 ± 0.020	1.373 ± 0.034
R_{20}	1.102 ± 0.026	1.251 ± 0.020
$R_{ring,20}$	0.039 ± 0.002	0.071 ± 0.005

Figure 5.4 Experimental Values of R_0 (LBL, 1987)

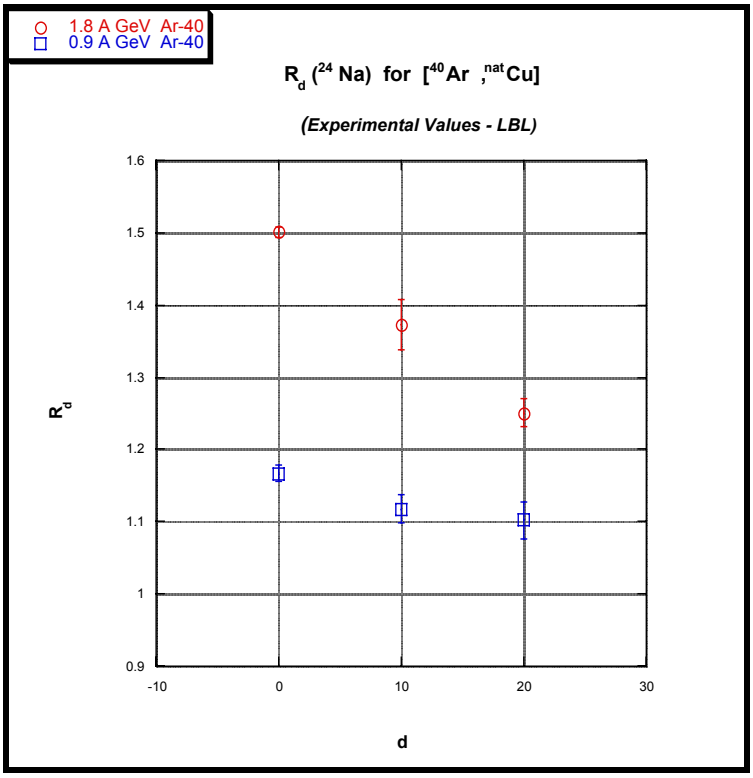

Table 5.2

R_0 for the Copper Block Calorimetry Experiments

Primary (Z)	Energy (A GeV)	R_0	Errors	Lab	Reference
1	0.6	**0.91**	0.03	SIN	Heck (1992)[1]
1	1.3	**0.99**	0.03	JINR	Heck (1992) [1]
1	2.6	**0.96**	0.02	Saclay	Heck (1992) [1]
1	4.5	**0.98**	0.05	JINR	Heck (1992) [1]
1	24	**1.1**	0.02	CERN	Dersch (1986)[1]
2	1	**0.92**	0.01	Saclay	Pille (1990) [2]
2	12	**1.21**	0.02	CERN	Dersch (1986) [2]
6	2.1	**1.13**	0.02	LBL	Dersch (1986) [2]
6	3.6	**1.24**	0.02	JINR	Heck (1992) [2]
18	0.9	**1.17**	0.02	LBL	Dersch (1986) [3]
18	1.8	**1.42**	0.05	LBL	Haase (1990)
18	1.8	**1.5**	0.02	LBL	Dersch (1986) [3]

In Figures 5.6(a,b) below these experimental R_0 values are displayed in successively expanded views.

[1] also Brandt et al (1993)
[2] also Brandt et al (1992b)
[3] also Aleklett et al (1988)

Figure 5.6a

R_0 for the Copper Block Calorimetry Experiments

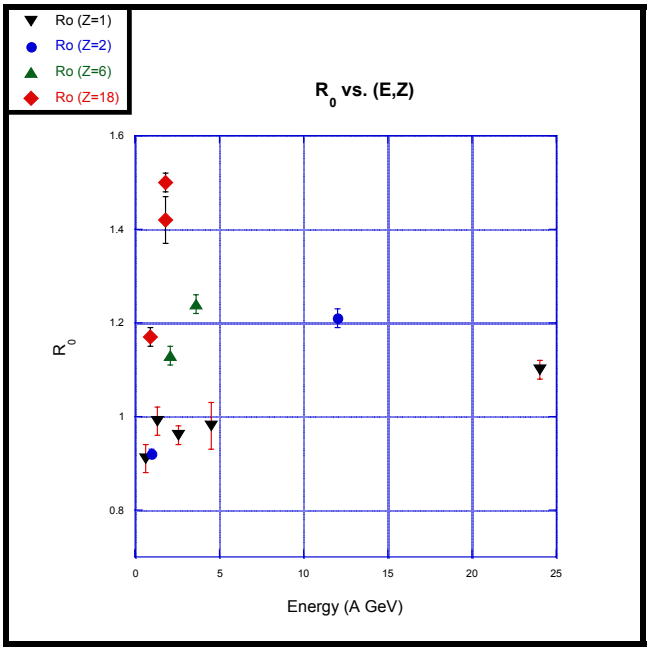

Figure 5.6b

R_0 for the Copper Block Calorimetry Experiments

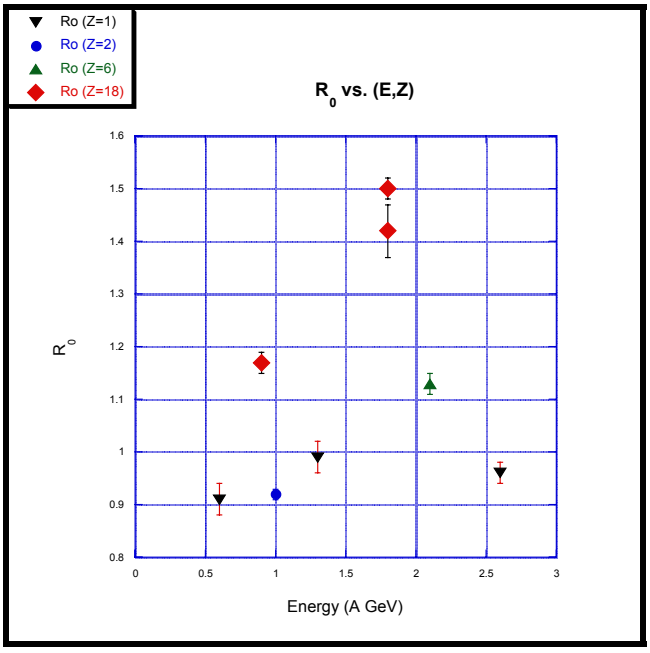

The key point is readily apparent:

A 1.8 A GeV ^{40}Ar projectile directed at a target of Cu (naturally occurring isotopes) has an experimentally determined ratio $R_0 \sim 1.5$.

This value of ~1.5 is ~ 50% greater than the nominal value of $R_0 \sim 0.96$ for a single nucleon (proton) at the equivalent energy. This 50% differential is also much larger than the error bars of a few percent associated with the copper experiments, the emulsion experiment described above, and the computer simulations described next.

VI The Simulations

RHIP is an experimentally based Monte Carlo analysis of relativistic heavy ion transport that embodies an important simplicity of approach. To finesse as much as possible assumptions and models, we worked backwards from measurements. The multiplicity and angular distribution of secondaries is drawn from the just described experimental database. They are NOT in any first-order sense model-dependent, though baryon conservation and azimuthal isotropy is assumed. The only other major experimental finding used is the standard experimentally derived exponential distribution of mean free path $e^{-(d/\lambda)}$. This relative lack of model dependency seems logically essential to any (Monte Carlo) simulation aspiring to provide insight into the physical systems tested; or to be a straightforward and valid test of the assumptions made and the variables used.

BFHLis the specific application of *RHIP* to simulate a relativistic Ar-Cu interaction, designed explicitly to understand the results of the suite of Copper Calorimetry Experiments were performed initially at LBL, and subsequently at CERN, Dubna, and Saclay. These experiments and their results are discussed in Chapter 5.

The basic target geometry of *BFHL* is a set of N cylindrical segments co-linearly arranged. The radii of the segments need not all be the same throughout. This generalization of geometry allows for both the inclusion of "guard-rings" about otherwise uniform target segments (see figure 5-1) as well as being readily expandable to simulate other azimuthally symmetrical targets.

Beyond the ability to change a large number of input variables (discussed below) a number of variations of *BFHL* exist. These include two different ways to incorporate baryon conservation, as well as a number of different computational approaches which taken together supports a far better calibration of the computational accuracy of the whole. Nor need the interaction variables such as mean free path or production cross-section be homogeneous. The program is written such that the effect of variable subpopulations is allowed.

6.1 Versions of BFHL

Baryon Conservation

1) Missing Mass : A mass balance of baryons is calculated for all stars
2) Twinning: All Z=1 particles are given neutron "twins"

Database Variation

1) The order of stars in the database is varied.
   (For small numbers of runs this can make a considerable difference.)

Simulation Variations (for Computational Convergence and Quality Control)

1) Only subsets of the random numbers of a given generator are selected
2) Percentages of subpopulations are generated both by statistical distributions and by 'deterministic' counters.

Two Disk and Full Cylinder Geometries

Much of the basic physics is best illuminated in the two disk configurations discussed below. But the full cylinder version is also useful, for it is in essence a multi-stage amplifier. Similar to such an amplifier, the increased gain of the cylinder model reveals clearly the essence of what seems a shy and subtle phenomena in the two disk configuration.

Visualizations

A number of visualization programs have been written in order to visually follow the physics

The physical logic common to all versions of BFHL follows:

6.2 A Basic Outline of BFHL's Physical Logic

Beam-Target

1) Take a circle of radius **R** cm
2) Assume the primary beam has a Gaussian Distribution in X-Y with dispersion σ_{beam}
3) Take a random point (X_0, Y_0) for a beam particle to intersect the face of the target
   Case I: Ideal Beam and Target Orientation (Perpendicular)
   Case II: Beam is at a non-90º angle to Target

Primary Argon-Cu Interaction

4) Mean Free Path (mfp)
   a) Known mean free path for Argon primaries (Z=18) in Cu
   b) Following an exponential distribution of $e^{-(d/\lambda)}$
5) Check if the resulting distance is within bounds of target…..if so, then have a star
6) If not, let it go and pick another from the exponential distribution $e^{-(d/\lambda)}$

Stars and Secondary Interactions

7) Stars
   a) Take the first interaction from the database
   b) Then follow each secondary with an $e^{-(d/\lambda)}$ interaction
   c) If within the target boundaries then take that interaction in turn from the database

The simulation follows every track from every star

8) When ALL the tracks are outside, go on to the next interaction from the database.

The basic mathematics of this physical logic are standard and outlined below.

1) Beam Distribution: Given X_0, Y_0, σ there exists a distribution across the face of the target for beam particles to 'hit'. The distribution is a product of two independent Gaussian distributions in X and Y whose product is:

$$D(x,y) = \frac{1}{2\pi\sigma^2} e^{\left(\frac{-x^2}{2\sigma^2}\right)} e^{\left(\frac{-y^2}{2\sigma^2}\right)} dxdy \tag{6.1}$$

where $x^2 + y^2 = r^2$ and the Jacobian is $dxdy = rdrd\theta$. Hence

$$D(x,y) = D(r) = \frac{1}{2\pi\sigma^2} e^{\left(\frac{-r^2}{2\sigma^2}\right)} rdrd\theta \tag{6.2}$$

Integrating over the azimuth $\int_0^{2\pi} d\theta = 2\pi$ so

$$D(r) = \frac{1}{\sigma^2} e^{\left(\frac{-r^2}{2\sigma^2}\right)} rdr \tag{6.3}$$

Letting

$$Q = \frac{r^2}{2\sigma^2} \tag{6.4}$$

one gets $dQ = \frac{rdr}{\sigma^2}$ yielding an exponential distribution from (6.3)

$$D = e^{-Q} dQ \tag{6.4}$$

All one needs to do here is to extract an exponentially distributed quantity like

$$Q = -\ln(rnd(u)) \tag{6.5}$$

So

$$r = \sqrt{2\sigma^2}\sqrt{Q} = \sqrt{2}\sigma\sqrt{-\ln(rnd(u))} \tag{6.6}$$

and given r, one gets $X = r\sin\theta$ and $Y = r\cos\theta$

2) Generalization to a Cylinder: In order to simplify the application of the code to a cylinder of many sectors all primaries are assumed to be created in an interaction at Z= (0 – δ) in front of the face of the target. Sector 1, the first copper block, is then considered to be the 'next' sector that these newly created Argon primaries are entering.

3) Mean Free Path: The integral distribution of path lengths is

$$F(x) = \int_0^x e^{-\frac{x}{\lambda}} \frac{dx}{\lambda} = e^{-\frac{x}{\lambda}} \tag{6.7}$$

So $x = -\ln F(x)$. In our case setting $F(x) = rnd(u)$

$$x = -\ln rnd(u) \tag{6.8}$$

and $rnd(u)$ will be defined later (section 7.5.1)

6.3 Classes of Variables Found in All Versions of *BFHL*

Overall Target Geometries

1) Radius and height of cylindrical sectors
2) Full cylinder made up of sequential cylindrical sectors
3) Two cylindrical sectors, touching (Figure 6-1 below)
4) Two cylindrical sectors, apart

Beam Variables

1) Number of particles in a pulse
2) Number of pulses in a 'run'
3) Central coordinates of the beam's interaction with the face of the target
4) The dispersion of the Gaussian beam distribution (see Appendix B, Fig. B2-f,e)
5) Polar and azimuthal angles of beam's interaction with target face

Kinematic Variables

The total energy E_p and the transverse momentum P_t of shower particles

Interaction Variables

1) Mean Free Path (absolute values or fitting parameters)
2) Fragmentation (limited control)
3) Production Cross-section

Computational Variables

Random number generating functions, modulos, seeds, and subsets

Baryon Conservation

1) Twinned protons (i.e. twinning the shower particles found in each star)
2) Missing Mass (mass balancing to the atomic number A of each local primary)

Subpopulations

1) Λ, E_p , σ_p , fragmentation, and other variables of the nucleus
2) Percentage of subpopulation

The programming details of BFHL are presented in Appendix B, including:

1. Figures of simulated beam trajectories (example below)
2. Flowcharts of BFHL
3. Variable List
4. Subroutine List
5. Matrices List

Figure 6.1 Simulations of Argon Beam on Copper Disks (close-configuration)

Beam Profile Variance σ_{beam} = 2.0

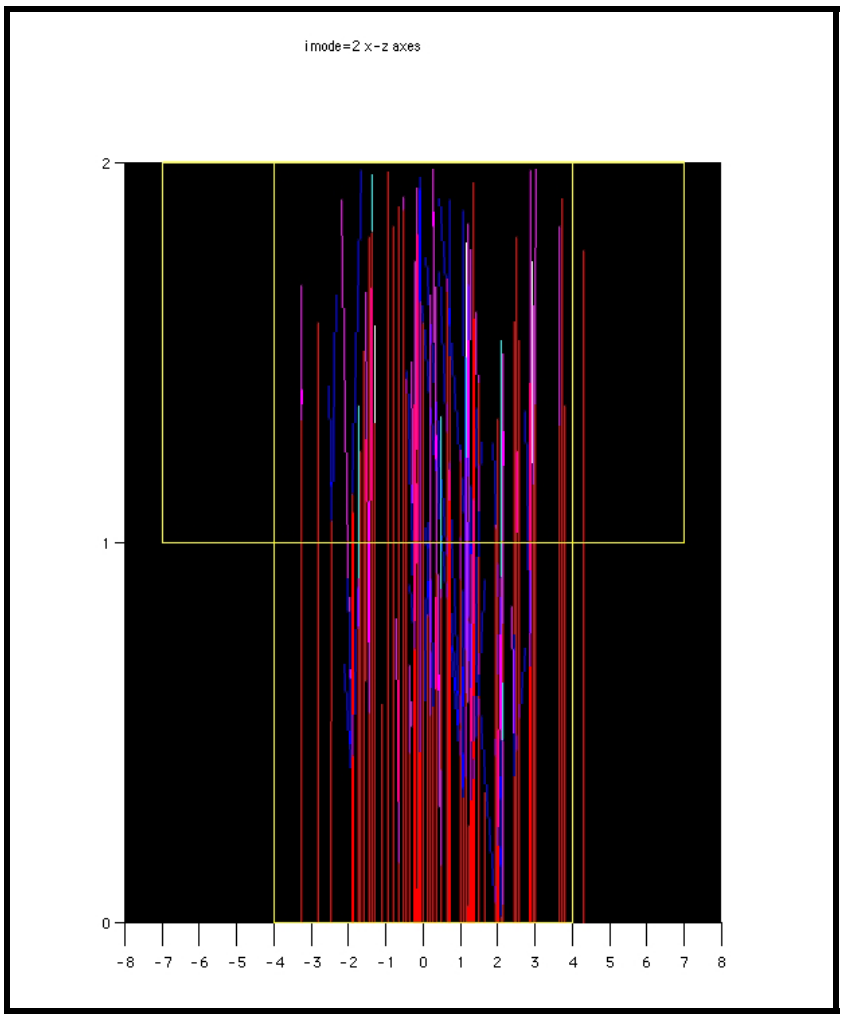

VII Initial Applications of the Simulation Program *BFHL*

(Ar-Cu Calorimetry Experiments)

The simulation program *BFHL* as outlined in Chapter 6 can be applied to a large number of specific situations. Application to ^{24}Na production in a copper target requires an explicit formulation of the partial cross-sections for ^{24}Na production.

7.1 ^{24}Na Production Cross-section

At the threshold of relativistic energies the production cross-section of ^{24}Na in copper behaves like a step-function:

Table 7.1 ^{24}Na Production Cross-sections in Copper*

Primary	Energy (GeV)	σ (mb)	σ-errors (mb)
^{40}Ar	80	15	2
^{12}C	18.5	9.7	1
^{12}C	1	4	0.5
^{12}C	0.42	1.5	0.1
^{12}C	0.3	1.1	0.1
^{1}H	400	3.83	0.21
^{1}H	30	3.5	0.25
^{1}H	3	3	0.21
^{1}H	1.5	2	0.2
^{1}H	1	1	0.2
^{1}H	0.8	0.6	0.1
^{1}H	0.6	0.1	0.02
^{1}H	0.5	0.05	0.01
^{1}H	0.35	0.025	0.005

* Production cross-section values are courtesy of Professor Dr.'s Brandt and Friedlander; and were compiled by them from the experimental work of Cumming, Cole, Porile, Lund, Hudis, Rudstum, Barr, and G. Friedlander (references with Figure 5.2).

Figure 7.1a ***^{24}Na Production Cross-section in Cu***

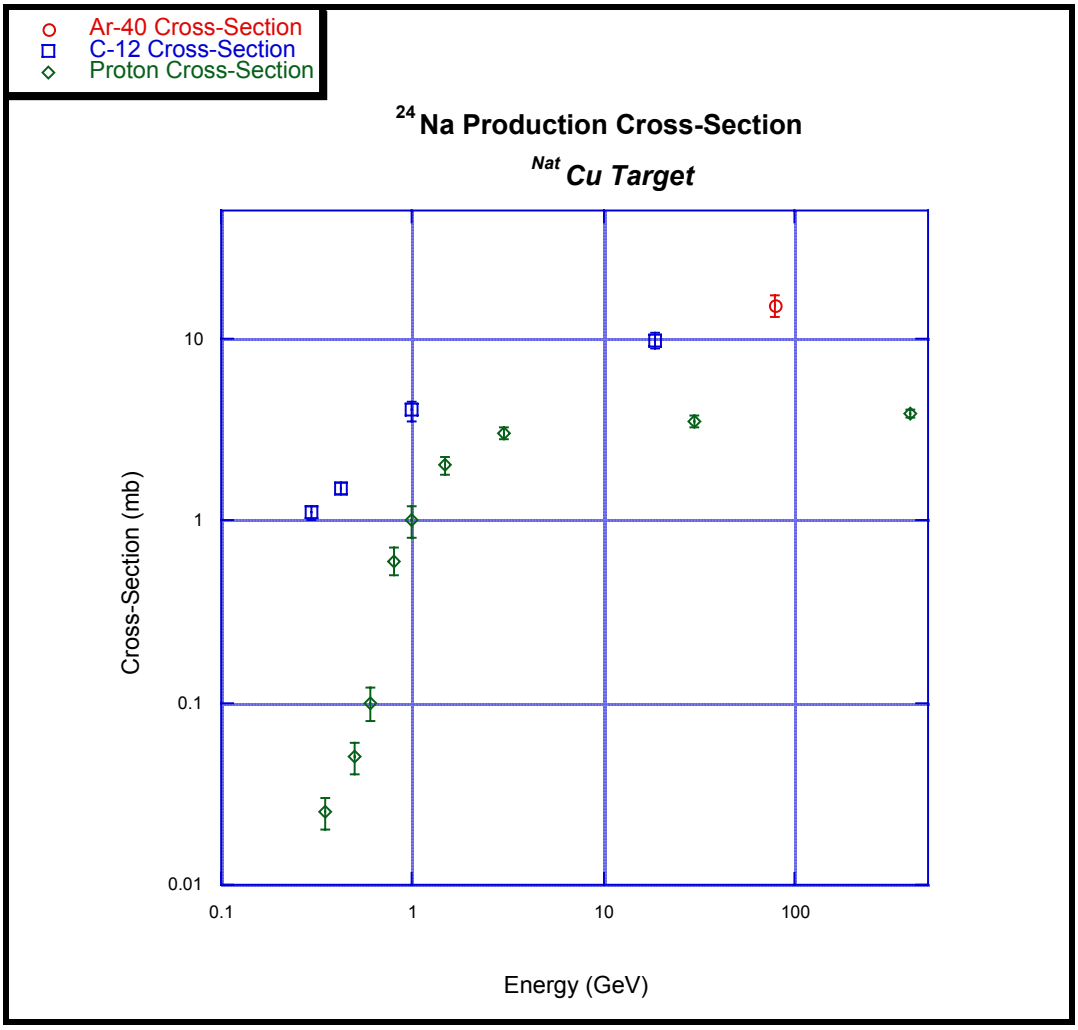

Hence only projectile fragments will be able to produce ^{24}Na from interactions with the Cu target nuclei. Quite usefully this makes the process of ^{24}Na-production a form of calorimetery, where the total amount of ^{24}Na produced in a target segment is a direct function of the cumulative target interactions with relativistic (projectile) primaries and secondaries. But the experimental ^{24}Na-production cross-sections available for copper as seen in Table 7.1 is comparatively sparse. Reassurance that the ^{24}Na production cross-section in Cu behaves in the same step-function-like manner pictured is seen in the following two graphs.

Relativistic protons on Ag yields a near-identical curve to that for protons on Cu (as seen in Figure 7.1a).

Figure 7.1b ***^{24}Na Production Cross-section***

[p + Ag→ ^{24}Na]

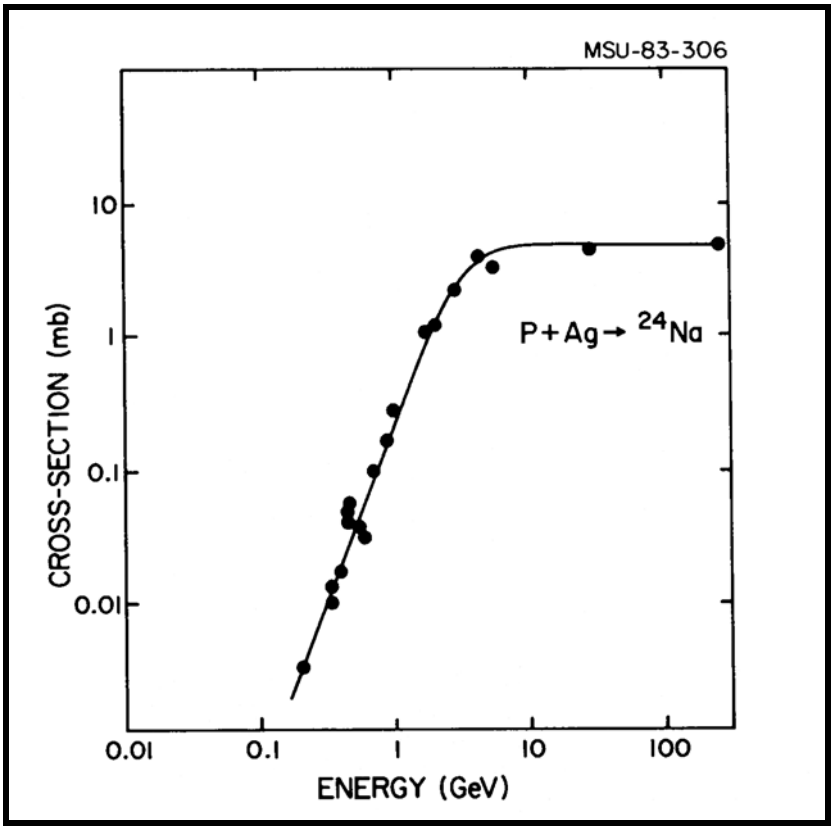

(Scott 1983)

This near-identicality of production cross-section for protons in both Cu and Ag also offers critical support for the utilization of the emulsion-measured database as the core of the Monte Carlo simulation in copper.

Another legitimate concern is the solitary data point for ^{24}Na production from a relativisitic Ar beam on Cu. That a congruent geometry to those of protons and carbon beams is the correct one for argon on copper is supported by the much more extensive studies done on gold; coupled to the experimental demonstrations that factorization and limiting fragmentation seem to hold in these regimes[1].

Figure 7.1c ***^{24}Na Production Cross-section for Au***

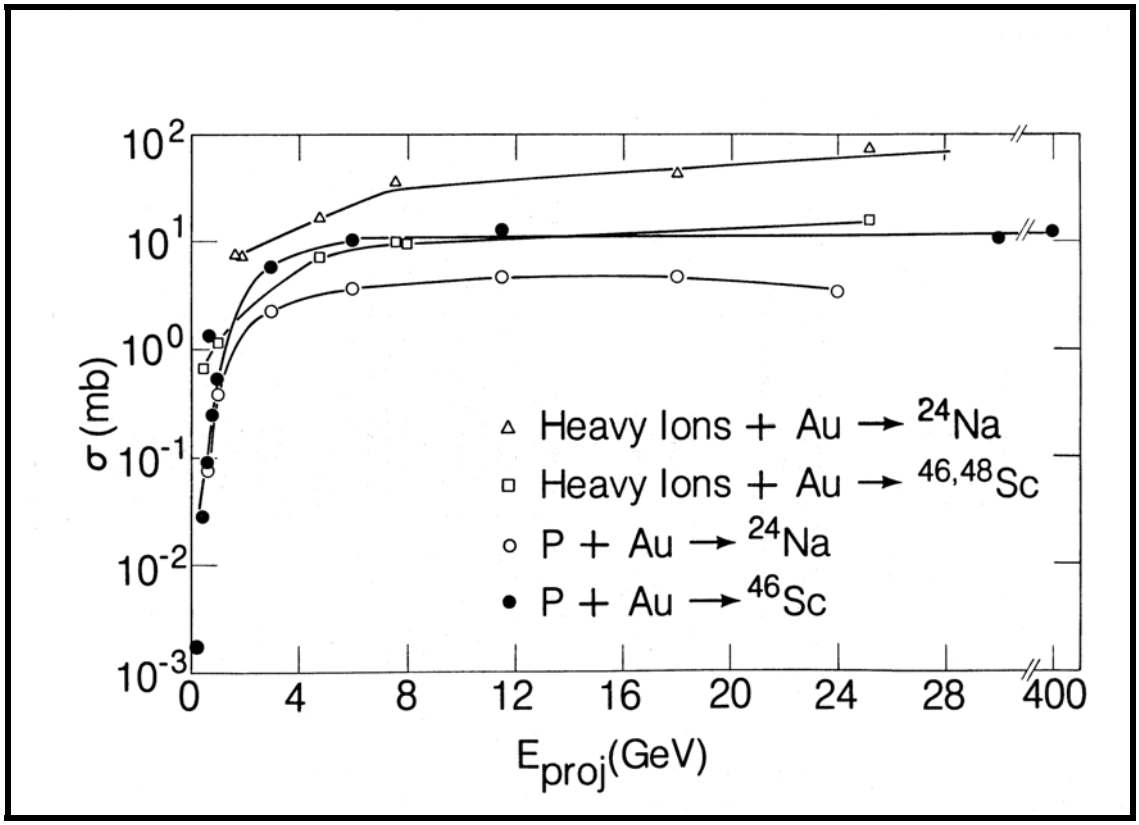

(Aleklett et al 1983)

[1] See for example Heckman et al (1978) for work at 2.1 A Gev in emulsion and references therein for other Bevatron experiments showing that fragmentation is independent of the target nucleus. Also see Chapter 1 for a much more extensive discussion of both limiting fragmentation and factorization.

Following Aleklett et al (1987), the data in Table 7-1 has been interpolated through the following parameterizations to create the following partial cross-sections (σ_P and σ_F) for the production of ^{24}Na in a native copper target:

1) For protons and pions with $E_k \leq 3$ GeV:

$$\sigma_p(E_k) = e^{-0.17 + 2.5u - 1.22u^2} \tag{7.1}$$

where $u = ln(E_k)$ and pions are assumed to behave identically to protons.

2) For protons and pions with $E_k \geq 3$ GeV

$$\sigma_p(E_k) = 2.88 E_k^{0.0496} \tag{7.2}$$

3) But for projectile fragments of Z$\geq$ 2 (i.e. A$\geq$ 4), the cross-section $\sigma_F(A)$ is assumed to be energy independent, and an interpolation between the above data yields:

$$\sigma_F(A) \cong 3.6 A^{0.387} \tag{7.3}$$

7.2 Baryon Conservation

Neutrons, being neutral, are unseen by emulsions. But baryon number must be conserved in any interaction. Two independent approaches were taken to satisfy this requirement.

1) *Twinning:* Each of the observed charge one particles, whether relativistic fragments or participants, is doubled. This is done by assigning to a neutral particle the same polar angle as the observed Z=1 particle, but with a randomly assigned azimuthal angle. This follows from observations made by Karol and others that projectile fragments frequently are produced with accompanying light secondaries, such as neutrons. At relativistic energies these shadowing secondaries would follow very close trajectories to the charged projectile fragment it was born with.

2) *Missing Mass:* A mass balance is done between the incoming and outgoing observable tracks, with neutral particles equivalent to charge one (i.e. neutrons) being added to balance any missing mass. When calculating the difference between the 'known' mass number of the local primary and the sum of the mass numbers of the observed local secondaries, the most common isotope for a given Z is assumed.

   In so doing, additional geometric constraints are imposed in order to differentiate between relativistic fragments and any participating protons or neutrons. Separate distributions of polar angle were created for Z=1 relativistic fragments and participants. The polar angle for an added particle is taken at random from the angular distribution of protons in the respective interval {0-12} degrees or {12-45} degrees, while the azimuth is taken at random from a uniform distribution between
   {0 – 360} degrees.

   Of the missing mass added, 90% was added to the interval {0-12} degrees (relativistic fragments); while 10% of any missing mass was added to the interval {12-45} degrees (participants). If the 10% is a 'fraction of charge', then one particle is added anyway as a participating particle.

Hence the Missing Mass approach will tend to overestimate the production of shower particles and for small numbers of events tends to fluctuate a little more than does Twinning. But the two approaches, Missing Mass and Twinning, rapidly converge as seen in the two figures that follow.

Figure 7.2 Comparative Approaches to Baryon Conservation (R_0)

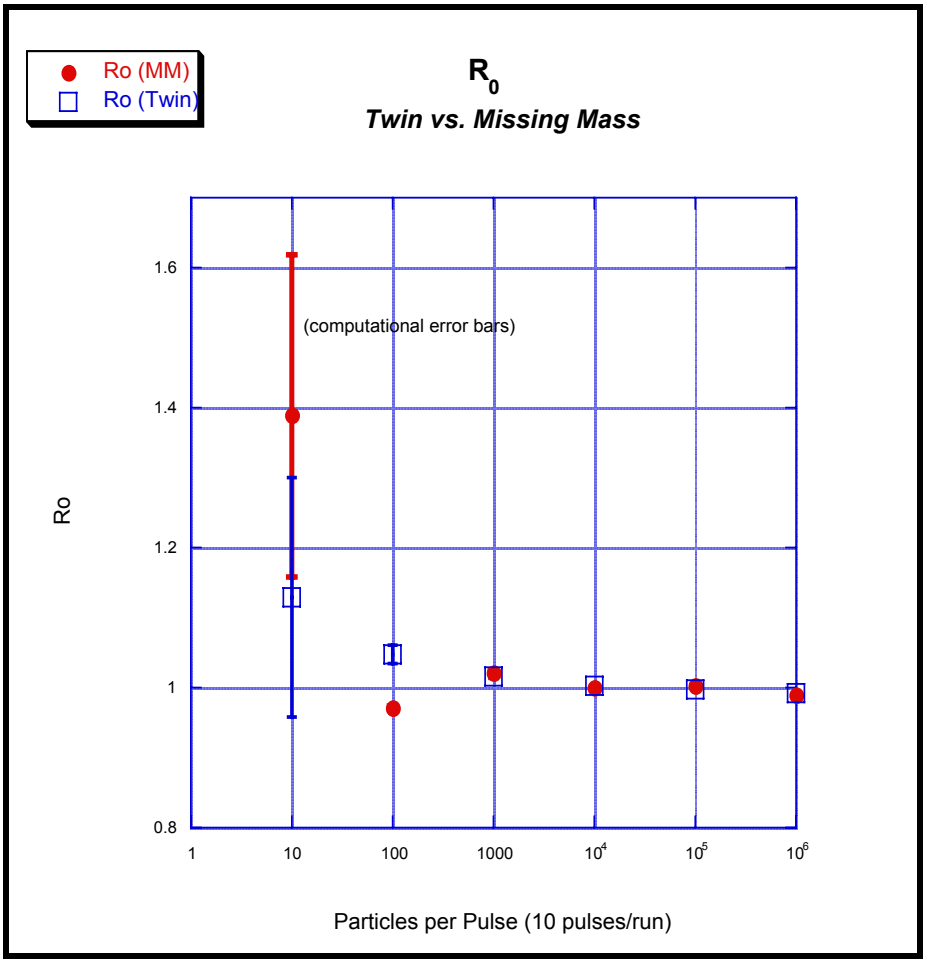

Figure 7.3 Comparative Approaches to Baryon Conservation (R_{20})

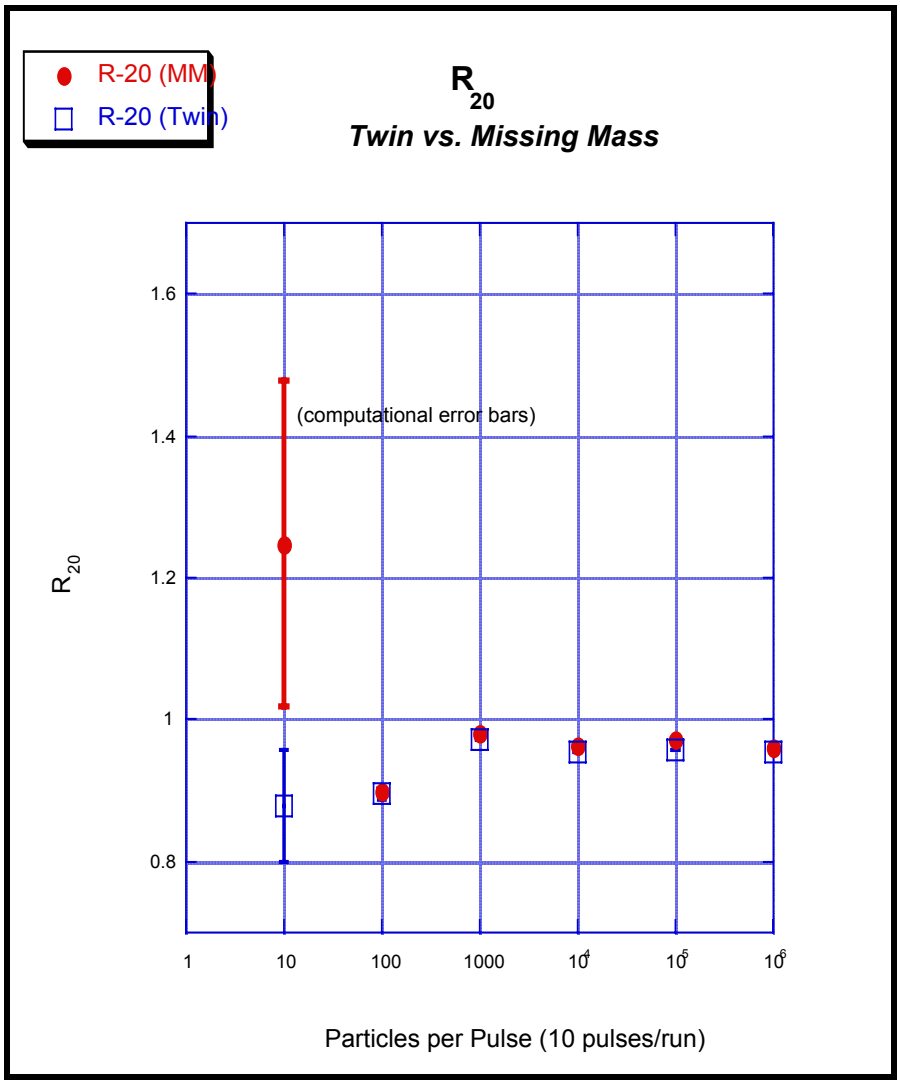

One sees throughout these studies that computational convergence begins to occur ~ 10K interactions. This is not surprising, since it is about ten times the order of magnitude of the number of stars in the database, allowing a proper mixing of the virtual probabilities.

7.3 Shower Particles

But the fact that two very different approaches to baryon conservation share this same rate of convergence hints that the shower particles play a less important role in whatever is going on experimentally. That this is likely the case is seen in the relative insensitivity of R_0 to the energy of the shower particles. A set of typical simulations is shown here using the twinning approach of baryon conservation along what will become one of our standard sets of geometric parameters

$$\mathbf{X_0 = Y_0 = \sigma = \theta = \phi = 0.0001} \qquad (7.4)$$

From section 6.4 these variables are:

$\mathbf{X_0}$ = X coordinate of the beam center at the face of the target

$\mathbf{Y_0}$ = Y coordinate of the beam center at the face of the target

σ = Standard deviation of beam distribution at the face of the target

θ = polar (theta) angle of beam as a whole

ϕ = azimuthal (phi) angle of beam as a whole

$\mathbf{X_0}$, $\mathbf{Y_0}$, and σ are all in cm, while θ and ϕ are in degrees.

As seen below, the higher energy shower particles seem to contribute only a 5% difference in the value of R_0.

Figure 7.4 Effects of E_p of Shower Particles on R_0

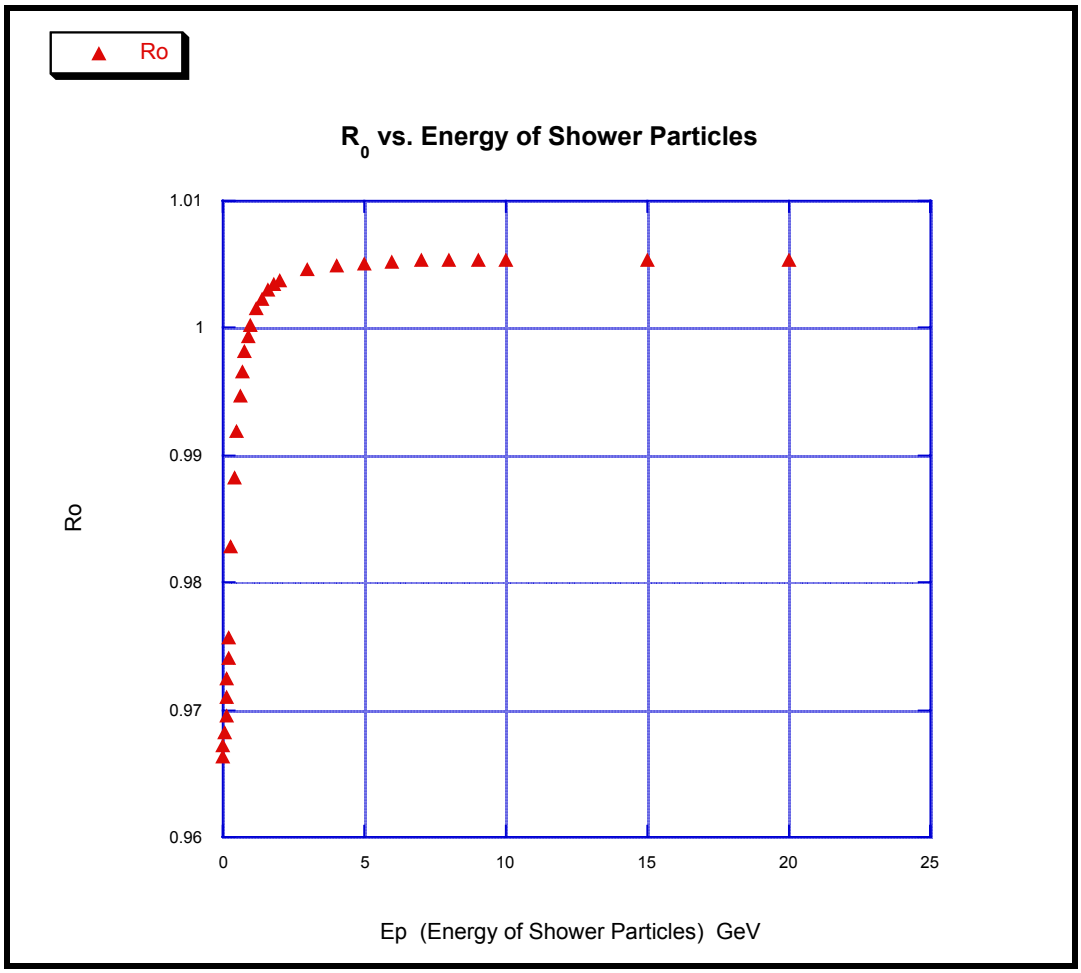

To further test the suggestion that high-transverse momentum particles of higher energy might possibly explain the results (Aleklett et al. 1987), along with Tolstov's subsequent attempts to explain the results using the same basic idea (Tolstov 1987, 1989), all runs in Fig. 7-5 below have the total energy of the shower particles set to the maximum E_p = 1.8 GeV.

Figure 7.5 Maximum Effects of Shower Particles' E_p on R_0

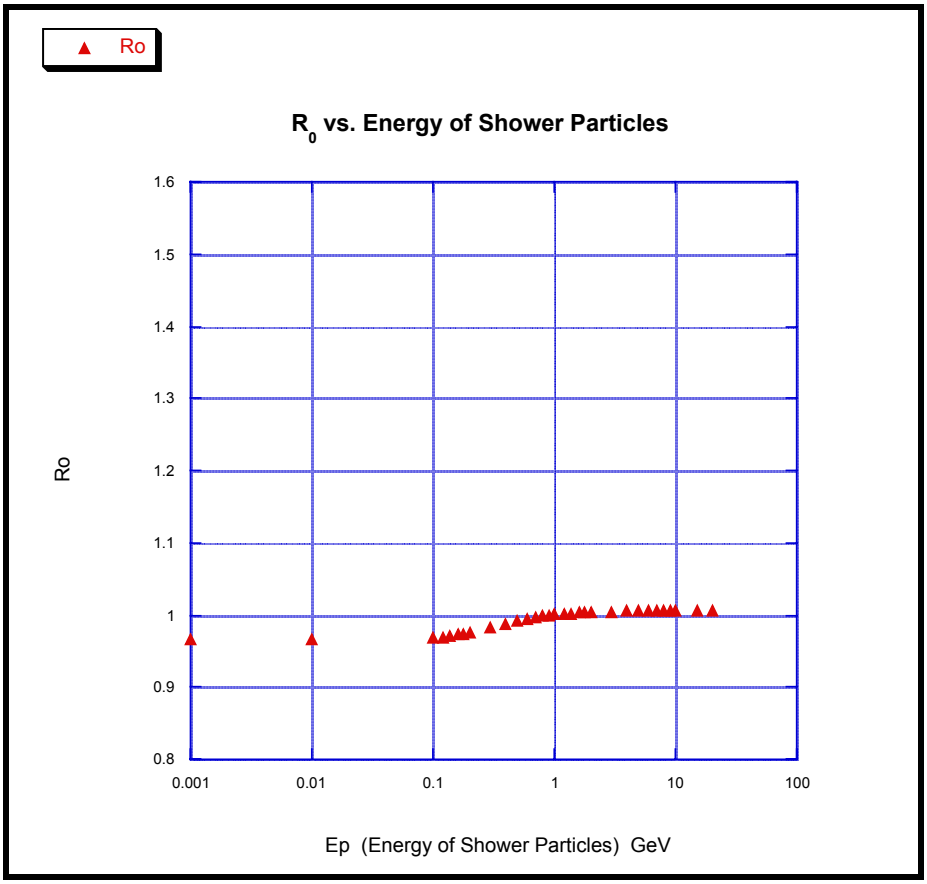

It seems, however, to make little difference. The explanation for the experimentally observed values would seem to lie elsewhere than high-P_T. Indeed, at a more physically reasonable value of 140 MeV for the shower particles of these relativistic heavy ion collisions, $R_0 \sim 0.96$.

It may be important that this is the same R_0 value observed experimentally for proton primaries. This offers an early hint that the assumptions and interpretations of these heavy ion collisions as bags of independently interacting nucleons is not sufficient. It also hints that the simple linear-log fit and scaling of cross-sections seemingly valid for primary interactions (Fig 7.1a,b,c,) may be incomplete when dealing with the interactions of secondaries.

Nonetheless, in order to fully test the high-P_t hypothesis, all simulations in the TRANSPORT section immediately following have a total energy of 1.8 GeV assigned to shower particles. For it is at least a priori conceivable that some combination of high P_T coupled to a pathological beam geometry could somehow increase the value of R_0.

This point will be explored more fully later, especially when performing 'mass spectroscopy' on the secondaries' transport in a multi-sector cylinder; for one can legitimately look at the cylinder configuration as a multi-stage amplifier for R_0 phenomena. The cylinder as multi-stage amplifier will be shown to be particularly useful in differentiating between physical models which might by chance 'fit' a two-sector cylinder but fail miserably a multi-sector one. This will be addressed in Chapter 10.

7.4 The Transport Variables: R_0 vs Beam Characteristics

Taking into account all the above, the following computational results* are of exposures of a million interacting particles, a twinning approximation to baryon conservation, and E_p = 1.8 GeV. Unless they are the variables under consideration on a given run our standard set of geometric settings will be used **($X_0 = Y_0 = \sigma = \theta = \phi = 0.0001$)**.

In order to better determine computational errors, these million particles are delivered in ten pulses of 100,000 each. But since the formally computed errors are so very small, they are often not shown on the plots below, but are instead included in the size of the data-marker chosen.

* All computations also have the computational variable RNDP=3, this variable being defined in section 7.5.1 (The Role of Random Number Generators).

7.4.1 R_0, R_{20} vs. Beam Angles

As would be expected there is no variation of R_0 with azimuthal orientation.

Figure 7.6 Azimuthal Dependence of *R_0 and R_{20}*

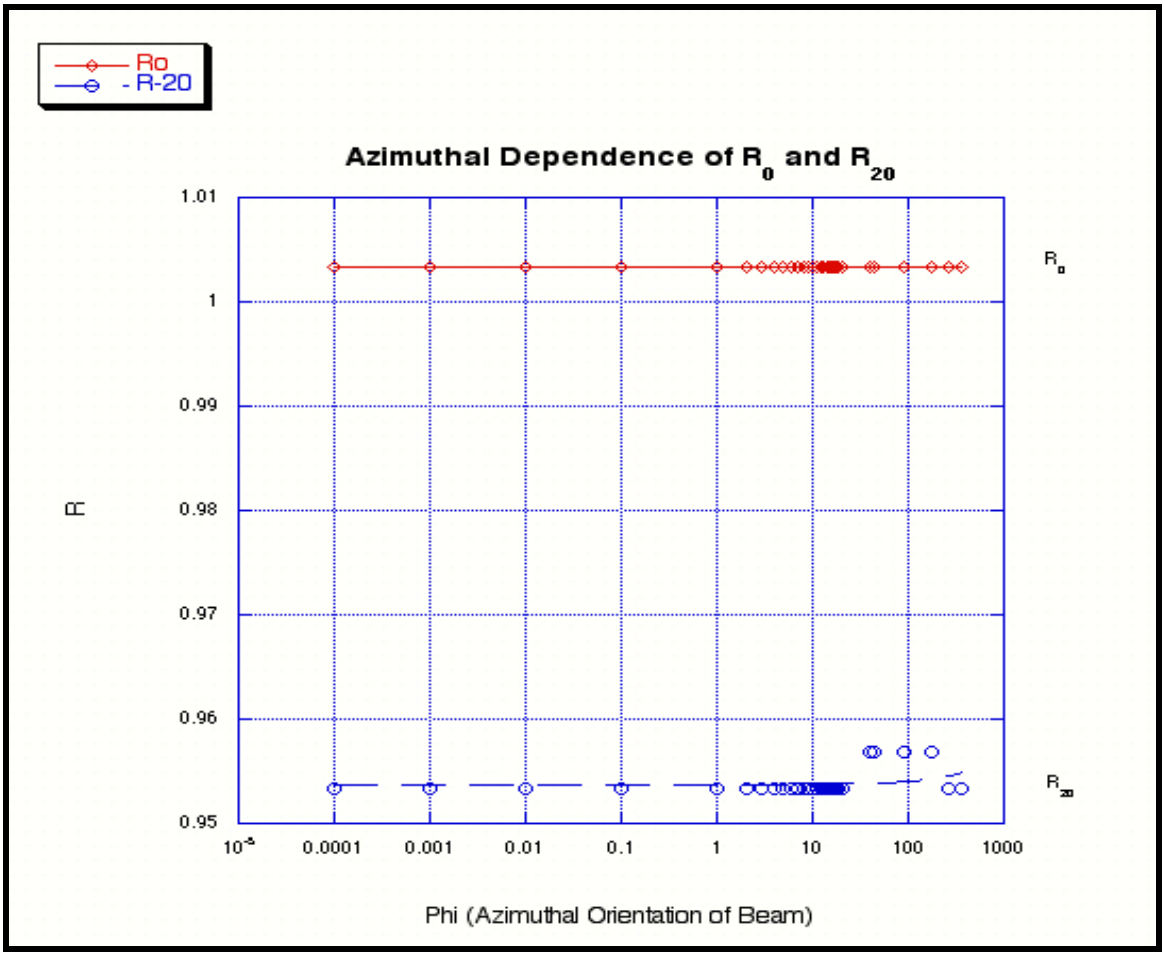

But as seen in Figure 7.7 there is the strong theta dependence at the critical angles dictated by the geometry of the target configurations (a sharp 12 degrees for R_{20} and ~60 degrees for R_0). This will be especially relevant when discussing shower particle models in Chapter 11.

Figure 7.7a R_0 and R_{20} Dependence on Angle of Beam to Target (theta)

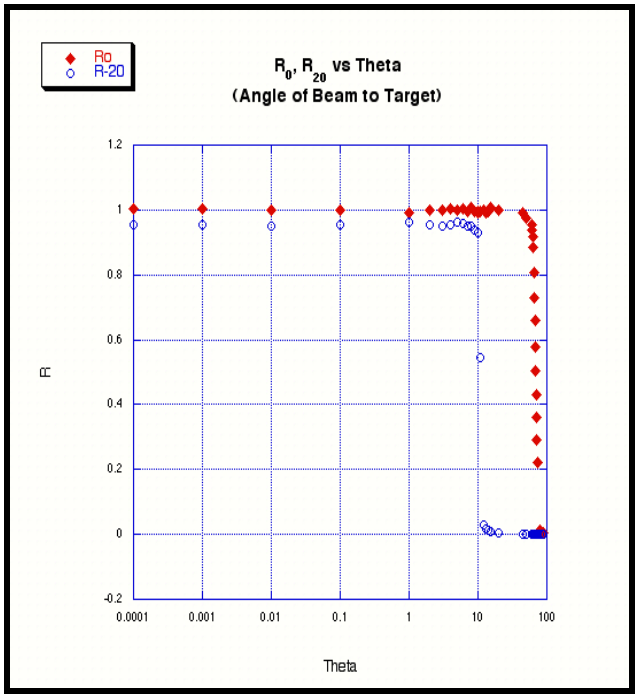

Figure 7.7b R_0 and R_{20} Dependence on Angle of Beam to Target (theta)

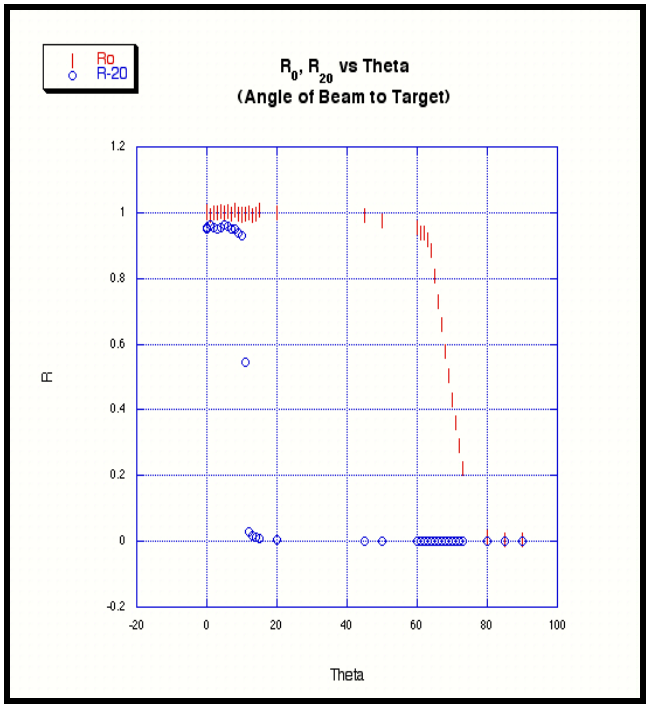

7.4.2 R_0, R_{20} vs. Beam Geometry (X_0, Y_0, σ)

Variations of the beam centers and dispersion are presented in this section. The choice of parameters, solo and in combinations, spans the phase space of beam-target geometric possibilities. Besides being important R_0 studies, these runs are representative of the exhaustive array of checks that have been performed on the geometry of the simulation. (A choice of $\sigma = .0001$, as below, is especially revealing of the Euclidean geometry.)

Figure 7.8 R_0 and R_{20} Dependence on Center of Beam Displacement (Y_0)

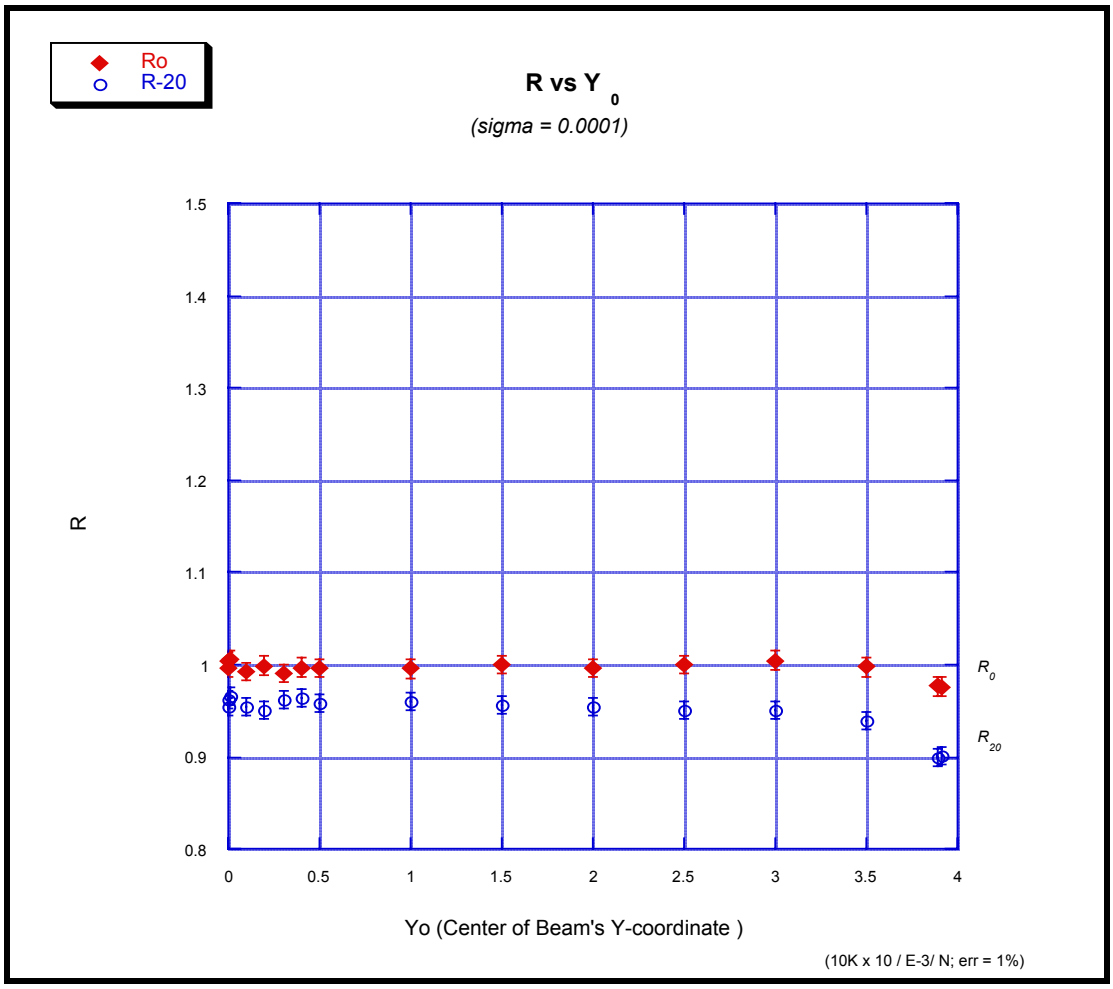

Figure 7.9 R_0 and R_{20} Dependence on Center of Beam Displacement (X_0)

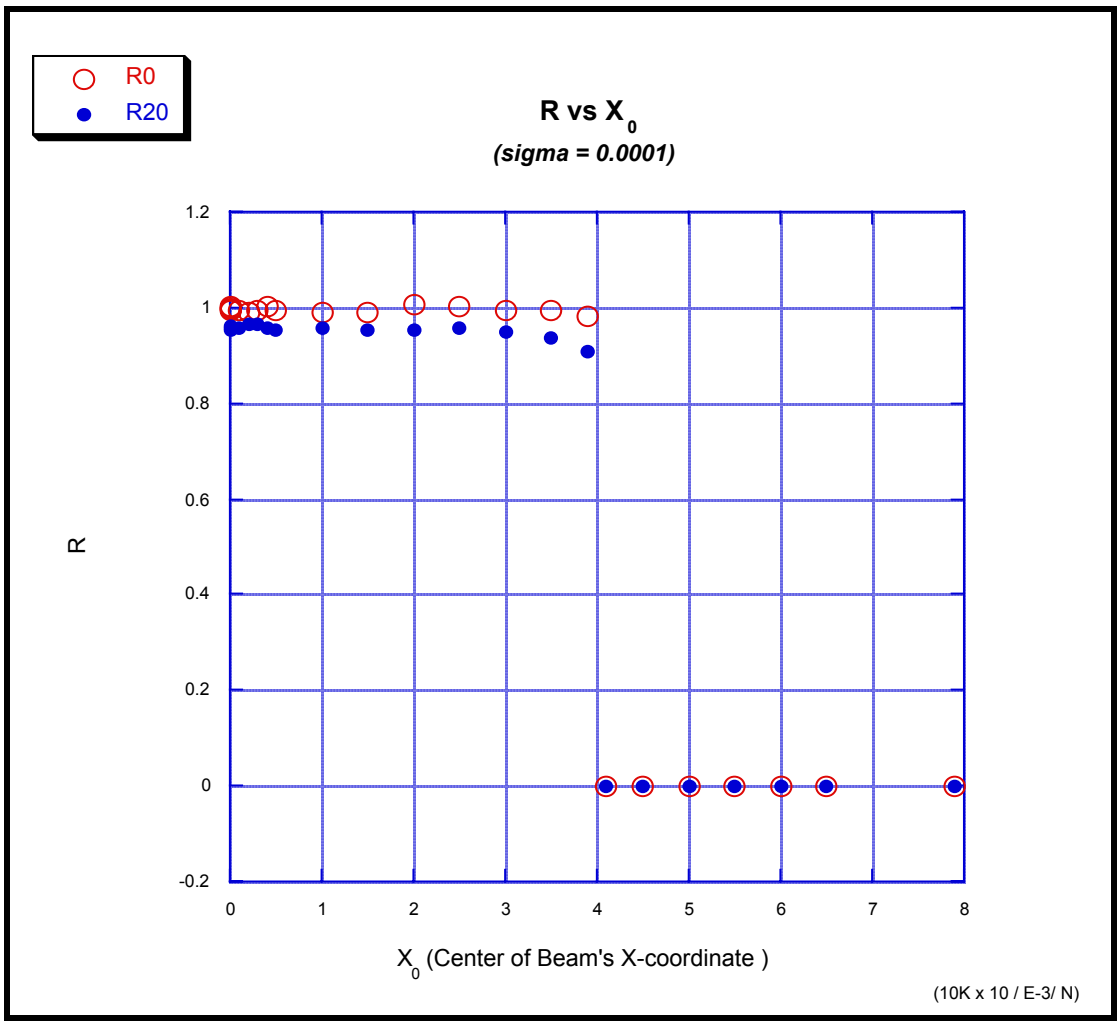

Figure 7.10 R_0 Dependence on Displacement and Dispersion of Beam Center

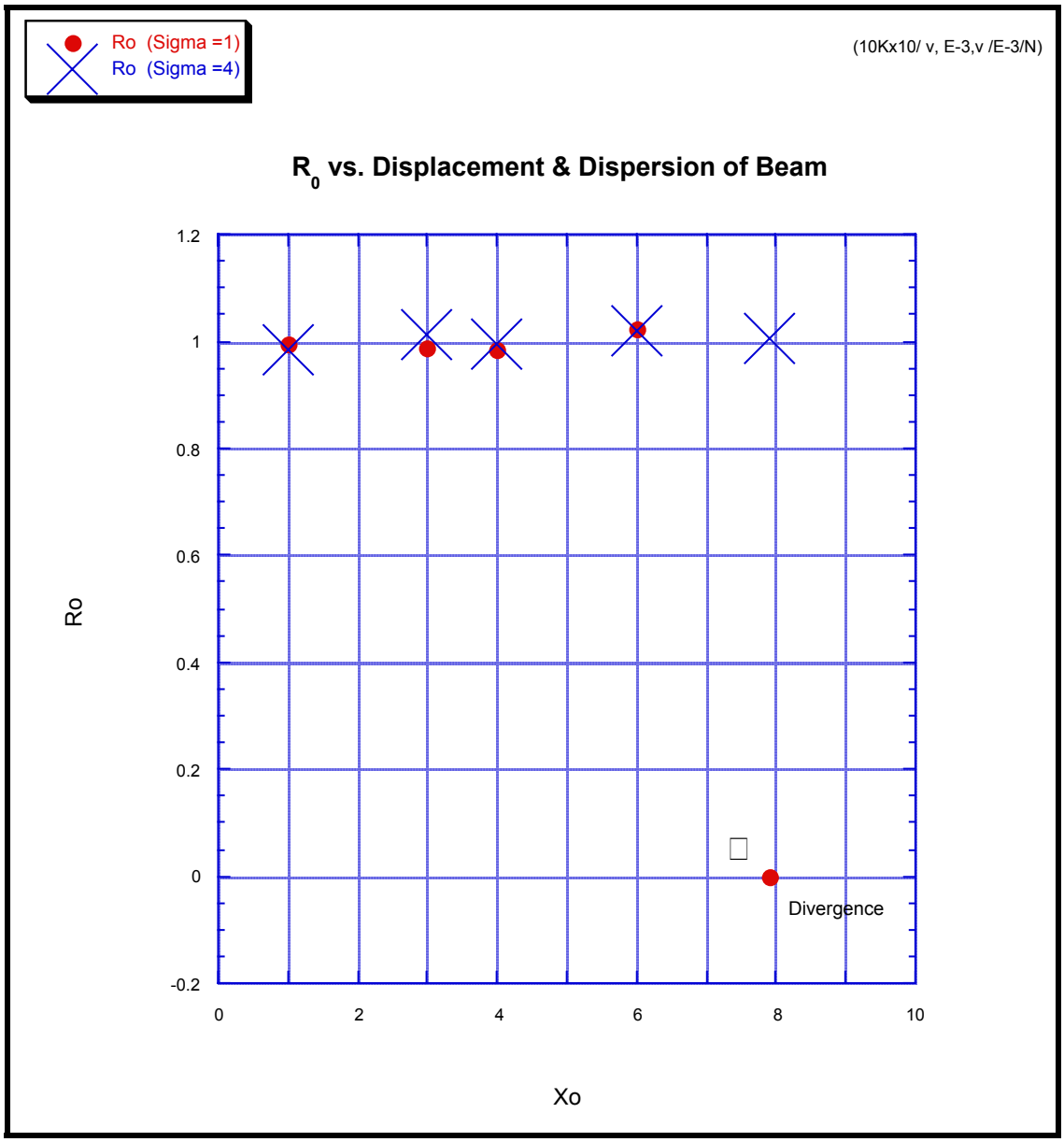

Figure 7.11a R_0 Dependence on Dispersion and Polar Angle of Beam

(Beam Dispersion σ_{beam}= 1,2,4)

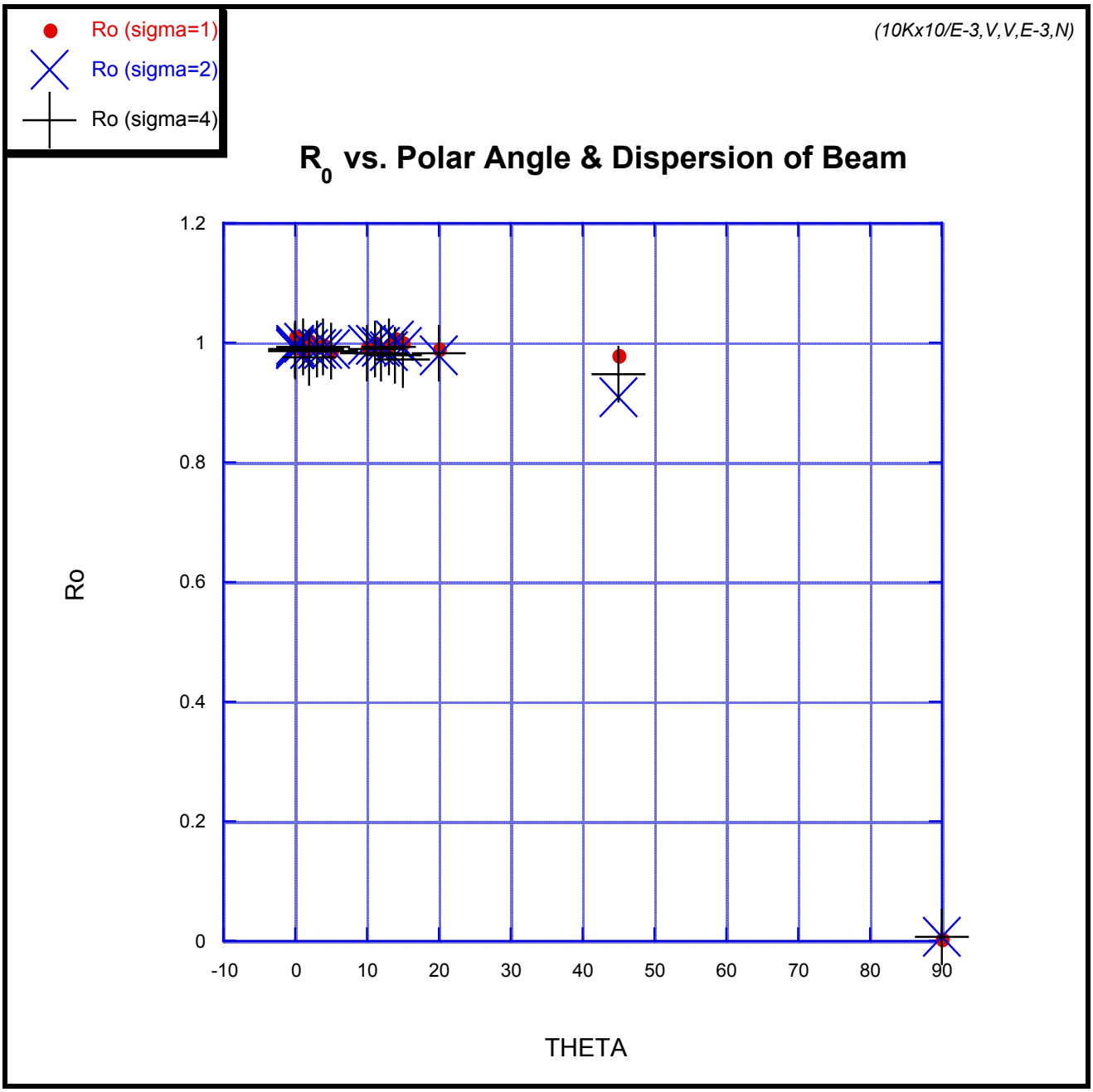

Figure 7.11b R_0 Dependence on Dispersion and Polar Angle of Beam

(Beam Dispersion σ_{beam}= 1,2,4)

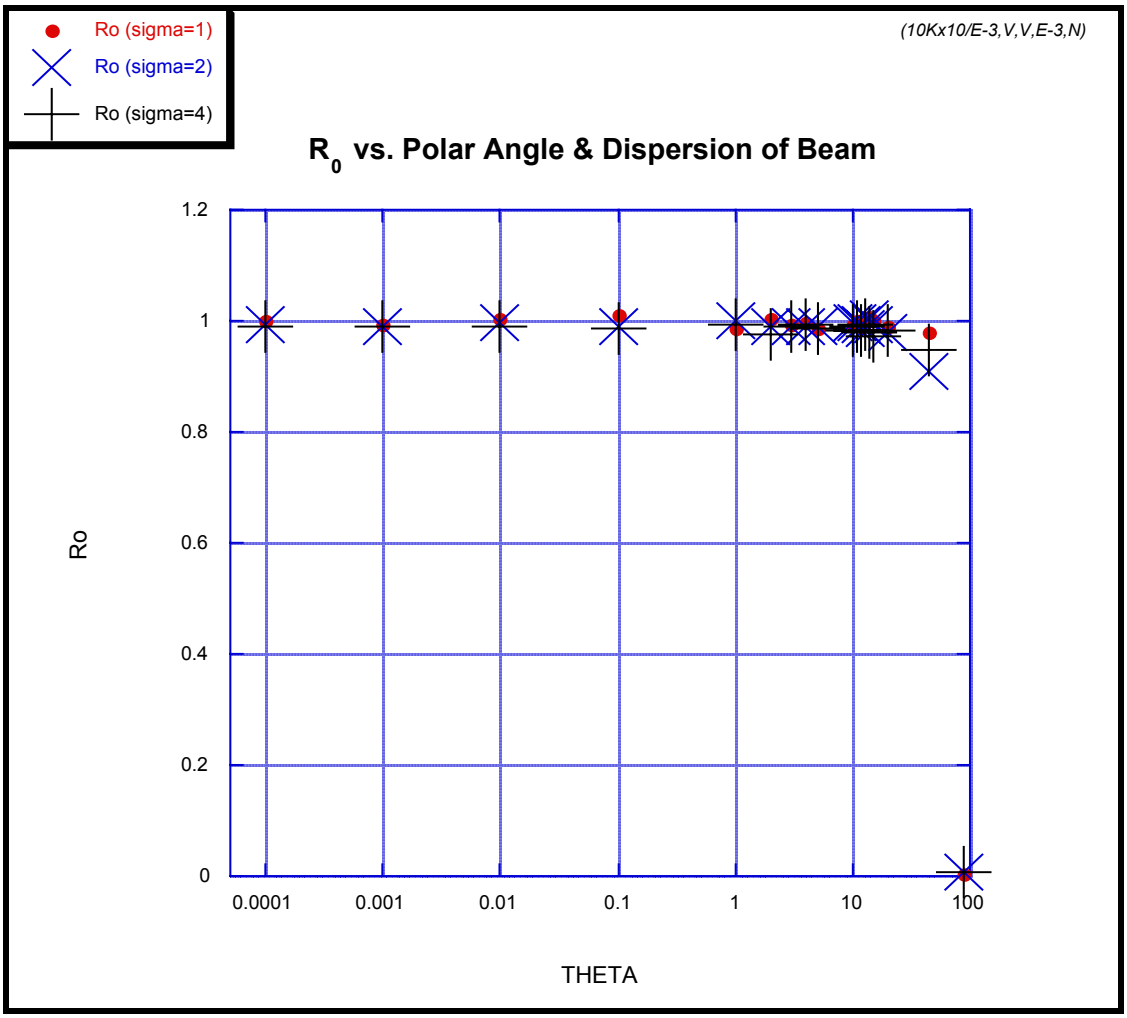

The above results yield a two-fold consistency. Using the standard geometric setting of a 'pencil beam' they provide the necessary demonstration that the dynamic geometry of the simulation behaves as would be expected. Physically, the results show that for all geometric variations:

$$R_0 \leq 1 \qquad \text{for } E_p = 1.8 \text{ GeV}$$

$$R_0 \leq 0.96 \qquad \text{for } E_p = 140 \text{ MeV}$$

7.5 **Computational Errors** *(Homogeneous Population & Transport Simulations)*

As seen in Section 7.2 beginning around 10,000 particles (that interact) there is a flattening of the convergence of computed values and by one million interactions a stabilization of computed values appears. The errors resulting from a Monte Carlo simulation formally scale as $N^{-1/2}$, but one must ask if the resulting extremely small errors truly reflect the accuracy of the simulations. For a one million star simulation (ten pulses of 100K particles per pulse) the computed errors are as small as 10^{-4}, or .01% for the computed values of R_0.

But as we'll see below, across different simulations of the same parameter set, it seems more reasonable to set an upper limit on computational errors of ~1%.

7.5.1 The Role of Random Number Generators

An investigation of the effects of the random number generator itself is representative of the detailed quality control checks to which the code and its methodological approach have been subjected. It also offers insight as to what may be the true computational errors involved, beyond Monte Carlo's theoretical $N^{-1/2}$ convergence. The basic random number generator selected utilizes a classic large number modulo approach:

```
function rndm()

      integer*4 idum,m,ia,ic,iy
      common/seedcom/idum
          m=714025
          ia=1366
          ic=150899
          rm=1.0/m

                    idum=mod((ia*idum+ic) , m)

          iy=idum

                    rndm=iy*rm+1e-18
```

Selected subsets of the random numbers were used to better determine true computational error, where the selection occurred through the introduction of the computational variable **RNPD** (Random Number Phase Delay)[*]. For each call of the random number generator… RNPD, an integer, spins the random number generator RNPD times before picking a random number to use. (If RNPD = 87 then 87 random numbers are generated before one is chosen for use.)

The following chart summarizes the times necessary to compute an exposure of 10^5 particles for a narrow, orthogonal, and central beam distribution (all geometric variables are set equal to .0001). As would be expected, the computational time for an entire calculation increased linearly, albeit slowly, with increasing RNPD.

Figure 7.12 Computational Time vs. "Random Number Phase Delay"

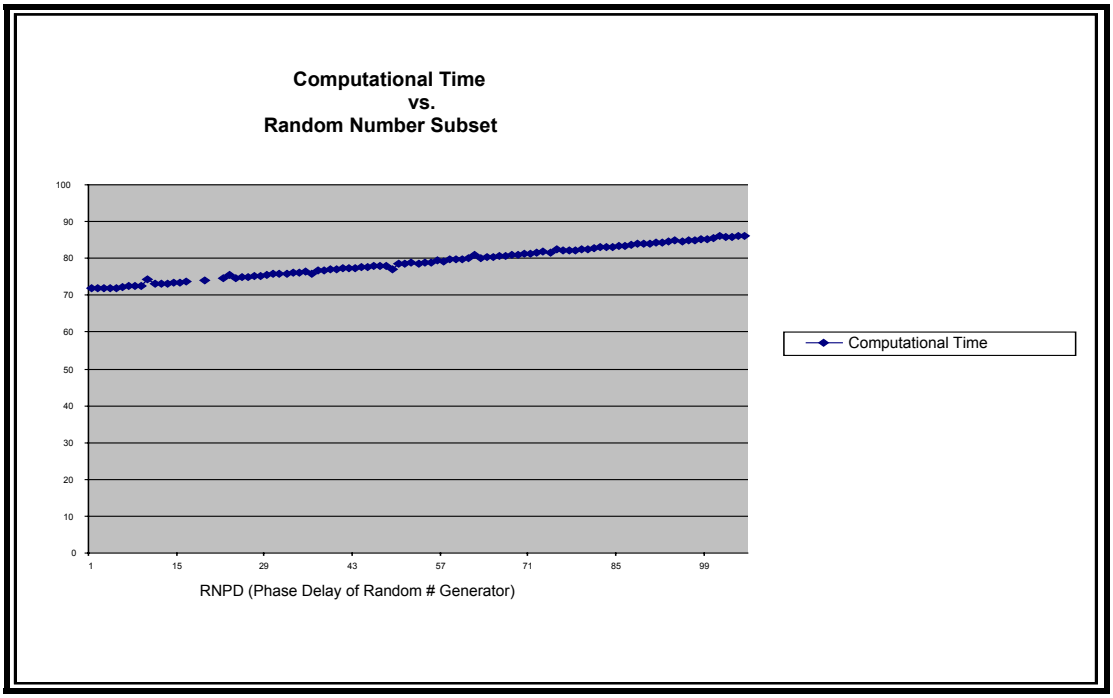

[*] In keeping with the casino-inspiration for the Monte Carlo technique itself, we shall also call this variable the '*Delayed Spin'* or **DS**.

There is a 20% increase in computational time over the RNPD sequence [1 – 100].
If the choice of RNPD does not influence the end result, a smaller one is desirable.
And the computational result does appear robust with respect to the choice of RNPD.

Figure 7.13 R_0 and R_{20} for Different Random Number Subsets

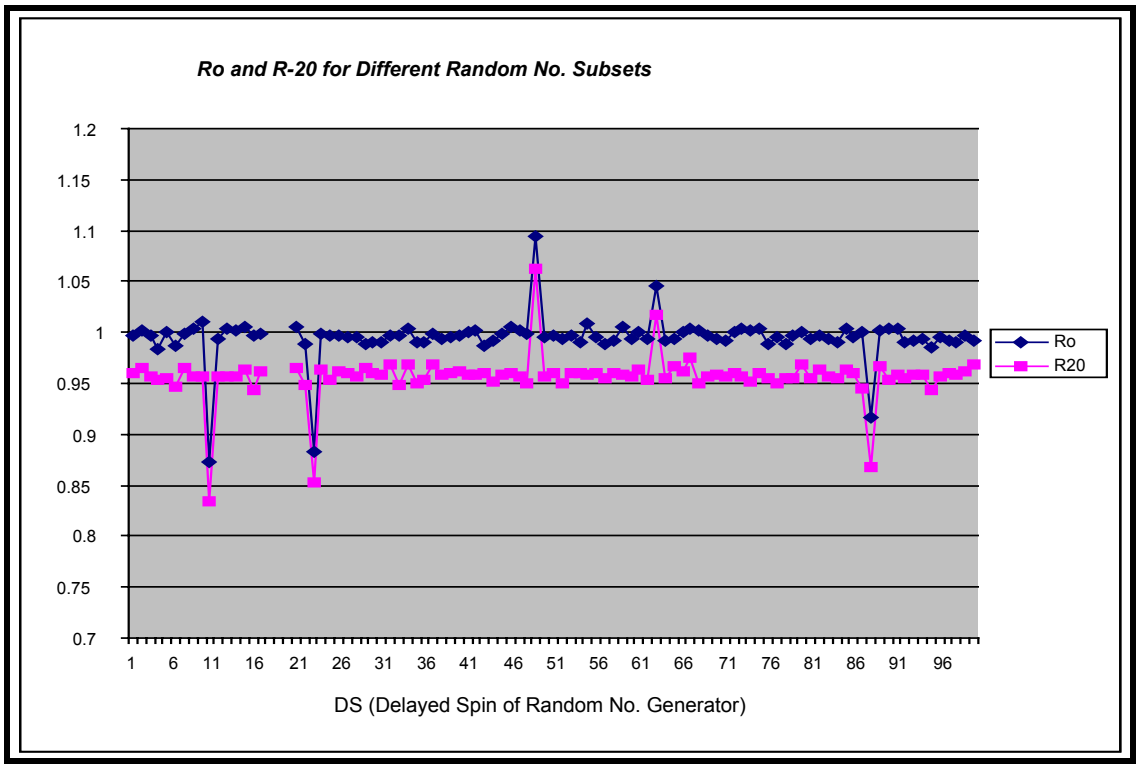

All but five values of R_0 lie within ~.02 of each other at values of (.99- 1.00). The five exceptions are listed in Table 7.2 below.

Table 7.2 Exceptional Cases of R_0 and R_{20}

RNPD (Phase Delay)	Ro	Error (Ro)	R-20	Error (R-20)
10	**0.8722**	0	0.8343	0.0001
23	**0.8836**	0.0001	0.8523	0.0001
49	**1.0949**	0.0001	1.0625	0.0001
63	**1.0448**	0	1.0169	0.0001
88	**0.9163**	0.0001	0.8686	0

The magnitude of their difference is the same as that of the fluctuations seen above for small computational samples of perhaps a few hundred events. Because random number generators are actually pseudo-random number generators there are, more frequently than is commonly imagined, subsets generated which do not adequately span the space being investigated. Or as von Neumann, the father of modern Monte Carlo methods, has said, *" Anyone who considers arithmetical methods of producing random numbers is, of course, in a state of sin."*

Hence one obvious possibility for these fluctuations is that they are computational artifacts due to such an incomplete sampling. That this is likely to be the case is confirmed by changing the value of the modulo of the random number generator. After such a change the computed values continue (for Ep = 1.8 GeV) to lie in the range R_0 = [.99-1.00].

Additionally, a completely different random number generator was used, the RAN function built into the fortran used (LS Fortran). This too showed the computed values of R_0 to be in the range .99 – 1.00, and with a variation of ±0.005. Furthermore, selected sub-sample runs were performed on three different machines, with similar results. Finally, the next section on database variations offers additional substantiation that the true source of the 10% differences for the 5 cases above (and others of their set) are computational fluctuations. **All of this continues to suggest that the true computational error for the transport variables is ≤ 1%.**

7.5.2 Database Variations

Implicit in our approach is the belief that a novel physical observation or effect exists in reality *only* if the experimental phenomenology differs in a statistically non-trivial way from all possible (i.e. likely) variations of the theoretical assumptions of *normalcy*. This *normalcy*, including fluctuations of both background and computation, is of course established through extensive Monte-Carlo simulation. Just discussed is the variation of the random numbers themselves chosen as the guiding footsteps in this computational exploration of phase space.

In our particular patois of experiment and simulation, it would seem then that the *order of stars* from the database chosen by these computational roulette wheels might conceivably make a difference in the computational end results. Indeed, for only a small number of computational steps chosen, such a difference in star sequence is likely to have a large effect. For in such a case it would only be exploring a limited sub-region, not necessarily different from the whole of its phase space. But if for a large number of stars there is a convergence of the final values, then indeed this particular variable can be safely ignored.

To test these hypotheses the database used in the above studies was randomly varied so that with the same random number Delayed Spin all stars chosen in sequence would be different[1]. This newly randomized database is referred to as "Database 1". A test of these two different databases shows exactly what was surmised: for small samples of stars there are extremely large fluctuations of R_0 which only begin to converge for samples of stars greater than 100.

[1] Maimon's version of Brouwer's Fixed Point Theorem might have something to say about the basic existence of at least one common ordinal point in the newly chosen sequence if it is very large, but such matters do not affect the statistical safety of our randomizing approach.

Figure 7.14 R_0 for Different Databases

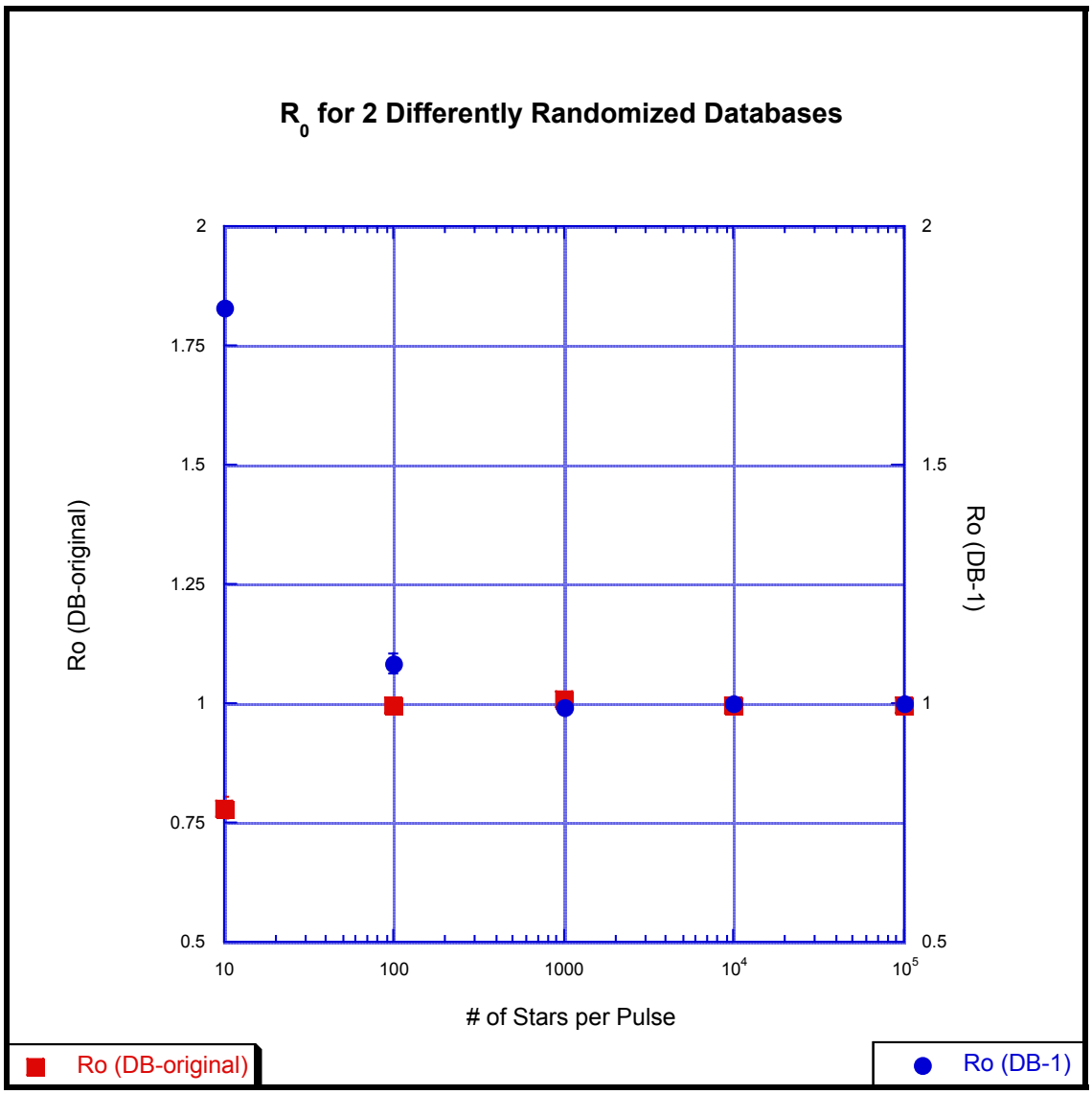

A closer look at the interval [10,100] for the number of stars in the database shows:

Figure 7.15 R_0 for Small Numbers of Stars in Different Databases

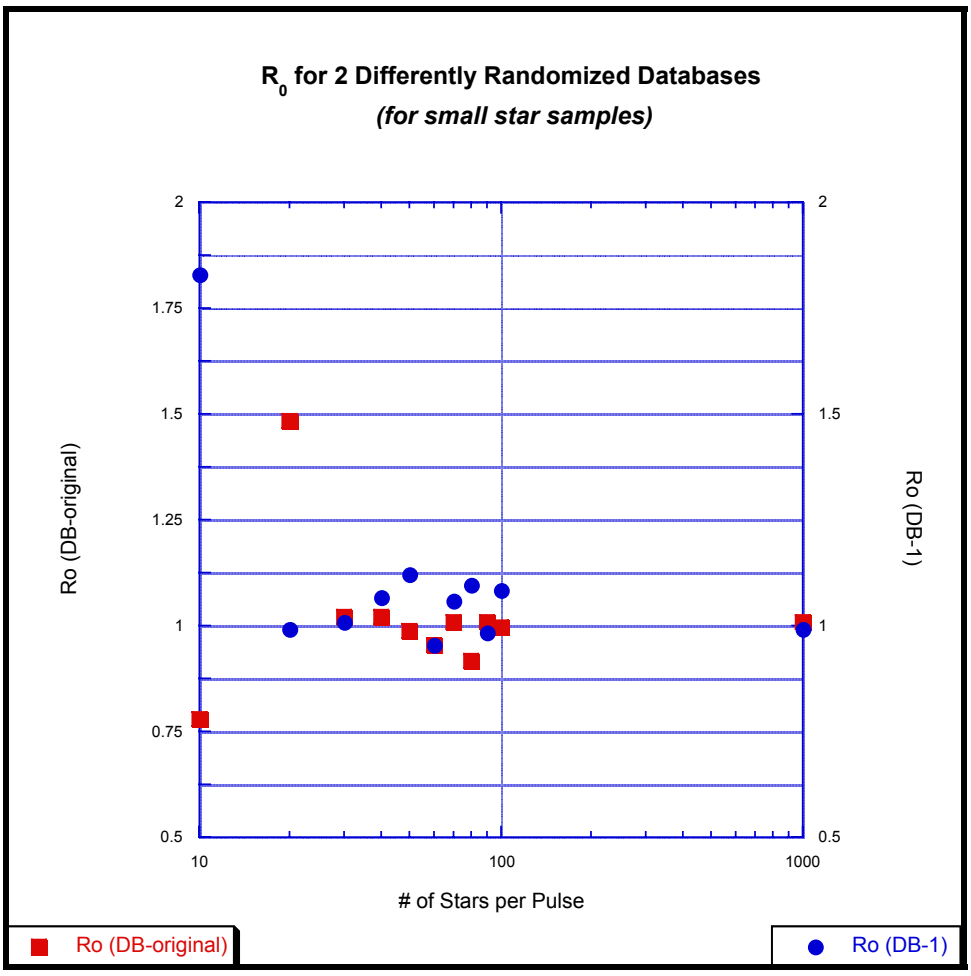

This limit of 100 stars *only* beyond which convergence occurs may play an important role in why the initial paper (Aleklett et al 1987) found a fit to their experimental data by subpopulations of *classical emulsion-defined "anomalons"* (secondaries with considerably increased total geometric cross-sections). Their database had only 50 stars for 0.9 GeV ^{40}Ar while their 1.8 GeV ^{40}Ar had 95 stars. This will be addressed more fully in when considering subpopulations in Chapter 8; with final support for the computational fluctuation origin of Aleklett et al's findings in section 8.2.

Before that however, additional evidence is presented for the existence and nature of the computational fluctuations discussed in the previous section. Recall that for DS=10, an $R_0 = 0.87$ was found. Indeed, this is the case for both databases under consideration.

Figure 7.16 R_0 for Different Databases (DS = 10)

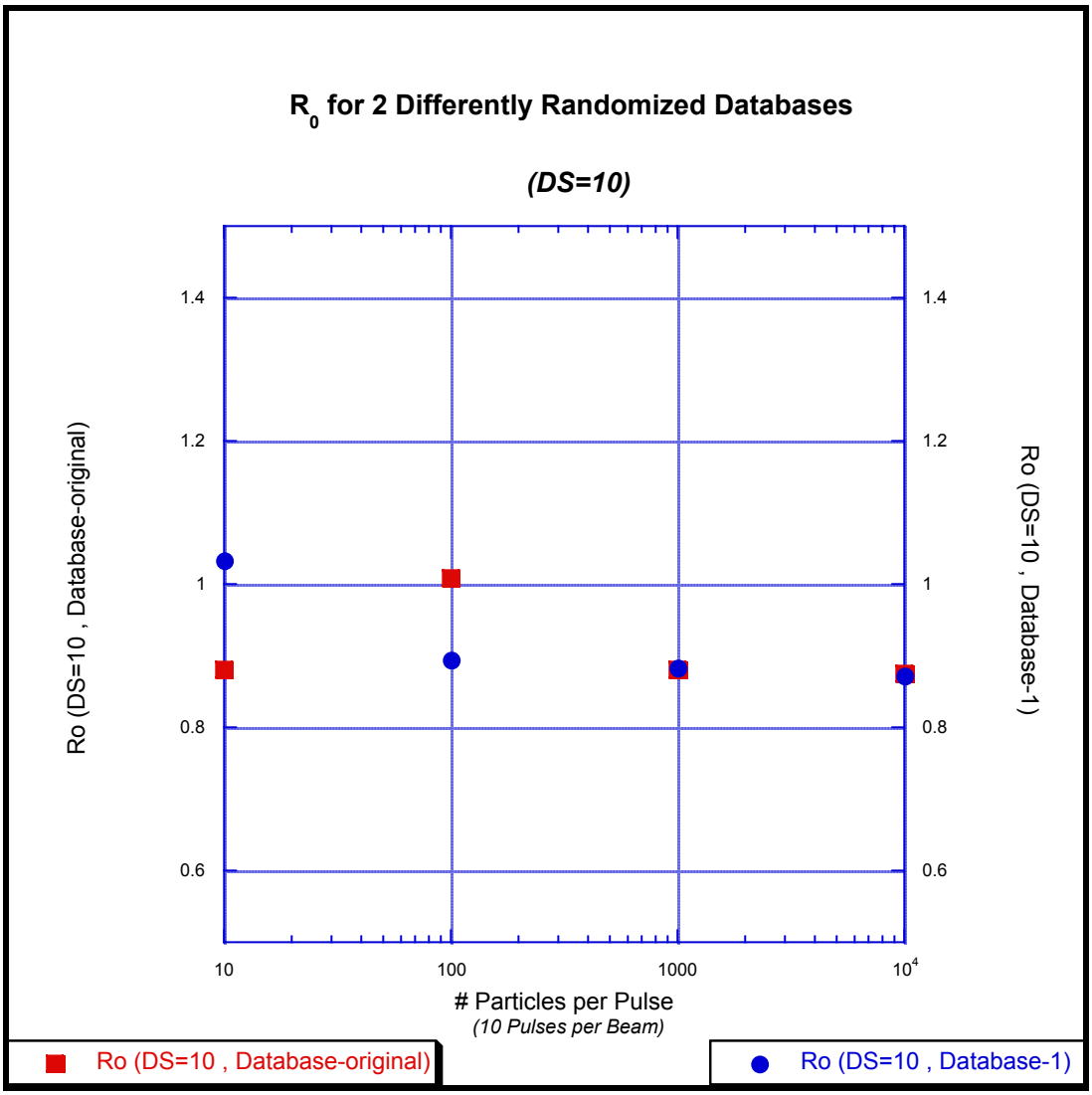

Nonetheless, for DS=10 and limiting the beam to 10 particles/pulse (where one would expect to find the most fluctuations!) one finds R_0 all over the proverbial map of phase space.

Figure 7.17 R_0 for Different Databases (DS = 10 and 10 particles/pulse)

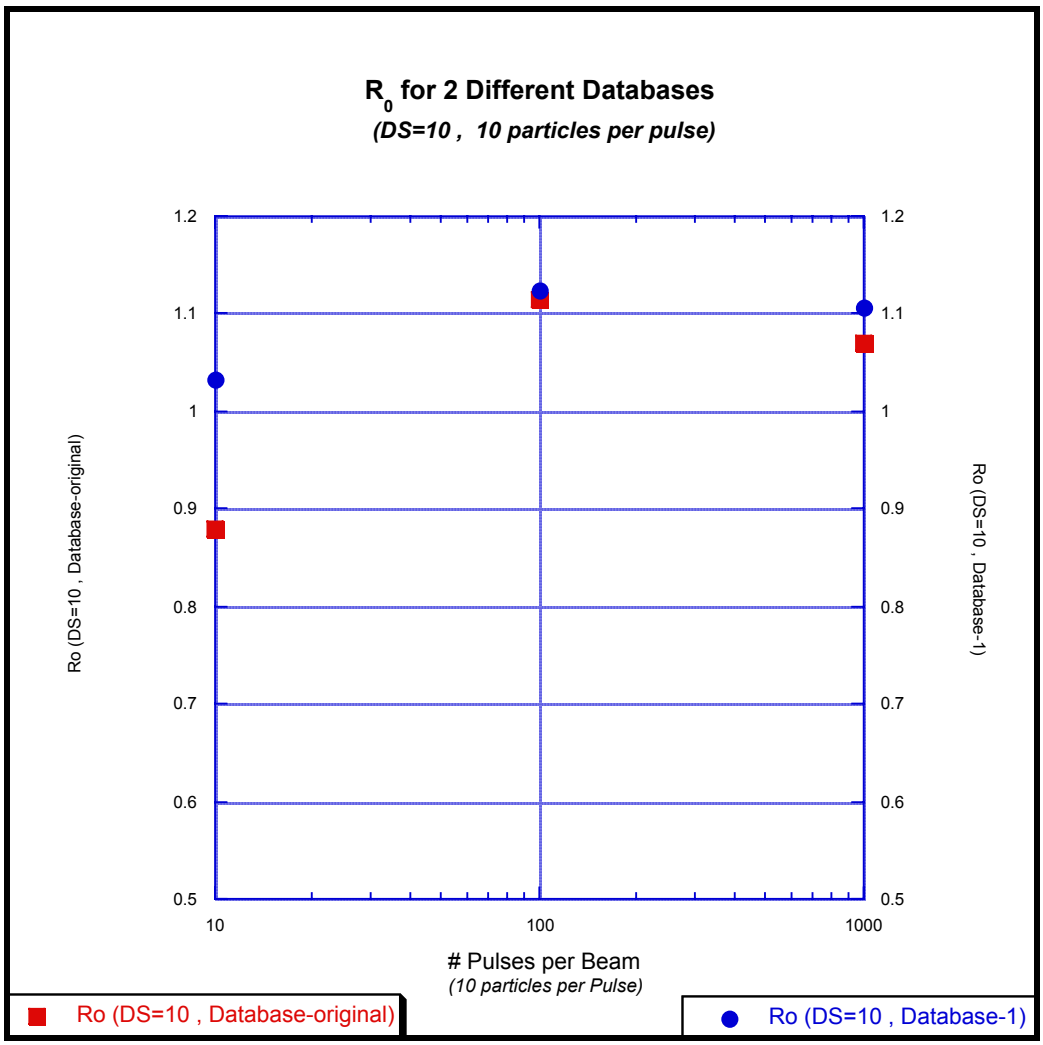

And referring to Table 7.2 these fluctuations are *exactly* at the extrema of the 10% range around $R_0 = 1^*$ that cover all five special cases of the DS!

* Recall that we are keeping $E_p = 1.8$ GeV to absolutely maximize any possible effects.

7.6 Variations on a Fragmented Theme

The fragmentation pattern for the emulsion experiments, embodied in the Fragmentation Matrix, was presented in Table 4.8. In all of the simulations described above the fragmentation patterns measured in the Ag and Br of the emulsion were then applied to Cu. This assignment of fragmentation patterns from emulsion to Cu may not be completely correct. To better account for both of these concerns simulations were run in which the fragmentation patterns were considerably varied from that used in the above simulations.

Instead, simulations were performed in which for a given run, displacements of the correct charge Z_i were made in increments of $(Z_i + n)$, where n = 1 through 8. For example, in a displacement of n = 3, if a charge 4 event should have been selected from the database, a charge 7 was picked instead. For charges in which $(Z_i + n) \geq 18$ the charges picked were assigned to be Z=18 secondaries.

Besides investigating whether alternative fragmentation patterns could in principle effect the value of R_0, this set of simulations allows an elegant check on the computational error limits due to any mismeasurements of the secondary charges. Although the measurement errors for smaller charges were ***~1/2*** charge unit; charge is assigned, for higher Z, relative to the charge measurements of the previous generation. Hence it is possible in principle to have an error of as much as 2 charge units for a given 3rd generation charge measurement*.

Simulation results are first shown for our canonical setting of an orthogonal pencil-thin beam ($X=Y=\sigma=\theta=\psi=0.0001$) which removes any dependence on the other variables. Results are then shown for more 'typical' beams ($X=Y=0.1$; $\theta=\psi=0.0001$) but with $\sigma = \{.1, 1, 2, 3\}$. Results are shown for both E_p=1.8 GeV and E_p=140 MeV.

* The diagonal nature of the Fragmentation Matrix strongly suggests that this is not a real problem, but nonetheless this is a worthwhile additional check.

Figure 7.29 R_0 vs. Fragmentation Displacement (Pencil-Beam)

σ= 0.0001

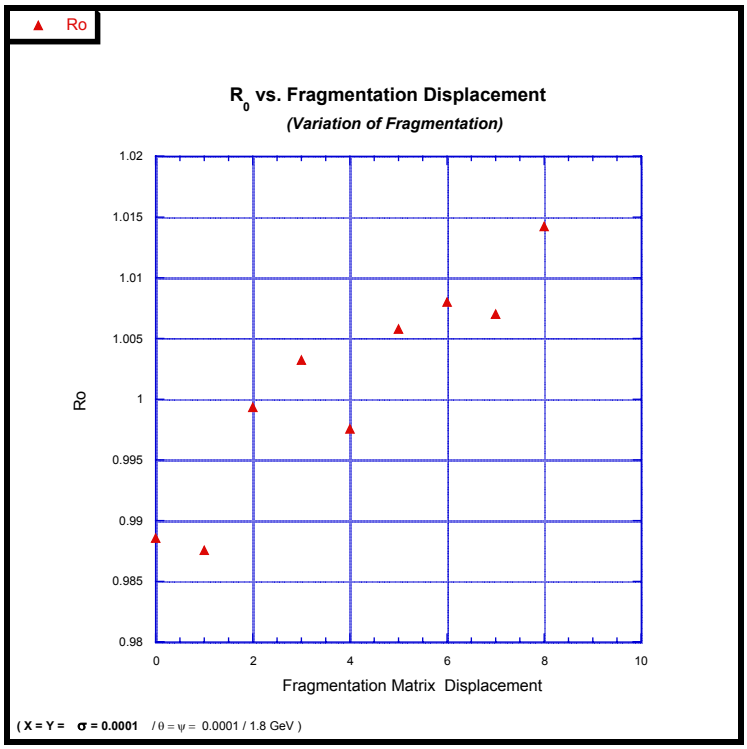

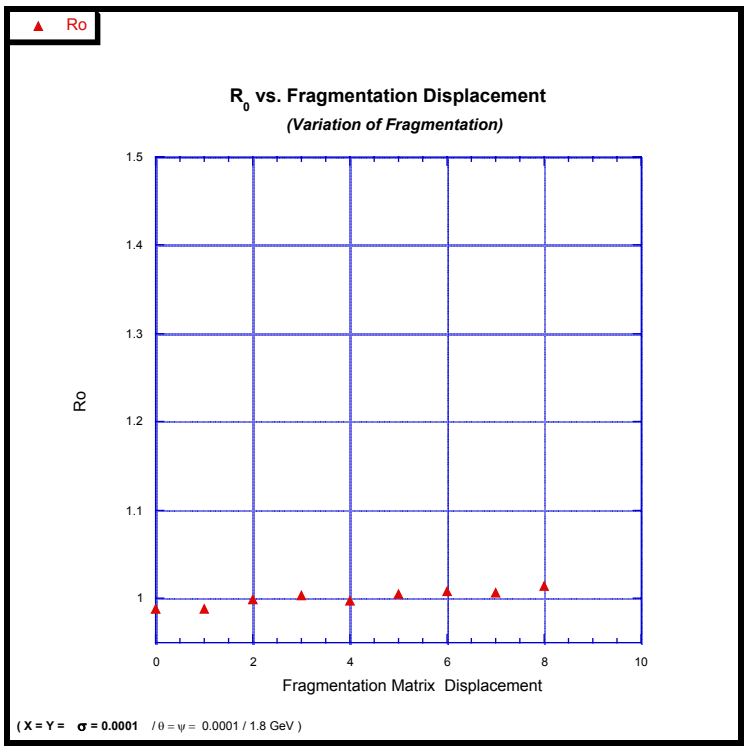

Figure 7.30 R_0 vs. Fragmentation Displacement

(Centered Beam at Sequential Dispersions)

σ= 0.1

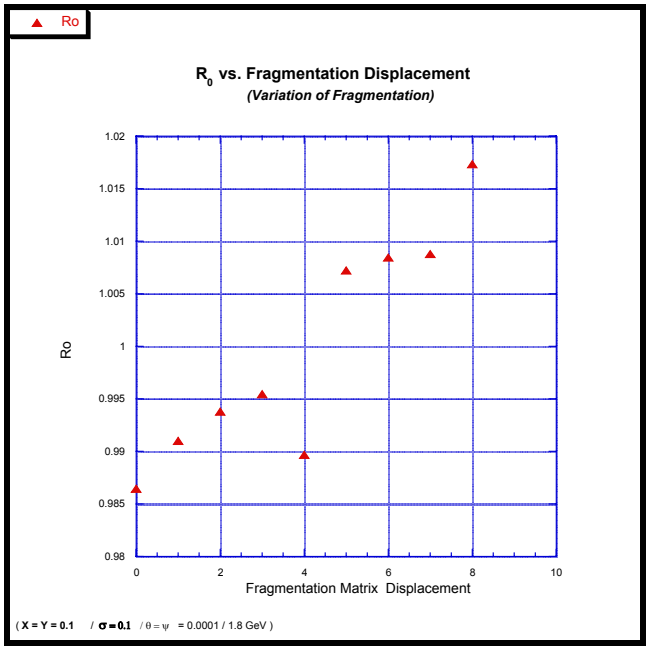

σ= 1.0

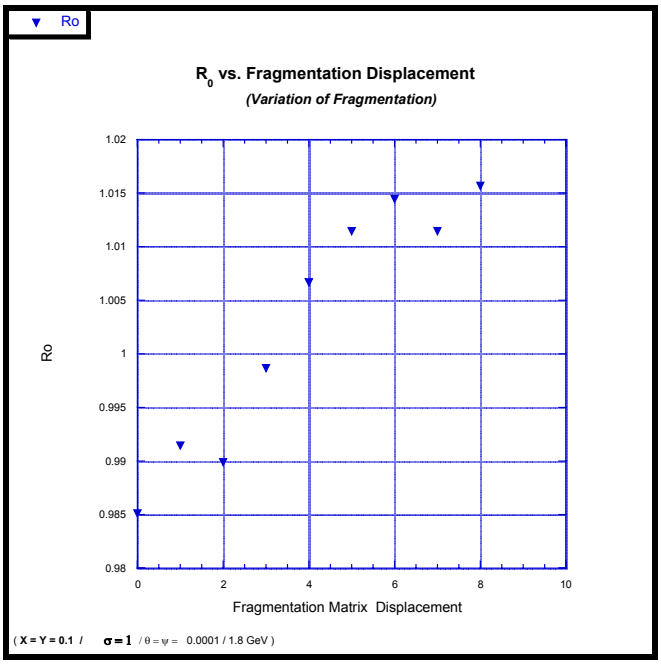

σ= 2.0

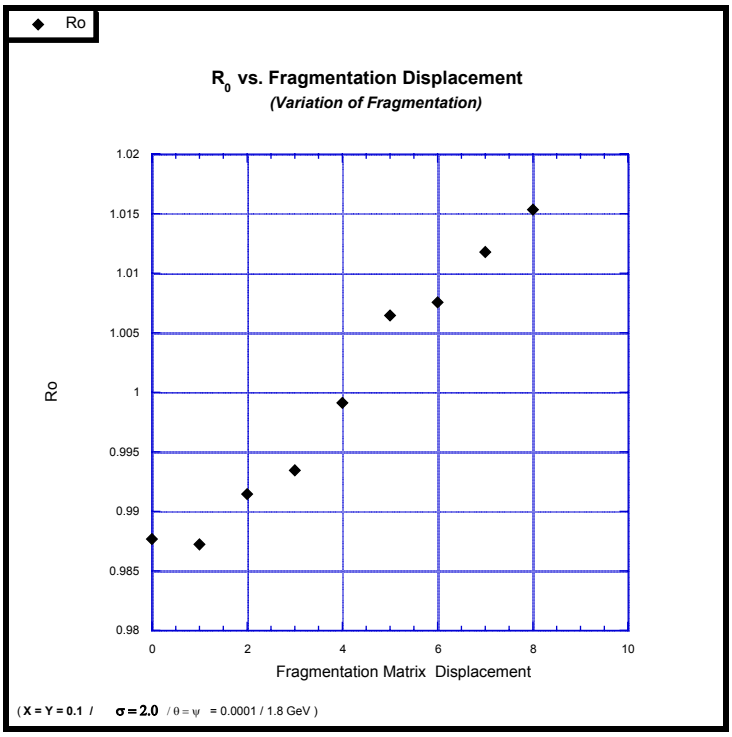
Ro
R0 vs. Fragmentation Displacement
(Variation of Fragmentation)
1.02
1.015
1.01
1.005
1
0.995
0.99
0.985
0.98
Ro
0
2
4
6
8
10
Fragmentation Matrix Displacement
(X = Y = 0.1 / σ = 2.0 / θ = ψ = 0.0001 / 1.8 GeV)

σ= 3.0

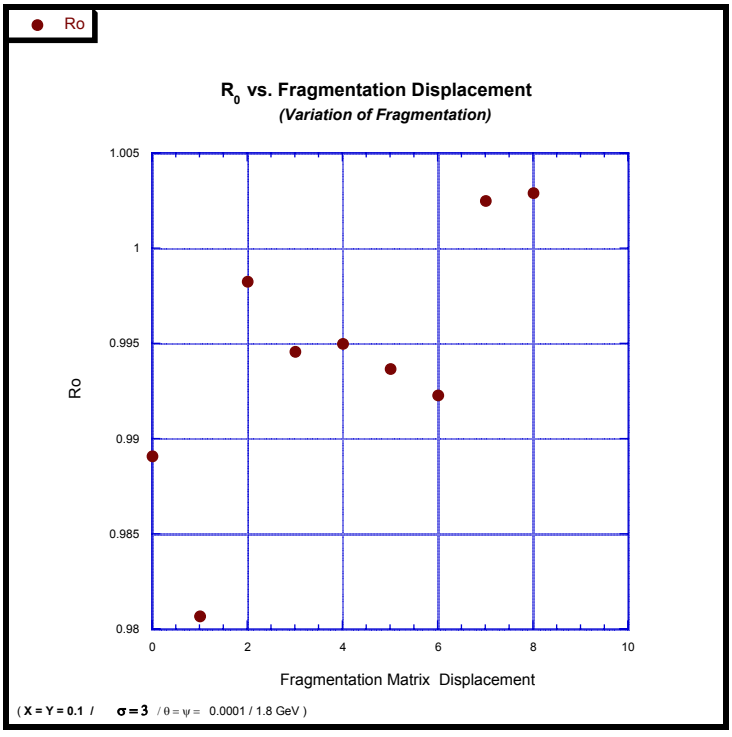
Ro
R0 vs. Fragmentation Displacement
(Variation of Fragmentation)
1.005
1
0.995
0.99
0.985
0.98
Ro
0
2
4
6
8
10
Fragmentation Matrix Displacement
(X = Y = 0.1 / σ = 3 / θ = ψ = 0.0001 / 1.8 GeV)

The variation is within R_0-values of 0.02, roughly the same as the 1-2 % seen in the other computational errors. To put this in more appropriate scale:

Figure 7.31a R_0 vs. Fragmentation Displacement (E_p=1.8 GeV)

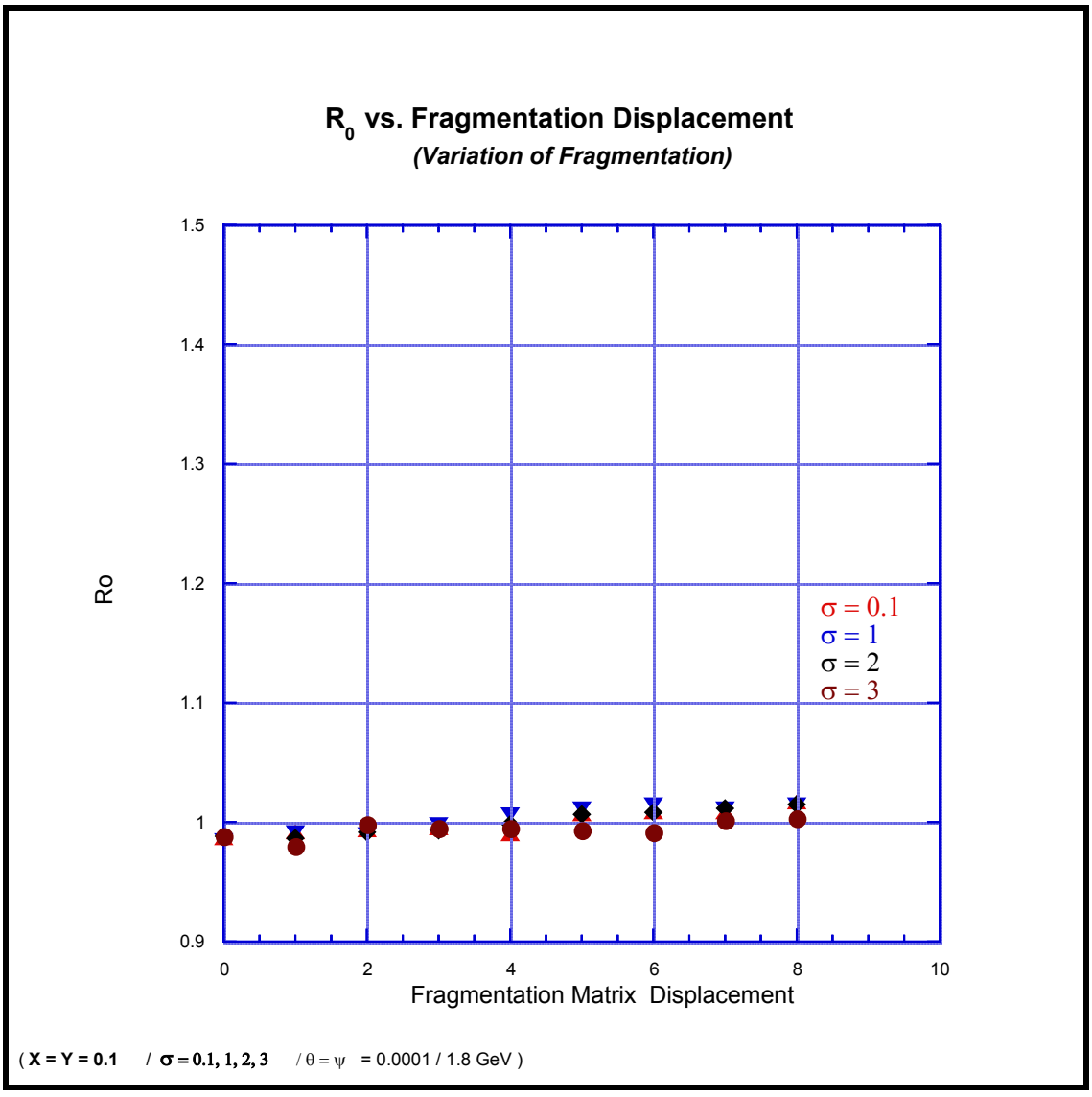

And for E_p = 140 MeV it is commensurately smaller with R_0 in the range [0.957 – 0.99].

Figure 7.31b R_0 vs. Fragmentation Displacement (E_p=140 MeV)

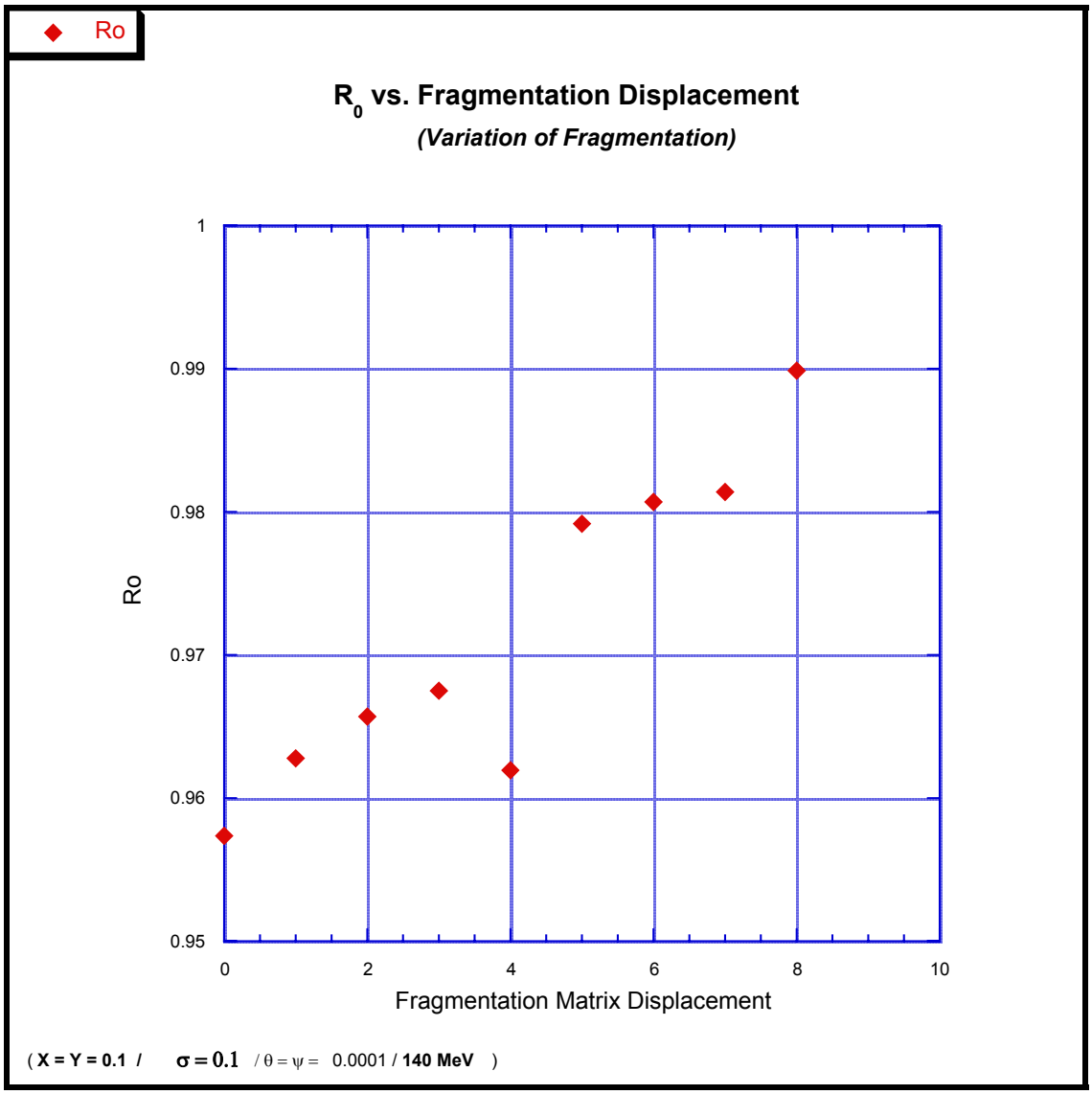

Putting this in proper scale and physical perspective:

Figure 7.31c R_0 vs. Fragmentation Displacement (E_p=140 MeV)

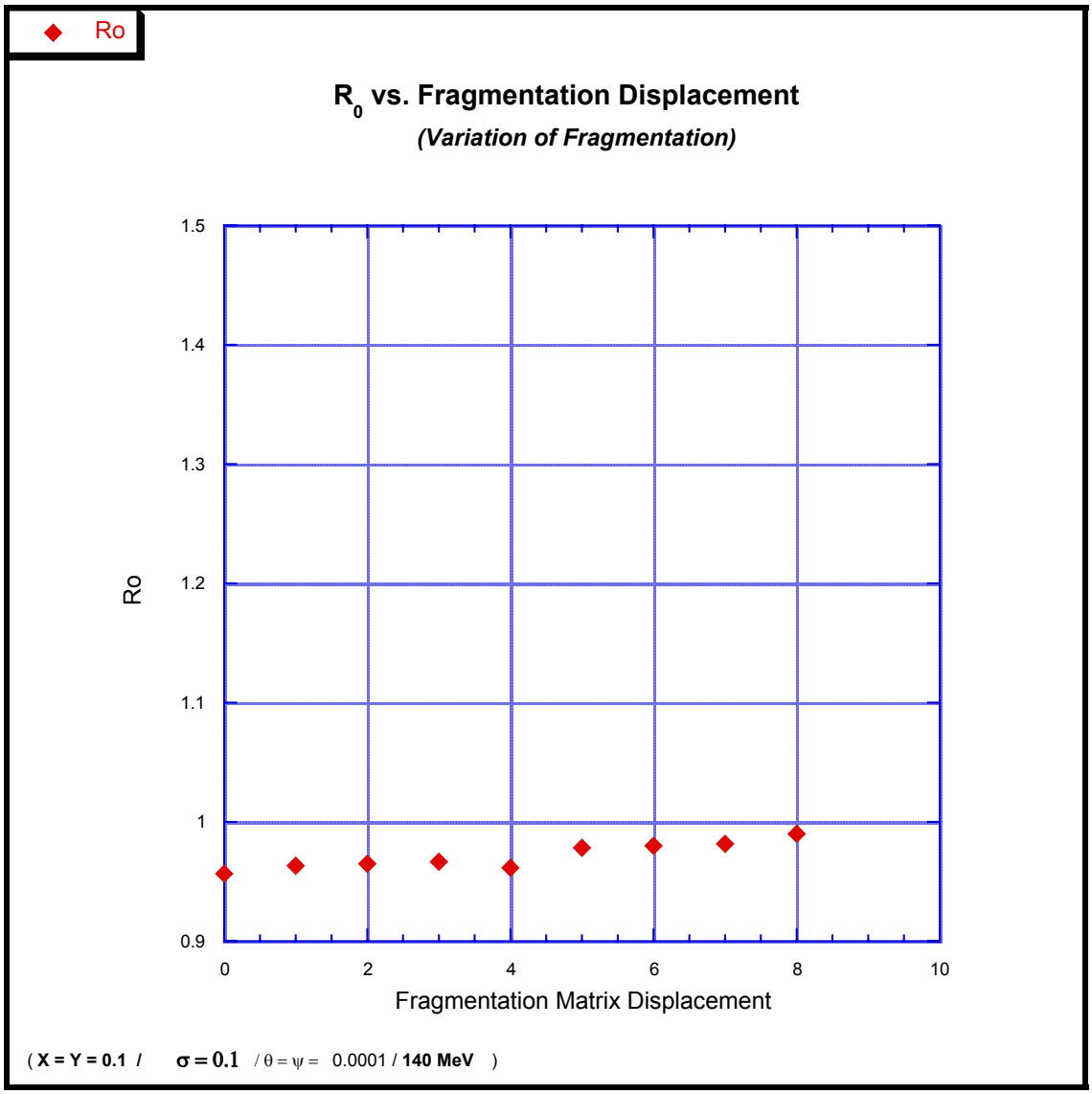

Z-Displacement

(variations on a variational theme)

The above samples only one of the many possibilities of Z-displacement. For contrast, another variation is presented. It is similar to the one presented above, but is computationally different and has Z-displacements from [0 – 15]. At a Z-displacement = 0 we are starting with the database as measured and used. As this displacement increases the charge families chosen in the simulations are displaced upward until Z=18 secondaries are the *only* ones being used. As before, in order to amplify and hence overestimate any possible effects due to the fragmentation variations, E_p=1.8 GeV. (Note that the computational error bars are smaller than the size of the symbols used.)

Figure 7.32a R_0 vs. Fragmentation Displacement (E_p=1.8 GeV)

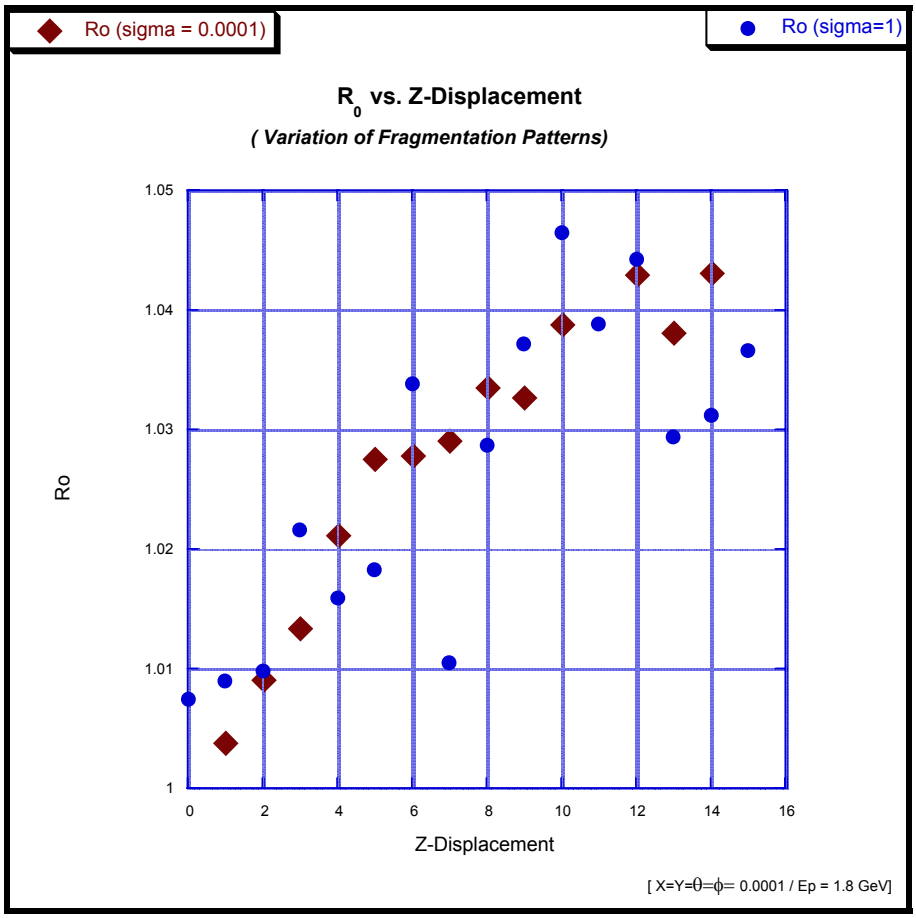

Putting these changes of R_0 in numerical perspective with the experimental values of $R_0 = 1.5 \pm 0.02$:

Figure 7.32b R_0 vs. Fragmentation Displacement (E_p=1.8 GeV)

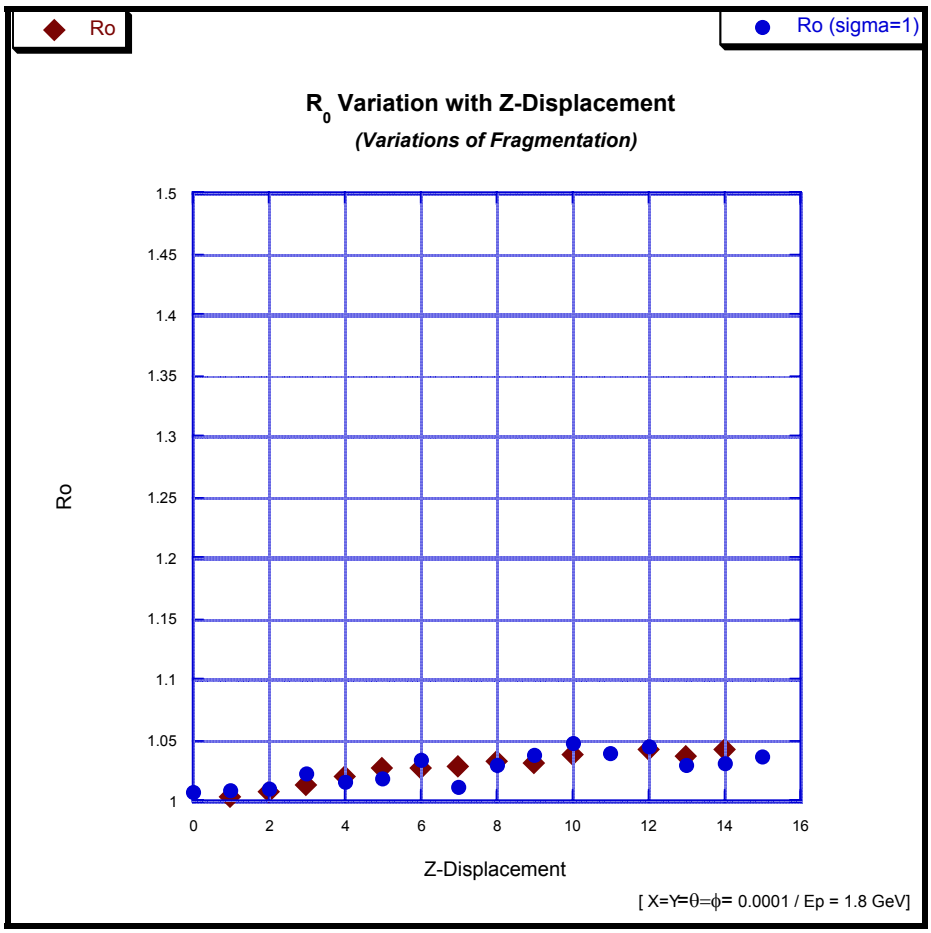

All the above establishes two limits to the computational error: one is derived from the maximal possible errors of charge measurement, and the other establishes the order of magnitude errors due to variations of the fragmentation pattern itself. The latter is of potential concern for fragmentation patterns measured from the Ag and Br of emulsion and used in the simulation of a Cu target. The asymptotic limit on the computational errors due to our versions of fragmentation variation is seen to be ~5%, while the computational error due to maximal charge measurement errors is 2-3% (for a Z-displacement = 6, which is *much* greater than could possibly be).

And we are still left with no reasonable explanation for the experimental values of R_0. Neither pathological combinations of transport variables nor numerical fluctuations of our computational approach and database are able to go beyond a value of $R_0 \sim 1$, and even that is for the extremely unphysical assumption of $E_p = 1.8$ GeV.

Obviously we must look further.

VIII Changes of Mean Free Path

(Homogeneous and Subpopulations)

8.1 Homogeneous Change of Mean Free Path

As discussed in Chapter 4, the mean free path λ can be parameterized from experimental measurements by

$$\lambda = \Lambda Z^{-b} \tag{8.1}$$

The following table lists the values of Λ and b used by ourselves and others[1]:

Table 8.1 (Λ , b) Parameters used in Different Studies

Study	Λ (cm)	b
Lerman et al	32.4	0.44
LBL-NRC	30.4	0.44
Friedlander et al	32.2 ± 2.5	0.44 ± 0.03
Judek	28.9 ± 2.5	0.43 ± 0.04
Barber et al	25.1 ± 1.7	0.34 ± 0.03
Baroni et al	23.3 ± 0.8	0.32 ± 0.01
Karol	25.2	0.43
Beri et al	24.1 ± 1.2	0.34 ± 0.03
Jain et al	33.6	0.45
Aggarwal et al	35 ± 1.8	0.42 ± 0.024

[1] The figures from Judek, LBL-NRC, and Friedlander can be found in Friedlander (1983). The others were collected from both the preprint and final volumes of the 5th and 6th LBL- sponsored "High Energy Heavy Ion Study" workshops.

In the figure below the mean free path of primary argon is taken to be the conventional 3.98 cm, but ALL SECONDARIES with $Z \geq 2$ have their mean free path vary with the change in Λ ($\lambda = \Lambda Z^{-b}$), an obviously unrealistic scenario. For shower particles (Z=1) values of $\mathbf{E_p}$ shown are 1.8 GeV, an obvious exaggeration and over-approximation to the more experimentally realistic 140 MeV.

Figure 8.1 R_0 vs. Λ

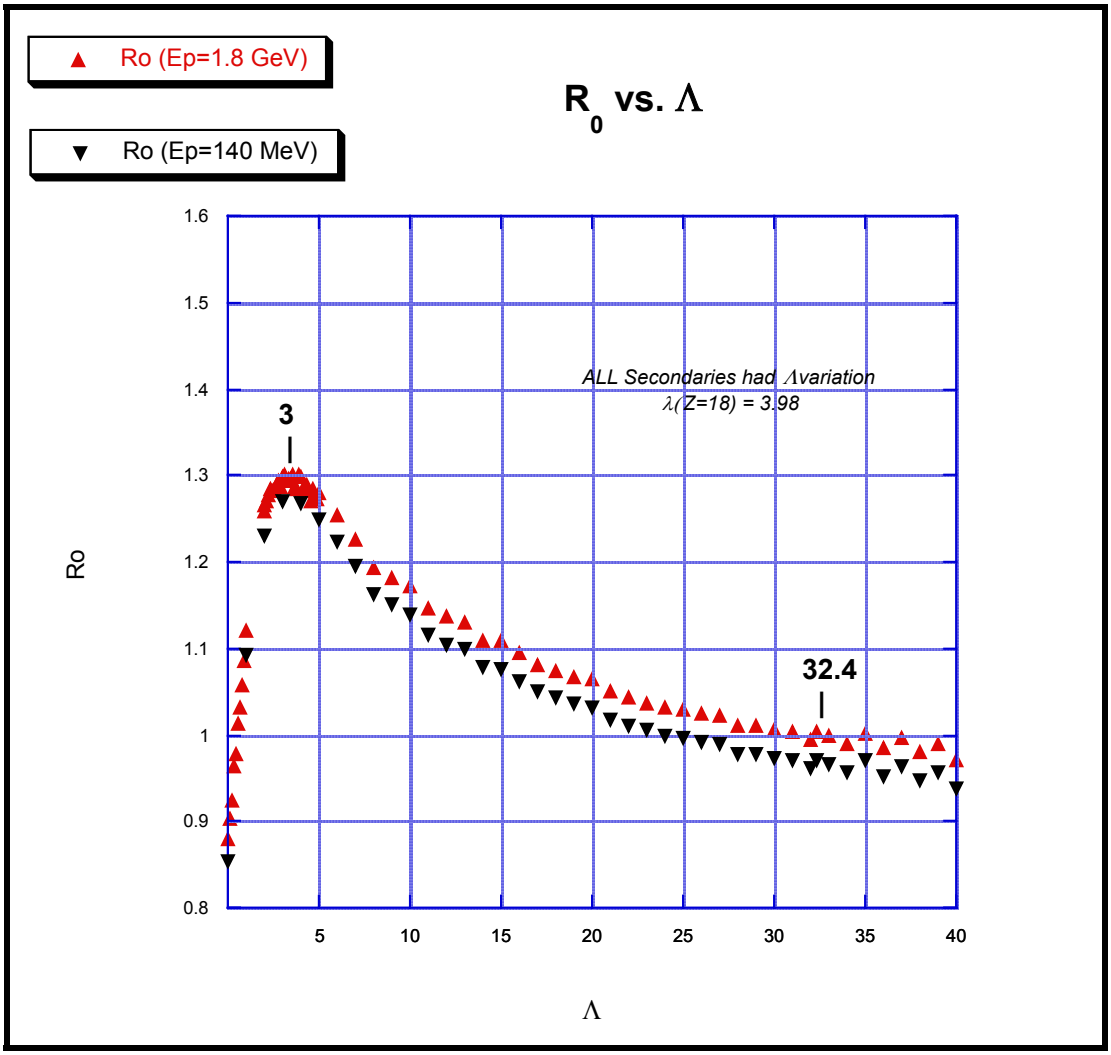

Only for a small region around Λ=3 is there a significant rise in R_0, peaking at a value of ~1.3. The large drop-off below Λ=3 is easily understood. For very small values of the mean free path, all secondaries interact in the cylinder in which they are created, hence there is no contribution in the second cylinder from secondaries created in the first. R_0 decreases in this case, for the ^{24}Na production in the second cylinder will solely be due to the exponentially decreased primary beam and its commensurately decreased secondaries. In the experimental region listed in Table 8.1 (i.e. Λ = 23 – 33) R_0 is in the range [1.00- 1.05] for $\mathbf{E_p}$ = 1.8 GeV and R_0 is [.95 – 1.00] for $\mathbf{E_p}$ = 140 MeV.

8.2 Subpopulations of Secondaries (Computational Approach)

The above discussion was based on program versions that dealt exclusively with homogenous populations of secondaries. But in the initial papers on the Copper Calorimetry Experiments (Aleklett et al 1987, 1988a,b) it was suggested that the experimental results could be explained by subpopulations of secondaries having either anomalously larger geometric cross-sections (mean free paths one or two orders of magnitude larger than primaries) or by having shower particles with considerably greater transverse momentum.

Hence it was important to model the potential effects of such subpopulations, keeping in mind that Monte Carlo results can be sensitive to the computational approach chosen. Especially because relatively small subpopulations were being modeled several different computational approaches were designed in order to insure (as much as possible) the actual convergence of the approaches to physically meaningful results. This approach also offered the opportunity to better evaluate the true computational errors inherent in our overall approach.

The computational variants included, as above, different sequences of the database. Also included were the two fundamentally different ways of (computationally) contributing subpopulations PERC and COUNT.

PERC: This approach is statistically analogous to how distance distributions are chosen in the rest of the program: a uniform distribution function is created from which the set percent P of subpopulation is chosen. A number X is chosen from a uniform distribution [0,1]. If $X < P$, then the star has the characteristics of the subpopulation. If $X > P$, then it has the 'conventional' characteristics. These programs are the PERC series (for percent).

COUNT: As a check to this first approach at simulating subpopulations, a simulation incorporating a simple counter was created: for a population with C percent subpopulation, it counts the number of particles in each "pulse" of the beam; and every C-times creates secondaries with the appropriate differing characteristics. These are the COUNT programs.

Each of the two statistical approaches was then applied to two different database sequences, resulting in four different subpopulation programs. Hence the PERC program uses the original database, while PERC-1 uses the randomly re-ordered one. So does the COUNT-1 program, while COUNT uses the original database*.

It must be noted that due to the nature of the counter approach, the stars are selected in an ordinal fashion from the database. The statistical approach outlined above randomly picks stars each time. Hence, as seen above, large fluctuations between the two would be expected for small samples of stars with a hoped for convergence occurring for large samples of stars (that are in essence statistically 'well-mixed').

Initial convergence tests between the four program variants led to the results shown below: a large fluctuation for very small samples of particles, and an excellent convergence of R_0 results by runs of {10 x 10,000}.

---

* In some of the graphs, the results of PERC routines are abbreviated by *perc;* while those of the COUNT routines are abbreviated *cont.*

Figure 8.2 Computational Convergence of Subpopulation Programs

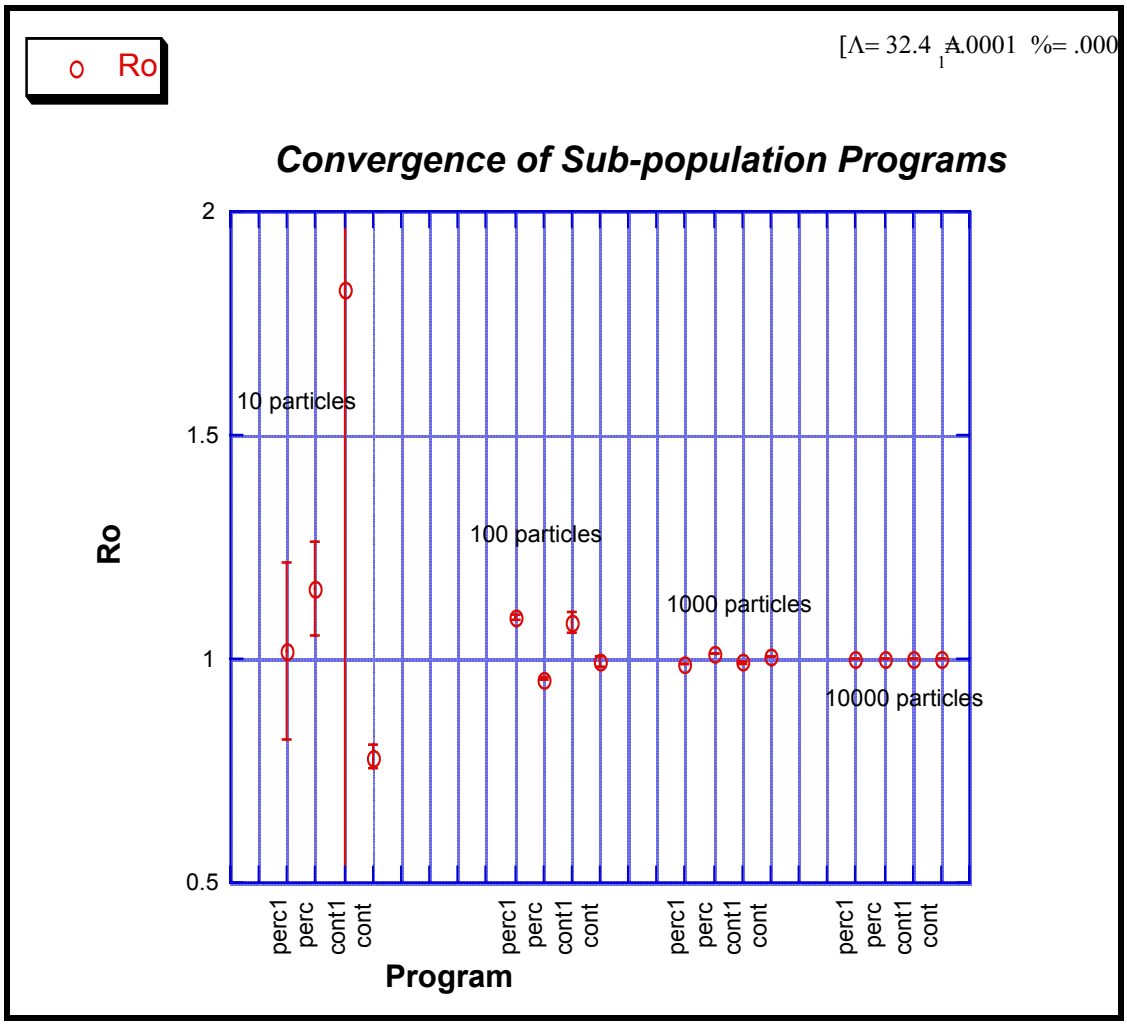

Continuing the discussion on database-dependent fluctuations from the previous section, the very large fluctuations seen between 10 and 100 particles offers an extremely important insight into why the original experimental paper (Aleklett et al 1987) may have gotten the results they did. The independence of the number of particles chosen is very much a function of the actual number of stars, tracks, and particles in the database from which one is doing the Monte-Carlo.

A large number of pulse particles chosen from a very small number of actual database particles is still a small number of particles, thus susceptible to all the potential fluctuations inherent in the Monte Carlo process. And for small numbers of pulse particles in our particular case, the order of the star families is seen here to result in the largest fluctuations (between *cont1* and *cont* for 10 particles and *perc1* and *perc* for 100 particles). The original paper utilized between 50 and 100 stars in their Monte-Carlo database…just the region where the fluctuations can do the most damage to the real-world accuracy of the simulation. In our case, the database is composed of several thousand stars which as the tests clearly demonstrate are in the computationally safe region.

8.3 Subpopulations of Secondaries with Differing Mean Free Paths

Because of the mutual convergence of the four different versions of subpopulation programs we can arbitrarily choose one of them to explore the effects of subpopulations in Λ. In order to best compare the results to the previous simulations the PERC version is chosen, for it is closest to the twin programs utilized above and operates on the original database is chosen. In all cases we are taking a subpopulation of P% of the secondaries having a value of Λ_1 , while the primaries and (1-P)% of the secondaries have a value of Λ=32.4. For the initial conditions of (X=Y= $\sigma = \theta = \phi$ = 0.0001) and the overestimating case of E_p = 1.8 GeV the following results are found:

As seen in Figure 8.3 for a 1% subpopulation, R_0 is essentially .995; with an almost indistinguishable rise above 1.00 for the region Λ_1 = 1- 10.

Figure 8.3 R_0 for a 1% Subpopulation of Λ_1

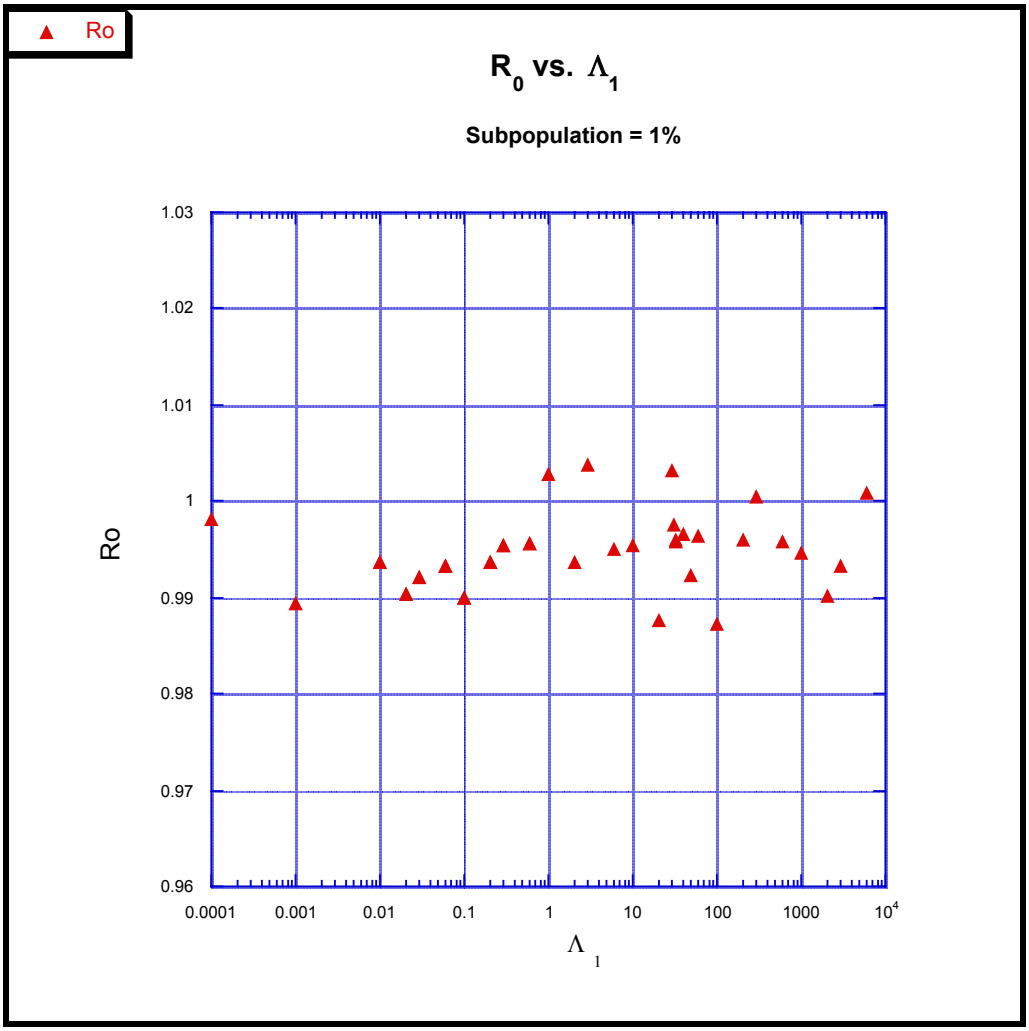

As seen in Figure 8.4, for a subpopulation of 10% this region of Λ_1. has a more evident peak; but it still only rises to a value of $R_0 = 1.025$ at the maximum for $\Lambda_1 = 3$.

Figure 8.4 R_0 for a 10% Subpopulation of Λ_1

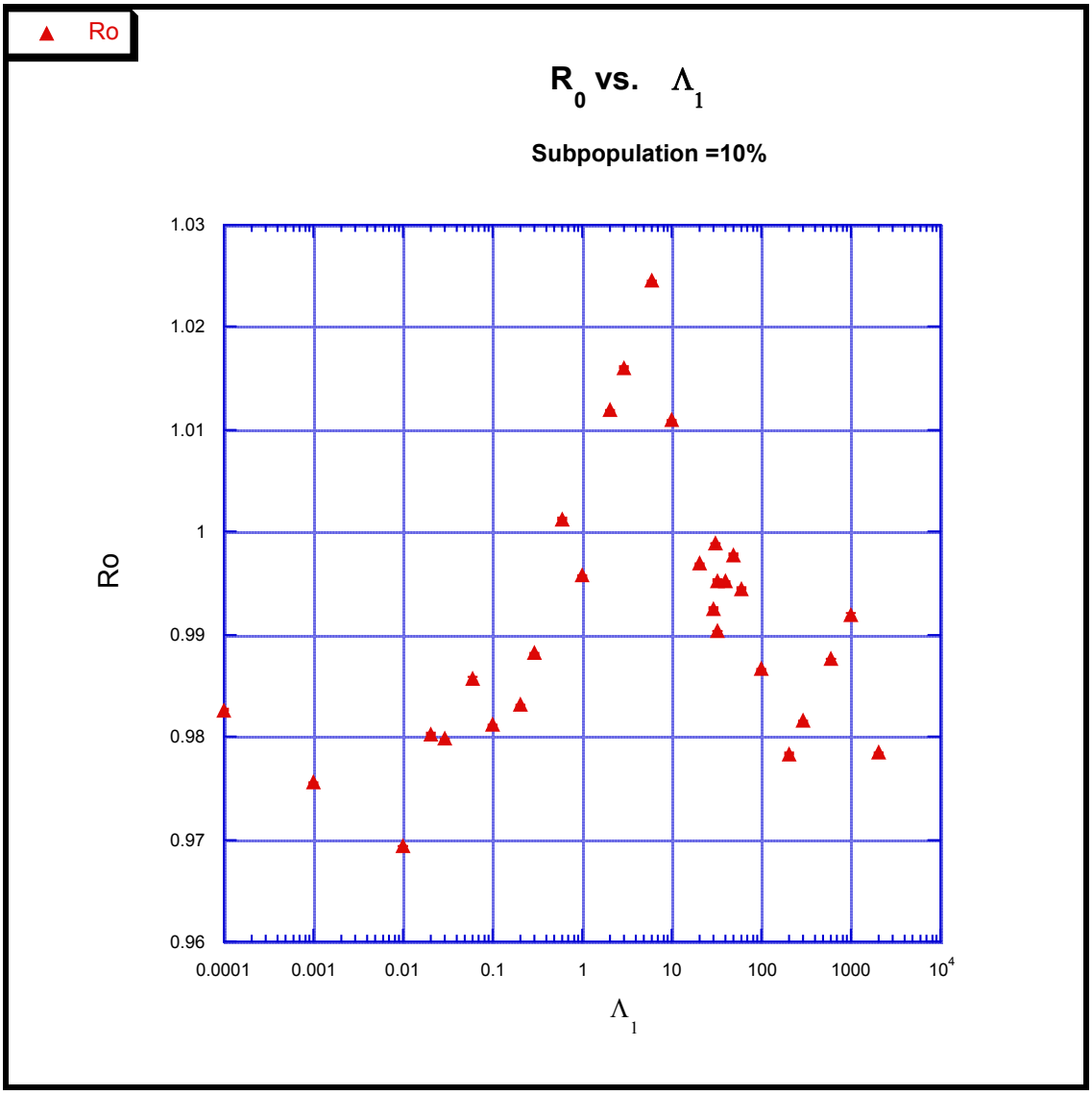

Only for a subpopulation level of 90% is there a significant increase of R_0, with a value of $R_0 = 1.29$ at $\Lambda_1 = 3$.

Figure 8.5 R_0 for a 90% Subpopulation of Λ_1

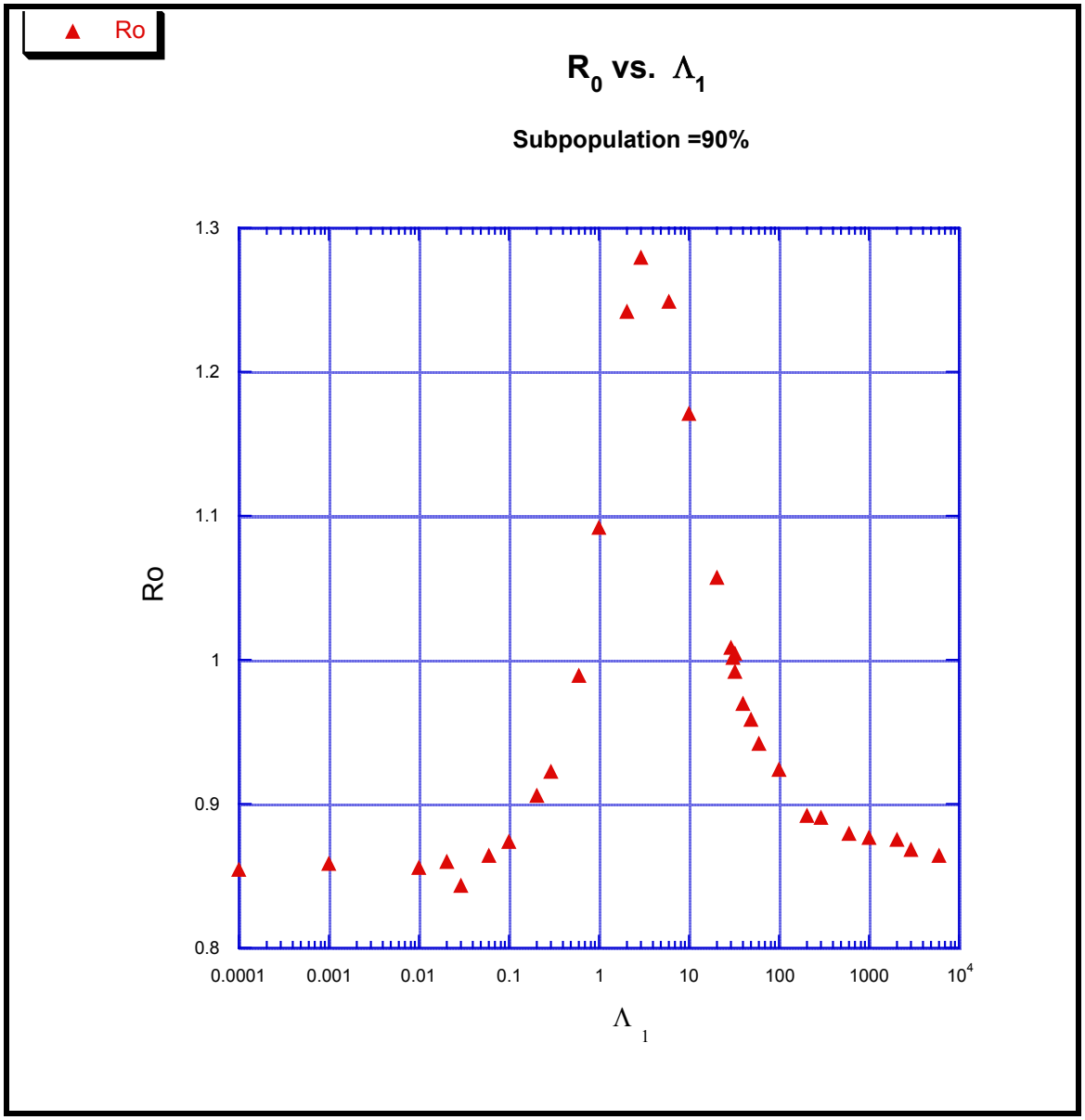

They are shown together on the same scale

Figure 8.6 R_0 for a Different Subpopulations of Λ_1

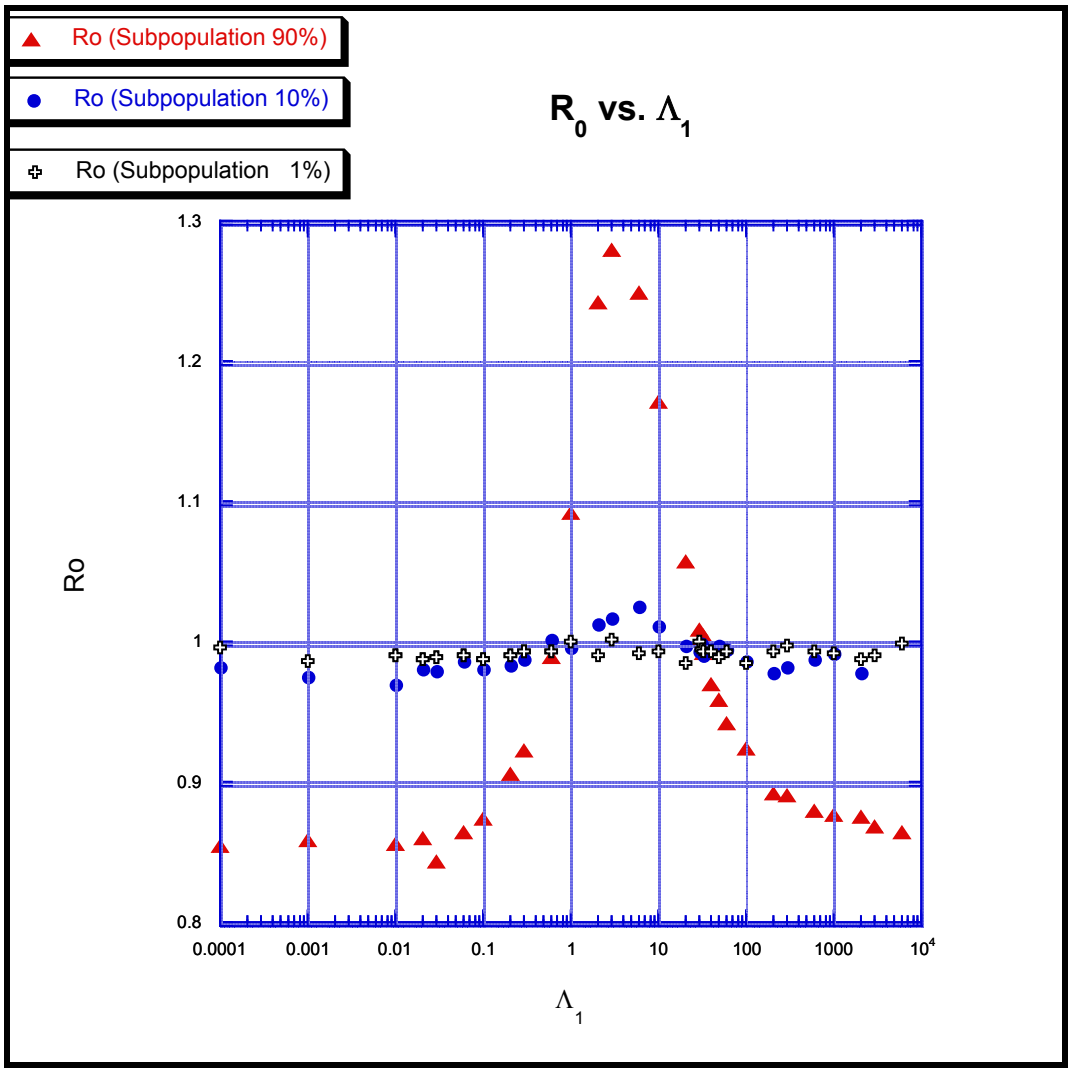

One of the reasons for going to such large values of Λ_1 (up to 6000) was a check on the remote but conceivable possibility that rather than a small mean free path, the subpopulation had a very large one, and that the experimental values of R_0 were the result of a statistical 'tail' effect. Obviously, this is not the case.

Examining $\Lambda_1 = 3$ more closely for each of the four subpopulation programs {and at the initial conditions of (X=Y= $\sigma = \theta = \phi = 0.0001$) and $E_p = 1.8$ GeV }:

Figure 8.7a R_0 for PERC Routines (Λ_1 Subpopulation)

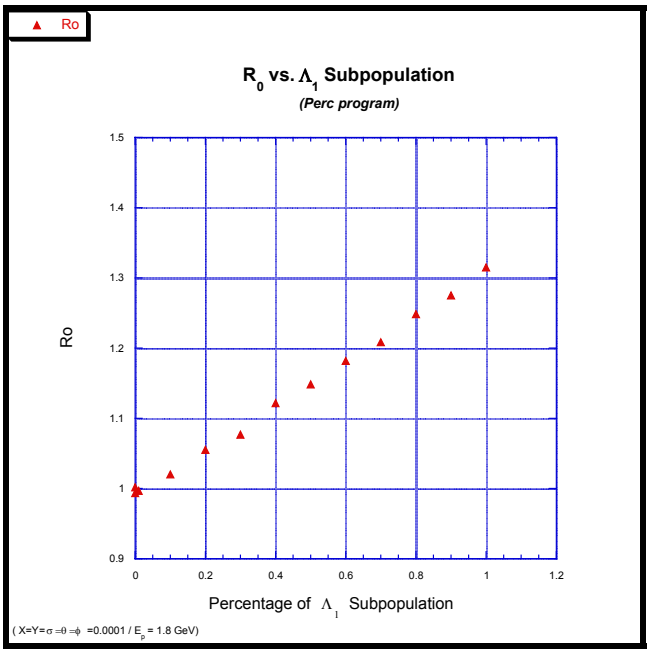

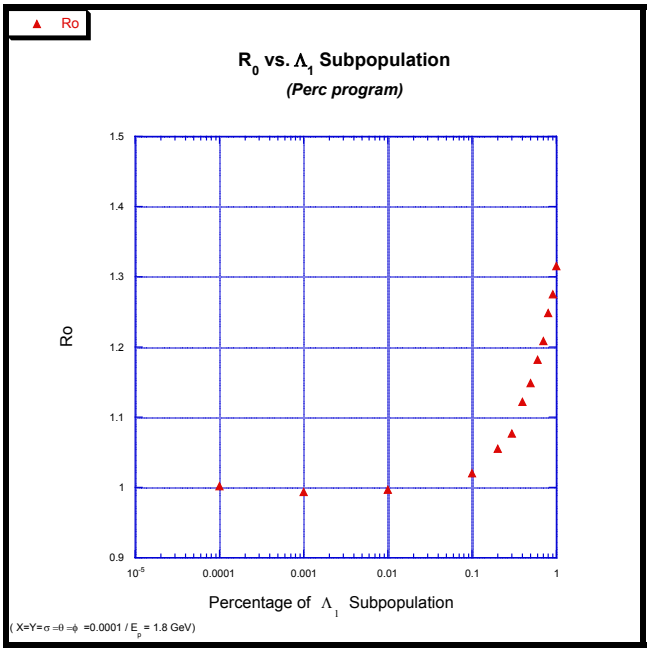

Figure 8.7b R_0 for PERC-1 Routines (Λ_1 Subpopulation)

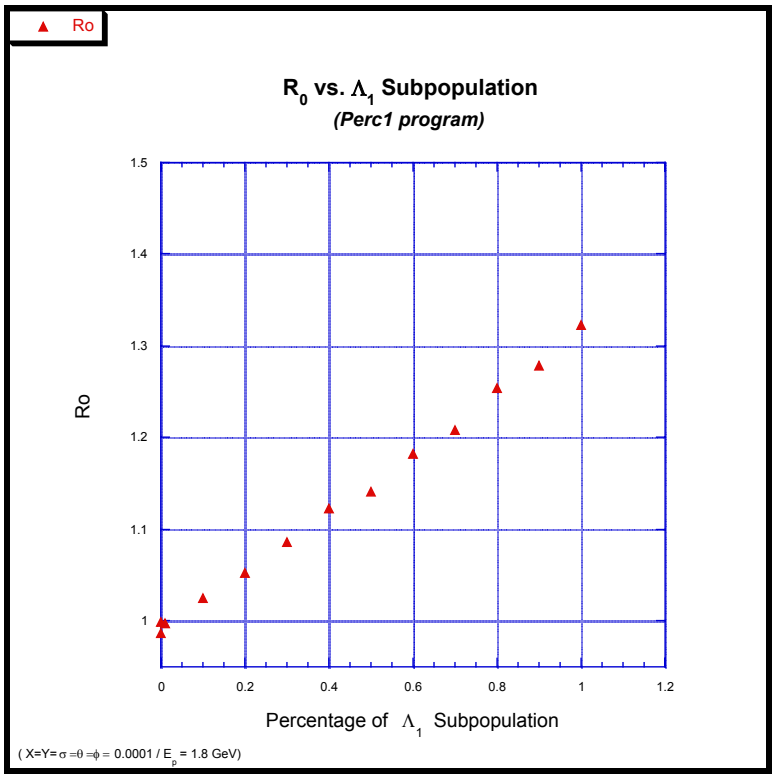

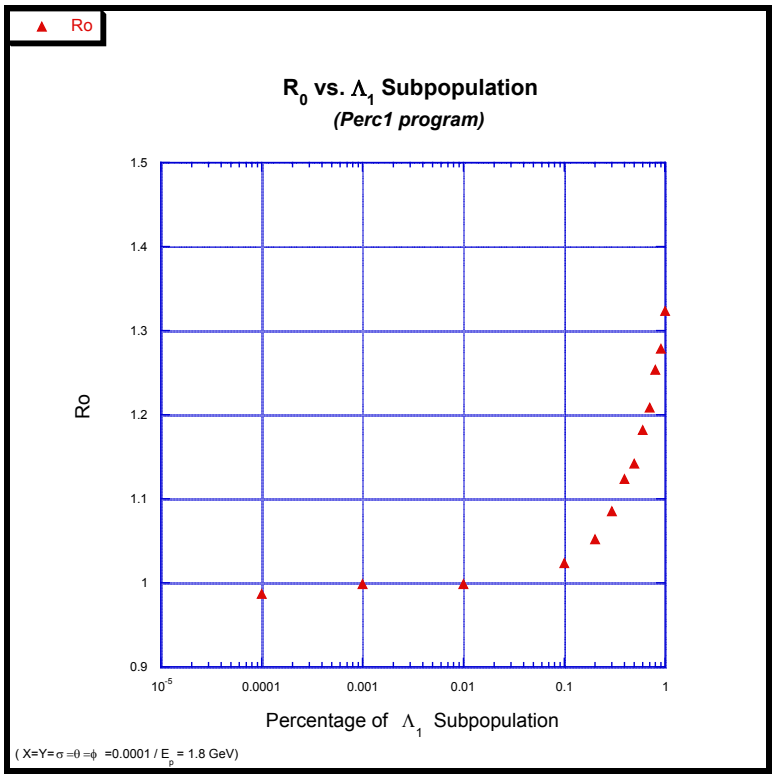

Figure 8.7c R_0 for COUNT Routines (Λ_1 Subpopulation)

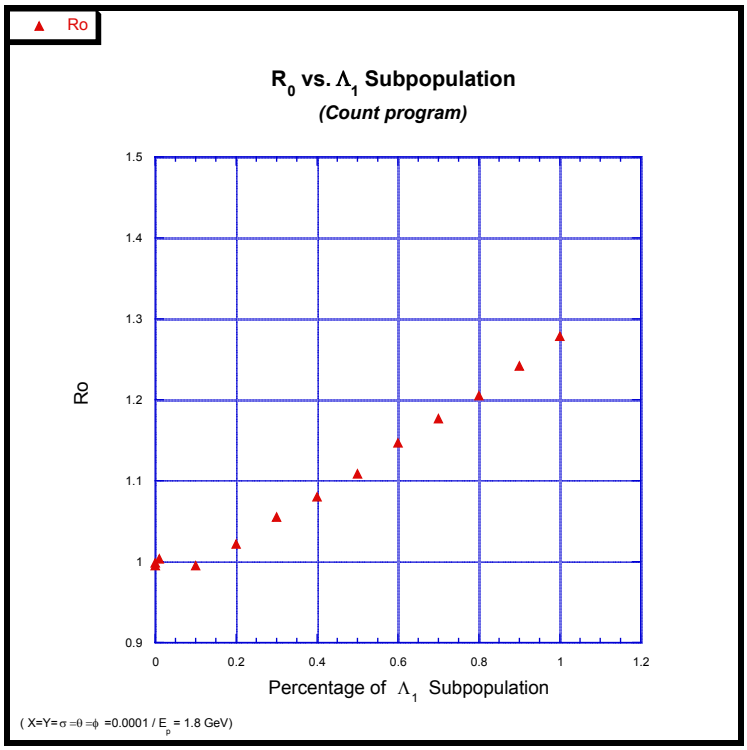

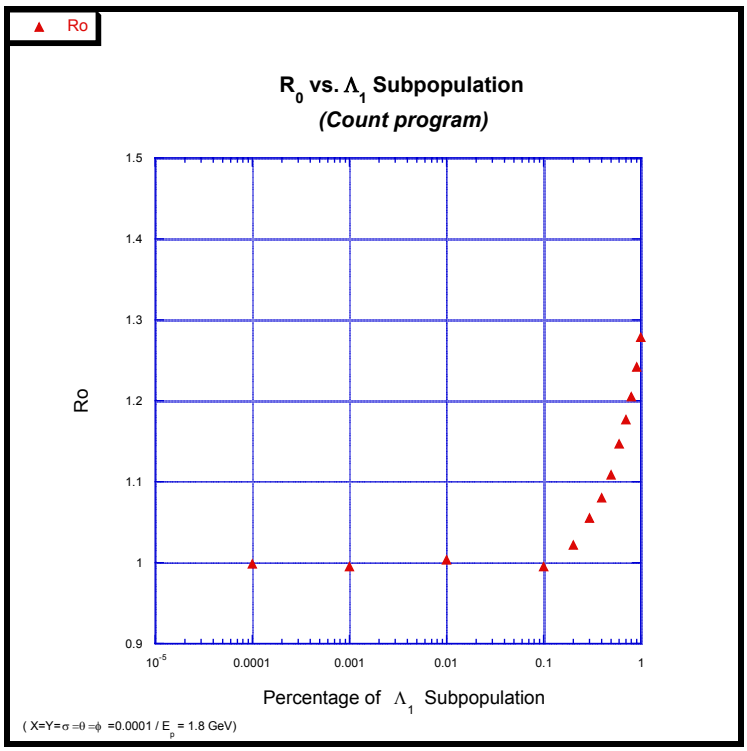

Figure 8.7d R_0 for COUNT-1 Routines (Λ_1 Subpopulation)

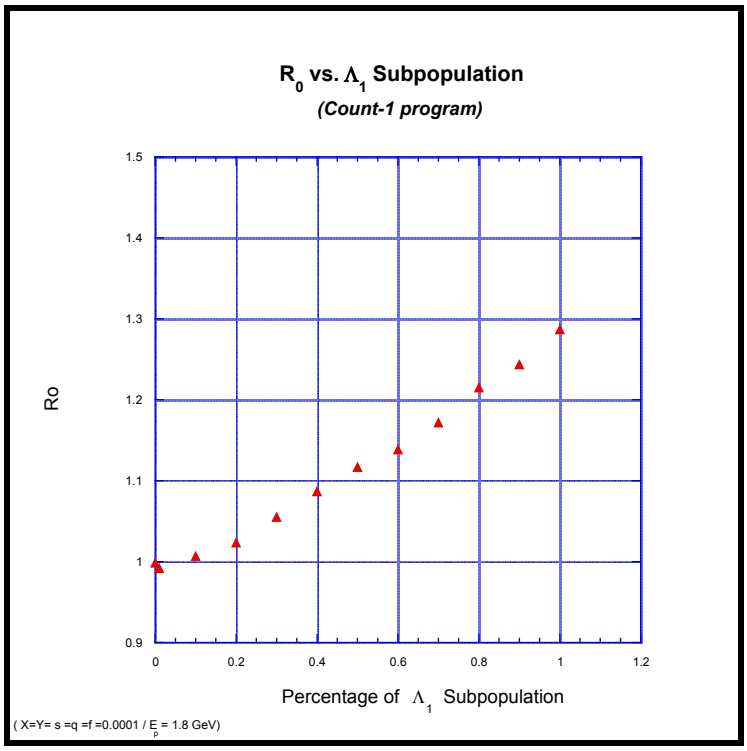

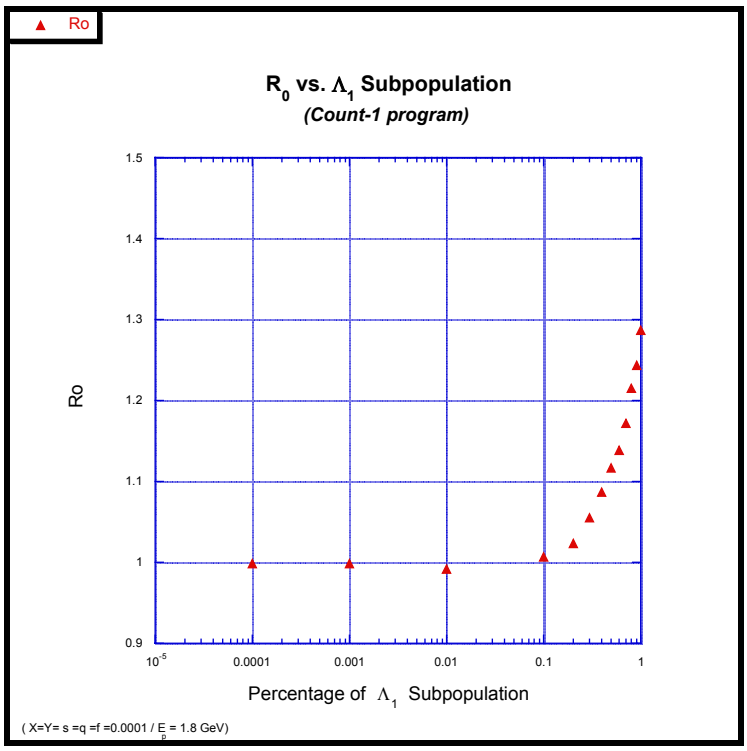

This also allows a comparison between the different subpopulation programs: the statistically driven PERC routines vs. the COUNT routines that use counters.

Figure 8.8 R_0 for Different Λ_1 Subpopulation Routines

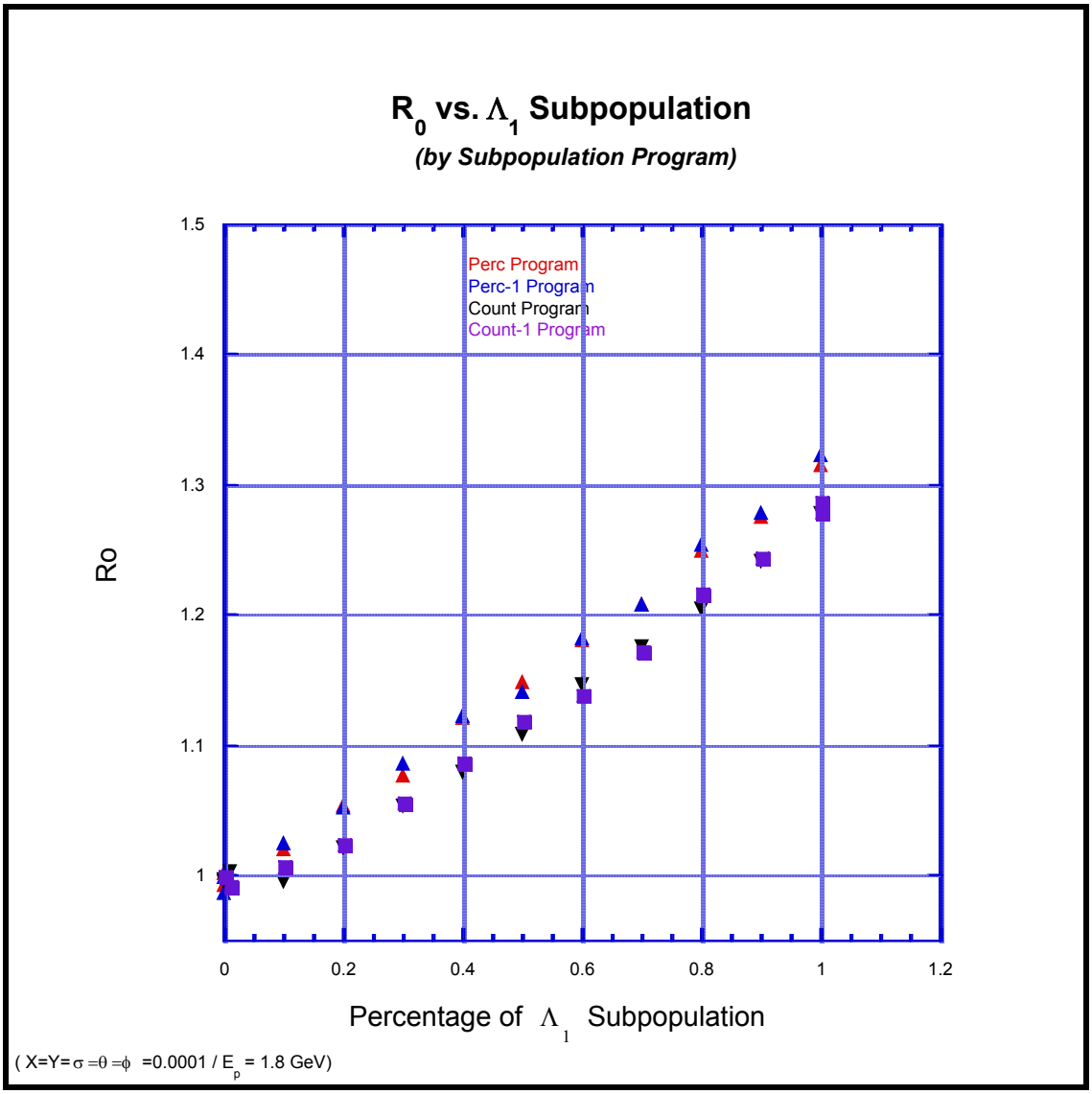

An excellent convergence is seen within each type and an incremental difference (~ 0.03) between the two different types. Choice of database order makes no difference within a given program category. All in all it is a further demonstration of the consistency of the different approaches to modeling subpopulations.

Taking a range of more realistic beam dispersions from $\sigma = 0.001$ up to $\sigma = 2$ shows near identical results:

Figure 8.9a R_0 vs. Λ_1 Subpopulation (σ = 0.001 PERC)

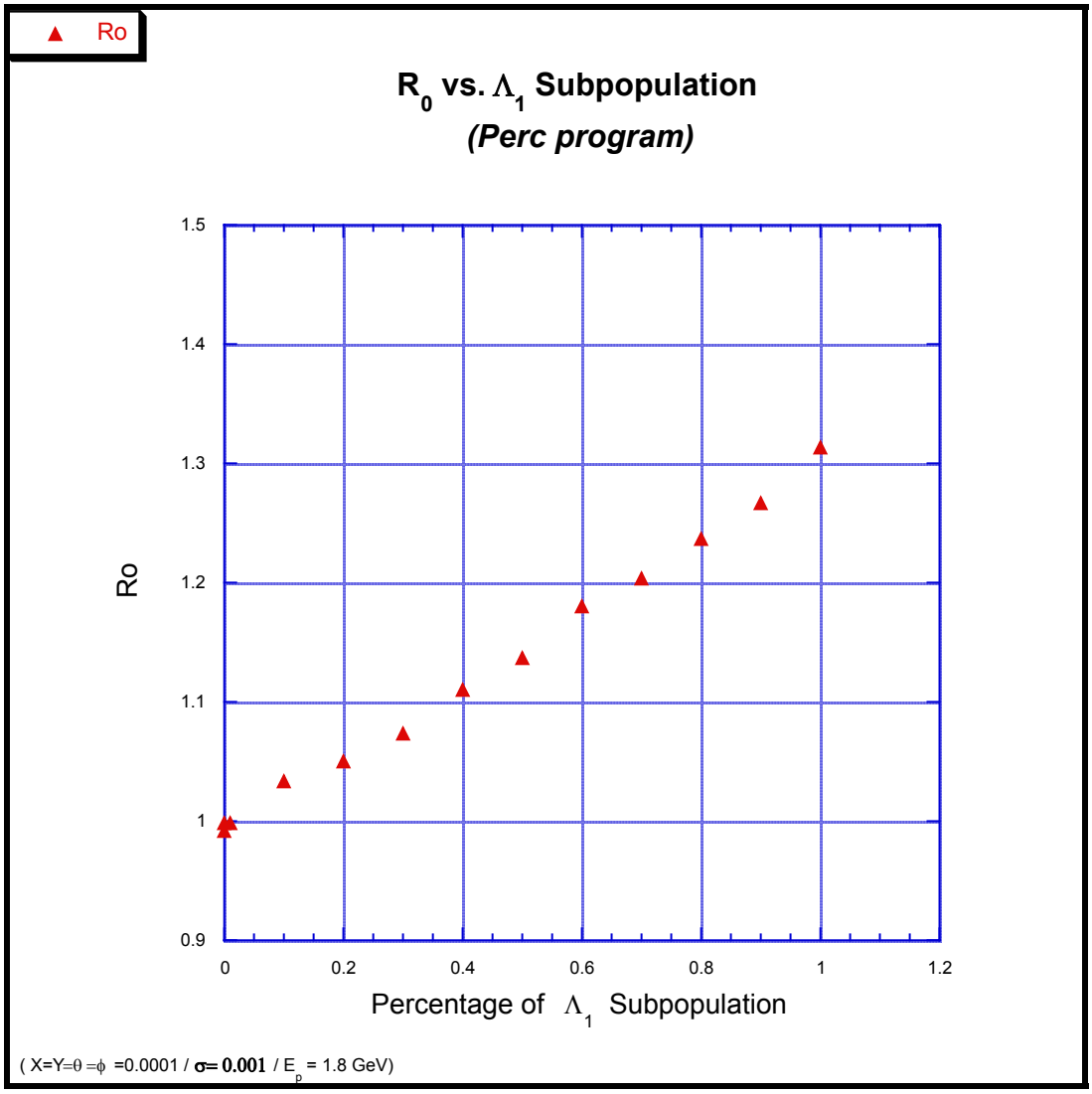

Figure 8.9b R_0 vs. Λ_1 Subpopulation ($\sigma = 0.1$ PERC)

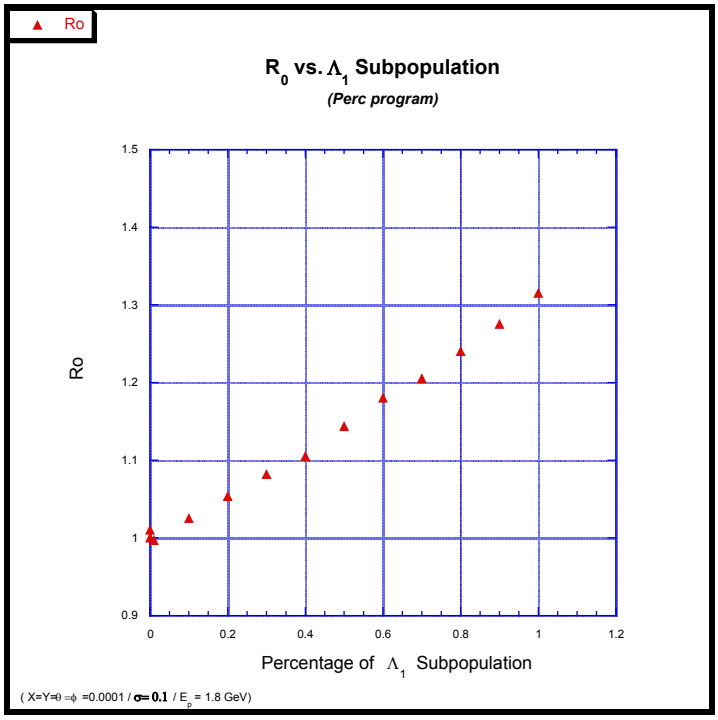

Figure 8.9c R_0 vs. Λ_1 Subpopulation ($\sigma = 1$ COUNT-1)

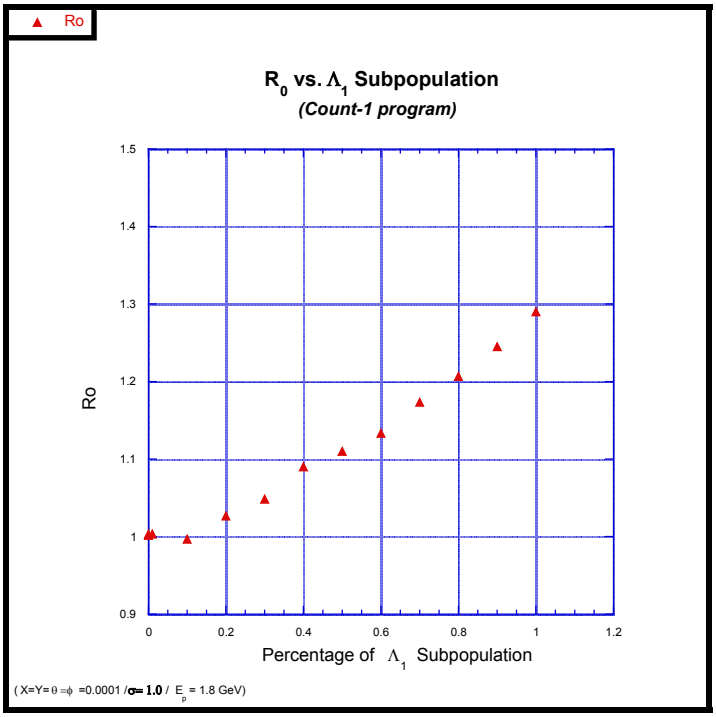

Figure 8.9d R_0 vs. Λ_1 Subpopulation ($\sigma = 2$ PERC-1)

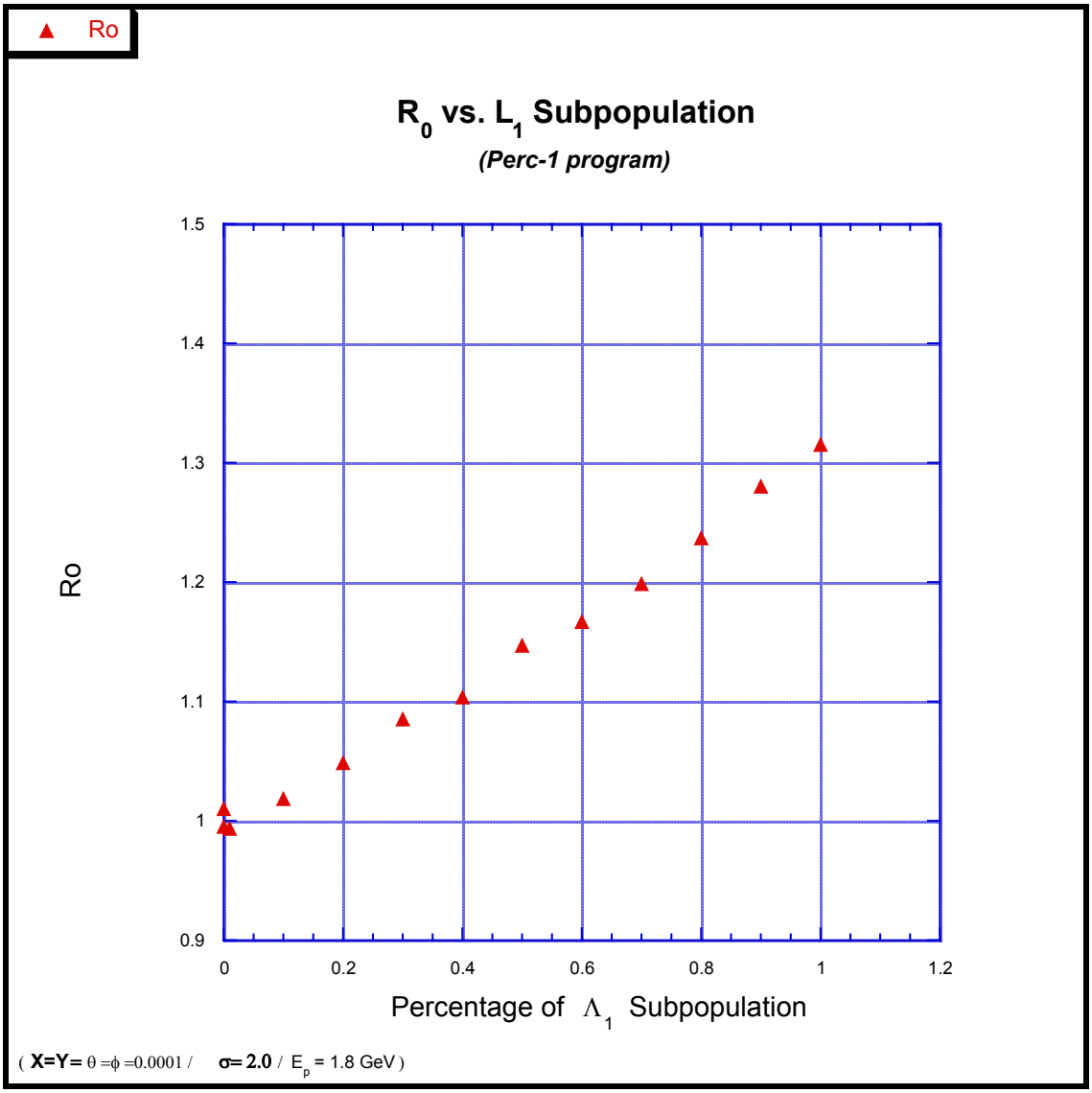

Taking now a 1 cm displacement of the beam center in both X and Y, along with a variation of the beam dispersion again shows no real change in the results. This is readily seen in Figures 8.10(a,b).

Figure 8.10a R_0 vs. Λ_1 Subpopulation ($X_0 = Y_0 = 1$; $\sigma = 0.0001$; COUNT-1)

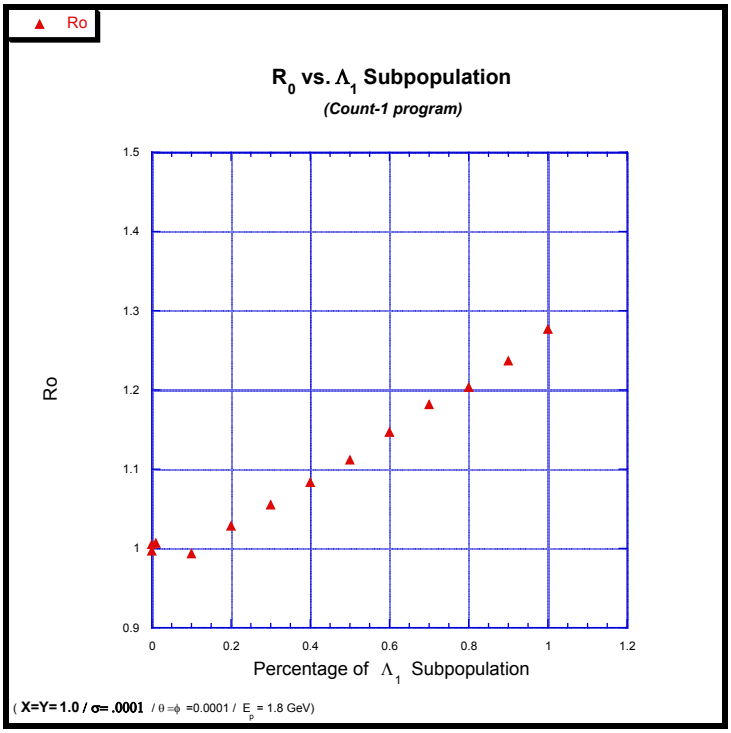

Figure 8.10b R_0 vs. Λ_1 Subpopulation ($X_0 = Y_0 = 1$; $\sigma = 1$; COUNT-1)

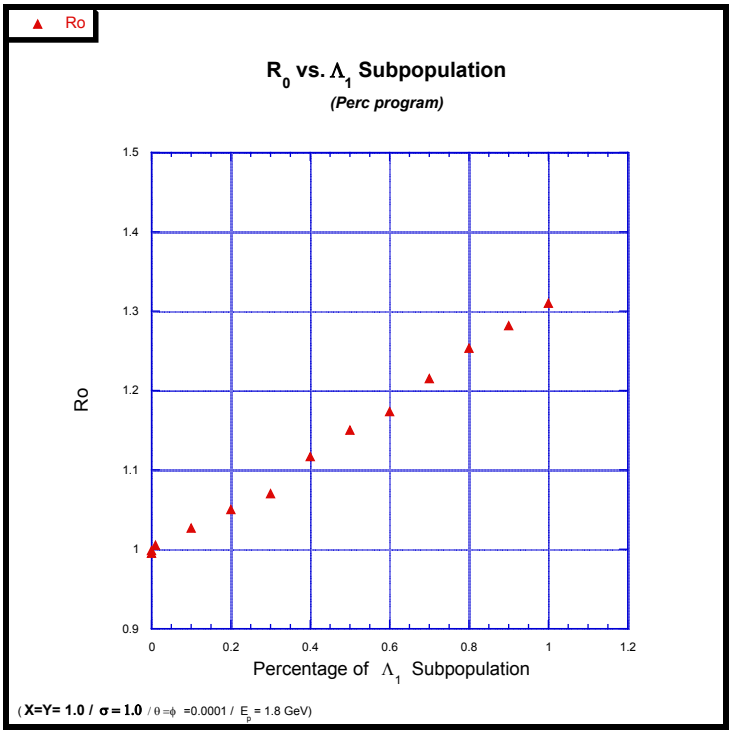

Including one of the many consistency checks on the different subpopulation programs, the results, to a high computational accuracy, are as before: even with E_p = 1.8 GeV to even break R_0 = 1.1 requires a 50% subpopulation of secondaries with Λ=3 (with a mean free path 10 times shorter than expected). And even with 100% of the secondaries having this attribute only takes one up to R_0 = 1.3.

Figure 8.11a R_0 vs. Λ_1 Subpopulation (100% of Secondaries having Λ=3)

E_p = 1.8 GeV

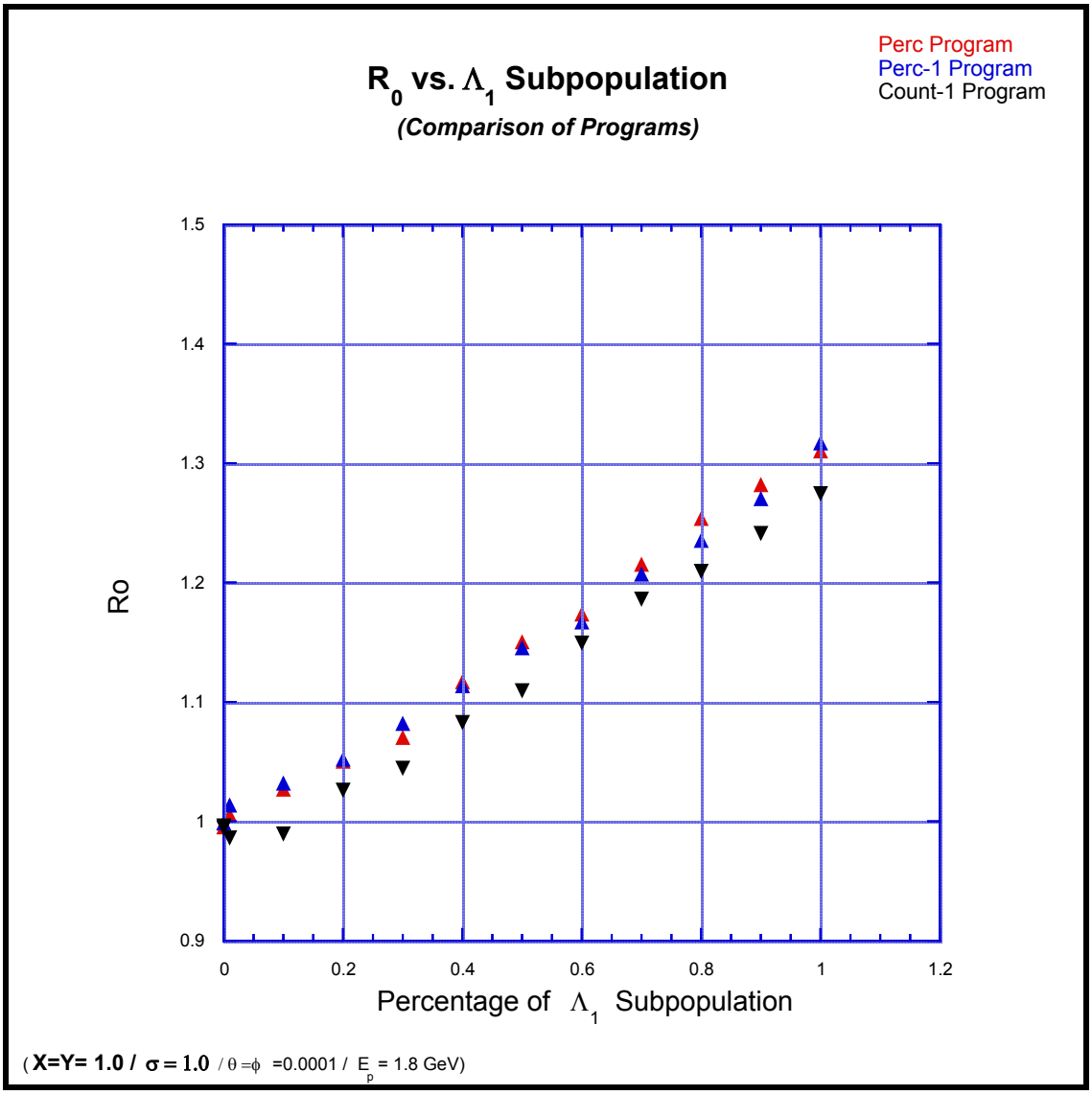

With the more realistic E_p = 140 MeV, the results for R_0 are even less, but just as consistent:

Figure 8.11b R_0 vs. Λ_1 Subpopulation (100% of Secondaries having Λ=3)

E_p = 140 MeV

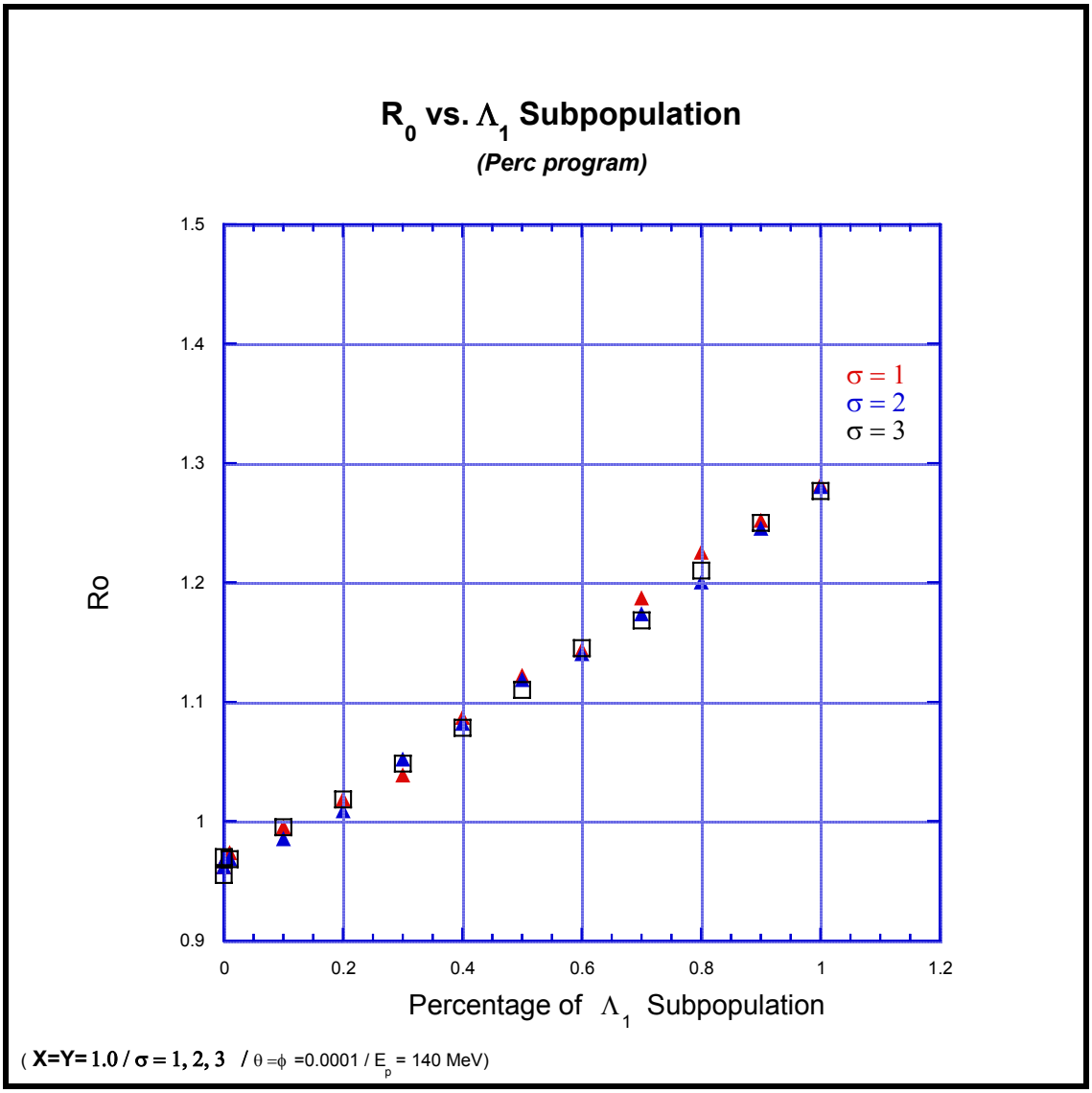

Many other simulations have been done, each of the parameters being varied to highly unrealistic conditions, singly and in combinations. Yet the results are the same and consistent with the values presented above. As such they are completely opposite to those of Aleklett et al, who explained the experimental values of $R_0 \sim 1.5$ by a subpopulation of a few percent (3-6%) having a Λ_1 of a tenth or a hundredth of the nominal value. In fact we show that for Λ_1 equal to a hundredth of its nominal value around 32.4, the value of R_0 drops dramatically. Only for a relatively narrow window around $\Lambda_1 = 3$ is there a significant increase in R_0, maxing out to value of $R_0 \sim 1.3$ for $E_p = 1.8$ GeV and $R_0 \sim 1.28$ for $E_p = 140$ MeV.

As discussed above, it is felt that their results were an unfortunate consequence of computational fluctuations due to too small an initial database from which the Monte-Carlo was performed. In addition, the large percentage of secondaries required to have any significant effect on R_0 is a situation that seems without physical substantiation. And even if it existed, it would not be enough to approach the experimental values, themselves having small error bars ($R_0 = 1.5 \pm 0.02$).

The conclusion seems straightforward: **The results of the Copper Calorimetry Experiments have little to do with the so-called 'anomalon' effect (short mean free paths) which catalyzed these experiments being done in the first place. Nor did we find a serious contribution from the shower particles having a high P_T .**

So, something seems to be going on. But it's not what the initial experimenters were looking for. It was mentioned almost in passing in their initial paper* that one of the advantages of their experimental approach was that

> *" Even if anomalous secondaries either do not exist, or do not contribute to the investigated partial cross-section, this method provides a new measure for secondary energy flow, and implicitly, may reveal interesting features of the reaction mechanism."*

* Aleklett et al (1988a)

This seems exactly the case! Hence what is investigated next is whether the one remaining physical variable, the production cross-section, can play a role in reproducing the experimental results.

IX The Production Cross-Section

(Theme and Variations)

So far it has been shown what *could not* explain the experimental observations. In the process all potential variables have been varied but one -- the production cross-section. This section will discuss the potential effects of varying the production cross-section, and conclude that the only reasonable explanation for the experimental results is a short-lived enhancement of the secondaries' ^{24}Na production cross-section.

As mentioned above, Aleklett et al (1987) interpolated experimental findings to obtain the following parameterizations (and assuming all Z=1 particles to behave identically):

1) For projectile fragments of Z≥ 2 (A≥4), an energy-independent

$$\sigma_F(A) \cong 3.6A^{0.387} \tag{9.1}$$

2) For protons and pions with $E_k \leq 3$ GeV:

$$\sigma_p(E_k) = e^{-0.17 + 2.5u - 1.22u^2} \tag{9.2}$$

$$u = ln(E_k)$$

3) For protons and pions with $E_k \geq 3$ GeV:

$$\sigma_p(E_k) = 2.88E_k^{0.0496} \tag{9.3}$$

9.1 Variations of Ε for Homogeneous Populations

It was seen above that maximizing the shower particles' energies to a physically unrealistic E_p = 1.8 GeV, (and hence optimizing their potential for ^{24}Na production) contributed only a 5% increase in R_0. Hence this section will focus only on the potential effects of the Z>1 projectile fragments' production cross-section, σ_p.[1]

In the remaining sections our σ_p is equal to the σ_F of Aleklett et al. The approach will be to vary the exponent in the expression for projectile fragments of Z≥ 2 (A≥4) $\sigma_p(A) \cong 3.6A^{\varepsilon}$, and which Aleklett et al found numerically equal to 0.387. In principle one could also vary the coefficient (equal to 3.6), but any qualitative effect due to the variation of this coefficient can be subsumed by a variation of the exponent's value. Variations of the coefficient K, in a more general context, are considered in section 10-2. Starting with a broad coverage of the variational phase-space, variations of increasing resolution will be presented. Akin to the exploration of Λ, both uniform and subpopulations are investigated. *E_p is taken to be 140 MeV.*

[1] Chapter 11 will present models in which the shower particles have an enhanced production cross-section.

A uniform population with the exponent, ε, ranging from [0.001 – 10] is shown below:

Figure 9.1a R_0 vs. Exponent ε of σ_p (E_p=140 MeV)

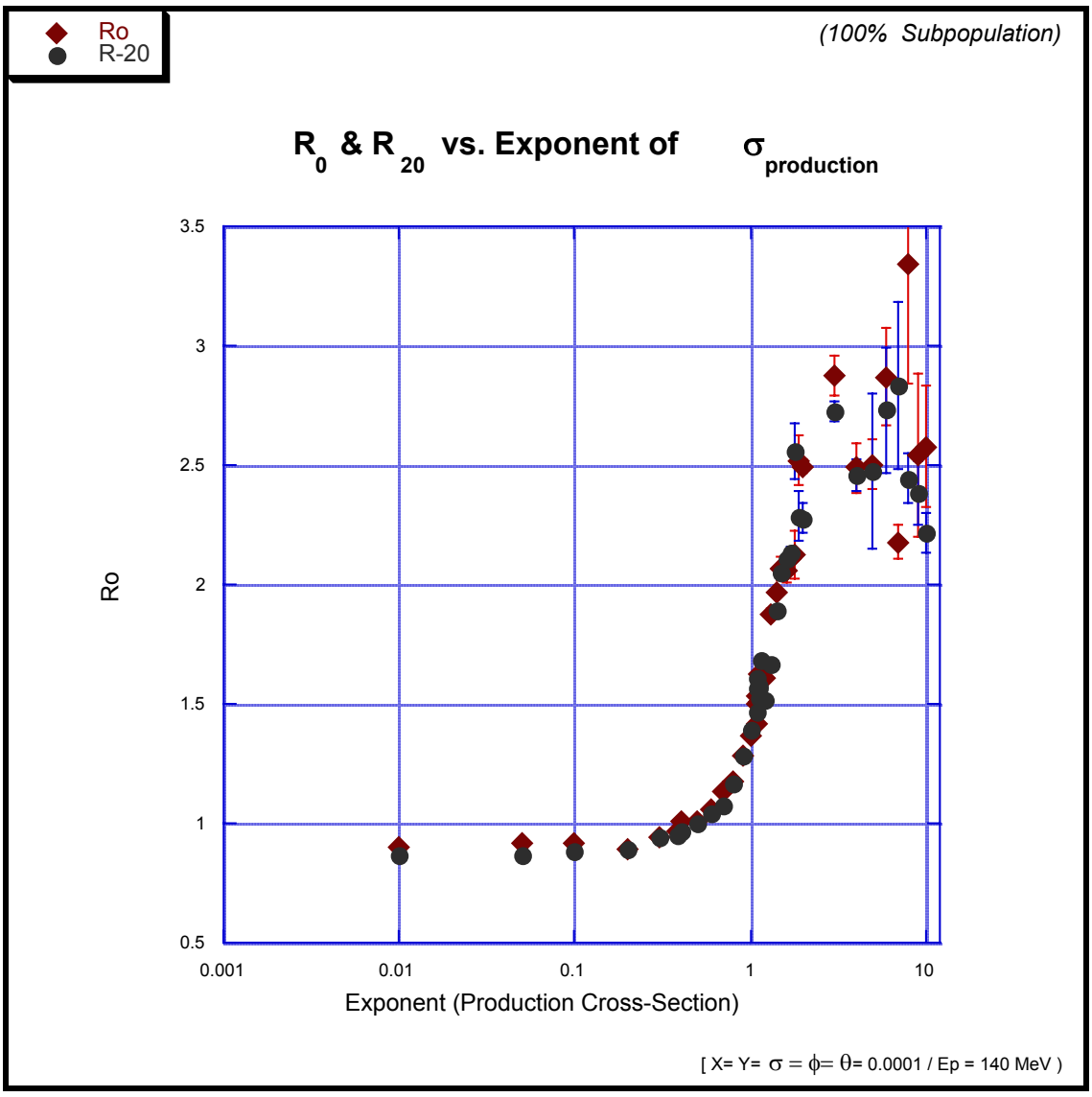

Figure 9.1b R_0 vs. Exponent ε of σ_p (E_p=140 MeV)

(100% Subpopulation)

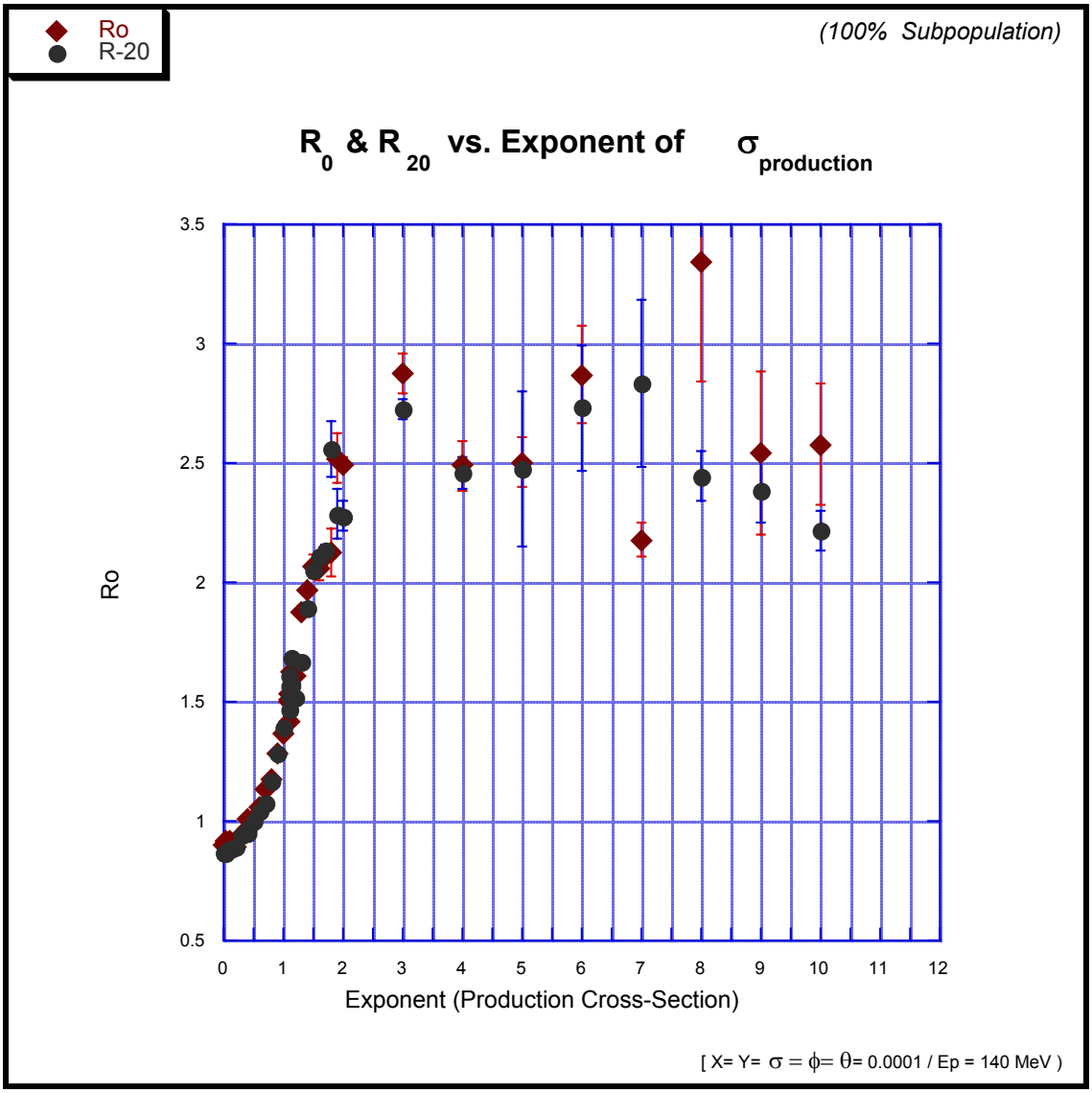

For the first time in these simulations, R_0 (and R_{20} for that matter) easily broach a value of 1.50. For populations of secondaries *all* having the same value of ε the interesting region to explore is ε = [1 - 2]. Numerical values are in the table below, with the conventional experimental value for ε=0.387 highlighted.

Table 9.1 R_0 vs. Exponent ε of σ_p (E_p=140 MeV)

(100% Subpopulation)

ε	Ro	Ro Errors	R-20	R-20 Errors
0.01	0.9013	0.0004	0.865	0.0008
0.05	0.913	0.001	0.8697	0.0005
0.1	0.9129	0.0008	0.882	0.0006
0.2	0.8944	0.0007	0.8942	0.0006
0.3	0.9461	0.0007	0.9397	0.0005
0.387	***0.9637***	***0.0006***	***0.9514***	***0.0008***
0.4	1.0095	0.0022	0.9711	0.0009
0.5	1.009	0.0005	0.9968	0.0007
0.6	1.0608	0.0012	1.0434	0.0012
0.7	1.1369	0.0011	1.0772	0.001
0.8	1.1765	0.0016	1.1638	0.0019
0.9	1.282	0.0023	1.2808	0.0035
1.0	1.3681	0.003	1.39	0.003
1.1	1.4976	0.006	1.5679	0.0062
1.11	1.5089	0.0043	1.527	0.0072
1.12	1.5075	0.0044	1.5742	0.0067
1.13	1.6282	0.0089	1.5664	0.0059
1.15	1.6213	0.0205	1.6874	0.0111
1.2	1.6098	0.0168	1.5168	0.0098
1.3	1.8779	0.0233	1.6629	0.014
1.4	1.9674	0.0072	1.8888	0.0126
1.5	2.068	0.0472	2.0493	0.0099
1.6	2.0555	0.0446	2.1089	0.0178
1.7	2.1086	0.0097	2.1338	0.0218
1.8	2.1287	0.1001	2.5579	0.1139
1.9	2.5209	0.1018	2.2858	0.1047
2	2.4958	0.027	2.2787	0.0595
3	2.875	0.0846	2.7253	0.0422
4	2.4885	0.1031	2.4585	0.0701
5	2.503	0.1037	2.4751	0.328
6	2.8682	0.2046	2.7316	0.2622
7	2.1788	0.0691	2.8336	0.3499
8	3.3451	0.5042	2.4455	0.104
9	2.5425	0.3396	2.3856	0.1328
10	2.5795	0.2507	2.2174	0.0871

Note that the computational errors quoted above are likely to be less than the true errors.

9.2 **Subpopulations of the Production Cross-Section**

The next broad sweep is to investigate which regions of phase-space might contribute a value of $R_0 \sim 1.5$, but having only subpopulations of an elevated ε. The results are first shown in consecutive sweeps by percentage of subpopulation. Only R_0 will be treated in this section; the critical role of R_{20} will be discussed later.

Figure 9.2a R_0 vs. Exponent ε of σ_p

(90% Subpopulation)

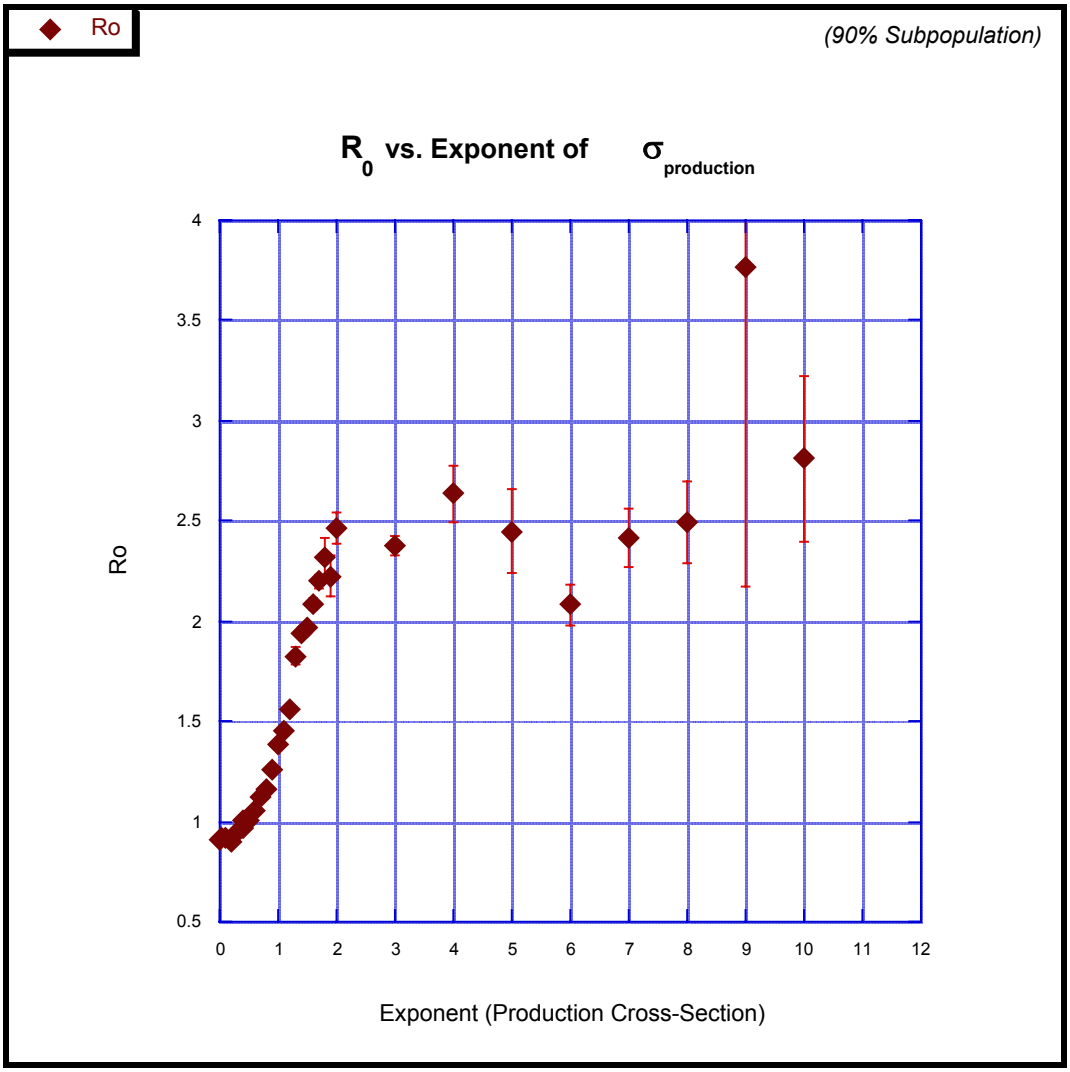

Figure 9.2b R_0 vs. Exponent ε of σ_p

(80%Subpopulation)

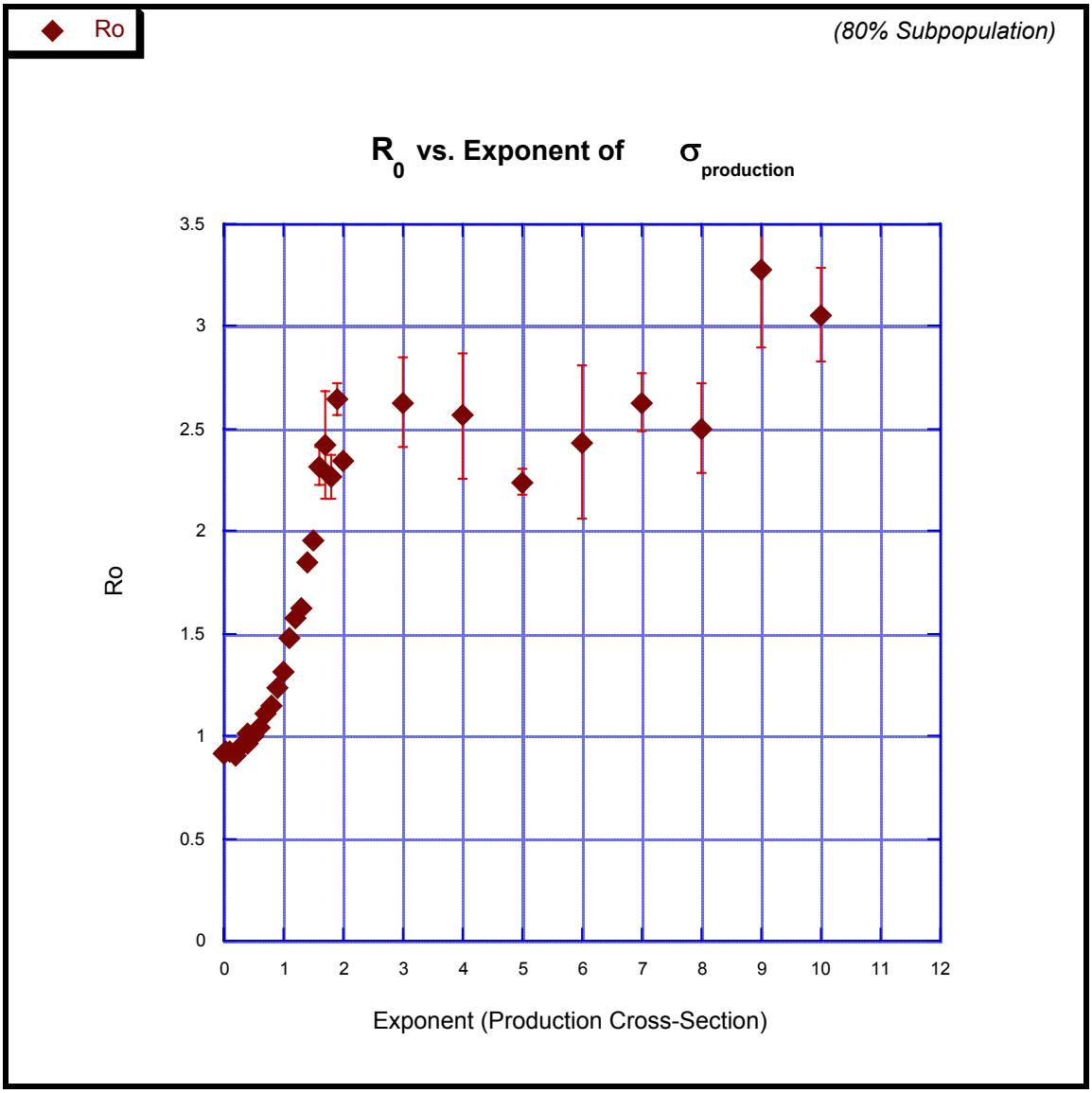

Figure 9.2c R_0 vs. Exponent ε of σ_p

(70%Subpopulation)

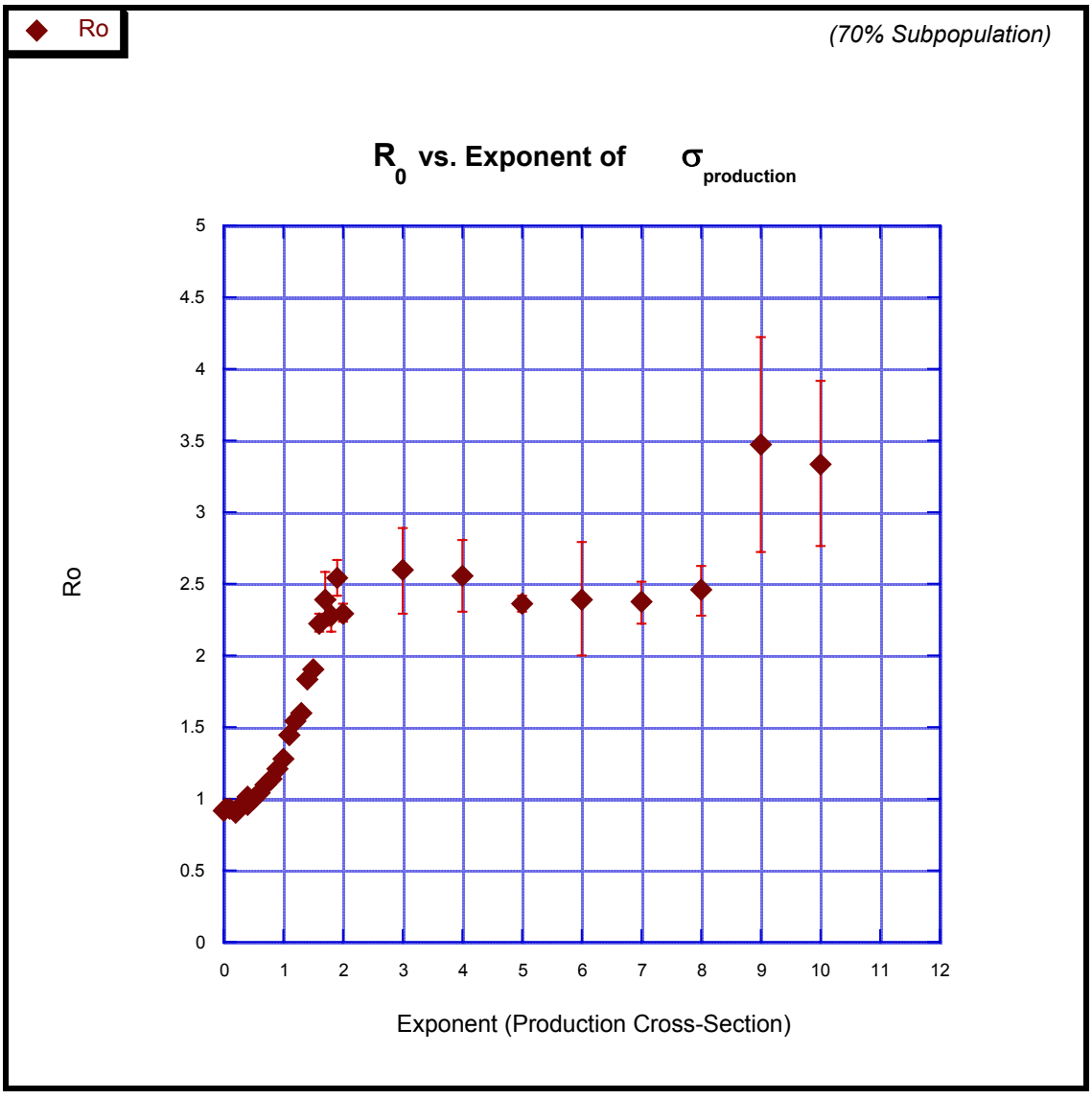

Figure 9.2d R_0 vs. Exponent ε of σ_p

(60%Subpopulation)

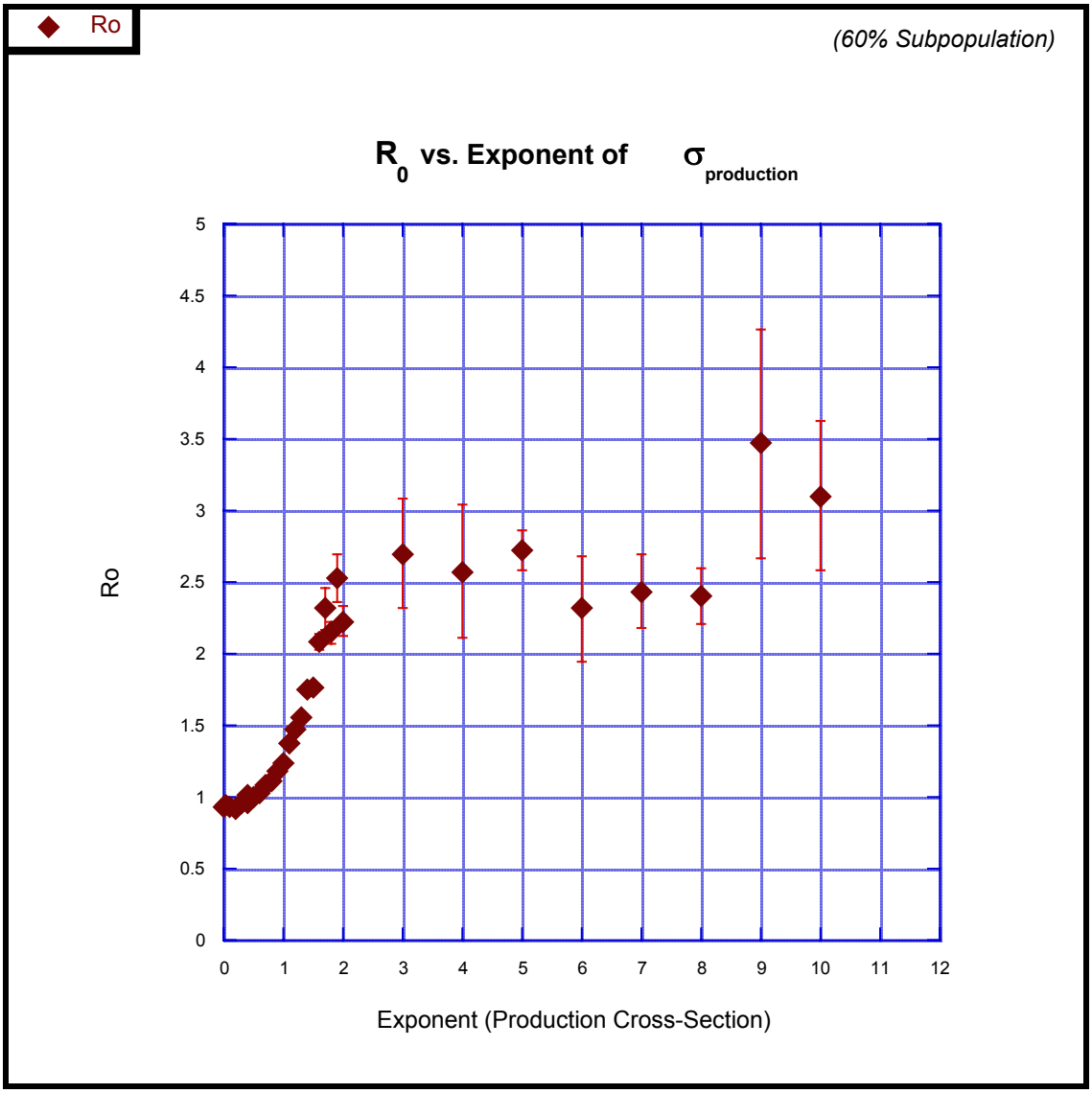

Figure 9.2e R_0 vs. Exponent ε of σ_p

(50%Subpopulation)

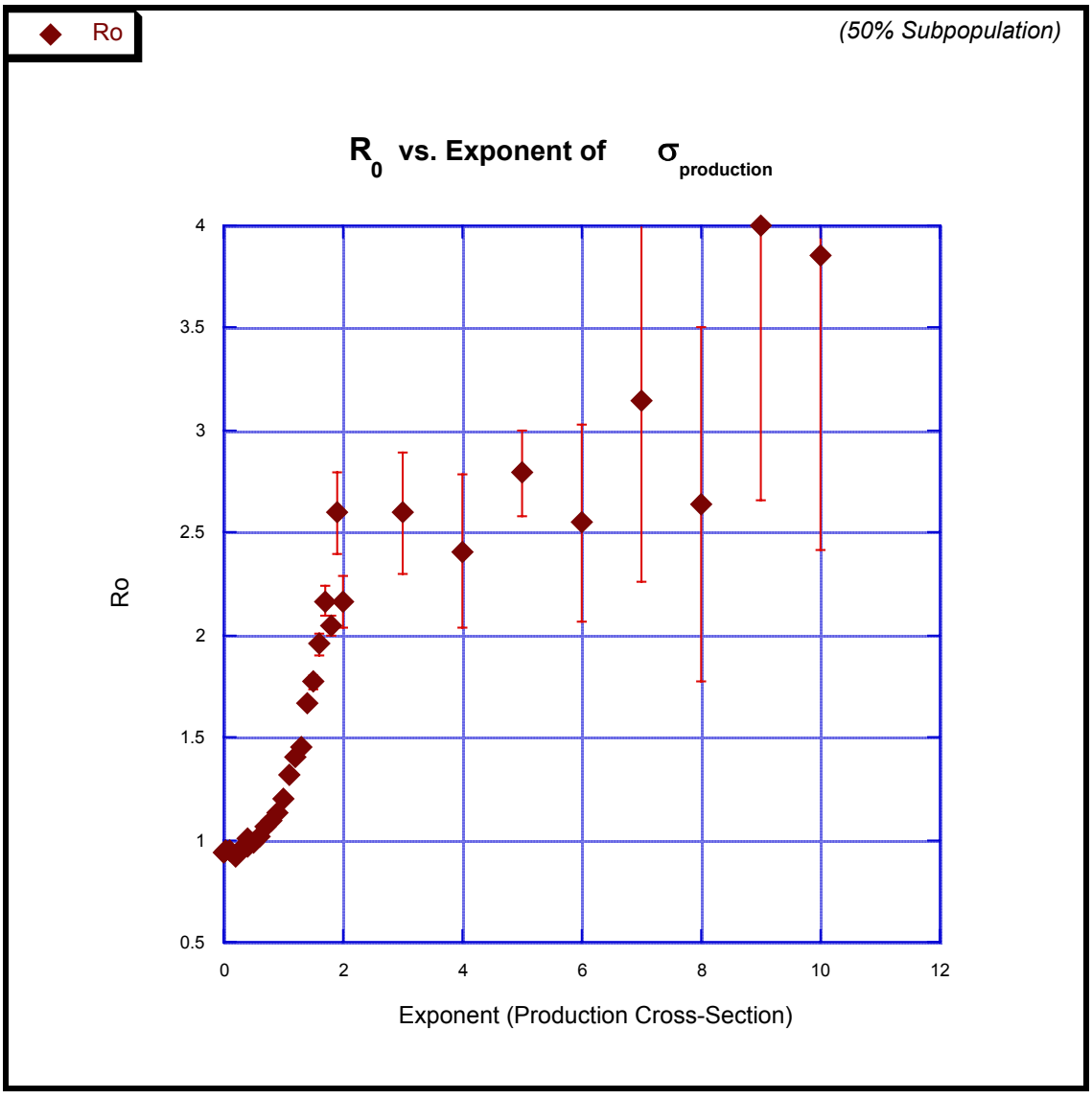

Figure 9.2f R_0 vs. Exponent ε of σ_p

(40%Subpopulation)

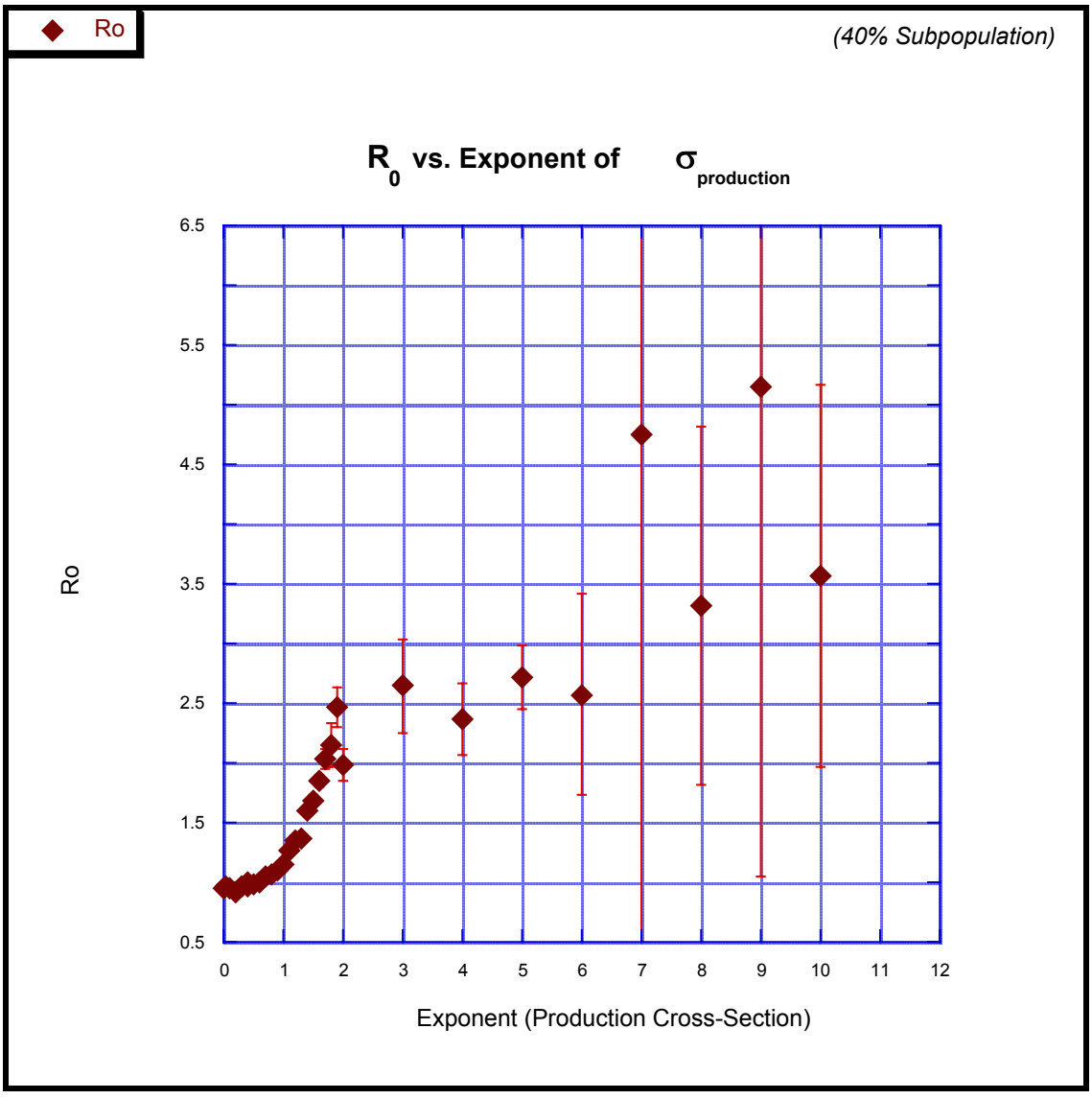

Figure 9.2g R_0 vs. Exponent ε of σ_p

(30%Subpopulation)

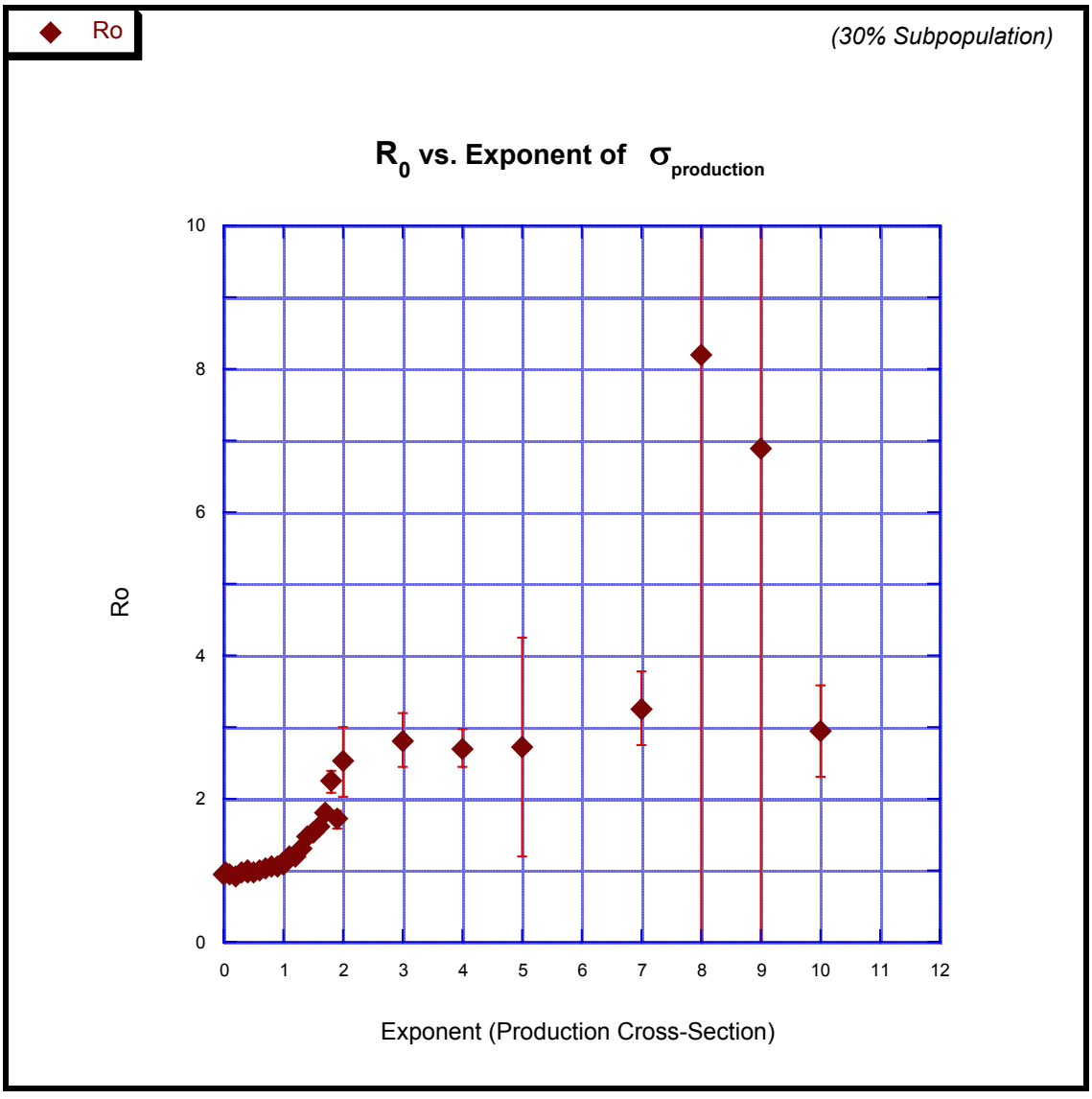

Figure 9.2h R_0 vs. Exponent ε of σ_p

(20%Subpopulation)

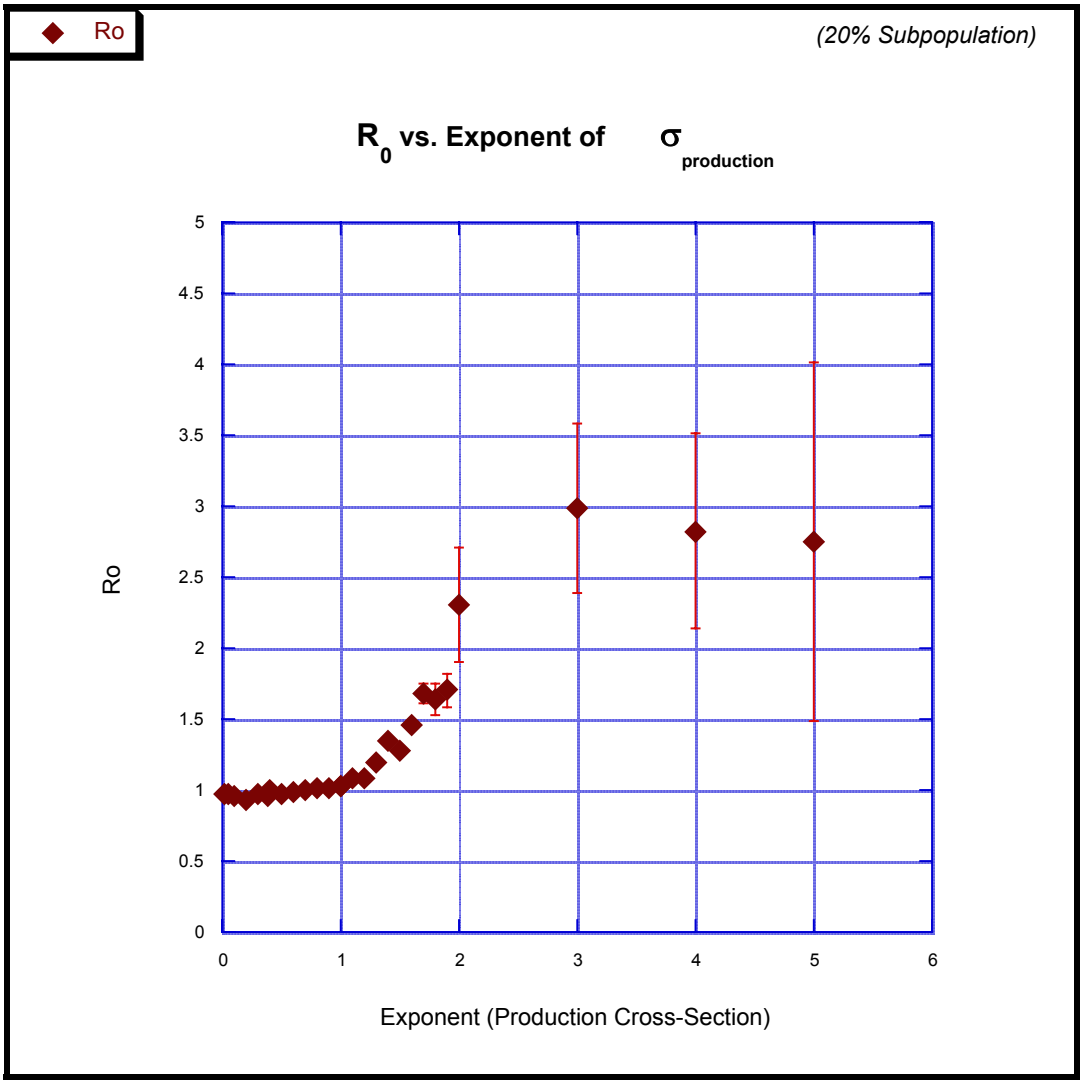

As seen in all the graphs above, there is a steep, almost linear rise between the R_0 values of 1 and 2, reaching a well-defined asymptotic value of $R_0 \sim 2.5$ for the larger percentage subpopulations and an asymptotic value between 2.5 and 3.0 for the smaller percentages of subpopulations. The variation in the latter asymptotic values is almost certainly due to greater statistical uncertainties as opposed to any true change in asymptotic value for different subpopulations.

But at or below a 10% subpopulation there is no chance of $R_0 > 1$ regardless of the ε–value, i.e the enhancement of σ_p.

Figure 9.2i R_0 vs. Exponent ε of σ_p

(10%Subpopulation)

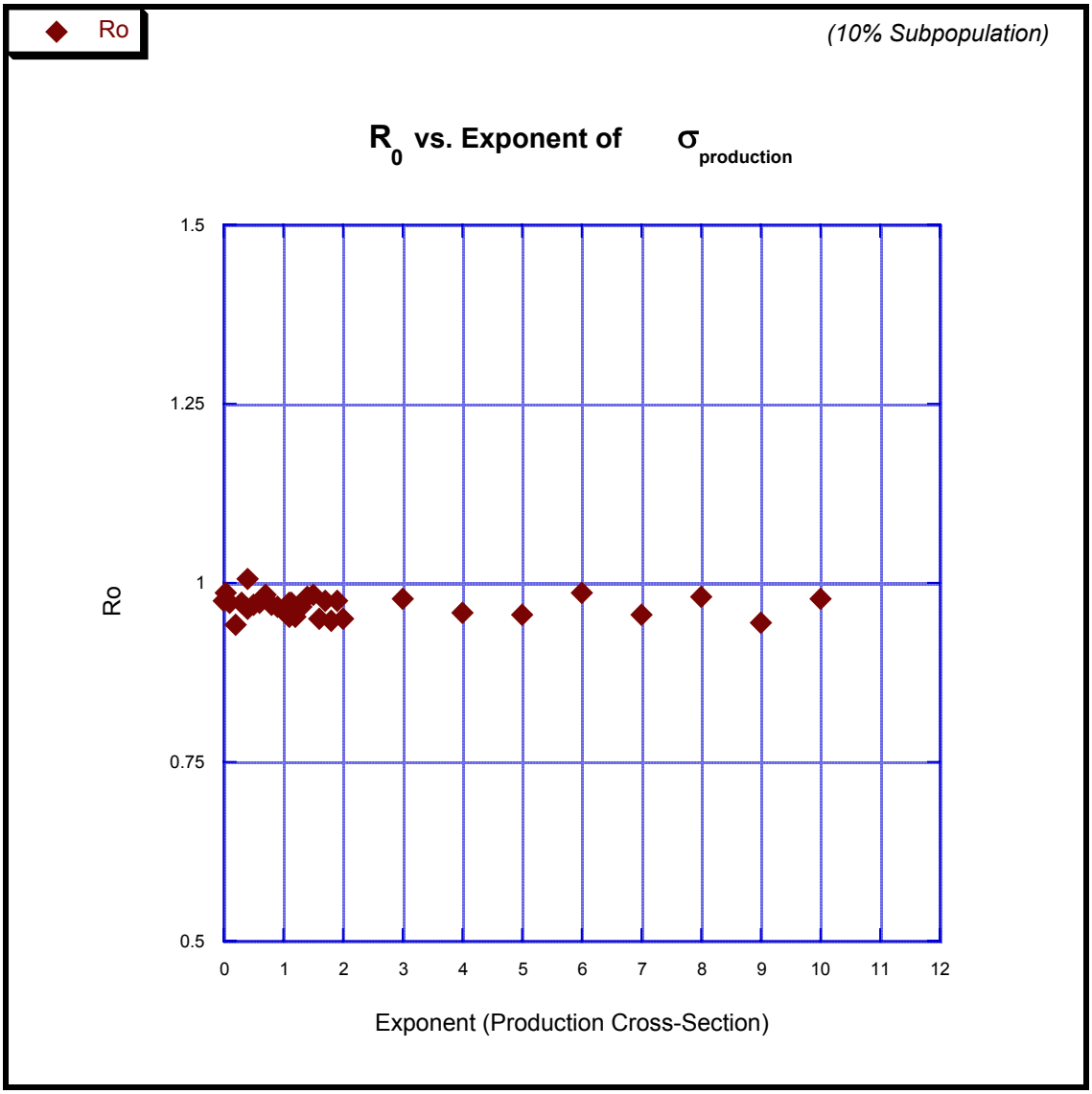

So what we have is the possibility for subpopulations only as low as 11%, with ε values in the range [1.7- 1.9], offering possible fits to an $R_0 = 1.5$. It must be noted that as before the $N^{-1/2}$ computational errors are likely to be gross underestimates. The errors of the true 'correspondence to nature' are likely to be much greater; but unlike the previous sets of simulations here we are in unknown territory: there is little physical reference from which to properly guide or estimate these errors. Hence these values on production cross-section are best used as a qualitative guide to that region of phase-space needing to be further explored, rather than as an exact quantitative measure.

The results shown in Figures 9.2 are a simulation of our canonical pencil-beam (X=Y= $\sigma = \theta = \phi = 0.0001$). The results are robust being essentially the same for variations of the basic beam parameters: for example the following three higher resolution studies in Figure 9.3 have the geometric distribution of the beam across the face of the front-target consecutively broadened (σ_{beam} = 0.0001, 1, 2).

Figure 9.3a R_0 vs. Exponent ε of σ_p

(σ_{beam} = 0.0001)

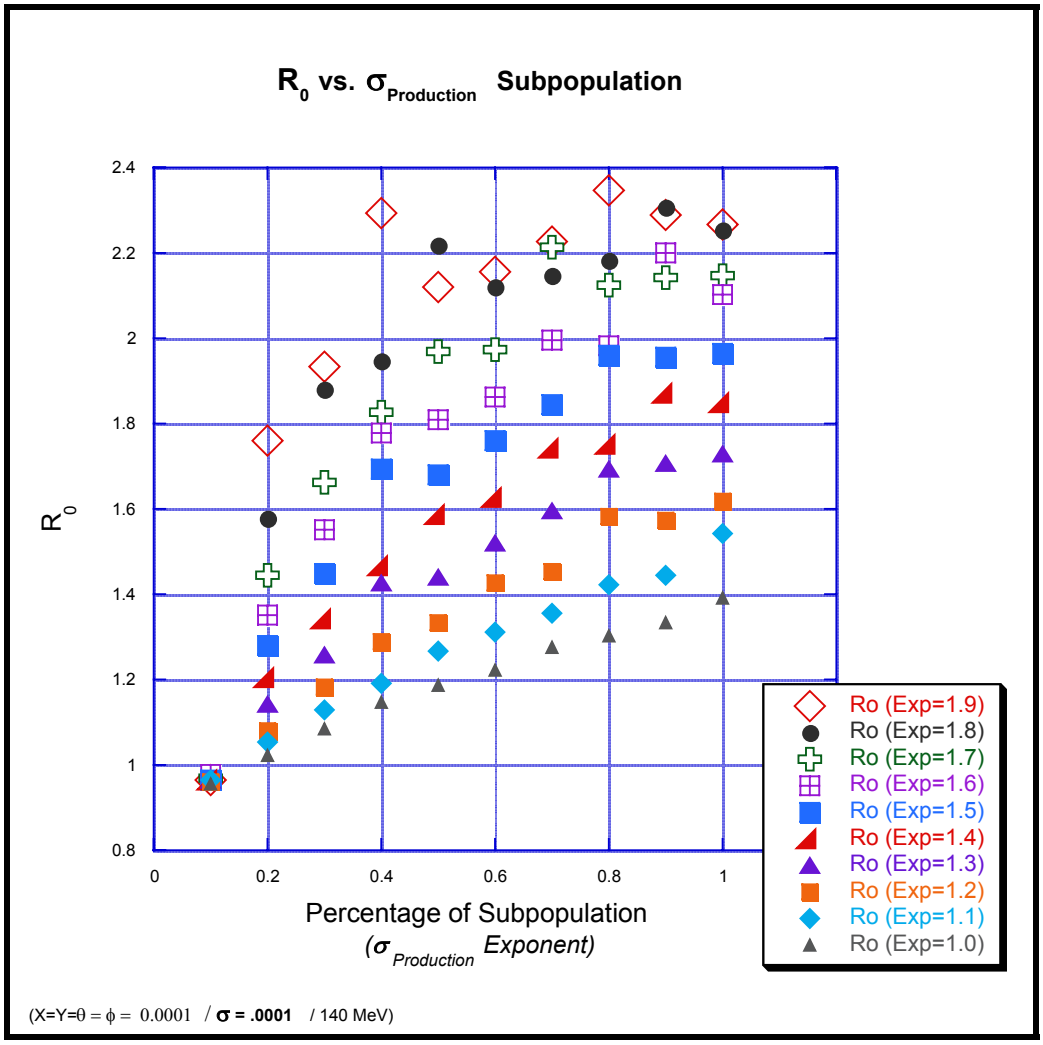

Figure 9.3b R_0 vs. Exponent ε of σ_p

(σ_{beam} = 0.0001)

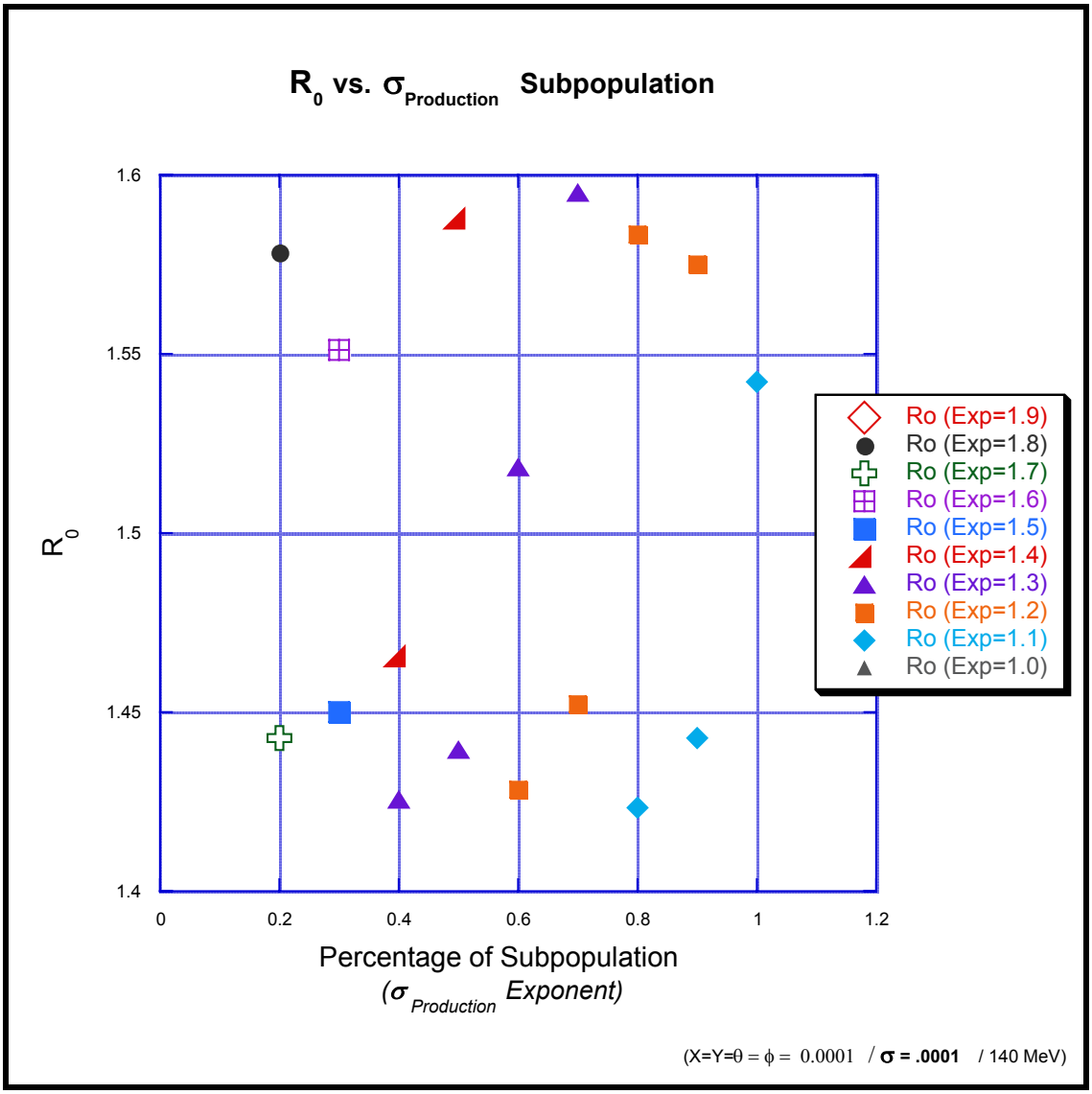

Figure 9.3c R_0 vs. Exponent ε of σ_p

(σ_{beam} = 1)

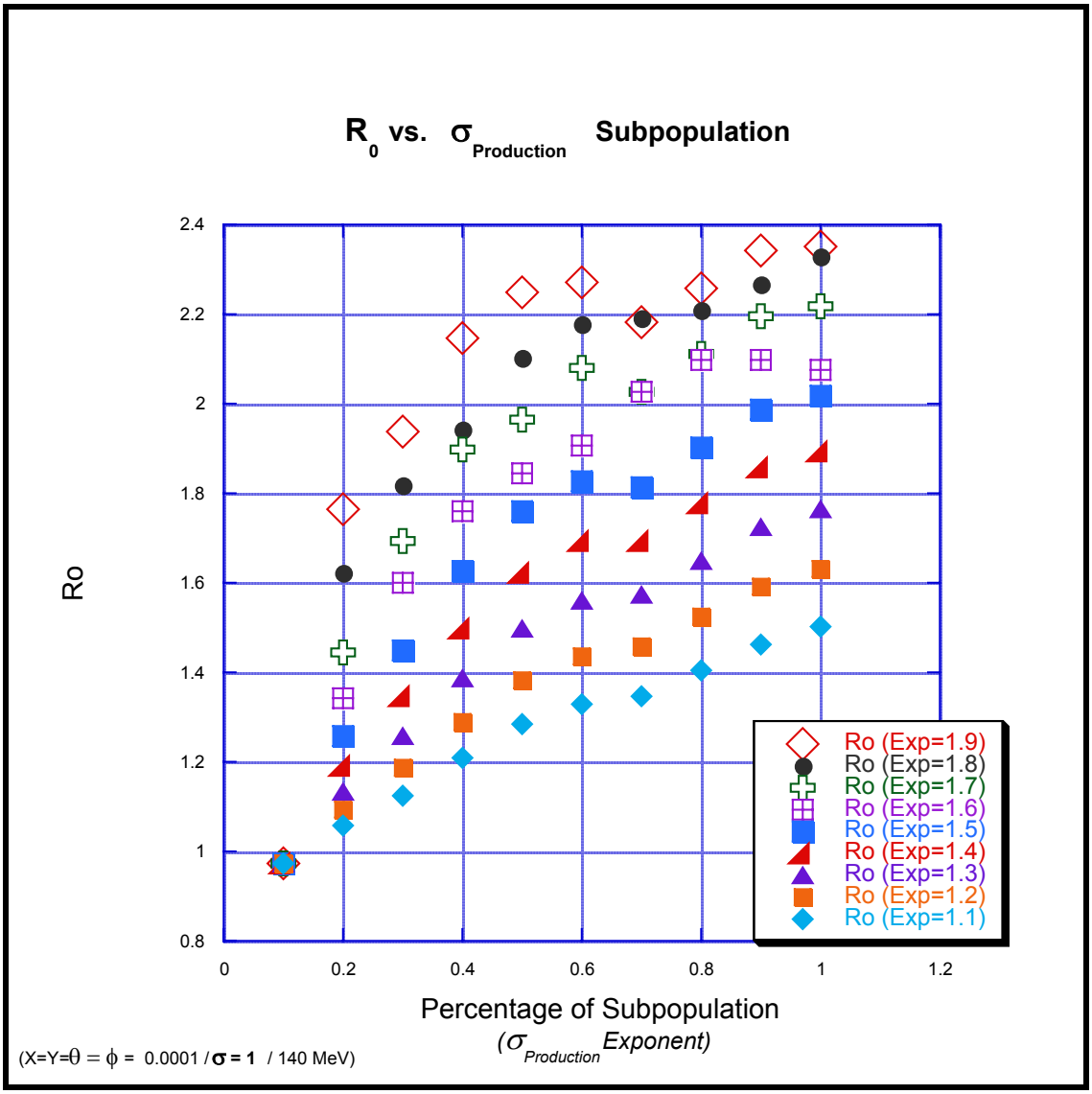

Figure 9.3d R_0 vs. Exponent ε of σ_p

(σ_{beam} = 0.0001)

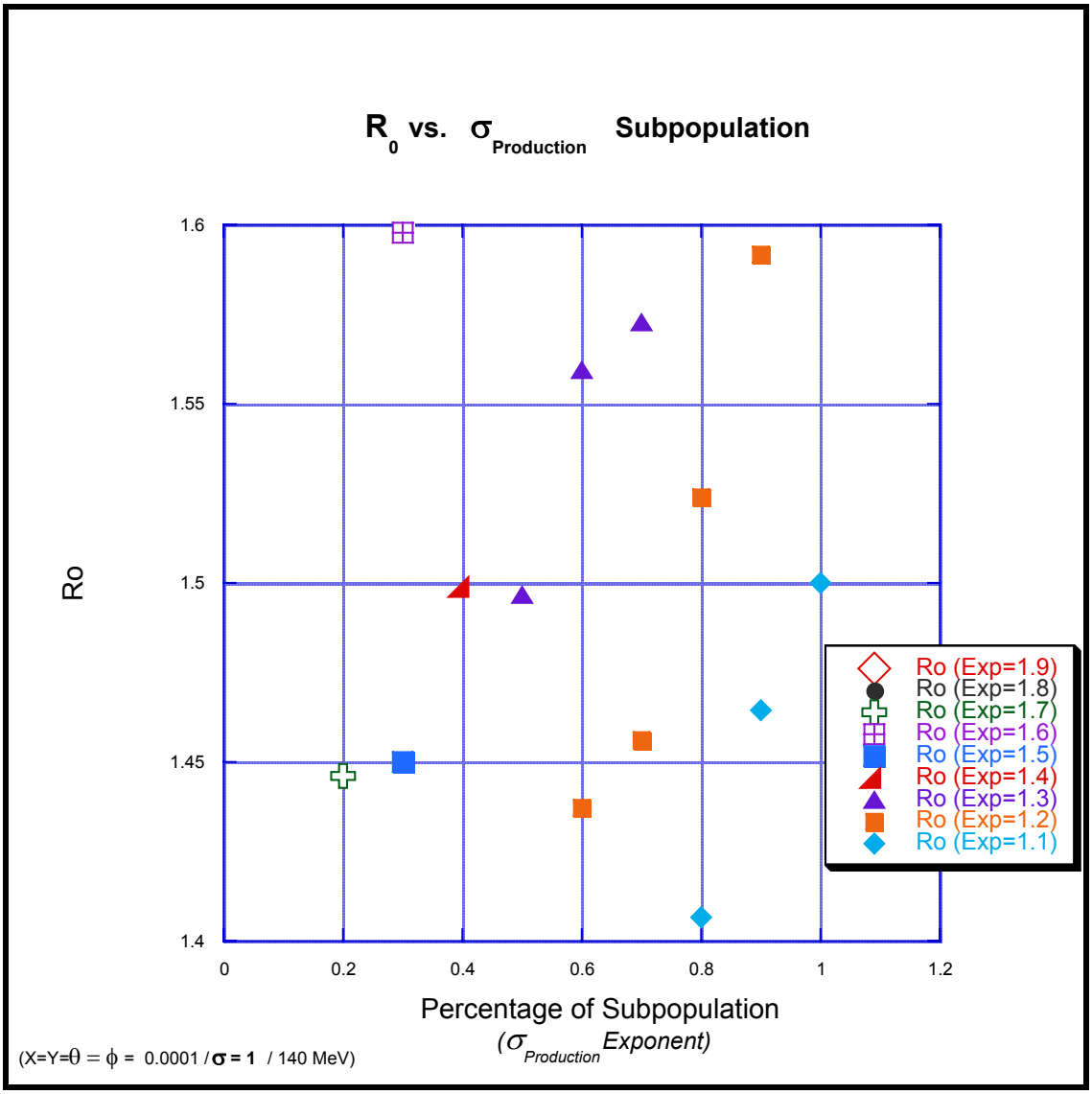

Figure 9.3e R_0 vs. Exponent ε of σ_p

(σ_{beam} = 2)

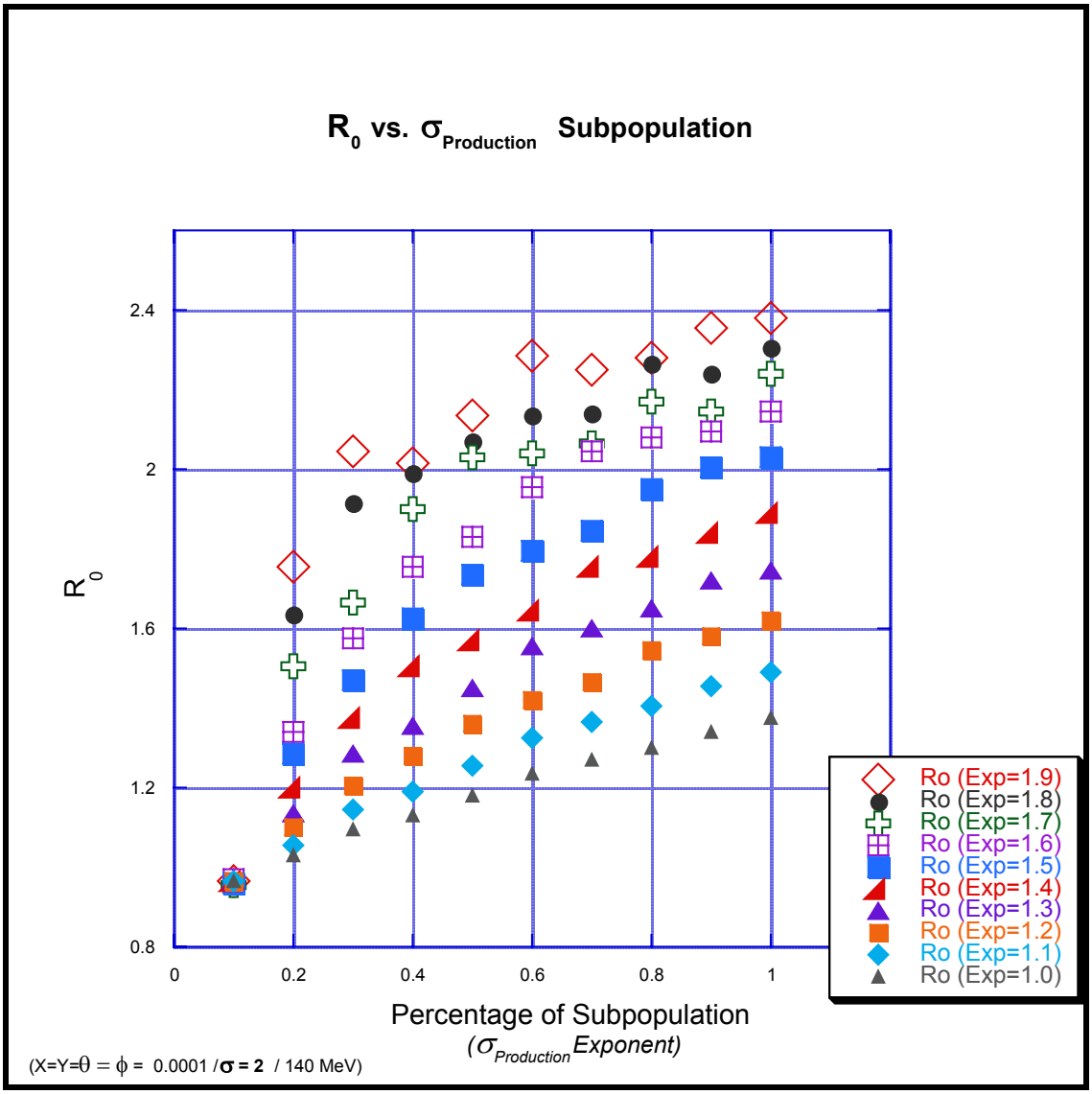

Figure 9.3f R_0 vs. Exponent ε of σ_p
(σ_{beam} = 2)

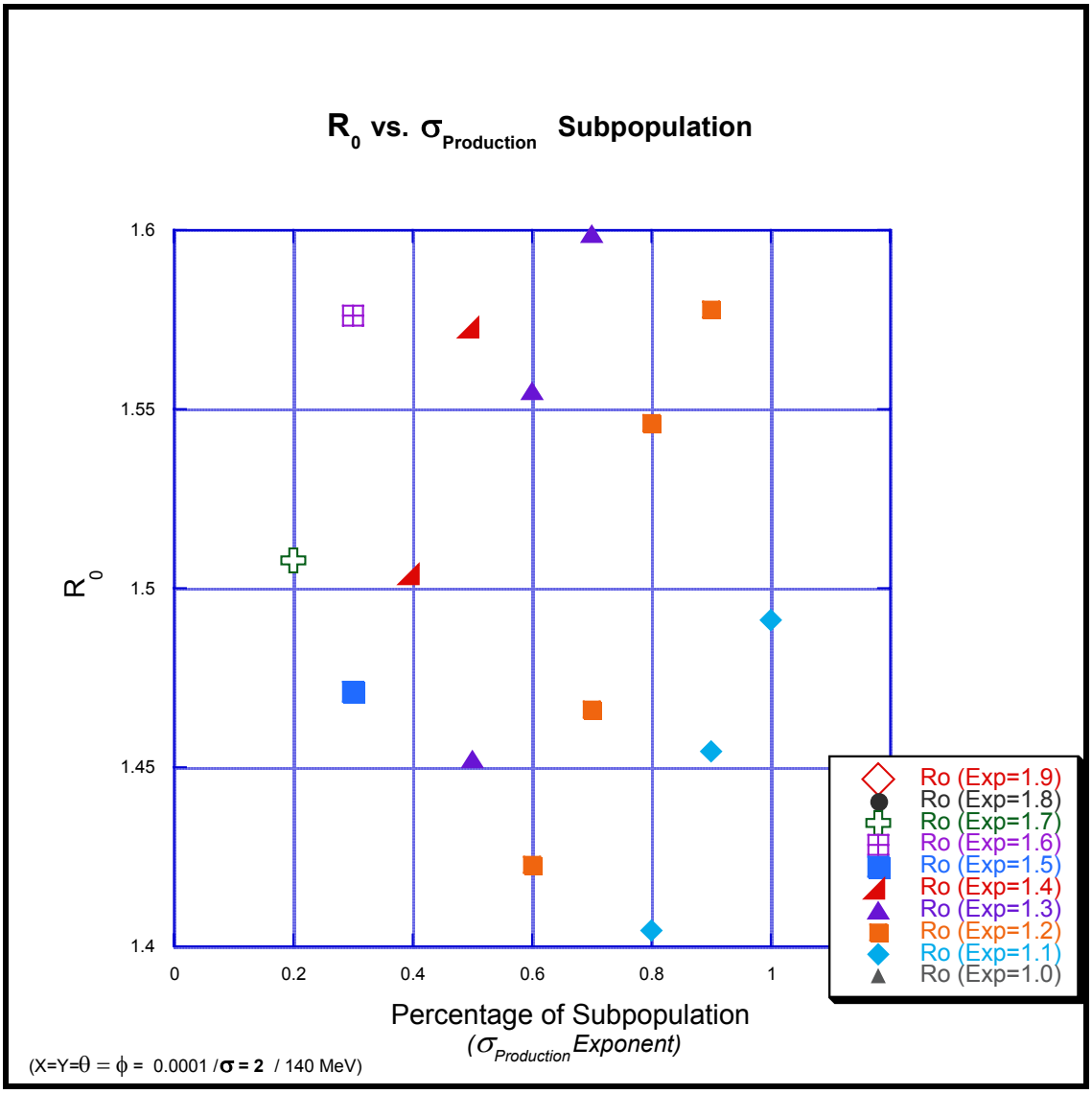

9.3 $\underline{R_{20}}$

We consider now the previously neglected R_{20}, recalling from chapter 5 the experimental set-up and results.

Figure 9.4 Experimental Setup for Copper Calorimetry Experiments

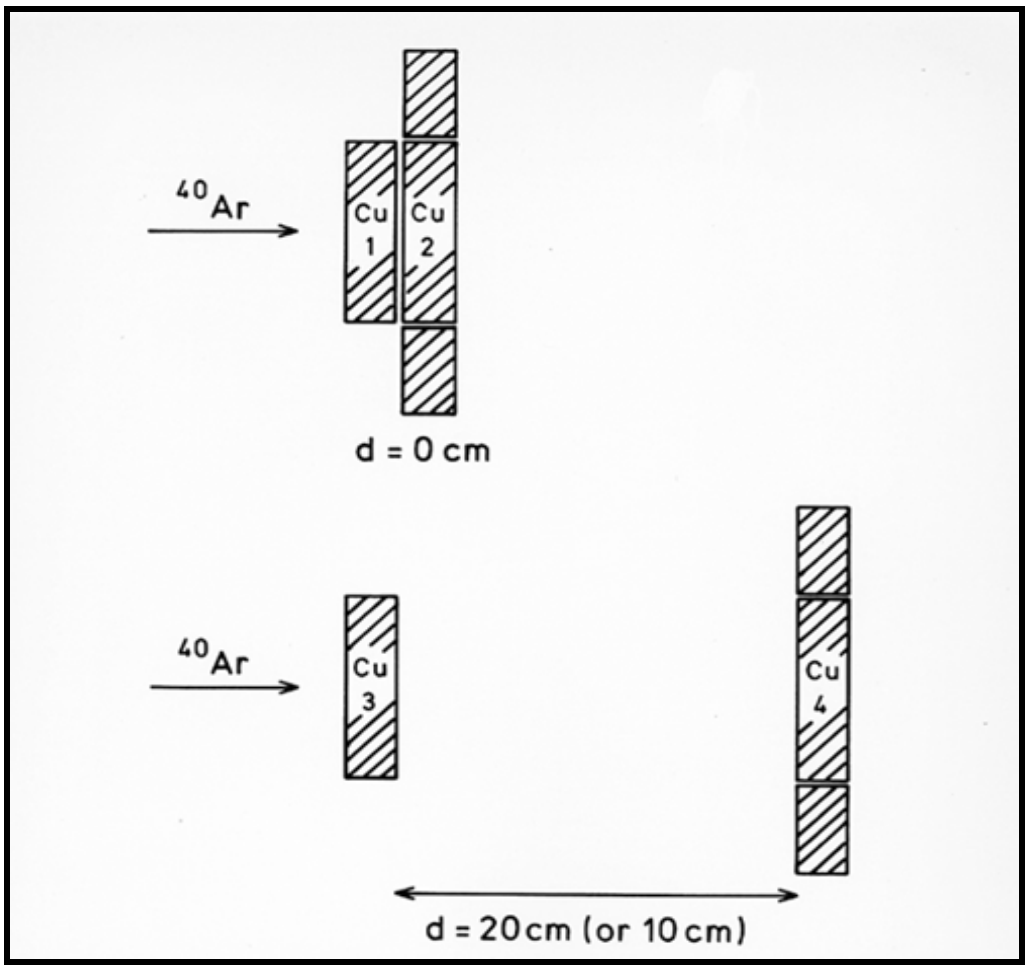

And recalling as well that the values listed below are averages of three separate experiments for R_0 and two separate experiments for R_{20}.

Table 9.2 Experimental Values of R_0 (LBL 1987)

	0.9 A GeV ^{40}Ar	1.8 A GeV ^{40}Ar
R_0	1.167 ± 0.011	1.501 ± 0.008
$R_{ring,0}$	< 0.01	< 0.01
R_{10}	1.118 ± 0.020	1.373 ± 0.034
R_{20}	1.102 ± 0.026	1.251 ± 0.020
$R_{ring,20}$	0.039 ± 0.002	0.071 ± 0.005

Figure 9.5 Experimental Values of R_0 (LBL, 1987)

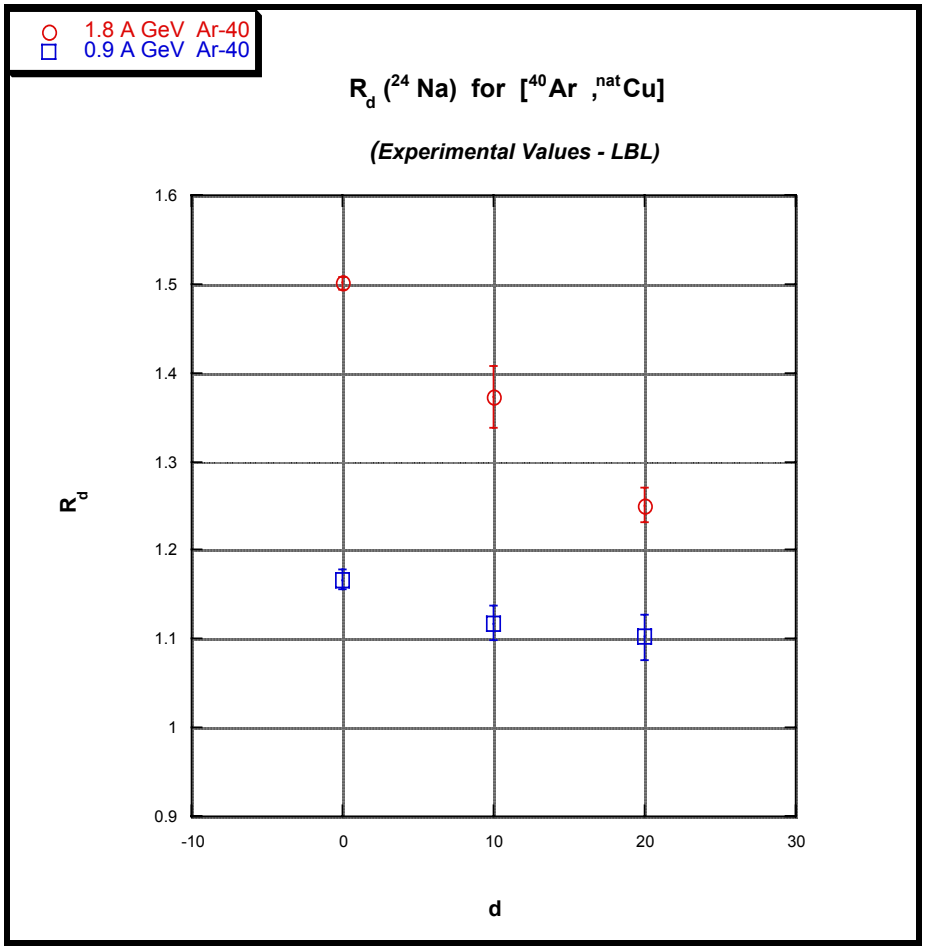

The results displayed in Figure 9.1 and Table 9.41 show that there is little computed difference between the values of R_0 and R_{20}. But that was for our canonical 'pencil-beam' with a geometric dispersion $\sigma_{beam} = 0.0001$. More realistic values of σ_{beam} continue to show little difference in computed values, for example $\sigma_{beam} = 2$:

Figure 9.6 R_0 vs. R_{20}

($\sigma_{beam} = 2$)

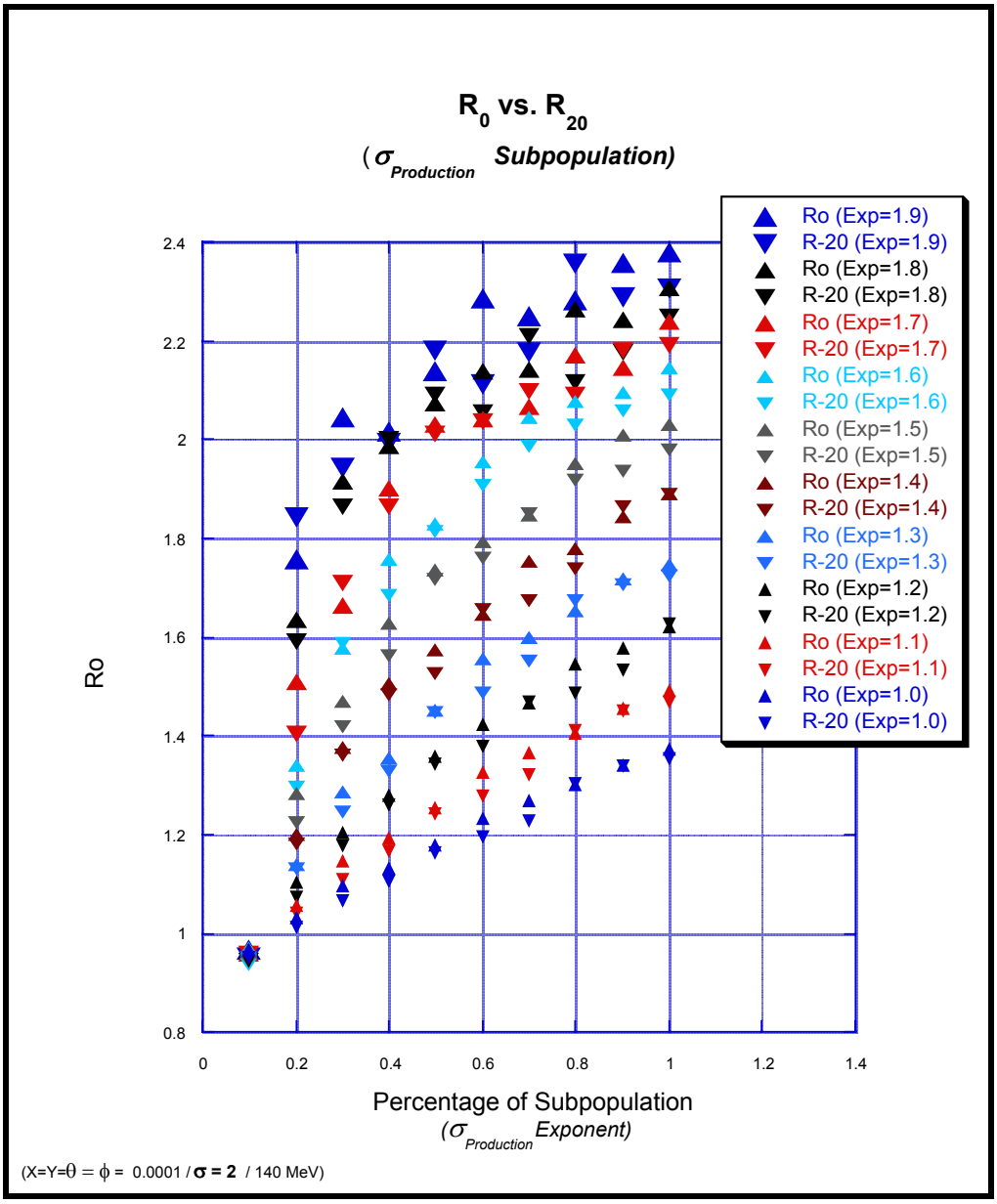

And for an arbitrary subset (ε = 1.7-1.9) of the above:

Table 9.2 R_0 vs. R_{20}

(σ_{beam} = 2)

Percentage (100% = 1.0)	Exponent ε	Ro	Ro Error	R-20	R-20 Error
0.1	1.9	***0.966***	0.0001	***0.9522***	0.0001
0.2	1.9	***1.7577***	0.0319	***1.8417***	0.027
0.3	1.9	***2.0442***	0.02	***1.9428***	0.0074
0.4	1.9	***2.0172***	0.012	***1.995***	0.0211
0.5	1.9	***2.1366***	0.012	***2.1813***	0.0056
0.6	1.9	***2.2855***	0.0128	***2.1115***	0.0088
0.7	1.9	***2.2512***	0.0142	***2.1789***	0.0062
0.8	1.9	***2.2812***	0.0075	***2.3576***	0.0072
0.9	1.9	***2.3562***	0.0052	***2.2899***	0.0037
1	1.9	***2.3781***	0.0077	***2.3075***	0.0092
0.1	1.8	***0.9667***	0	***0.9446***	0.0001
0.2	1.8	***1.6359***	0.0047	***1.5916***	0.004
0.3	1.8	***1.9157***	0.0114	***1.8652***	0.0135
0.4	1.8	***1.9887***	0.0089	***2***	0.0165
0.5	1.8	***2.0726***	0.0092	***2.0899***	0.0085
0.6	1.8	***2.1364***	0.0057	***2.0548***	0.0066
0.7	1.8	***2.1412***	0.0103	***2.2096***	0.0062
0.8	1.8	***2.2634***	0.0071	***2.1166***	0.0049
0.9	1.8	***2.2414***	0.0088	***2.1777***	0.0059
1	1.8	***2.3056***	0.0084	***2.2493***	0.0052
0.1	1.7	***0.9573***	0.0002	***0.9596***	0
0.2	1.7	***1.5077***	0.008	***1.4038***	0.0046
0.3	1.7	***1.6646***	0.0038	***1.7114***	0.0064
0.4	1.7	***1.9001***	0.0044	***1.8645***	0.0077
0.5	1.7	***2.0296***	0.0106	***2.0124***	0.007
0.6	1.7	***2.0422***	0.0066	***2.0388***	0.007
0.7	1.7	***2.067***	0.005	***2.0973***	0.0055
0.8	1.7	***2.1696***	0.0041	***2.0928***	0.0045
0.9	1.7	***2.1441***	0.0082	***2.1824***	0.0023
1	1.7	***2.2381***	0.0084	***2.1928***	0.0018

The experimental set-up is a straightforward and classic approach to the measurement of lifetime or time-of-flight. Assuming for the moment that the enhanced value of the production cross-section has physical meaning, the experimental results listed in Table 7.5 strongly suggest a partial decay of the enhanced production cross-sections that within the context of our approach uniquely explain the R_0 values. At 20 cm, the integrated activity ratios of the guard rings and the central block is $(R_{20} + R_{ring,20}) = 1.32 \pm 0.02$. This is about the same value as $R_{10} = 1.373 \pm 0.034$. Hence the time-scale for this hypothetical decay is no longer than [10 cm/c] = 10^{-9} seconds, and could be as short as 10^{-10} taking into account relativistic dilatation.

Is there an alternative explanation? An exploration of the simulation phase-space turned up the following: it is possible to get reasonably close to the experimental R_0, and R_{20} but not $R_{ring,20}$. This occurs in a few very narrow windows about (X=Y=1, σ_{beam}= 2 , θ = 3) and with large subpopulations of enhanced $\sigma_{production}$ such as ε=1.1 at 100%. But it's a very narrow window in phase-space; and depends on enough of the beam missing the rear block due to an off-set beam center coupled to a skewed angle at which the primary beam hits the initial target face. Needless to say, such beam-target misorientations are not likely to have occurred in *all* of the exposures done. And as one would expect this then throws the $R_{ring,20}$ values way off, making them an order of magnitude too large. And it still requires enhanced production cross-sections.

Hence, assuming that our fundamental approach is valid (a close shave perhaps by Occam's razor which demands that one always take the simplest explanations and reasonings that 'work') we are left with the idea that a percentage of the secondaries have an enhanced production cross-section analogous to a new channel in low-energy nuclear physics; and one that decays in reasonably short order.

One must now ask if this is merely a mathematical nicety or if further experimental evidence exists that corroborates this model-derived enhancement of the production cross-section for ^{24}Na. Such evidence does indeed exist and is presented next.

X On the Phenomenology and Calorimetry of Cylinders

It was mentioned earlier that a cylinder composed of similar copper blocks (Figure 10.1) could in principle act as a multi-stage amplifier capable of enhancing the signal of any unusual effects due to secondaries. Recalling the schematic of Figure 5.3 it is apparent that any block beyond the second will contain interactions due to two sources: the exponentially decreasing primary beam and the cascade of secondaries integrated from all preceding blocks.

Depending on the nature of the secondaries' cascade, blocks 3 to N will have an increasing ratio of secondaries to primaries. If there is any property or effect of the secondaries that is different from the primaries…such differences should be amplified by the increasing cascade of heavy secondaries. This is the amplifier part of the multiple stages.

Figure 10.1

Simulated Beam Transport through a Cylindrical Target

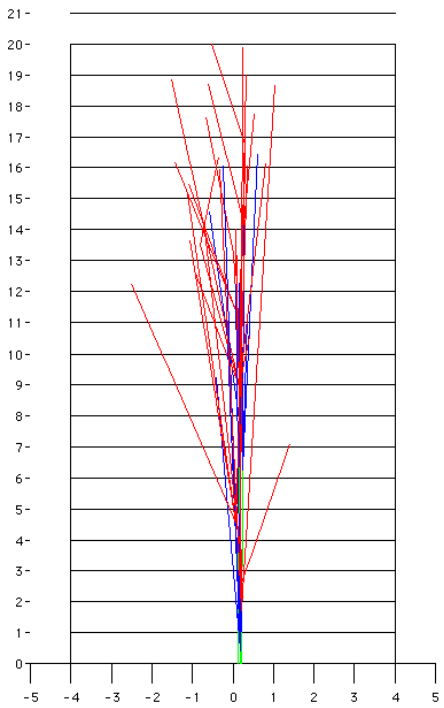

10.1 Experimental Results vs. Previous Models

Using LBL's 1.8 A GeV ^{40}Ar beam on a natural copper cylindrical target, similar experiments to the ones previously discussed have been performed (Haase 1990), the results being presented in Table 10.1 and Figure 10.2.

Table 10.1

^{24}Na R-values for 1.8 A GeV ^{40}Ar on a Cu-Cylinder

Block #	R-value	Error
1	1	
2	1.42	0.05
3	1.727	0.020
4	2.07	0.019
5	2.12	0.025
6	2.203	0.027
7	2.252	0.03
8	2.277	0.04
9	2.083	0.039
10	2.071	0.04
11		
12		
13		
14		
15		
16	1.639	0.033

In the cylinder geometry the (R_0,R_{20}) combination of the 2-block experiments is replaced by the concept of the R-value; where the $\mathbf{R_i}$ is the ratio of ^{24}Na in the *i-th* block to that of the 1st block. Hence Haase's R_2 value is equivalent to the R_0 value of the previous discussions. And it is numerically equal as well within the overlapping error bars (1.42 ± 0.05 vs 1.50 ± 0.008). It is also easy to see in Figure 10.2 that a cascade phenomena is present, peaking at a plateau in blocks [6-8].

Figure 10.2 R-values for 1.8 A GeV ^{40}Ar on a Copper Cylinder

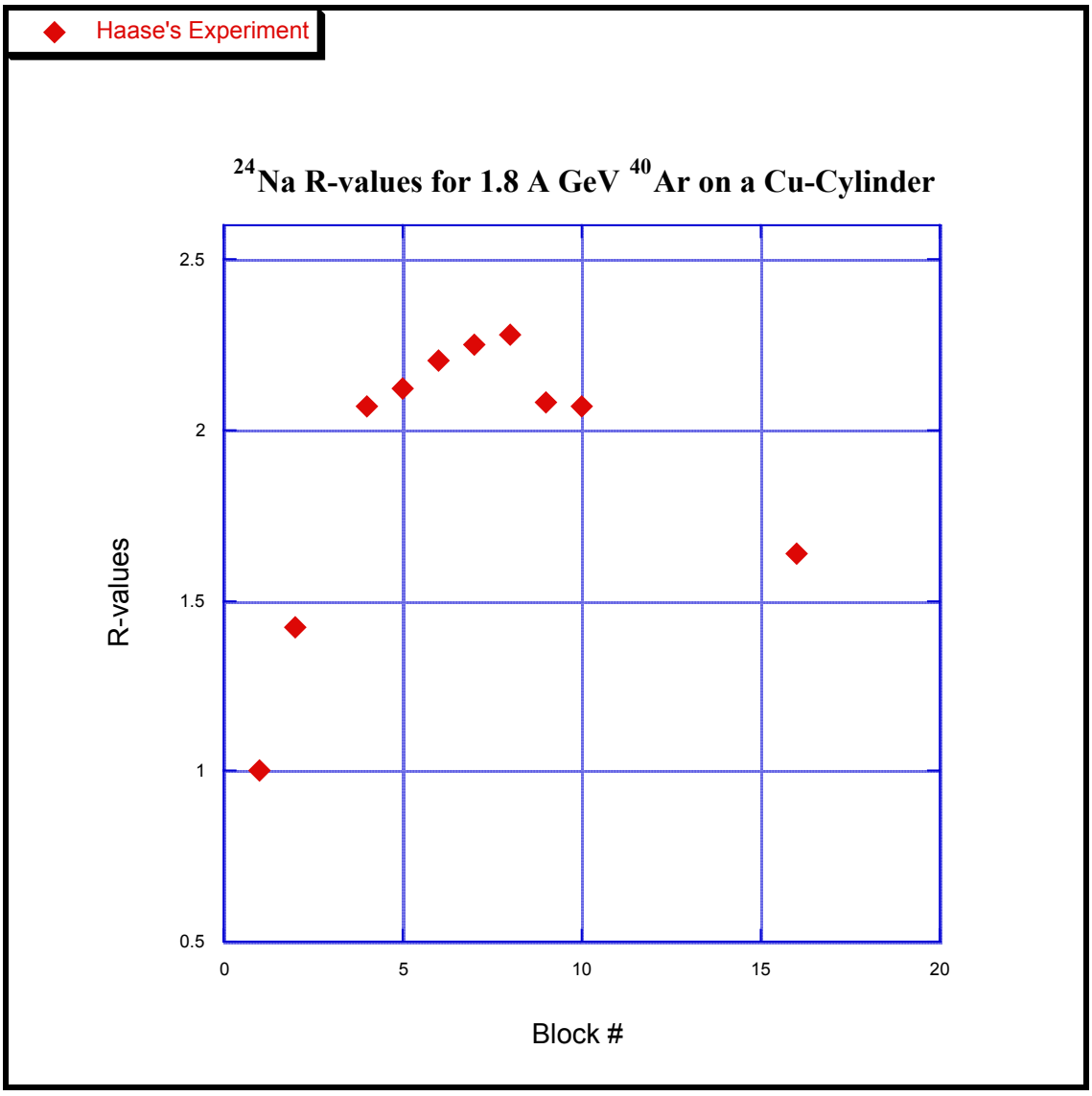

The obvious question now is how well do the previous models fit this data? Figure 10.3 answers this in principle for both models initially proposed by Aleklett et al – there is no fit. Exploring first the decreased mean free path model, the Λ-subpopulation shown has 100% of the secondaries set at their minimum possible mean free paths (Λ=3). After the initial rise to a value of R_0=1.28, as seen in the previous sets of simulations, the R-values drop off rapidly and monotonically.

Figure 10.3 Comparison of R-values between Models and Experiment

(1.8 A GeV ^{40}Ar on a Copper Cylinder)

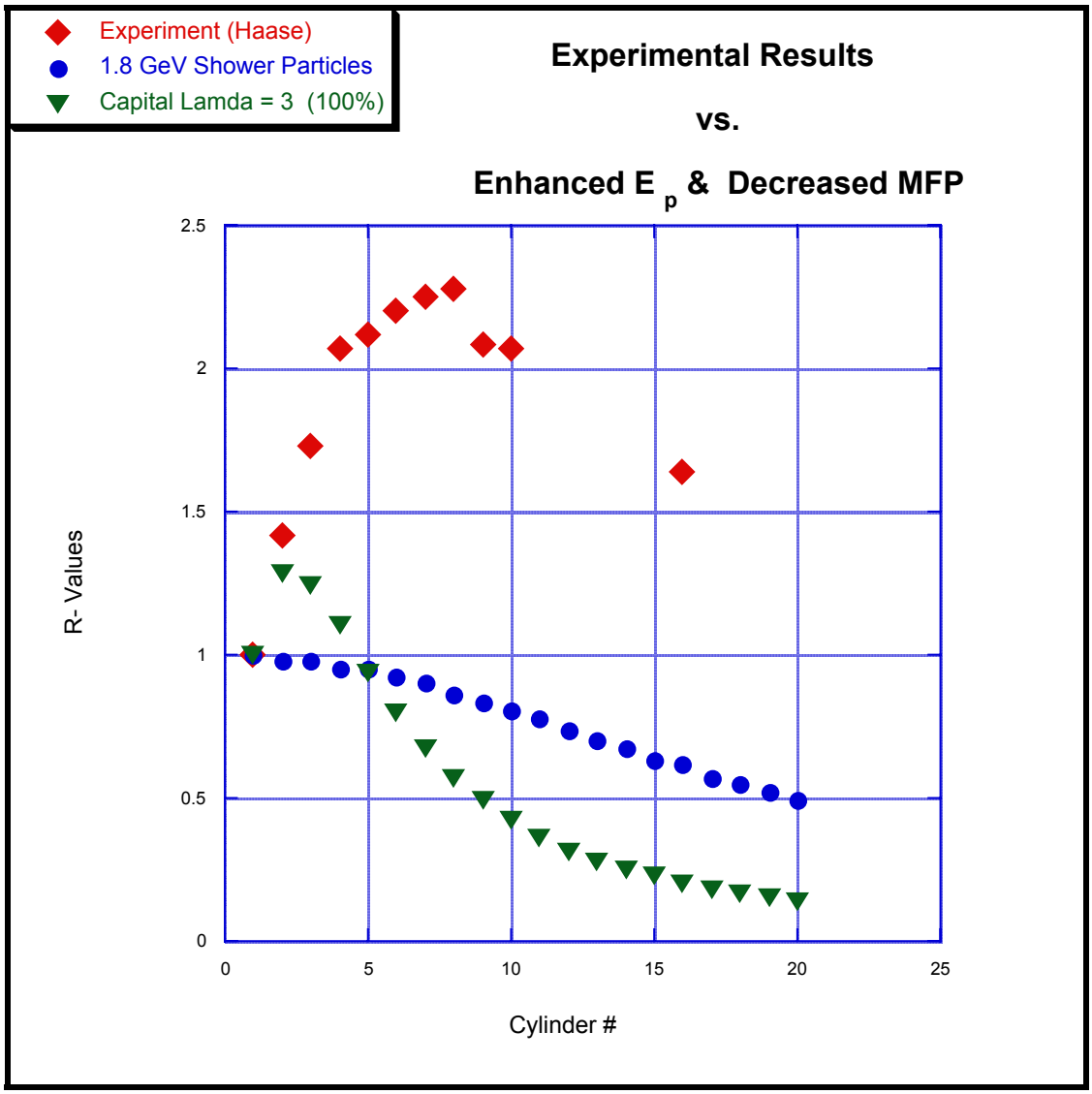

This is a powerful demonstration that decreased mean free path subpopulations cannot be the cause of the R_0 values in the two-block experiments. This is confirmed by a detailed studying of the R-values as a function of Λ, conclusively demonstrated in the successive graphs of Figure 10.4.

Figure 10.4a Experiment vs. Decreased Mean Free Path (Λ)

(1.8 A GeV ^{40}Ar on a Copper Cylinder)

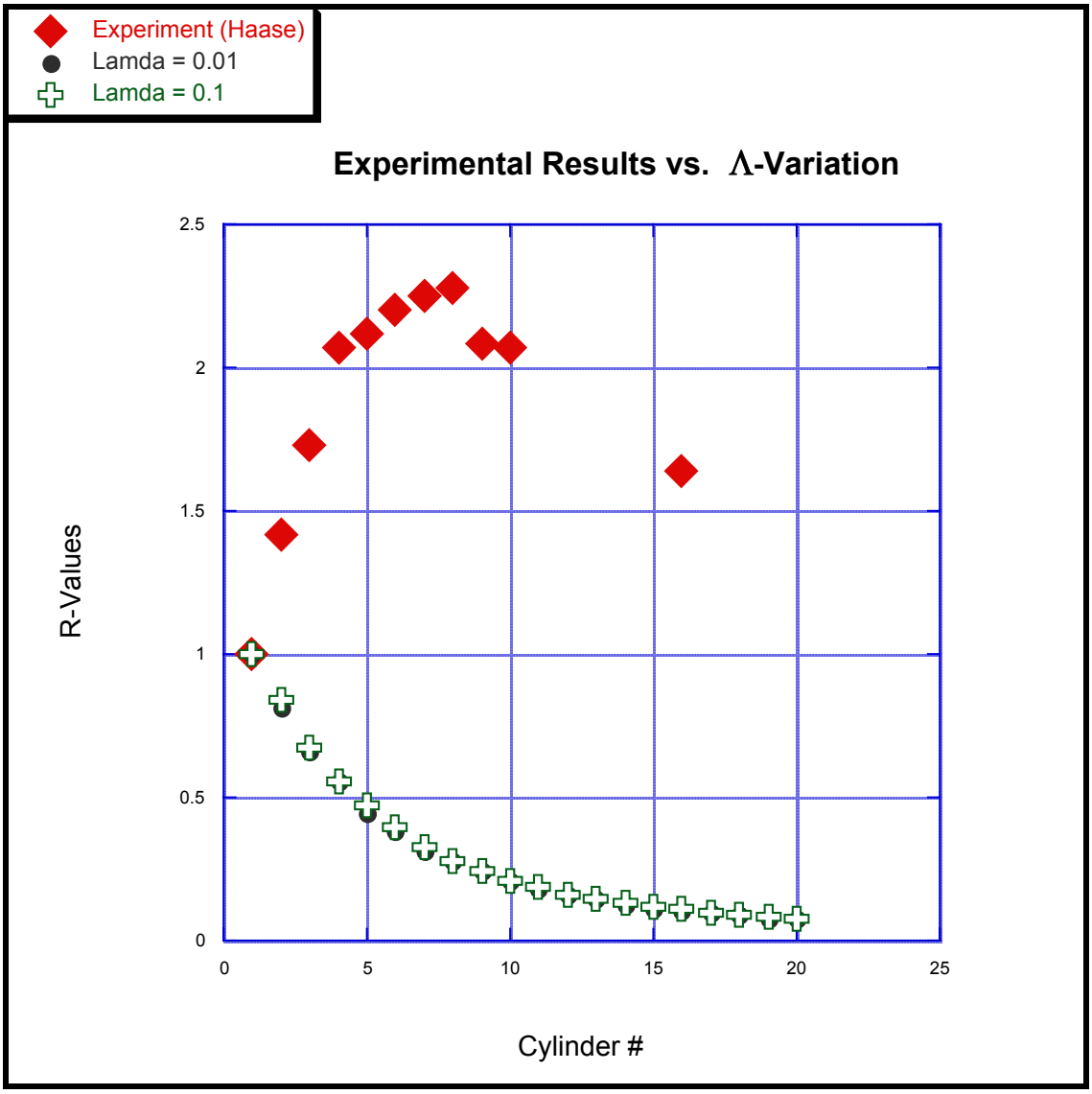

Figure 10.4b Experiment vs. Decreased Mean Free Path (Λ)

(1.8 A GeV ^{40}Ar on a Copper Cylinder)

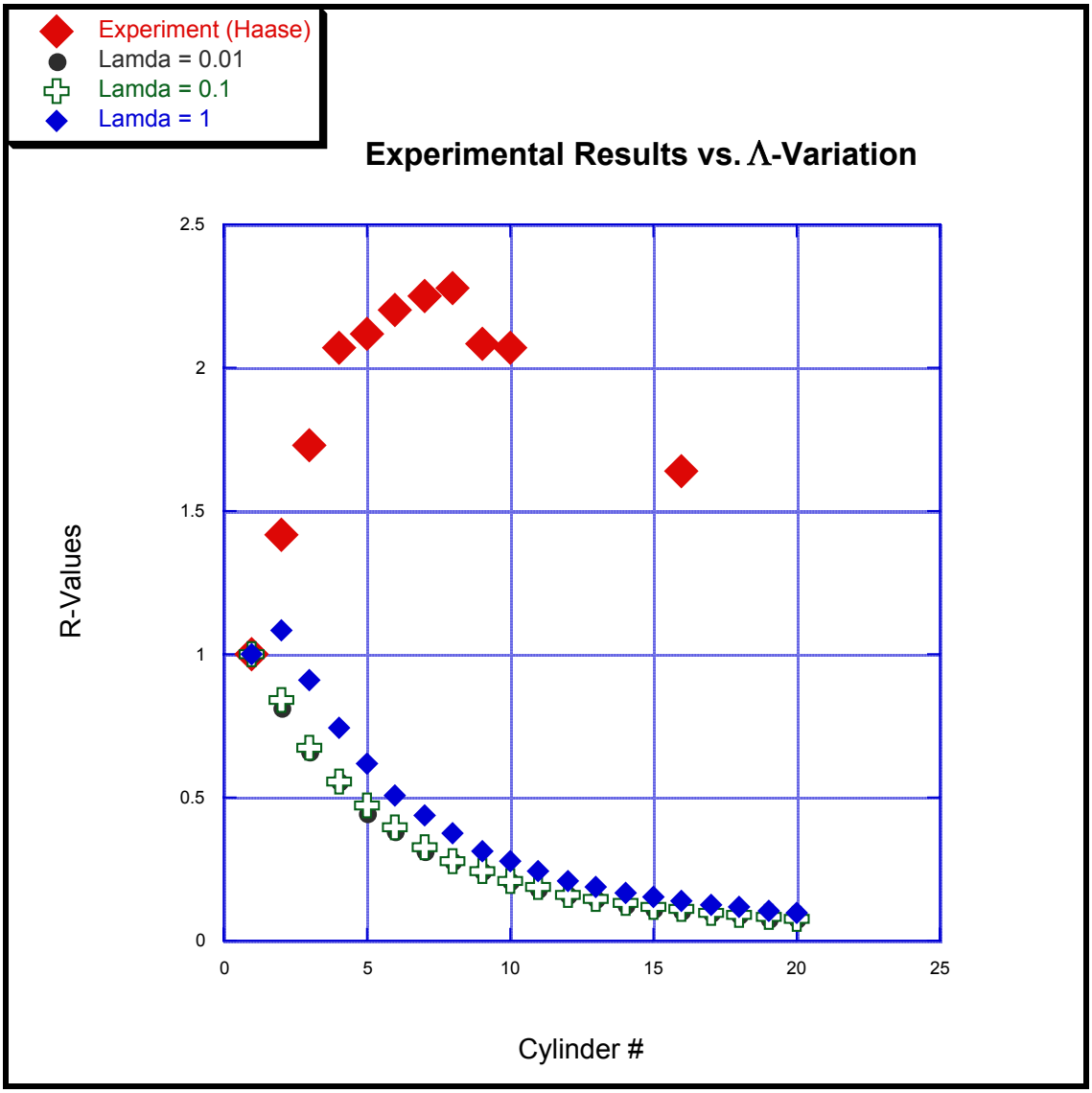

Figure 10.4c Experiment vs. Decreased Mean Free Path (Λ)

(1.8 A GeV ^{40}Ar on a Copper Cylinder)

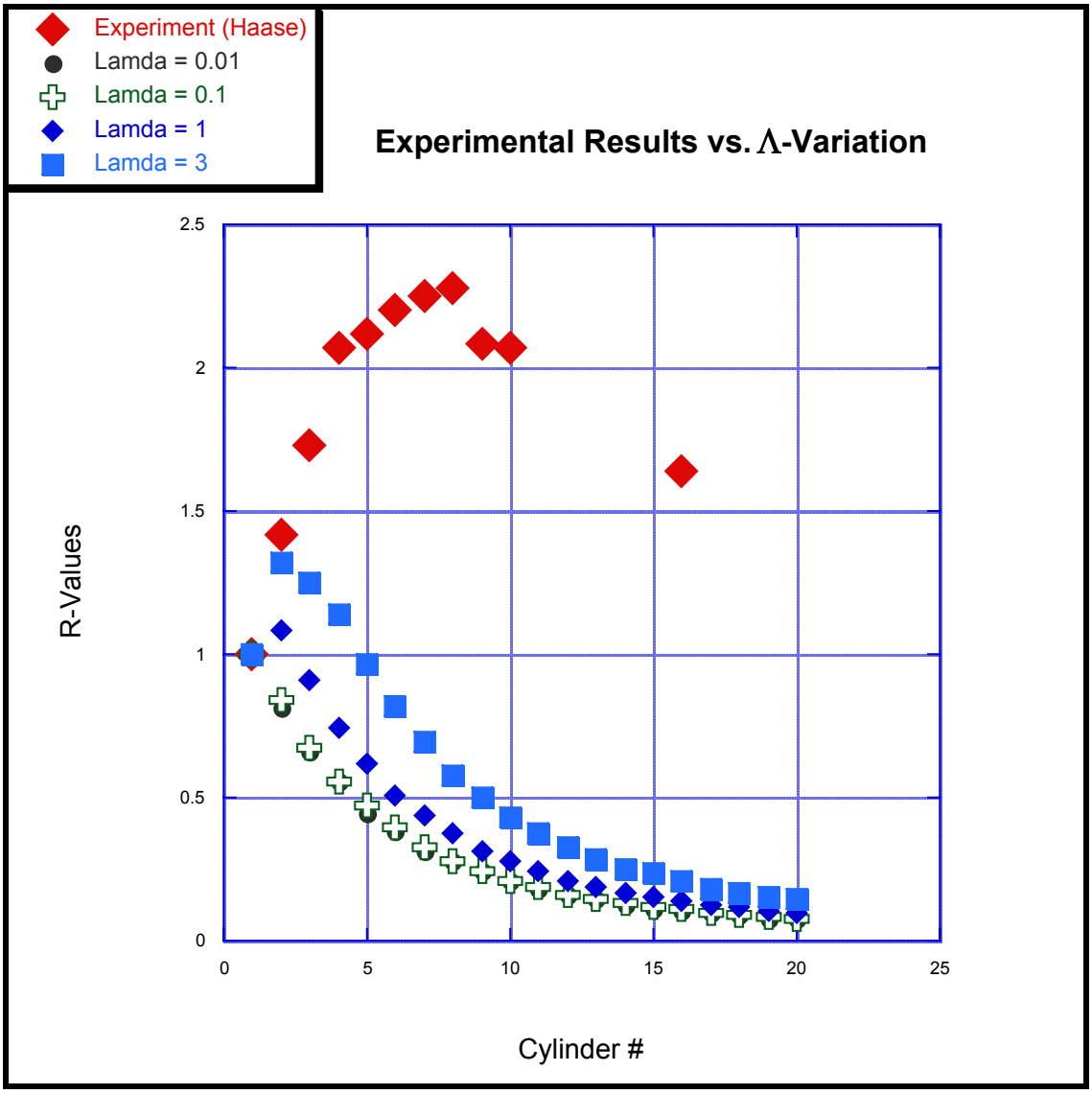

Figure 10.4d Experiment vs. Decreased Mean Free Path (Λ)

(1.8 A GeV ^{40}Ar on a Copper Cylinder)

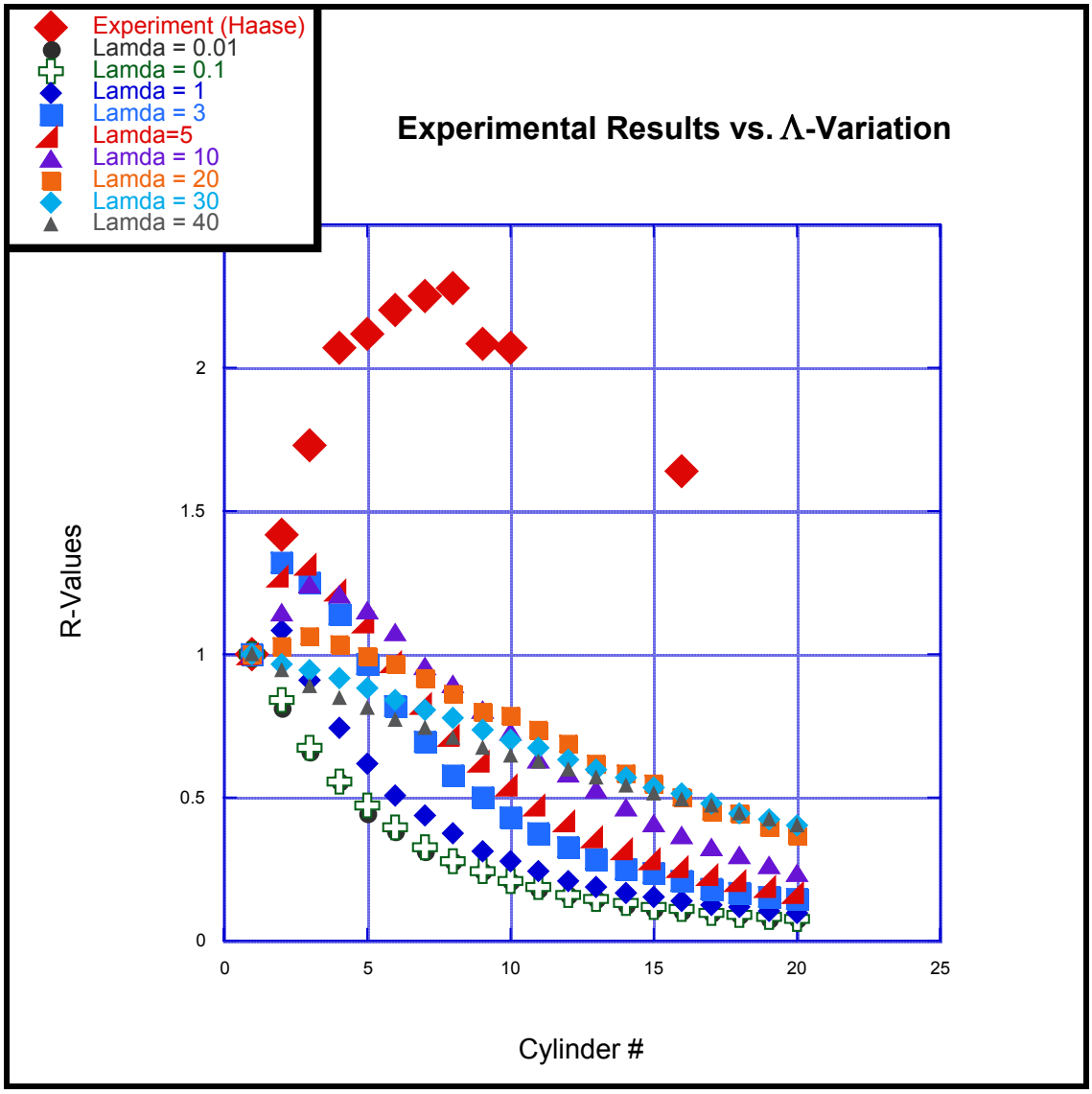

Figure 10.3 further shows the R-values monotonically decreasing throughout the cylinder, even if all the shower particles had an E_p=1.8 GeV. This is in spite of the large number of shower particles (yellow tracks in Figure 10.5 below) created in the course of the cascade.

FIGURE 10.5 Cascade Development in Cylindrical Target

(A simulation of the cascade due to 3 primary interactions[1])

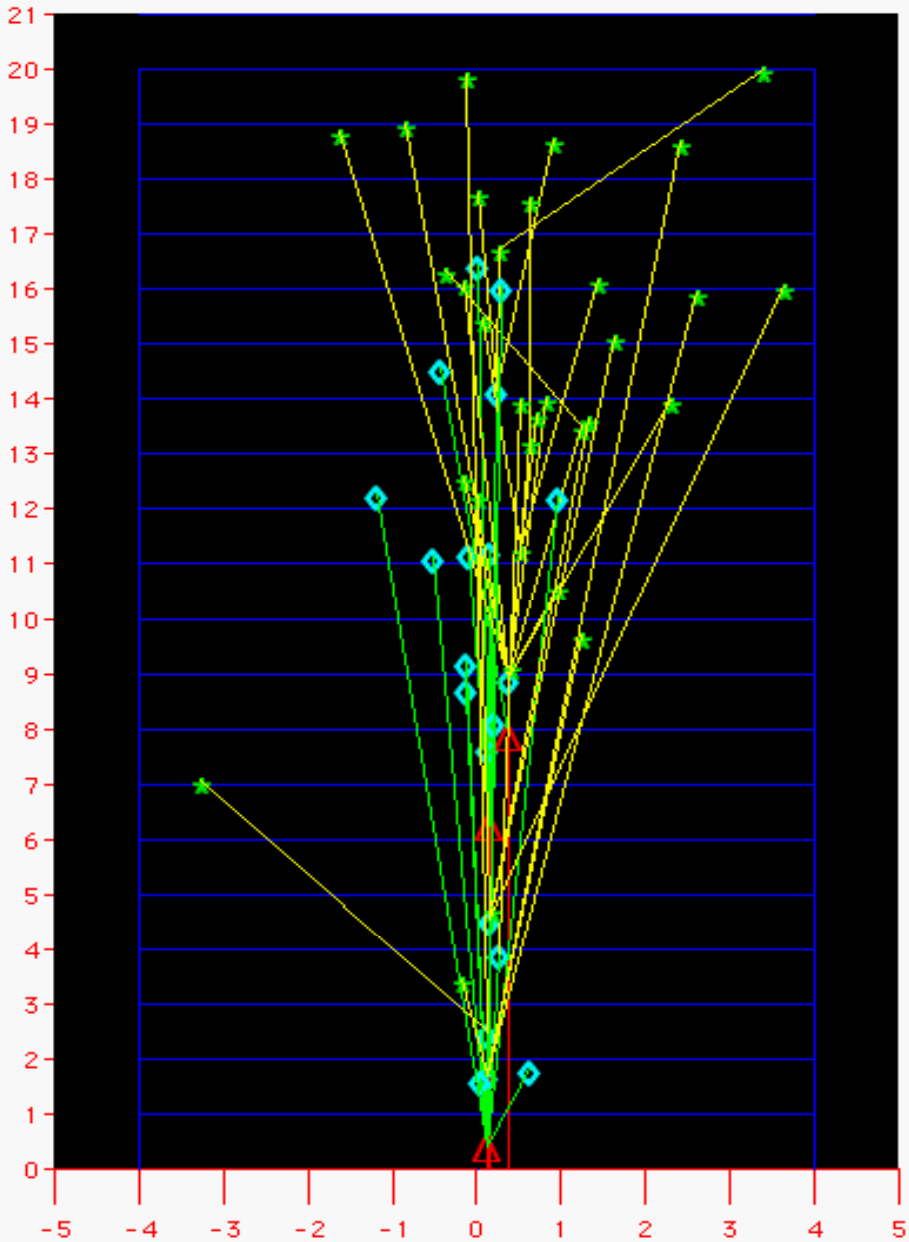

[1] Primary interactions take place at the open red triangles in cylinder numbers (1, 6,7)

And as a quality control check, the charge Z is given a patently unrealistic error of $\Delta Z=6$, the equivalent of assuming that every charge measured was off by 2 charge units per generation[1].

Figure 10.6 Comparison of R-values between Models and Experiment

(1.8 A GeV ^{40}Ar on a Copper Cylinder)

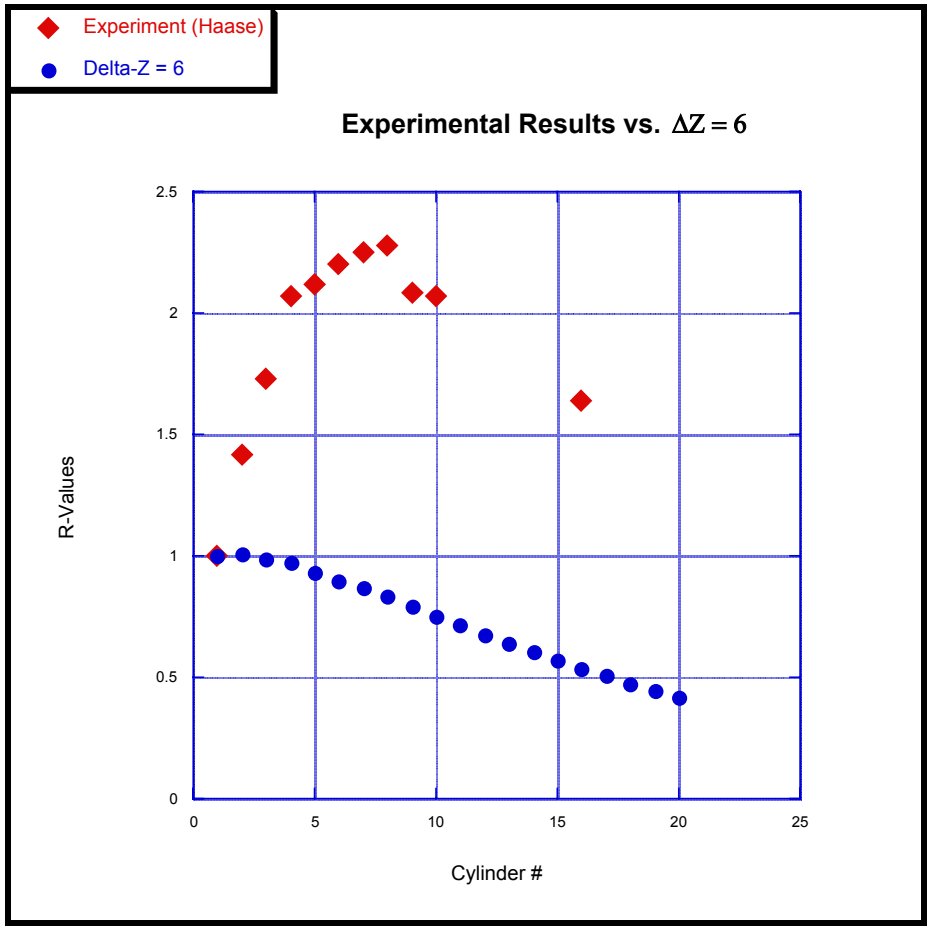

As expected, there is a monotonic decrease in R-values. Charge measurement errors cannot explain away experimental results or the simulation conclusions presented next.

[1] This amount of measurement error is impossible for many reasons, including quality control checks like those of the Fragmentation Matrix in Section 4.4.

10.2 The $\sigma_{production}$ Subpopulation Model Applied to the Cylinder

Recall from equation 9.1 that projectile fragments of Z≥ 2 (A≥4) have an energy-independent production cross-section $\sigma_F(A) \cong 3.6A^{0.387}$. Generalizing this to

$$\sigma_p = KA^{\varepsilon} \qquad \textbf{(10.1)}$$

a considerable number of combinations of K and ε are possible. Trying first those values of ε that worked in the two-block case above, along with the commensurate percentages of subpopulation, one finds the following remarkable result:

Figure 10.7 R-values of $\sigma_{production}$ Subpopulation Model vs. Experiment

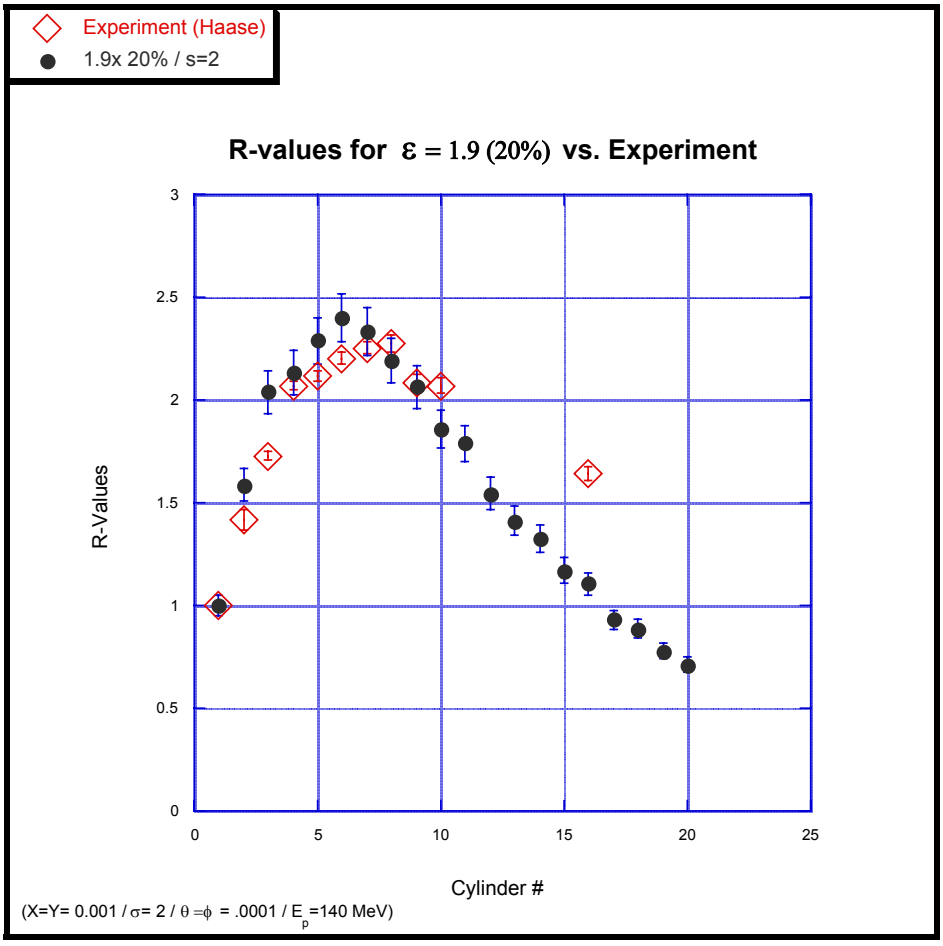

An enhanced production cross-section model is a remarkably good fit, especially considering the relative crudity of the model (no decay characteristics, for example). Indeed the fit is excellent until block 10 (i.e. 10 cm), after which it diverges. Assuming for the moment, the physical reality of the enhanced nuclear cross-sections discussed in the previous section, this divergence at 10 cm may be the scale-length for decay, as suggested in the R_0-R_{20} set of copper calorimetry experiments. Exploring other values of ε that worked in the two-block case (still keeping the coefficient K=3.6):

Figure 10.8 R-values of $\sigma_{production}$ Subpopulation Model vs. Experiment

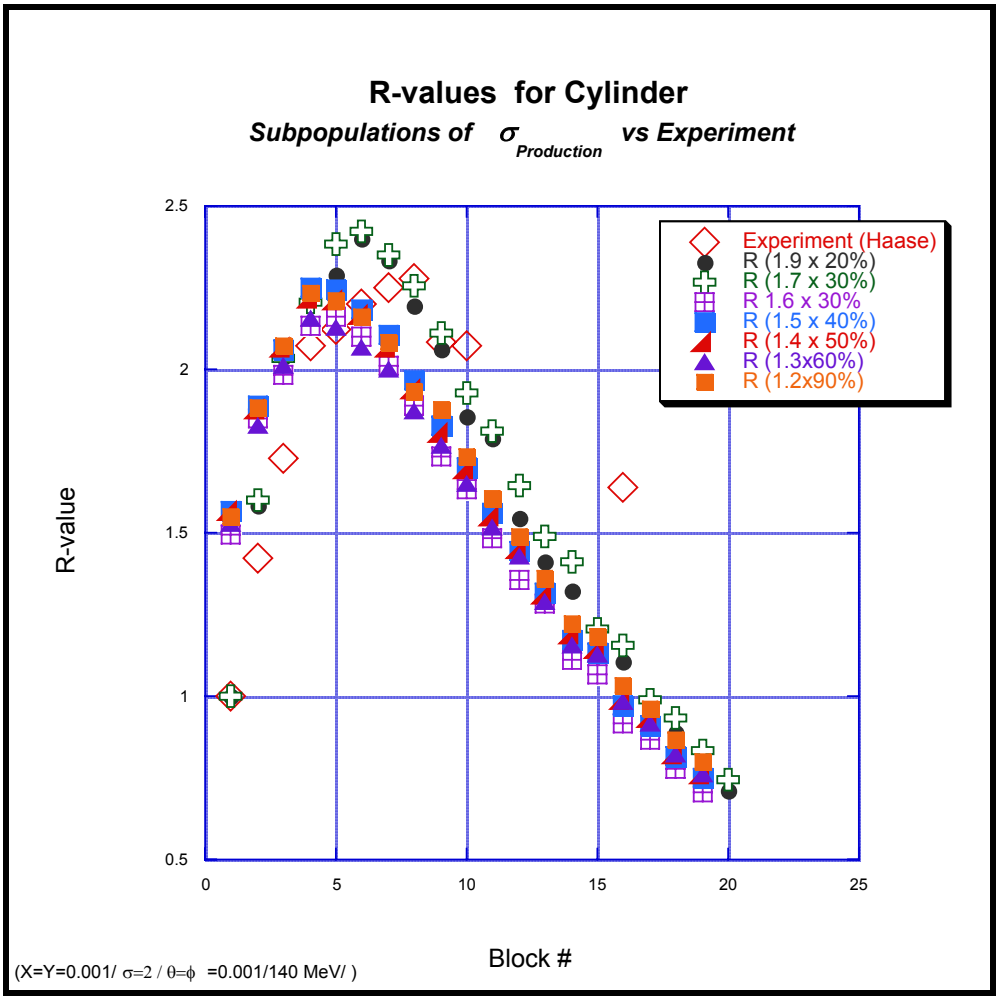

These other combinations of σ_p subpopulations show a similar fit; and at 10 cm a similar divergence from the experimental results, the 10 cm drop-off particularly well illustrated below.

Figure 10.9 R-values of $\sigma_{production}$ Subpopulation Model vs. Experiment

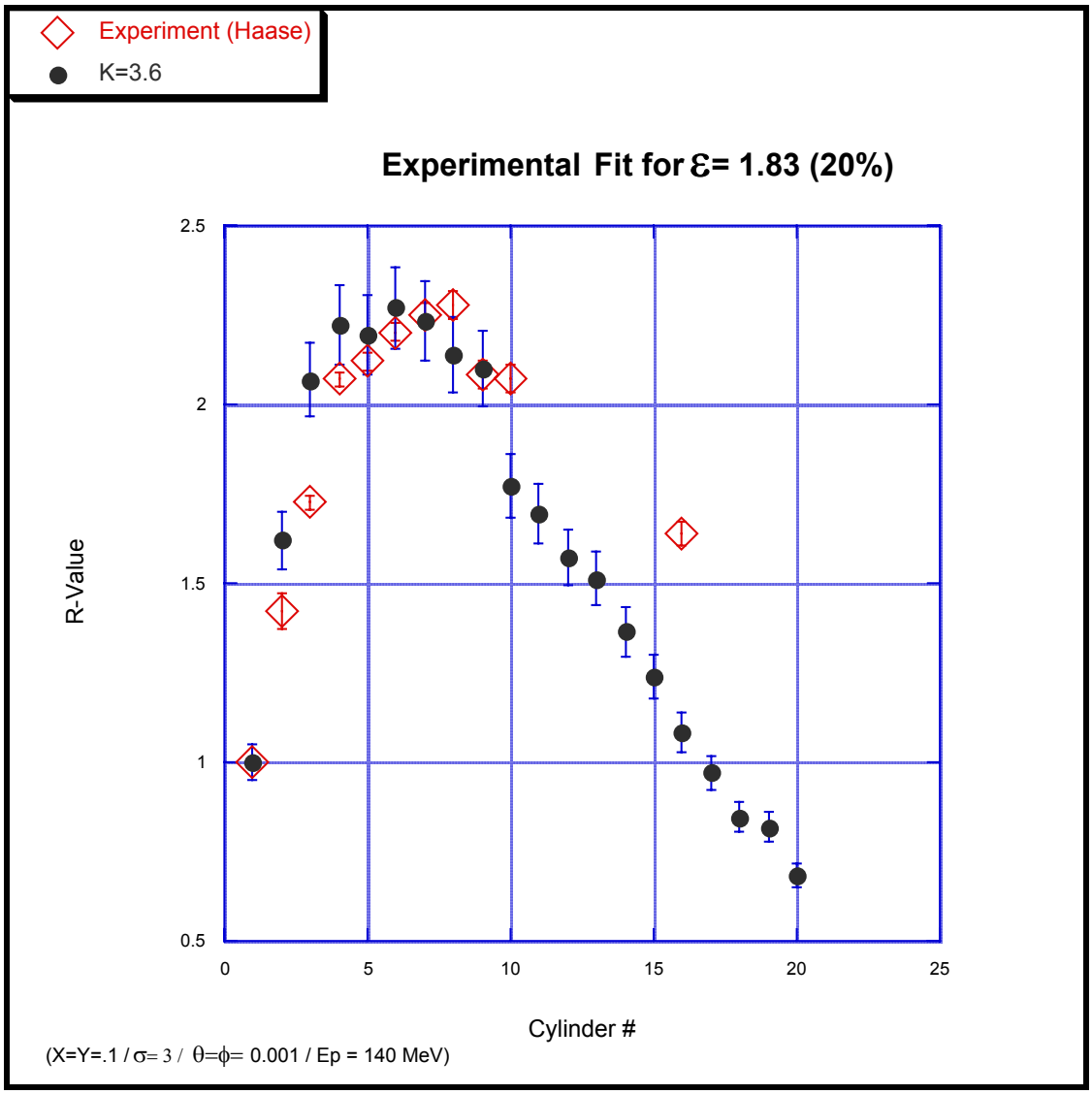

Varying the coefficient K allows a host of other fits, some better than others, but all diverging from experimental results at 10 cm. For example, for ε =1.9 the best fit lies in the region K= 3 to K= 3.6 as seen in Figure 10.10.

Figure 10.10 R-values as a Function of K

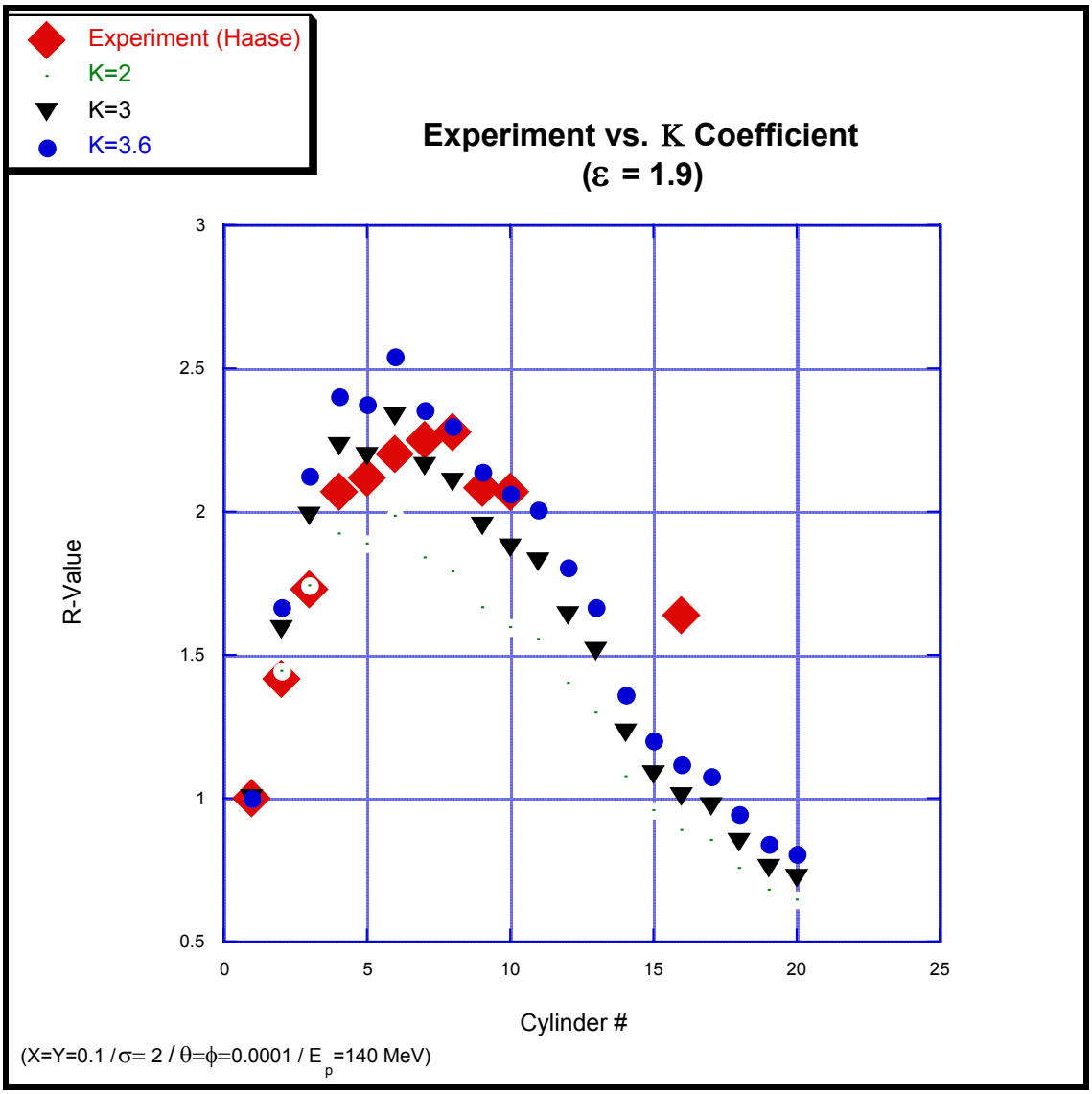

While for ε = 1.6, K = 4 offers a marginally better fit:

Figure 10.11 Experimental Fit for ε = 1.6 (30%)

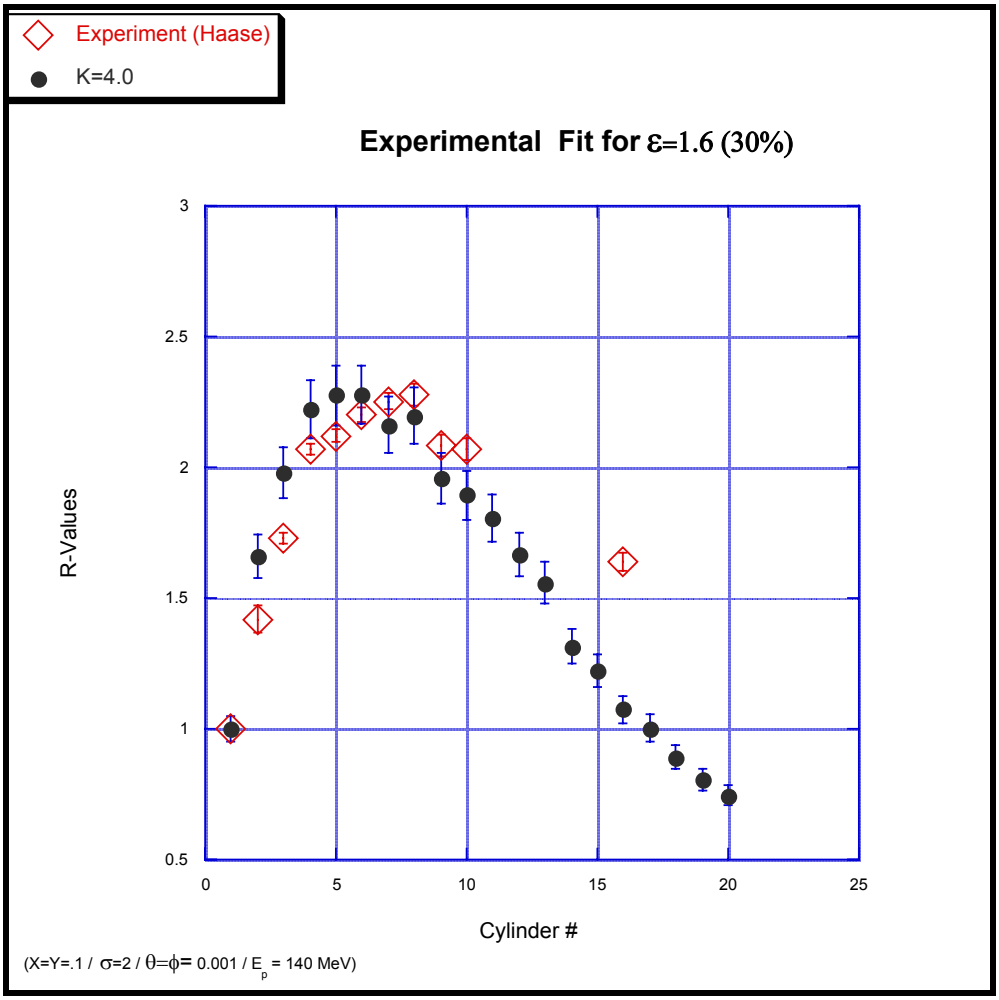

In summary, a comparison of the different model classes clearly shows that only the enhanced production cross-section model has any reason to be considered (Figure 10.12a). The enhanced $\sigma_{production}$ model used here has a 20% subpopulation of $\varepsilon = 1.9$, which is represented in the legend of the graph as < Exp=1.9 (20%) >.

Figure 10.12a Comparison of R-values between Model Classes and Experiment

(1.8 A GeV ^{40}Ar on a Copper Cylinder)

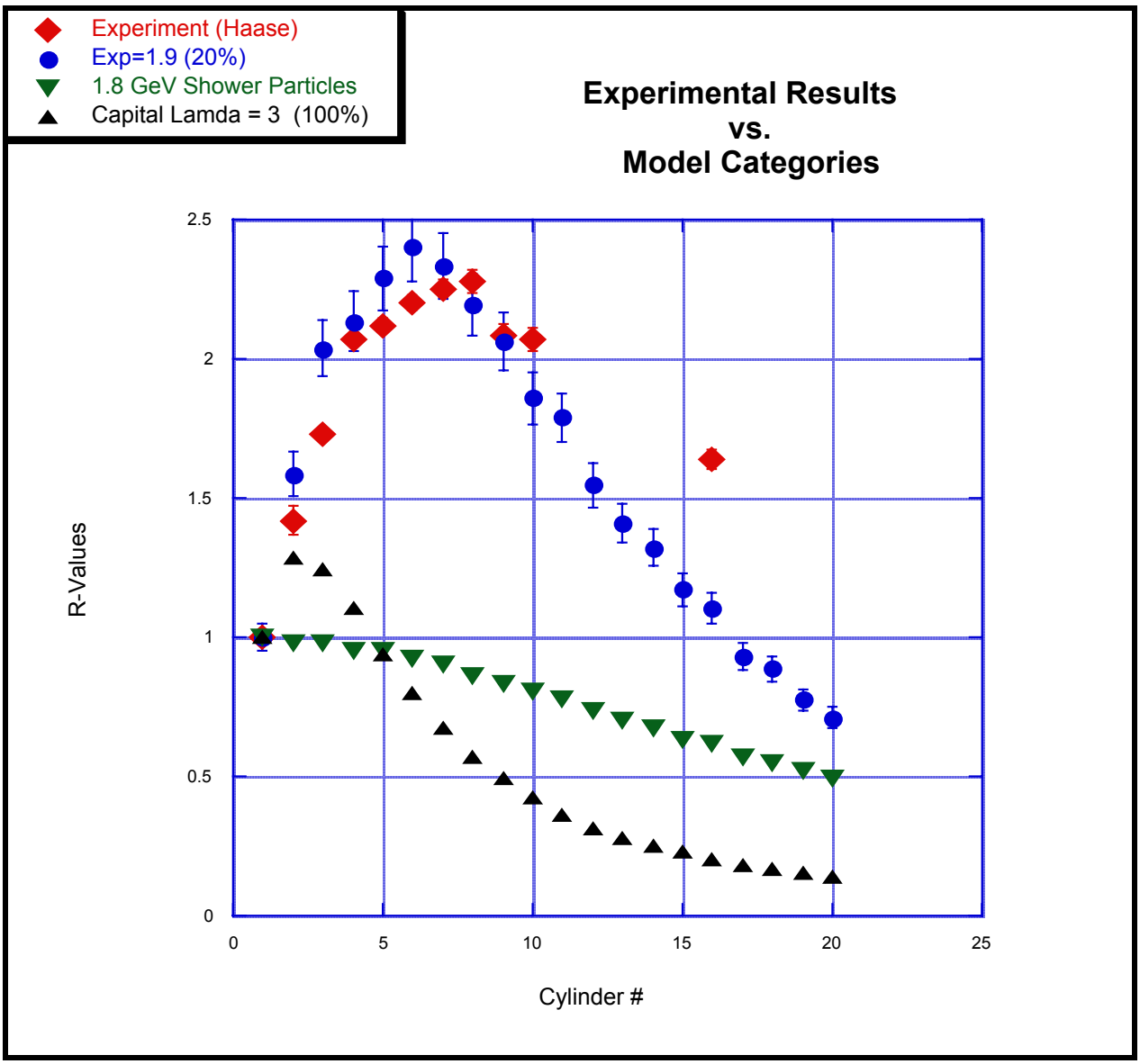

The above graph used the experimental errors reported in the single experiment done of the cylinder (Haase 1990), that reported an equivalent $R_0 = 1.42 \pm 0.05$. Comparing this value to the original copper calorimetry experiments that were performed 3 times, and yielded an averaged $R_0 = 1.50 \pm 0.02$, suggests that the true experimental error for Haase's work is ~5%. A similar 5% error is arbitrarily chosen for the $\varepsilon = 1.9$ (20%) simulation results. Revising the above graph to include this more realistic error yields a fit by the enhanced $\sigma_{production}$ model that, under the circumstances, is almost breathtaking.

Figure 10.12b Comparison of R-values between Model Classes and Experiment

(1.8 A GeV ^{40}Ar on a Copper Cylinder)

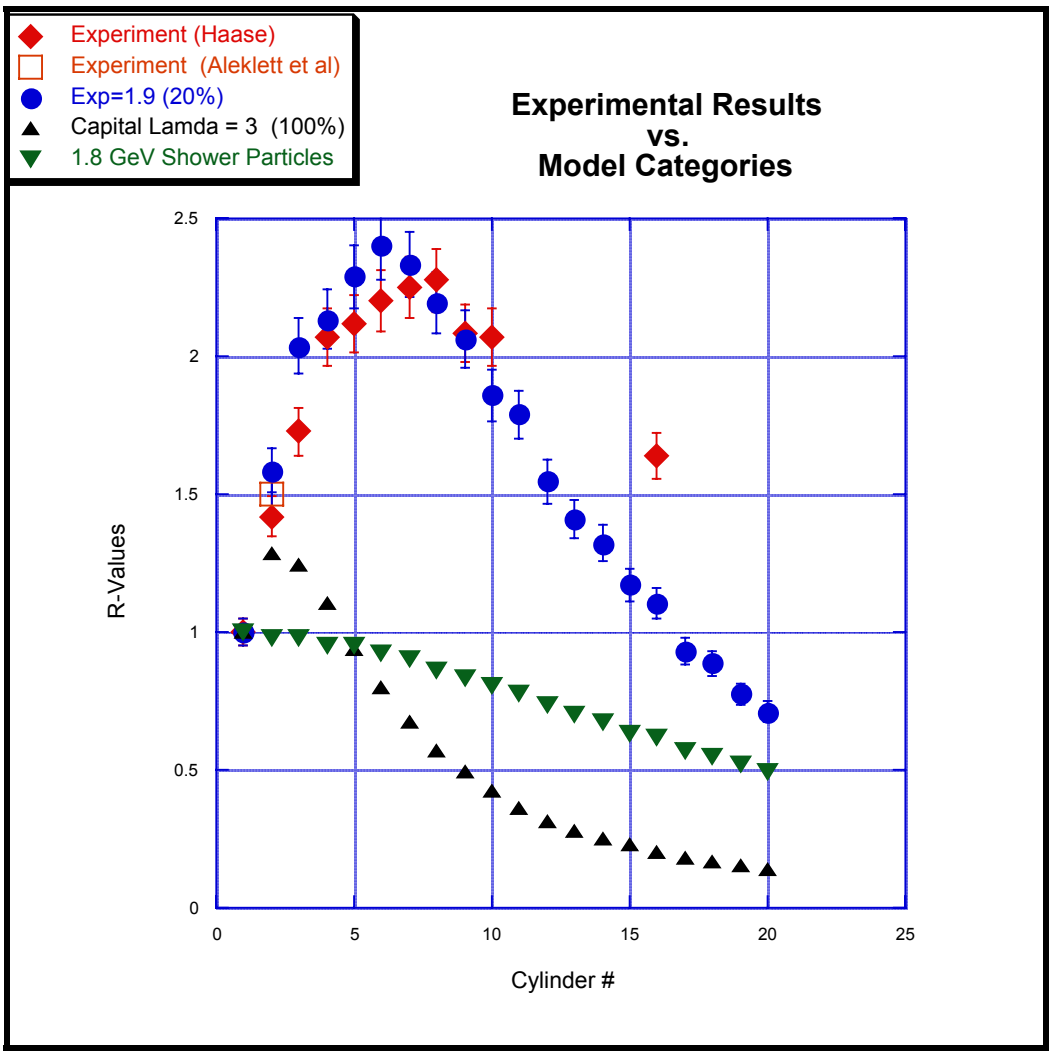

Finally, to drive the point home even more, a 'Normal' model with 140 MeV shower particles is shown. This latter model is a simulation with variables at the default setting…what one would expect to see if everything was 'normal'.

Figure 10.12c Comparison of R-values between Model Classes and Experiment

(1.8 A GeV ^{40}Ar on a Copper Cylinder)

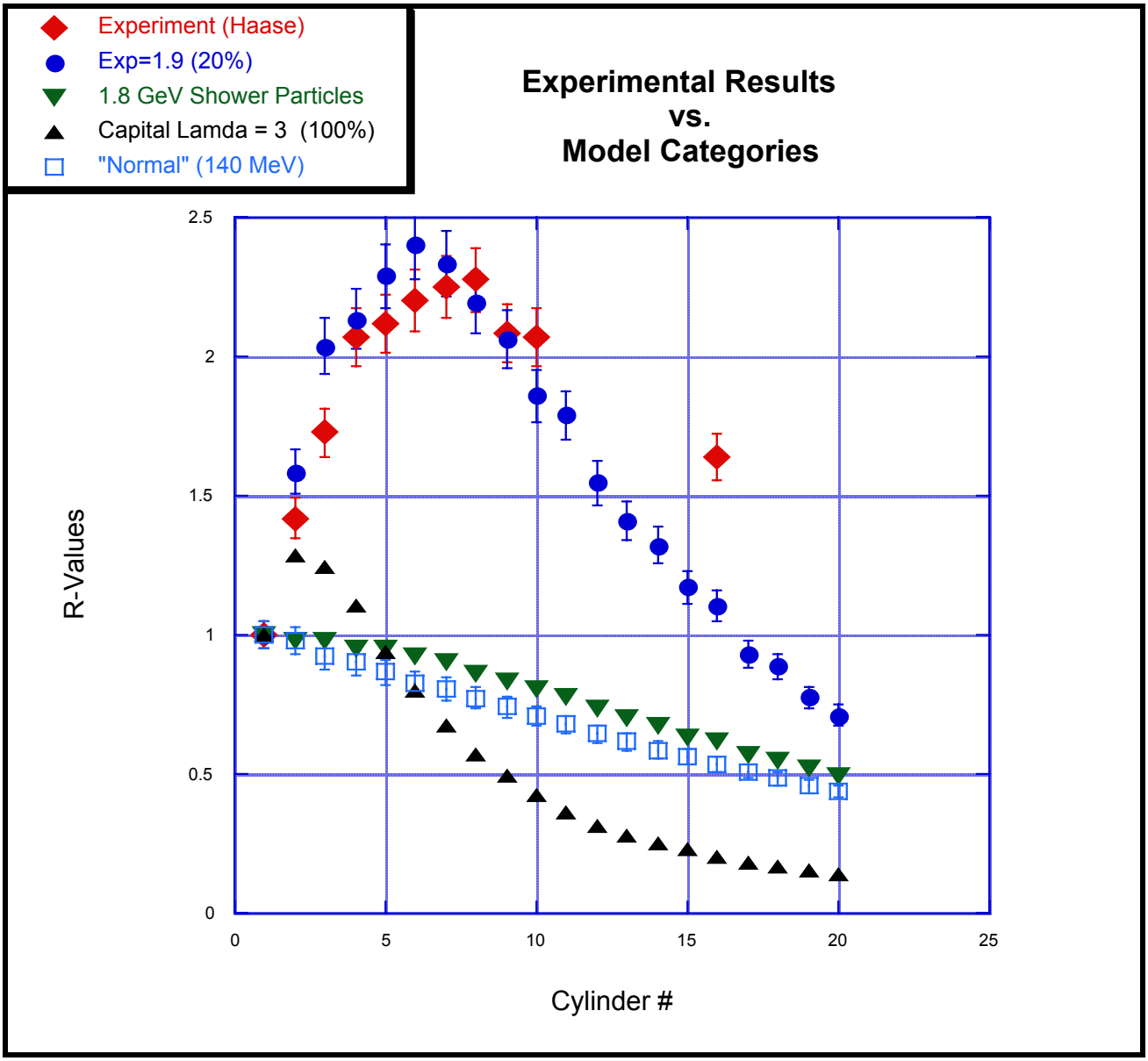

The only disparity for the production cross-section model (before block 10) is at block 3. Taking at face value the relative accuracies of these measurements and simulation-values it is conceivable that this discrepancy may be due to the fact that the posited decay is not taken into account. By the third block the cascade is still in its pre-peak growth phase. If there is a simultaneous decay factor then the value would be lower than is simulated. Alternatively, the singly-performed experimental results of Haase, compared to the triply-performed experiments of Aleklett et al may in fact just be too low by ~ 5%. This too would clear up much of this perceived discrepancy. And recall that the fitted subpopulation chosen (20% with $\varepsilon = 1.9$) is chosen only to be representative of its potential solution-class. A host of more exhaustive and fine-tuned simulations is of course necessary.

An important point must be emphasized: *The necessary subpopulation involved seems to be in the range of (10 – 20)%. Hence we must be dealing with an effect which is not exactly reticent in showing itself. It thus offers us a hint that we may be dealing with a variation of an otherwise well-known phenomena.* This will be taken up again in Section 10.6.

10.3 Variations of K applied to the Cylinder

From equation (10.1) the production cross-section $\sigma_p = KA^{\varepsilon}$. Variation of the exponent ε led to the extraordinary fit of simulation to experiment seen above. But one must now ask the question if this due only to an increase in the absolute value of σ_p. In other words, is the Z-variation explored above necessary or can the same results be had by increasing σ_p solely by increasing the coefficient K. This is a phenomenologically important distinction, for a lack of Z-dependence would strongly suggest that no new channels have been opened up (and consistent with the ideas of limiting fragmentation).

To test this point, simulations have been run over the range of σ_p values examined in previous section, but with ε having the fixed (normal) value of 3.6 and the coefficient K changing. The results are seen in Figure 10.13.

Figure 10.13 R-values as a Function of K
(secondaries only)

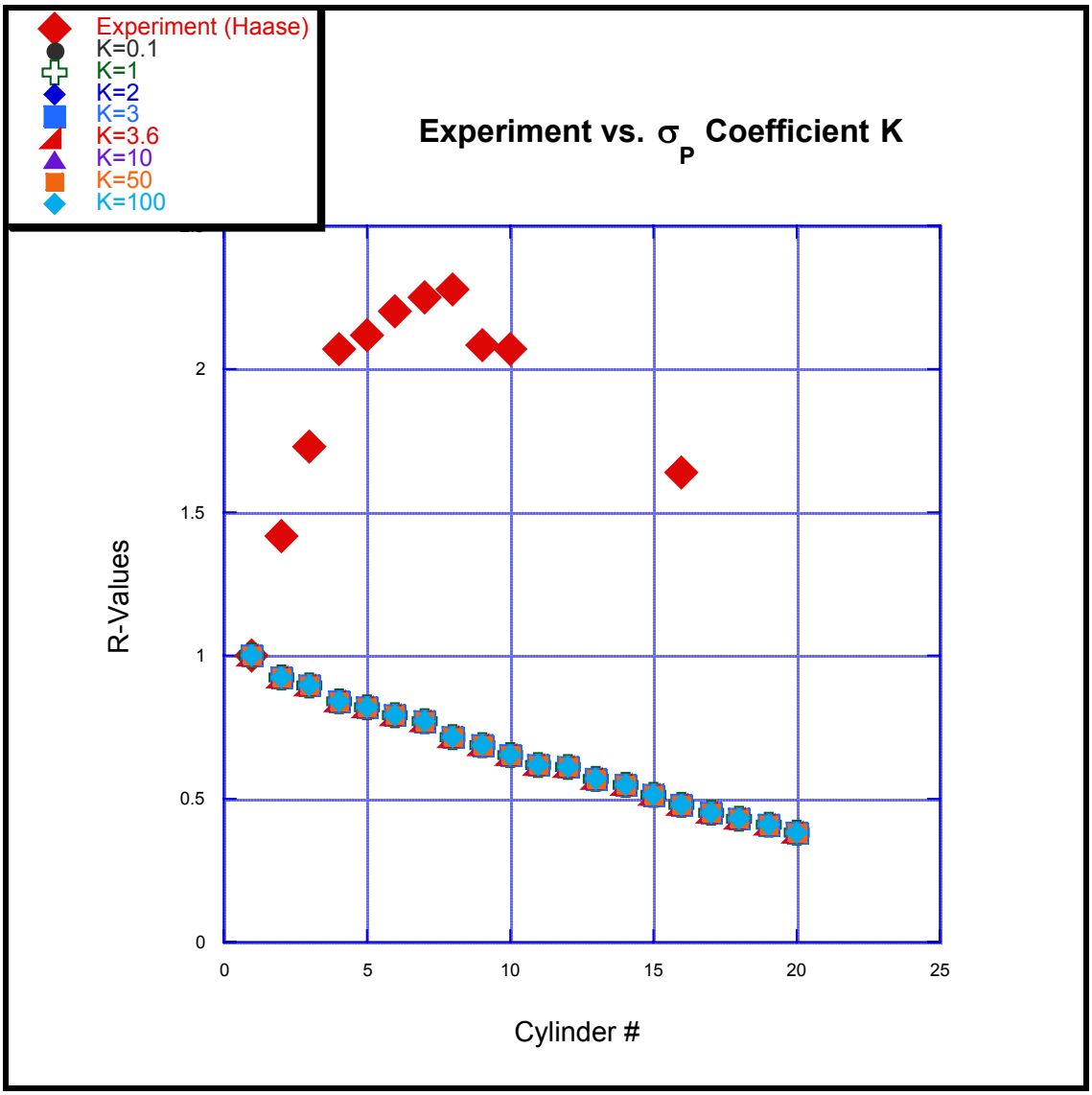

This obviously doesn't work. *The total lack of variation of R-values with K, the lack of qualitative fit to the experimental data, and the results of the previous section clearly demonstrates a Z-dependency of theenhanced production cross-section increase. This strongly suggests that new channels are being formed, and new varieties of interactions are occurring.*

10.4 Are Secondaries Secondary?

Throughout this chapter we have assumed that, regardless of variable varied, only the secondaries were affected. Much of the physical importance of our findings, as well as its overall believability, rests upon this critical assumption that whatever is going on is going on *only* in the population of secondary particles (only $Z \geq 2$ considered so far). This can be checked. If we are correct in our assumptions, and in our methodology, then the root cause of the effects under study is due to two fundamental asymmetries of the secondary population:

1) The ratio R_0 and the its more generalized R-values selectively samples the secondaries as seen in Figure 5.3 and discussed in Section 5.1.

2) The secondaries themselves have some interaction characteristic which is distinctly different from that of otherwise 'identical' primaries.

Hence it is fundamental to our logic that any unusual effects will be diluted by any decrease of either of these asymmetries. In our simulations this dilution can be accomplished by giving the properties of #2 above to subpopulations of primary nuclei. This has been done for both the variables Λ and ε, representing the mean free path and production cross-sections respectively. In Figures (10.14a,b) this dilution is shown to occur. For both variables, a 20% subpopulation of primaries having the same special characteristics as do the secondaries completely destroys the effects of the unusual secondaries.

Figure 10.14a Primary Subpopulations "Diluting" Secondaries (Λ- Variation)

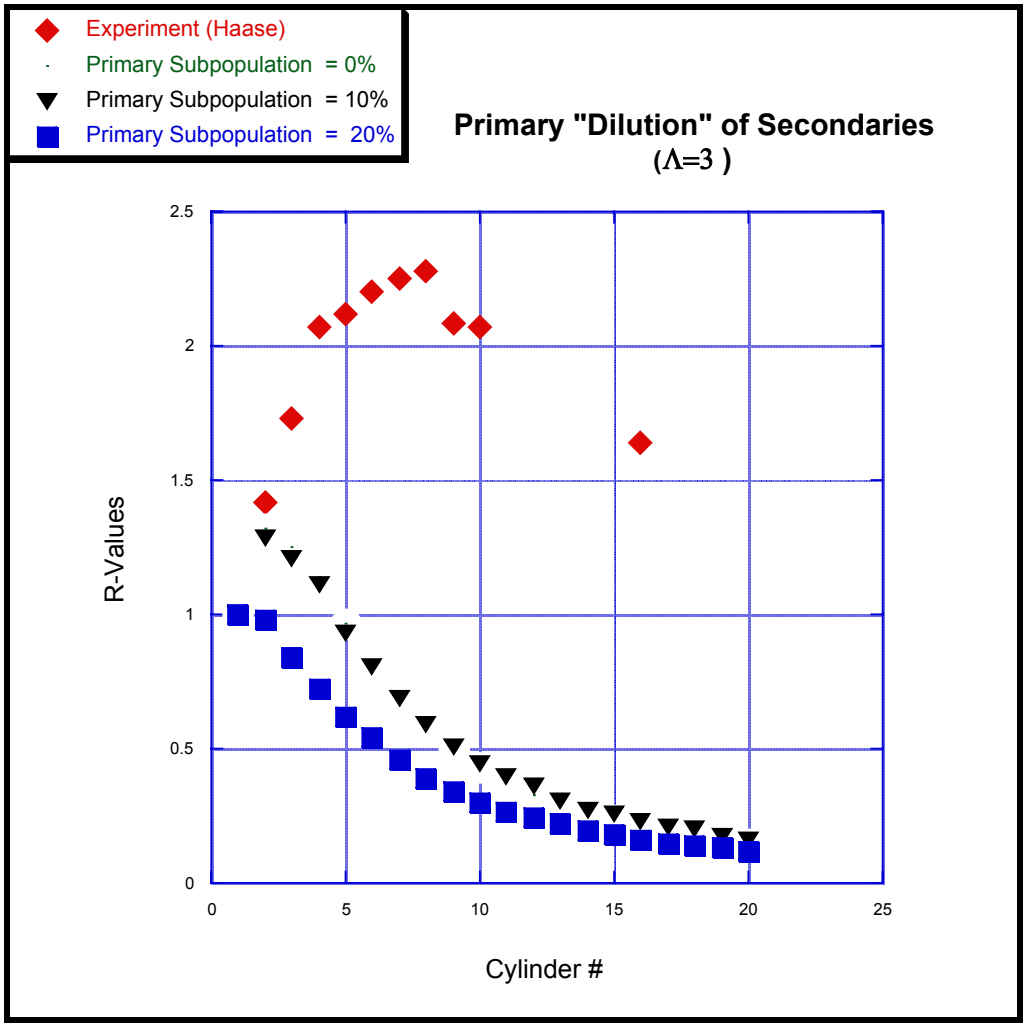

Figure 10.14b below shows the same effect with ε=1.9 (20% of secondaries).

This strongly suggests that whatever special effects, interactions, or properties are involved… they lie in the secondaries. The magnitude of these dilution effects (10-20%) also supports the order-of-magnitude of the subpopulation of secondaries necessary to generate the effect in the first place, i.e. (10-20%).

Figure 10.14b Primary Subpopulations "Diluting" Secondaries

(ε=1.9 / 20%)

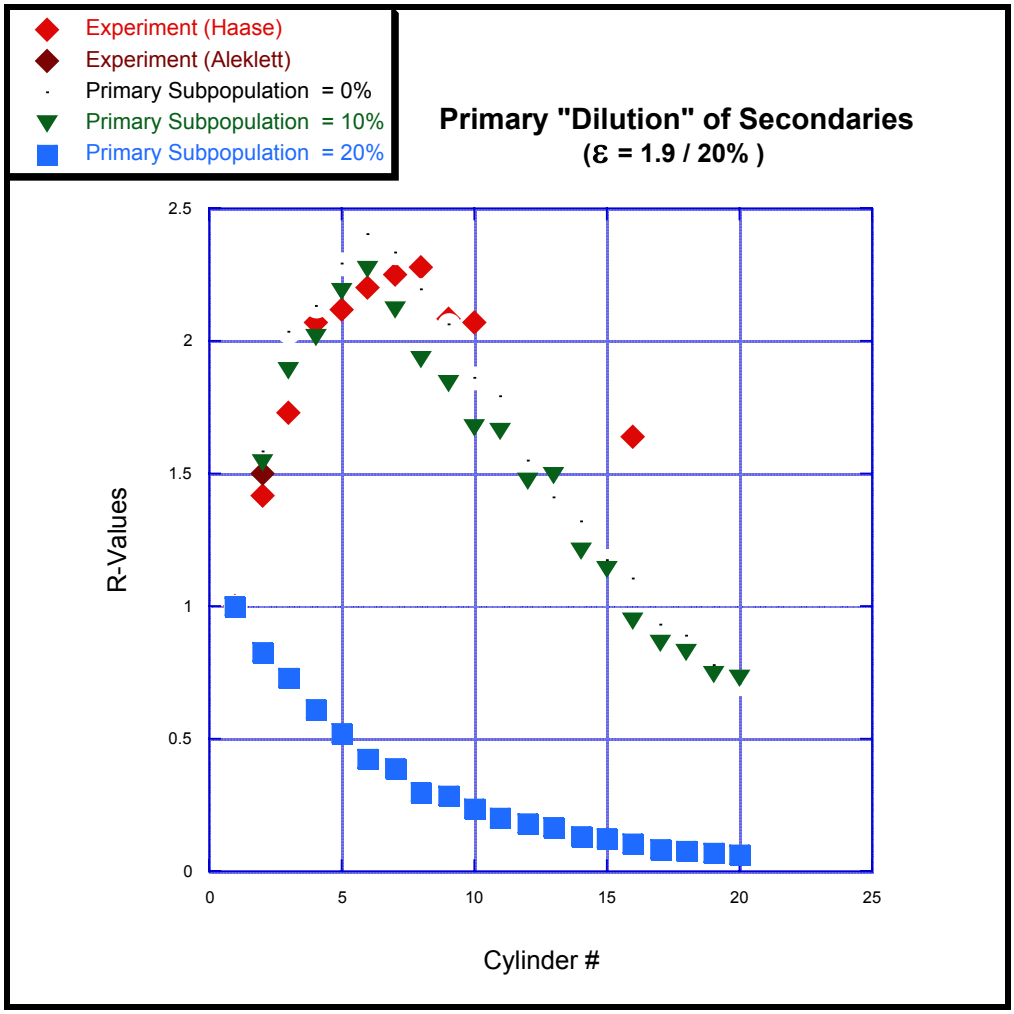

If 10% of the primaries also have ε=1.9 a drop-off of the fit begins after block #6.

Nonetheless the marginally closer fit to blocks #3-6 is intriguing. It may be spurious. More likely it suggests the existence of non-linearities or complications, quite possibly of completely different variables than are considered in this overly simplistic model.

10.5 Discussion

A complete exploration of the phase-space of potential fits to the cylinder data is not the intent of this work. What is important has been demonstrated: the ubiquity and robustness of fit of a simple model that incorporates an enhanced production cross-section for secondaries. It is the only model of those which has been suggested which, within the context of our simulations, is able to fit the two-block R_0 data. And when applied to the entire cylinder, it offers a visibly superior fit as well. It seems to fall off faster beyond 10 cm, but this is the same scale-length that was found in the two-block experiments. Is this additional support for an enhancement of secondary (partial) cross-sections that decays over the time-scale of $\left(\frac{10}{c}\right) = 10^{-9}$ seconds?

If so, this dramatic difference in production cross-section in secondaries is most unexpected. Recall from equation 9.1 that projectile fragments of $Z \geq 2$ ($A \geq 4$) have an energy-independent production cross-section $\sigma_F(A) = 3.6A^{0.387}$; and where we've generalized this to $\sigma_P(A) = KA^{\varepsilon}$. For exponents that seemed to fit, those in the $1 < \varepsilon < 2$ range, the resulting differences in cross-section are mostly factors of 3-10, but can go as high as 100. These factors are reminiscent of resonances in low-energy nuclear processes; but what are they doing in these high-energy regimes where factorization and limiting fragmentation are supposed to rule?

Considering the scarcity of the cross-sectional data represented in Figure 7-1, one might instead question whether there exists a conventional resonance close to the energy of the argon primaries. Ignoring for the moment the question of just why a resonance should occur in this high-energy regime, conventional resonances are typically a few hundred MeV in width. Hence the initial experiments to establish the argon-induced ^{24}Na would be expected to have seen at least a tail of it since secondary argons, along with the rest of the well-focused projectile fragments suffer little change in energy after collision with nuclei; a comparable few hundred MeV at most. If no conventional resonance was found for the primary argons, there is no reason to expect one to exist for the secondary argon nuclei.

Interestingly, what is predicted with ordinary assumptions matches very well the experimental results for protons on copper. Somewhat simplistically, one would expect this if there was in fact a linear separability between target and projectile, *and* the involved nucleons of each. This is because the R-values we're dealing with are ratios; hence the larger absolute value of the relativistic heavy ions production cross-section would cancel out.

Instead the inferred enhancement of partial cross-section (at these energies) suggests, like in low-energy resonances, that some form of cooperative phenomena is occurring; but for seemingly quite different reasons. If real and generalizable (a big stretch from our one set of experiments and interpretations) this cooperative phenomena could mean that for some secondary reactions the linear separation of target and projectile described by factorization no longer holds. Nor of course does limiting fragmentation.

The possibility of non-linear effects is further supported by the fact that a production cross-section exponent of $\varepsilon=1$ gives the ordinary, expected exponential decay; while exponents $\varepsilon=2$ and above rapidly hit an asymptotic limit. The transition to a potential fit to the data at just above $\varepsilon=1$ suggests, by definition, that a transition into a non-linear regime is occurring. Meanwhile, the transition to an asymptotic limit at $\varepsilon=2$, just above the values for at ε that allow an experimental fit, further suggests a cooperative effect. This is because one would expect an $\varepsilon=2$ to represent some form of saturation effect based on total area of the involved scale; or on a complete set of mutual interactions within the set under consideration or between two sets of (equal) quantity. Of course such saturation effects need not be independent. Still thinking in abstract phenomenological terms: with these exponential values lying somewhere between 1 and 2 the smallest subpopulations occur for higher values of ε. This suggests that a great deal of this mutual interaction is occurring (between whatever). Alternatively, for small values of ε one needs very large populations of seemingly less mutual interactions.

What might this exponent represent vis-à-vis interactions? An exponent $\varepsilon < 1$ in the expression $\sigma_p = KA^{\varepsilon}$ can heuristically be interpreted as the probability for production in a collision being dependent only on some subset of the total number of nucleons in the projectile nucleus. This is certainly consistent with the assumption of factorization, essentially a linear independence between projectile and target.

Consider now an alternative. If the production cross-section were due to some mutual interaction between all of the nucleons in both target and projectile, $\sigma_p = KA_{target}A_{projectile}$. If the target and projectile were roughly the same size OR the projectile's nucleons only interacted with an equivalent number of the target's nucleons, then $\sigma_p \sim KA^2_{projectile}$ would describe the functional relationship if all the projectile nucleons were involved. Having an ε such that $1 < \varepsilon < 2$ makes eminent sense then, suggesting as it does some form of collective interaction between the nucleons of the target and projectile which is less than completely saturated (at $\varepsilon=2$).

What could explain these non-linear collective effects? The most common cause in nature of such non-linearities is to be at the border (one side or the other) of a phase transition. One intriguing possibility is that we're seeing some form of hypermatter induced nuclear chemistry. The time-scales of 10^{-10} could potentially fit; along with the transition to strange matter production lying between 1 and 2 GeV/Nucleon as seen in Figure (10.15)[1]. Section (10.6) discusses this possibility in more depth.

Alternatively, the 1.8 AGeV interactions approach, in principle, the still unseen border of the quark-gluon phase transition (Figure 10.16)[2]. Perhaps there is some pre-critical point fluctuation that is a zone of metastability. These two ideas are not necessarily mutually exclusive, for both new channels and an increase in strange matter are posited to occur close to the quark-gluon phase transition.

---

[1] Fuchs (2001) Experimental data from KaoS [C. Sturm Ph.D. Thesis; Sturm (2001)]
[2] Schaffner—Bielich (2001)

Figure 10.15 Excitation Function of K^+ Production

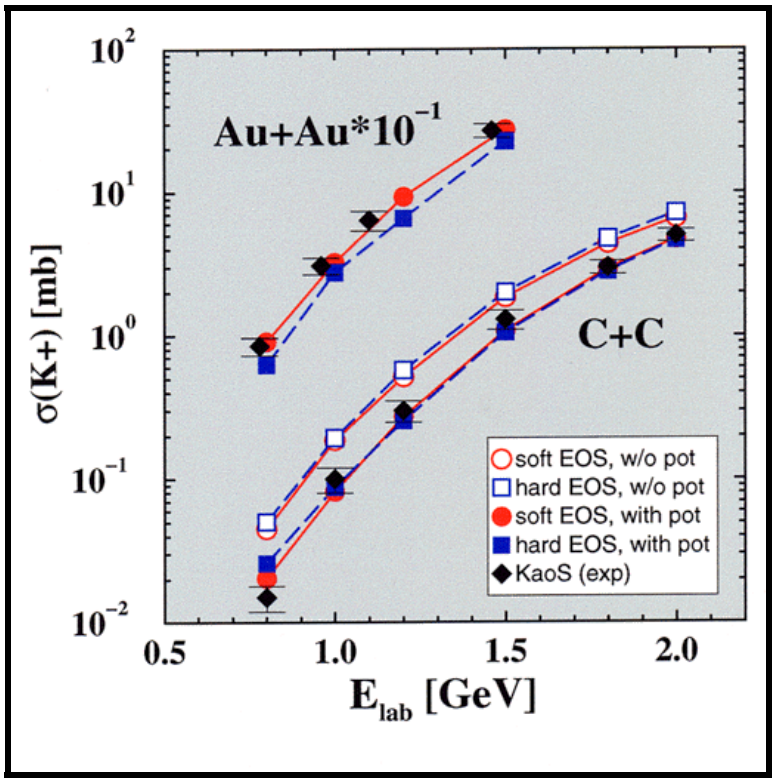

Figure 10.16 Phase Diagram of Nuclear Matter

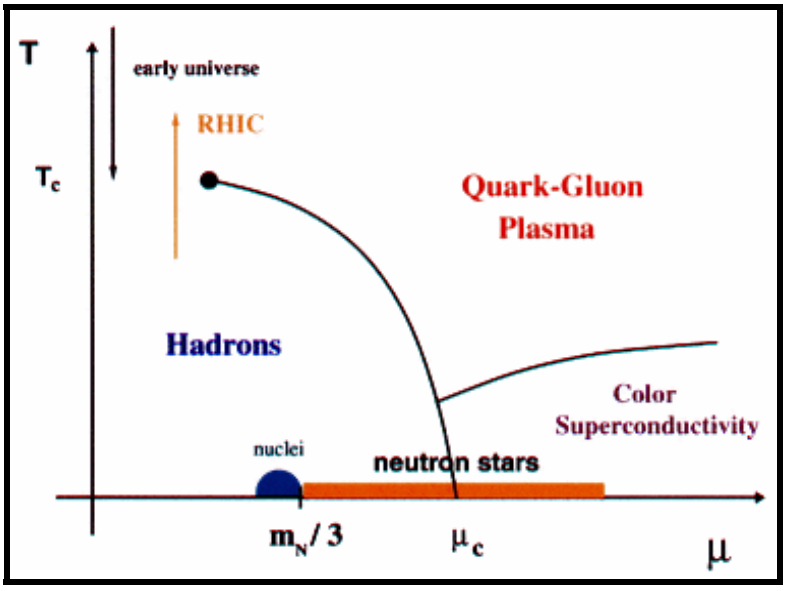

Might this be what we are seeing… a manifestation of the existence of a quark-gluon plasma phase transition? In particular, is it one of the collective fluctuations that come into being as one approaches a phase transition? Some form of phase transition would seem a likely cause for a new 'channel'. But 1.8 A GeV is a rather low energy for the actual quark-gluon phase transition to manifest itself. And other experiments in this energy range might be expected to have seen indications of this boundary if it indeed was 'here'. Perhaps though we have found a small 'sweet' zone where cooperative effects in parts of the overlap region are able to come into being as conditions approach this boundary without actually arriving at it.

Or perhaps it is something else. In light of the still unknown demonstration of the quark-gluon phase transition, and the coincidence of strange lifetimes and energy thresholds with what we are seeing in the Copper Calorimetry Experiments… it seems worthwhile to explore a 'hypermatter-induced nuclear chemistry threshold'. The following section presents a brief overview of some of the relevant characteristics of collective strange matter, leading to a thought-provoking analogy with what we see in this study.

10.6 Is Something *Strange* Going On?

The additional degree of freedom due to strangeness makes possible new classes of composite matter, termed hypermatter. Figure (10-17)[1] shows several of these experimentally found classes of hypermatter. This first step into S(trange)-space is the addition of a single strange particle to an ordinary nucleus which produces the well-studied class of single hypernuclei. One step further leads to doubly strange hypernuclei, recently confirmed using emulsions[2].

[1] Intermediate Energy Nuclear Physics Laboratory, Physics Department, Seoul University
[2] Ken'ichi Imai of Kyoto University

Figure 10.17 Phase Diagram of Nuclear Matter (Experimentally Found) with Strangeness Degree of Freedom

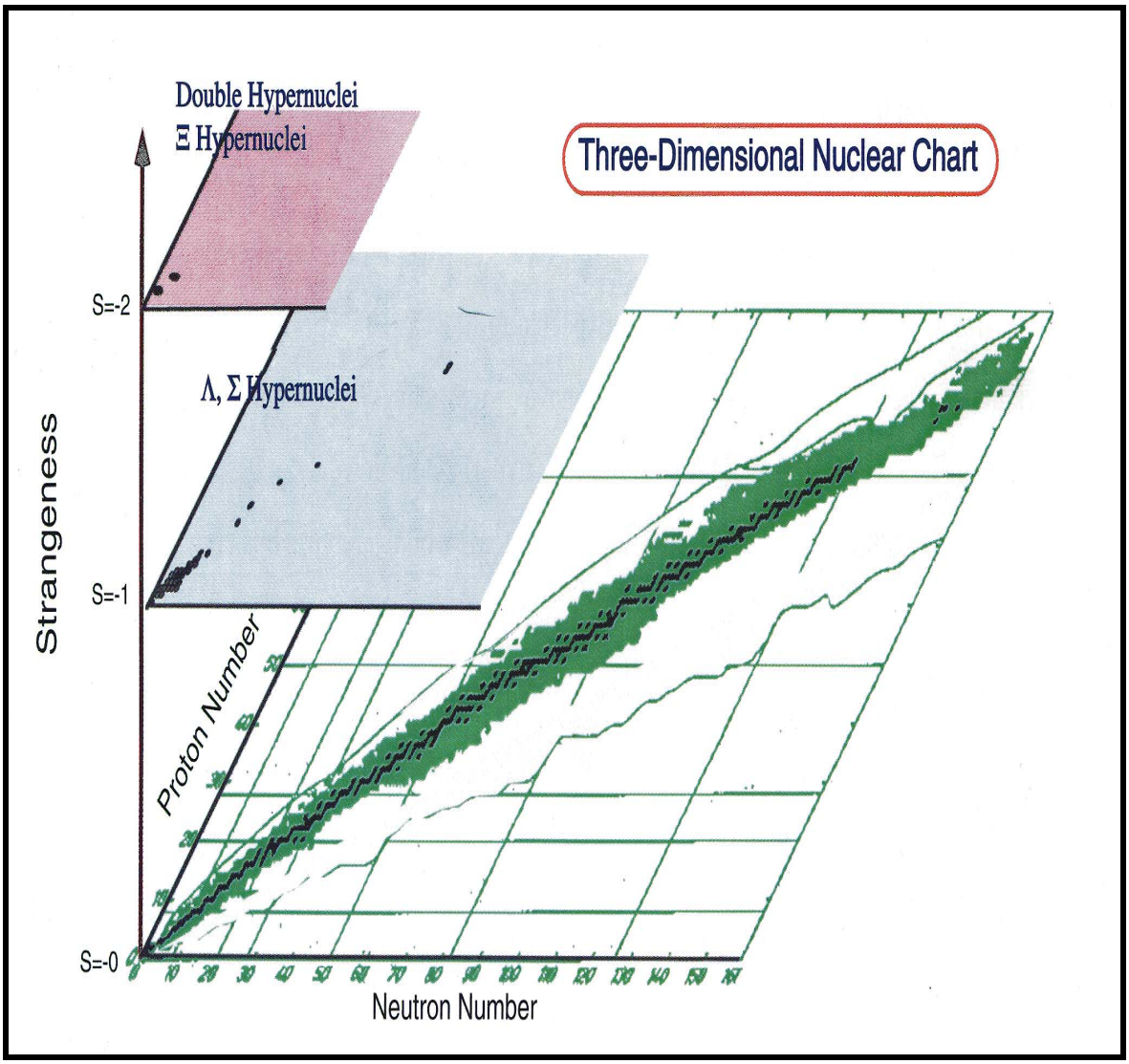

Steps beyond this point have until recently been more theoretical[1] than experimental.

[1] Gerland (1996), Greiner & Schaffner-Bielich (1998), Greiner (1998, 2001)

Figure (10-18) [1] shows several of these new hypothetical classes and their relationship in S-space to 'normal' nuclear matter which lies in the (S=0) Density-Temperature plane.

Figure 10.18 Phase Diagram of Nuclear Matter

(Theoretical with Strangeness Degree of Freedom)

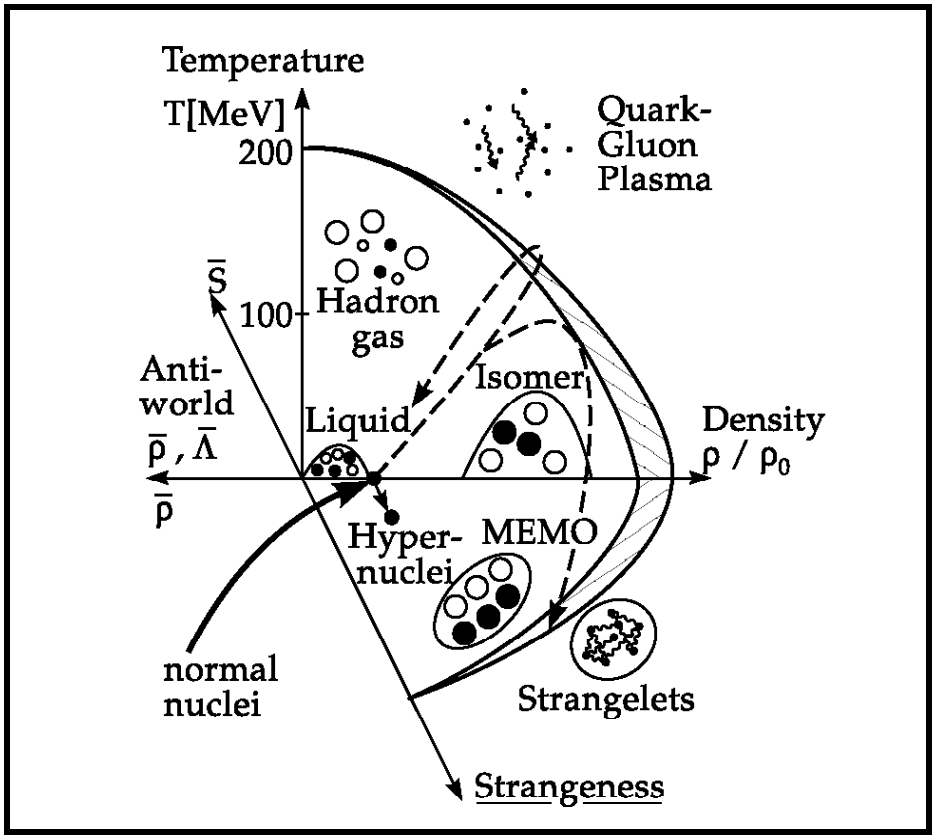

Extensive calculations suggest that some of the finite or bound matter that is further into S-space could in fact have a degree of stability[2]. Two classes in particular have been shown to potentially be able to exist, MEMO's and Strangelets. MEMO's (Metastable Exotic Multihypernuclear Objects) are akin to conventional hypernuclei but with multiple strange particles bound within. Going further still, there is nothing in QCD that would seem to exclude the possibility of multi-quark states as opposed to the upper limit of 3

[1] Bass et al (1998)

[2] Greiner & Schaffner-Bielich (1998)

quarks seen in conventional baryons and mesons. Such strange multi-quark matter, nuclear matter with a number of s-quarks along with the standard u and d quarks, has been termed Strangelets.

Until recently such multi-quark hypermatter was purely speculative. Its existence has been made much more probable, however, by the Chandra (X-Ray) Telescope's observations of the stars RXJ1856 and 3C58. These observations provide the first evidence for 'quark stars': cool stars half the size of neutron stars, with cores now presumed to be made of strange quark matter. Twisting round a telescope now to make a microscope, Schaffner-Bielich (2001) reminds us of the relationship between the astrophysics and the heavy ion physics of strange matter:

> *"If hyperstars exist, strange hadronic matter has to exist and can possibly be formed in relativistic heavy-ion collisions…. If strange stars exist, Strangelets accessible to heavy-ion experiments are likely to be stable, but they are short-lived…"* [1]

The lifetimes of strange particles varies about the 10^{-10} seconds of the weak decay. Kaons (K) have lifetimes from $[10^{-8} – 10^{-11}]$ seconds, while lamdas (Λ) live from $[10^{-10} – 10^{-13}]$ seconds. Comparable to that of a solitary Λ, the measured lifetimes of Λ–hypernuclei are all ~ 10^{-10} seconds. Lifetimes of MEMO's are of course theoretical, but are calculated to similarly be ~10^{-10} seconds. Strangelets have been hypothesized to be both stable and metastable. The latter falls into two categories, short and long-lifetime depending on the decay mode assumed[2]. The short-lifetimes are perhaps $[10^{-7} – 10^{-9}]$ seconds and due to weak hadronic decay, while the longer-lived ones are hypothesized to live $[10^{-4} – 10^{-5}]$ seconds commensurate with weak-leptonic decays.

---

[1] Notwithstanding the fact that compact stars and relativistic heavy ion conditions exist in anti-symmetric regions of Quantum Chromodynamics (QCD) phase-space. Compact stars are regimes of high density and low temperature, while relativistic heavy ion collisions generate regions of high temperatures but low densities. [Schaffner-Bielich, 2001]

[2] Greiner (1998), p. 9, 10

Production rates and cross-sections of these hypotheticals are not dealt with here, but strange particle production is increasingly prodigious in central collisions above 1 A GeV. For example, Greiner and Schaffner-Bielich (1998) estimate that *"on average the occurrence of 20 Λ's, 10 Σ's, and 1 Ξ per event for Au(11.7 A GeV)Au and of 60 Λ's, 40 Σ's, and 5 Ξ per event for Pb(160 A GeV)Pb are expected to be created.* This would seem equivalent to production efficiencies > 10%.

Applying the above to the Copper Calorimetry Experiments, the quantitatively suggestive points are:

1) Energy Thresholds: The ^{24}Na enhancement that we see in the Copper Calorimetry Experiments exists at 1.8 A GeV but does not at 0.9 A GeV. The threshold for strange particle production lies between 1 and 2 A GeV.

2) Time-Scales: The time-scale for the decay of phenomena we seem to be dealing with is ~10^{-9} or 10^{-10}. This is also the time-scale for strange hadronic decays.

3) Distance-Scales: An intriguing correlation with the centimeter-scale resolution of the Copper Calorimetry Experiments is the observation by Gerland et al (1996) on the experimental difficulties in the search for strangelets:

> *Experiments geared to proof the (non)existence of strangelets therefore should clearly cover such short lifetimes. Unfortunately, this is hard due to the large background of charged hadrons at the target in violent events with high multiplicities. To date all experiments concentrate on long flight-path (to minimize background) and large masses, although our prediction is that only metastable strange clusters with cm flight path seem to have a chance of being created.* [1]

[1] Note how the design of the Copper Calorimetry Experiments not only finesses the 'background' problems that Gerland speaks about, but actually makes use of them.

4) Production Rates: Production rates for strange particles of [.1 - .3] per central collision at higher energies, along with hints of enhanced K production rates at sub-threshold conditions leads to the following intuitive leap:

> **For secondaries of heavy ion collisions greater than ~ 1A GeV a sub-threshold strange hadronic complex can come into existence for a short period of time (10^{-9} – 10^{-10} seconds). During this brief lifetime these sub-threshold complexes have the ability to catalyze changes 'from the ordinary' in subsequent nuclear interactions.**

Chapters 9 and 10 suggest that to explain the results of the Copper Calorimetry Experiments a 10% order-of-magnitude subpopulation of $Z \geq 2$ secondaries is needed to have an enhanced production cross-section. Along with a much greater production of strange matter, central and near-central events yield a greater multiplicity of fragmentation. It is not inconceivable then that if such short-lived sub-threshold strange effects exist, a subpopulation of secondaries having them is actually produced in sufficient quantity. *If strange hadronic matter does actually exist, it would seem that one of its likely manifestations would be a difference in partial production cross-sections (i.e. a redistribution of channel probabilities).*

More qualitatively suggestive and intuitive points include:

5) Phase Transitions: Some form of phase transition may be involved. The canonical one to invoke is the still-to-be found Quark-Gluon Plasma phase transition, especially since strange particle emission is one of the consequences of this transition. Yet it has also been found that extensive kaon production occurs at the border of hot dense regions of nuclear matter (that need not be the QGP). And if strange hadronic matter (MEMO's for example) actually exists in relativistic heavy ion collisions it too need not be a direct consequence of the QGP, but instead be due to a coalescence of hyperons[1].

[1] Schaffner-Bielich, (1998)

6) New Channels: Our results can be looked at as the opening of a new channel. Having a new degree of freedom (strangeness) allows this to naturally occur.

7) Resonance: Alternatively, one can look at our results as an analogue to low-energy resonance-like behavior occurring at higher energies (but in a region where it's not 'supposed' to). This 'resonance' may be more 'acceptable' if it occurs in a region of phase-space where the threshold of a new degree of freedom has just been crossed. (For with regard to that new degree of freedom, such a 'resonance' will be a 'low-energy' effect.)

8) Newly Discovered Stars of Strange Quark Matter: The increasingly likely existence of bulk strange matter vis-à-vis 'quark stars' does not directly inform our particular circumstances; but it does suggest that the existence of cooperative strange matter must be taken more seriously.

It must be noted however that the above discussion on the possible role of strangeness is a conceptual riff initiated by the seemingly congruent lifetimes, energy thresholds, and production efficiencies between strange matter and the phenomena under study. It need not, of course, be the 'actual' solution for what is going on in the Copper Calorimetry Experiments. But following one of the classic texts on qualitative measurement[1]:

Isabella: Is it not strange, and strange?
Duke: Nay, it is ten times strange.
Isabella: Then this is all as true as it is strange…
(though) I should not think it strange; for 'tis a physic

[1] Shakespeare, (1623) *Measure for Measure*

XI Alternative Phenomenological Models

Although the fit of the above model seems exceptional and the inferred physics is intriguing, alternative phenomenologies must be investigated. Without for the moment saying whether it makes numerical, phenomenological, or physical sense…one other class of model could logically exist. This new model class still requires an enhanced production of ^{24}Na; but in this case the property would be carried by the subpopulation shower particles rather than the secondary heavy ion fragments.

The line of logic follows from the fact that in the 1.8 A GeV two-block experiment $R_0 > R_{20}$. This can logically come about in two distinct ways. The first is for the same number of particles to pass through both blocks, but with the ^{24}Na-producing enhancement restricted to the first blocks due to an appropriately scaled decay time. This possibility has been extensively discussed above. The alternative logical possibility is that as the second block moves away from the first block a different number (or population) of ^{24}Na-enhancing particles traverses the second block relative to the first.

This particular logic warrants a closer examination due to the observation that for the Z=1 shower particles (protons, neutrons, and pions) there are two different subpopulations. The shower particles themselves tend to be 'evaporation'-residues and as such are initially isotropically distributed in the projectile-frame; and highly peaked forward in the laboratory-frame. The essential difference in subpopulations is the degree of intra-nuclear scattering suffered by the shower particle during the projectile-target collision. The subpopulation of shower particles which have not suffered intra-nuclear collisions follows a path essentially co-linear with the $Z \geq 2$ heavy fragments. But there is also a subpopulation of shower particles which will have suffered interactions with target nucleons sufficient to change the angle of their trajectory. This latter population is easily seen in Figure 10-3 as the wide-angle (scattering) yellow trajectories. Nominally, the dividing line between the two populations is a trajectory with a polar angle of ~12 degrees.

This is important to our reasoning for particles emitted in the first block with a polar angle greater than 12 degrees will miss the second block situated at 20 cm. If the second block is in the adjacent R_0 position, a polar angle of >60 degrees of emission is required to miss the second block.

Hence one could in principle consider the possibility that (for unknown reasons due to their different physical history) only the shower particles >12 degrees have ^{24}Na-enhancing properties. This would allow the production of an enhanced R_0 along with a reduced R_{20}..

But before one worries about what could be causing such an effect, we must see if this model class can phenomenologically reproduce the observed measurements.

11.1 The Shower-Particle Model

Preliminary simulations have been done of this conceptual possibility, but the results using the current versions of *BFHL* are considerably less satisfying than those of the heavy-fragment model. Two simplified shower particle models were run for each of the two-block and cylinder geometries.

Only the shower particles are given an enhanced production cross-section, a factor **Q** times their 'normal' one

$$\textit{Enhanced Production Cross-Section} = Q\sigma_p(E_k) \tag{11.1}$$

where the 'normal' one, $\sigma_p(E_k)$, is

$$\sigma_p(E_k) = e^{-0.17+2.5u-1.22u^2} \tag{11.2}$$

and where $u = ln(E_k)$ and pions are assumed to behave identically to protons.

All Z≥2 fragments behave 'normally', including having a 'normal' production cross-section of $\sigma_F(A) \cong 3.6A^{0.387}$. (See Section 7.1 for the extended discussion of ^{24}Na production cross-sections.) Two populations of shower particles have been considered:

1) All shower particles have an enhanced production cross-section ($Q\sigma_p$)
2) Only shower particles with a polar angle ≥ 12 degrees have an enhanced production cross-section ($Q\sigma_p$)

The first of these models we shall call the *All Shower Particles* model or 'ASP'.
The second is termed the *Wide Angle Only* model or 'WAPO'.

Each of the simulations also included:

i) The twinning approximation to neutron production
ii) A centrally placed, orthogonal primary beam with a geometric dispersion of $\sigma_{beam}=1$
iii) An energy over-approximation of 1.8 GeV per shower particle
iv) No loss of energy per collision

For comparison, recall the 1.8 A GeV experimental values from Table 9.2:

$$\begin{aligned} R_0 &= 1.501 \pm 0.008 \\ R_{20} &= 1.251 \pm 0.020 \\ R_{Ring\text{-}20} &= 0.071 \pm 0.005 \end{aligned} \qquad (11.3)$$

All Shower Particles **Model**

Giving all secondary shower particles a production cross-section enhanced by a factor Q yields the results in Figure 11.1. It is seen that for Q = [10 – 15] there is a rough matching of the values of R_0 and R_{20} (though R_0 is actually too large for a desired R_{20}). What is most interesting here is that $R_{Ring\text{-}20}$ also has the right order of magnitude (~ 0.1).

Figure 11.1 **R_0 vs. Production Cross-Section Enhancement**

(All Shower Particles)

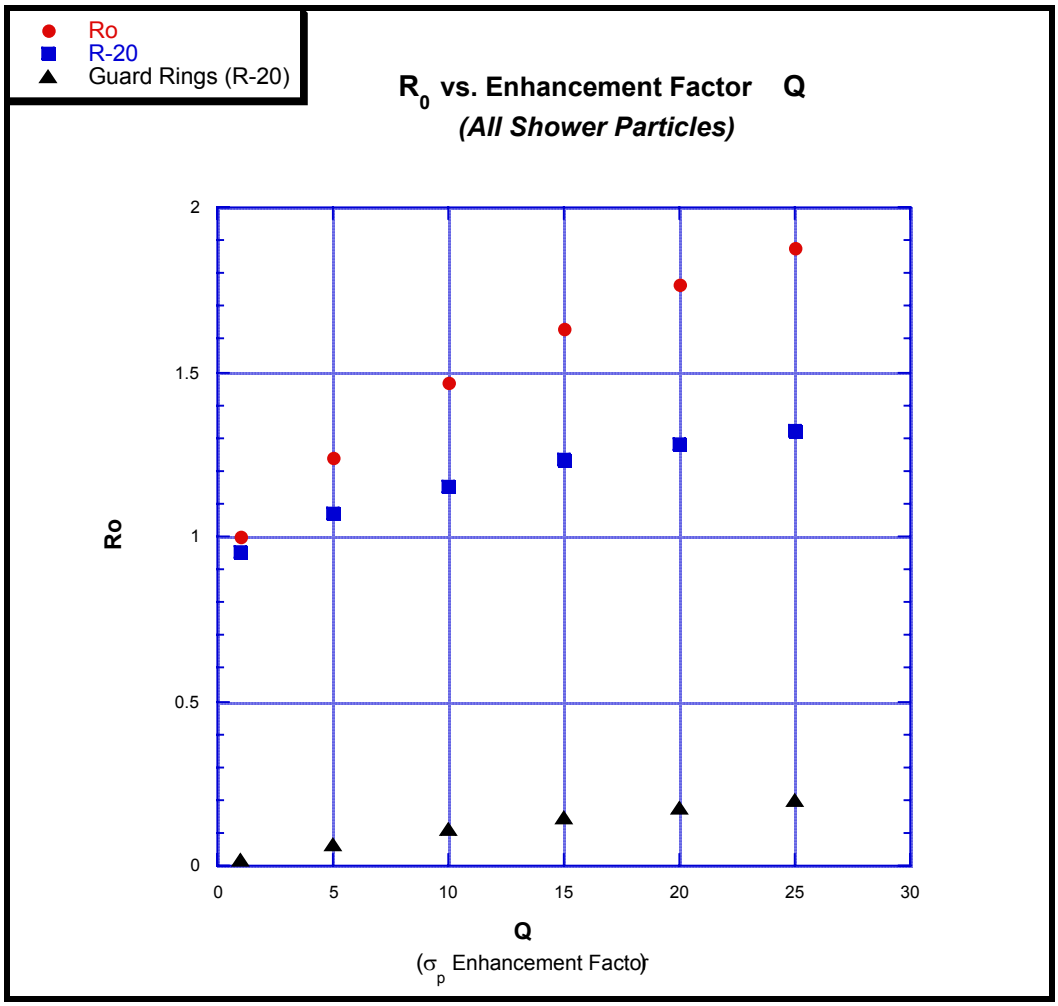

It turns out that for subpopulations of shower particles in this model, a similarly crude "matching" of values occurs whenever the product

(% Subpopulation) x (Q-value) = [10 –11] (10.3)

This is explored more explicitly in Table 11.1 below from which a number of interesting points can be surmised. The first is yet another example of the constantly performed quality control and consistency checks. The two highlighted lines of {Subpopulation, Q} equal to {0,1} and {1,1} give identical simulation results…as well they should. {Subpopulation, Q} = {0,1} means that there is 0% subpopulation, so all secondaries behave 'normally'. Equivalent to the situation where all secondaries behave 'normally', {Subpopulation, Q} = {1,1} means that 100% of the subpopulation has an enhancement factor equal to one. The fact that physically identical populations calculated by completely different computational routes is a necessary reassurance to the internal consistency of both the program and the overall computational approach.

Secondly, it is seen that the experimentally obtained R_0 values are almost exactly generated by the condition (% Subpopulation) x (Q-value) = [10 –11]. This is equivalent to saying that there is a necessary integrated enhancement of ^{24}Na of about 10.

Nonetheless, R_0 and R_{20} don't exactly match up in these results. (For a given percentage of subpopulation the best fit is bold-faced.) For $R_0 \sim 1.5$, R_{20} is consistently too low by 4 times the experimental error bars. (The simulation errors are not listed in Table 10.2 because they are formally so small, $\leq 10^{-3}$.) And the simulation values for the guard rings, although 'in the neighborhood' of the experimental values are too large by 10 times the experimental errors. Nonetheless, these simulation results demonstrate that this overall approach does give 'ball-park' figures without relying on a decay phenomena as does the heavy-fragment approach.

Table 11.1 Simulations of Production Cross-Section Enhancement for *All Shower Particles* Model

Subpopulation (1=100%)	*Q*	*(% x Q)*	*Ro*	*R-20*	*Guard Ring (0 cm)*	*Guard Ring (20 cm)*
0	**1**	**0**	**0.9984**	**0.9525**	**0.0002**	**0.0155**
0.1	10	1	1.0573	0.9959	0.0003	0.0279
0.1	20	2	1.1225	1.007	0.0004	0.0407
0.1	50	5	1.2805	1.0816	0.0005	0.0753
0.1	**100**	**10**	**1.4941**	**1.1715**	**0.0008**	**0.128**
0.2	10	2	1.1152	1.0071	0.0003	0.0409
0.2	20	4	1.2162	1.0539	0.0006	0.0628
0.2	**50**	**10**	**1.4974**	**1.1785**	**0.0005**	**0.1189**
0.2	100	20	1.7685	1.2923	0.0008	0.179
0.3	10	3	1.1617	1.0239	0.0004	0.0522
0.3	20	6	1.3146	1.0946	0.0007	0.0852
0.3	30	9	1.4423	1.1456	0.0007	0.1109
0.3	**35**	**10.5**	**1.487**	**1.183**	**0.0006**	**0.1197**
0.3	**36**	**10.8**	**1.5173**	**1.1823**	**0.0008**	**0.1251**
0.3	40	12	1.5582	1.2003	0.0008	0.1338
0.3	50	15	1.6579	1.2354	0.0012	0.1551
0.3	100	30	1.9571	1.3777	0.0009	0.2213
0.4	20	8	1.4032	1.129	0.0008	0.1023
0.4	25	10	1.473	1.1775	0.0006	0.1148
0.4	**27**	**10.8**	**1.5099**	**1.1759**	**0.0009**	**0.1252**
0.4	30	12	1.5584	1.1988	0.0007	0.1336
0.5	10	5	1.2637	1.0677	0.0006	0.0713
0.5	15	7.5	1.3754	1.1336	0.0005	0.0941
0.5	20	10	1.4839	1.1664	0.0007	0.1181
0.5	**21**	**10.5**	**1.4972**	**1.1697**	**0.0009**	**0.121**
0.5	22	11	1.5158	1.1775	0.0009	0.1248
0.5	25	12.5	1.5638	1.2075	0.0007	0.1353
0,5	30	15	1.6472	1.2334	0,0008	0.1479

Subpopulation (1=100%)	*Q*	*(% x Q)*	*Ro*	*R-20*	*Guard Ring (0 cm)*	*Guard Ring (20 cm)*
0.6	10	6	1.3084	1.0863	0.0006	0.0804
0.6	15	9	1.4363	1.1607	0.0006	0.1065
0.6	17	10.2	1.482	1.1809	0.0006	0.1161
0.6	**18**	**10.8**	**1.5062**	**1.1717**	**0.0009**	**0.1221**
0.6	20	12	1.5511	1.1939	0.0008	0.1321
0.6	25	15	1.642	1.2412	0.0008	0.1508
0.6	30	18	1.722	1.2667	0.001	0.1647
0.7	5	3.5	1.1739	1.0279	0.0004	0.0519
0.7	10	7	1.3517	1.1209	0.0005	0.0884
0.7	**15**	**10.5**	**1.4953**	**1.1695**	**0.0007**	**0.1198**
0.7	20	14	1.611	1.2271	0.0008	0.144
0.7	25	17.5	1.7092	1.2585	0.001	0.1625
0.8	5	4	1.1965	1.0378	0.0005	0.0566
0.8	10	8	1.3917	1.137	0.0005	0.0965
0.8	13	10.4	1.4876	1.1669	0.0007	0.1181
0.8	**13.5**	**10.8**	**1.5011**	**1.1691**	**0.0008**	**0.1201**
0.8	14	11.2	1.5155	1.1899	0.0006	0.1223
0.8	15	12	1.5448	1.1918	0.0008	0.1301
0.8	20	16	1.6684	1.251	0.0008	0.156
0.8	25	20	1.7702	1.2823	0.001	0.1754
0.9	5	4.5	1.2177	1.0469	0.0005	0.061
0.9	10	9	1.4296	1.1518	0.0005	0.1046
0.9	**12**	**10.8**	**1.5001**	**1.1691**	**0.0007**	**0.1201**
0.9	15	13.5	1.5912	1.2088	0.0008	0.1394
0.9	20	18	1.7182	1.2717	0.0008	0.1668
0.9	25	23.5	1.8262	1.3034	0.001	0.1874
1	**1**	**1**	**0.9984**	**0.9525**	**0.0002**	**0.0155**
1	5	5	1.24	1.0719	0.0004	0.0657
1	10	10	1.4672	1.1543	0.0007	0.1131
1	**11**	**11**	**1.4992**	**1.1835**	**0.0006**	**0.1201**
1	12	12	1.5393	1.1846	0.0008	0.1285
1	15	15	1.6295	1.2322	0.0008	0.1488
1	20	20	1.7661	1.2797	0.001	0.1757
1	25	25	1.8746	1.3214	0.0011	0.2014

Wide Angle Only **Model**

Applying now the model where only the wide-angle shower particles have the enhancement Q > 1 a critical problem becomes evident.

Figure 11.2 R_0 vs. Production Cross-Section Enhancement
(Wide Angle Shower Particles Only)

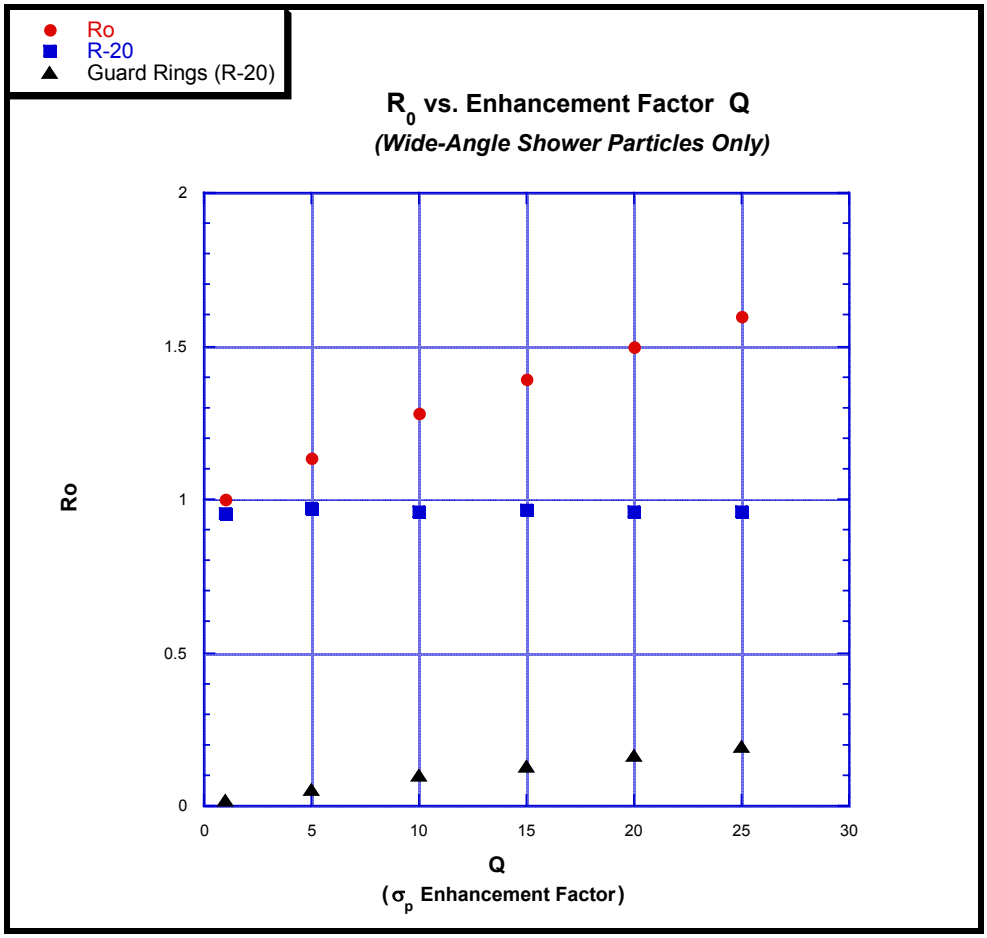

In this model, Q ~20 for R_0 ~1.5, but no possible fit exists for R_{20}. Indeed, NO value of Q generates an $R_{20} > 1$. **Based on this alone we should in principle consider the "Wide-Angle Only" shower particle model to be phenomenologically untenable**.

Interestingly, like the ASP model R_0 has the right order of magnitude. This suggests the obvious likelihood that in this class of models the source of the $R_{Ring\text{-}20}$ fit are the shower particles greater than 12 degrees.

The next critical question is obvious: how well does the general class of shower particle models fit the cylinder geometry? For it is likely that the multi-stage amplifier attribute of the cylinder can again be put into service to delineate the phenomenologically possible from the impossible.

11.2 Shower Particle Models Applied to the Cylinder

Simulations have been done with both shower particle models. And both the '*All Shower-Particle'* and the *"Wide-Angle Only"* model quantitatively fail the cylinder tests. The problem of each is the same. Any simulation which matches the R_0 value has R-values for the other segments much larger in value than observed; qualitatively suggesting a rising cascade with a slow dying off only at the end of the cylinder. This can be seen for the '*All Shower-Particle'* model in Figure 11.3 which has a 100% 'subpopulation' with Q=10.

Figure 11.3 R-Values for a Cylinder with *'All Shower-Particle'* Model

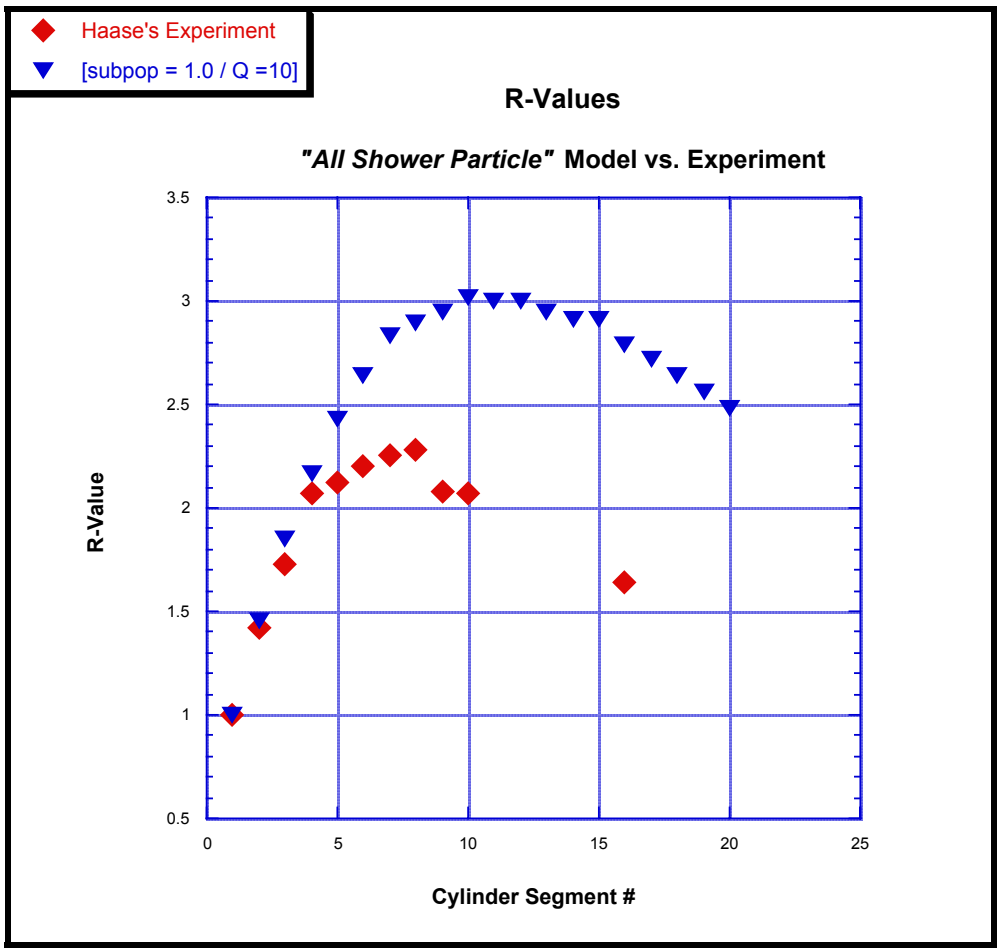

The ASP model's fit to the R-value of the second cylinder block is quite good (by definition of the fits selected!), but beyond that lies a rapid divergence. As Figure 11.4 clearly shows, this is representative of all simulation results for the ASP model*.

Figure 11.4 R-Values for a Cylinder with *'All Shower-Particle'* Model

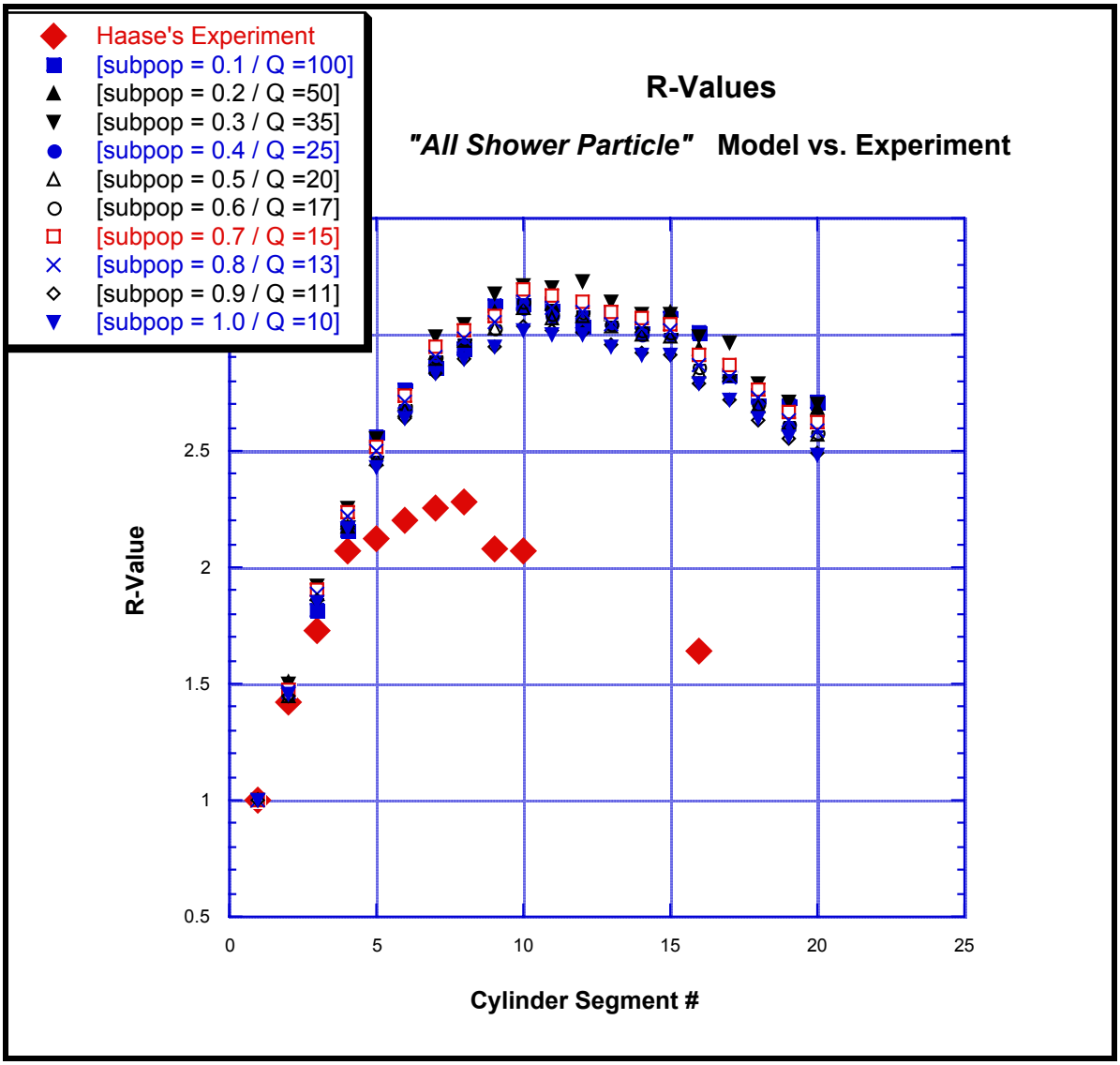

* Individual curves can be found in Appendix C.

Salient qualitative points are a faster and more sustained rise than experimentally seen, as well as a slower drop-off. This is characteristic of what one would expect from a cascade of shower particles that grows nonlinearly faster than its parent (the primary beam and secondary heavy ion fragments). The maximum peak value is greater by ~50% and shifted several blocks down-beam. This lag in position of the shower particles' cascade-maximum behind that of the parent beam (primary ions and fragments) is also what one would expect from such a non-linear birth. Allowing a nominal 5% error for the smallest subpopulation examined (10% with Q=100) the lack of fit for the class as a whole is underlined.

Figure 11.5 R-Values for a Cylinder with *'All Shower-Particle'* Model

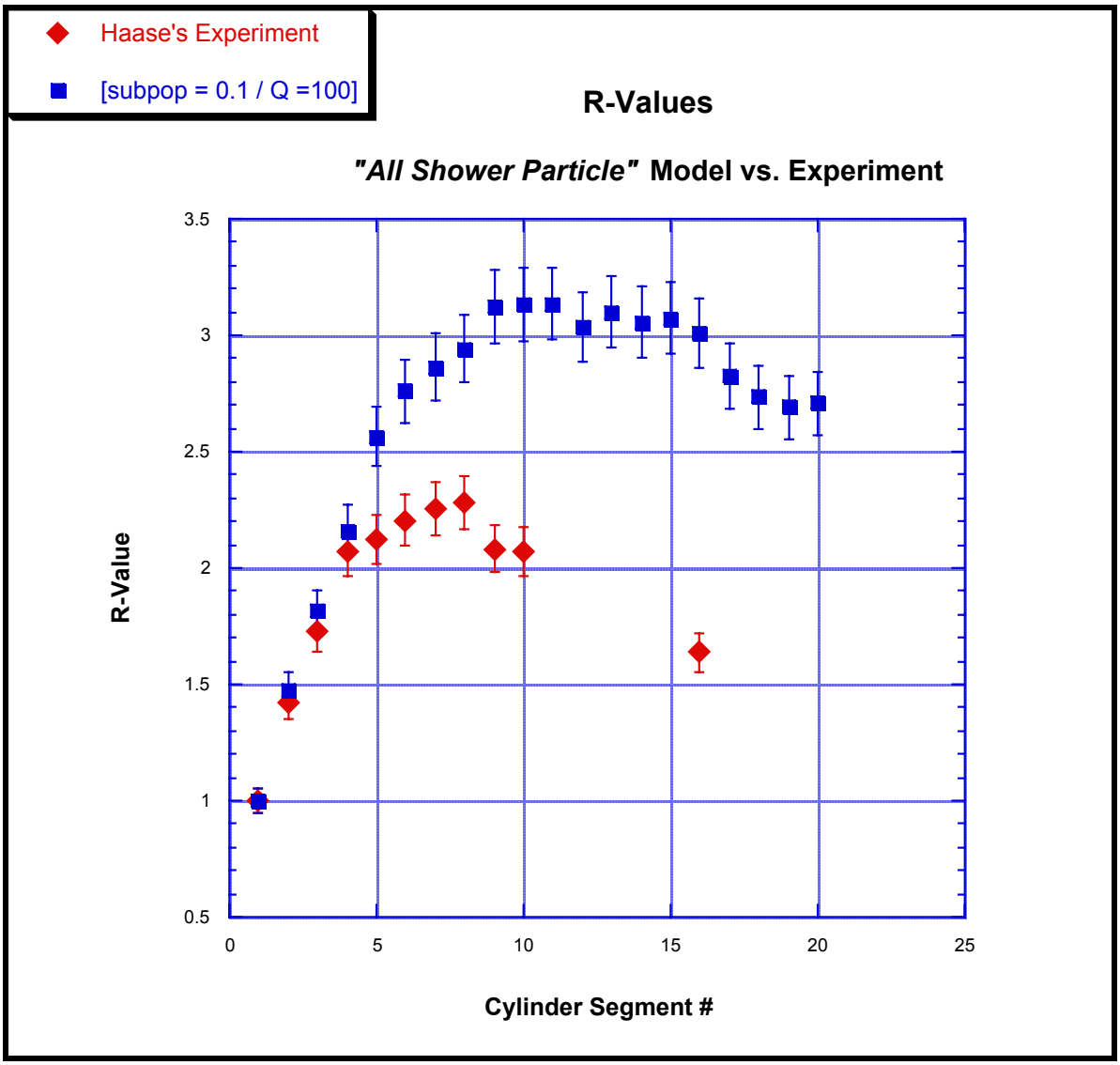

Application of the *"Wide-Angle Only"* model yields similar results. A 100% 'subpopulation' is shown along with a computational convergence test that further demonstrates that the lack of fit is not the result of a computational fluctuation.

Figure 11.6 R-Values for a Cylinder with *"Wide-Angle Only"* Model

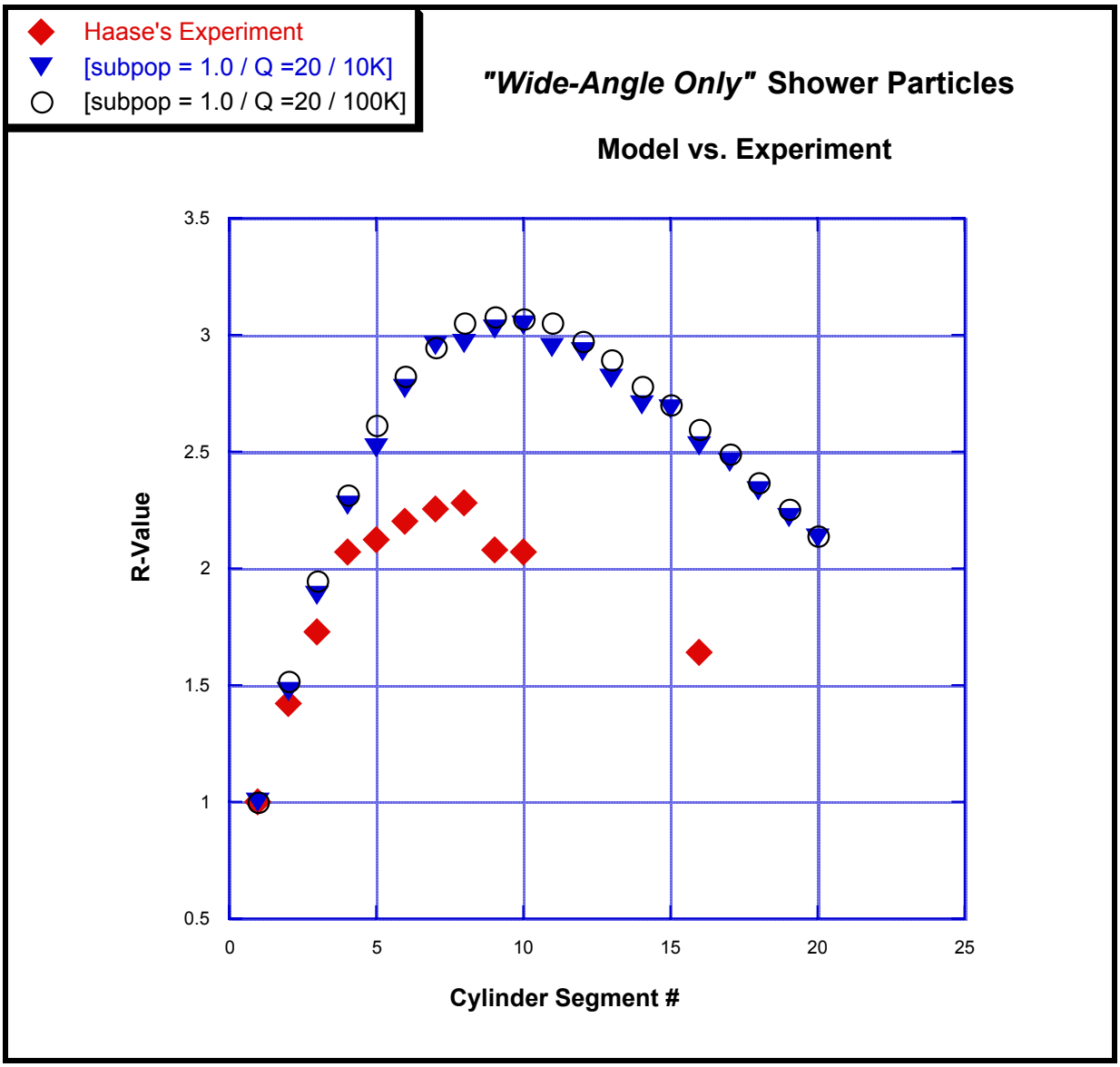

Relative to the '*All Shower-Particle'* model there is a similar fast rise, but a faster drop-off after the cascade-maximum. The cascade maximum of the *"Wide-Angle Only"* model is also shifted to the right of the experimental values but less so than that of the '*All Shower-Particle'* model. This is to be expected as there is no enhancement contribution from any of the protons < 12 degrees. Subpopulations behave in a similar manner with a representative illustration below. Appendix C includes a suite of the other simulations of the *Wide-Angle Only* model for subpopulations ranging from 10% – 100%.

Figure 11.7 R-Values for a Cylinder with *"Wide-Angle Only"* Model

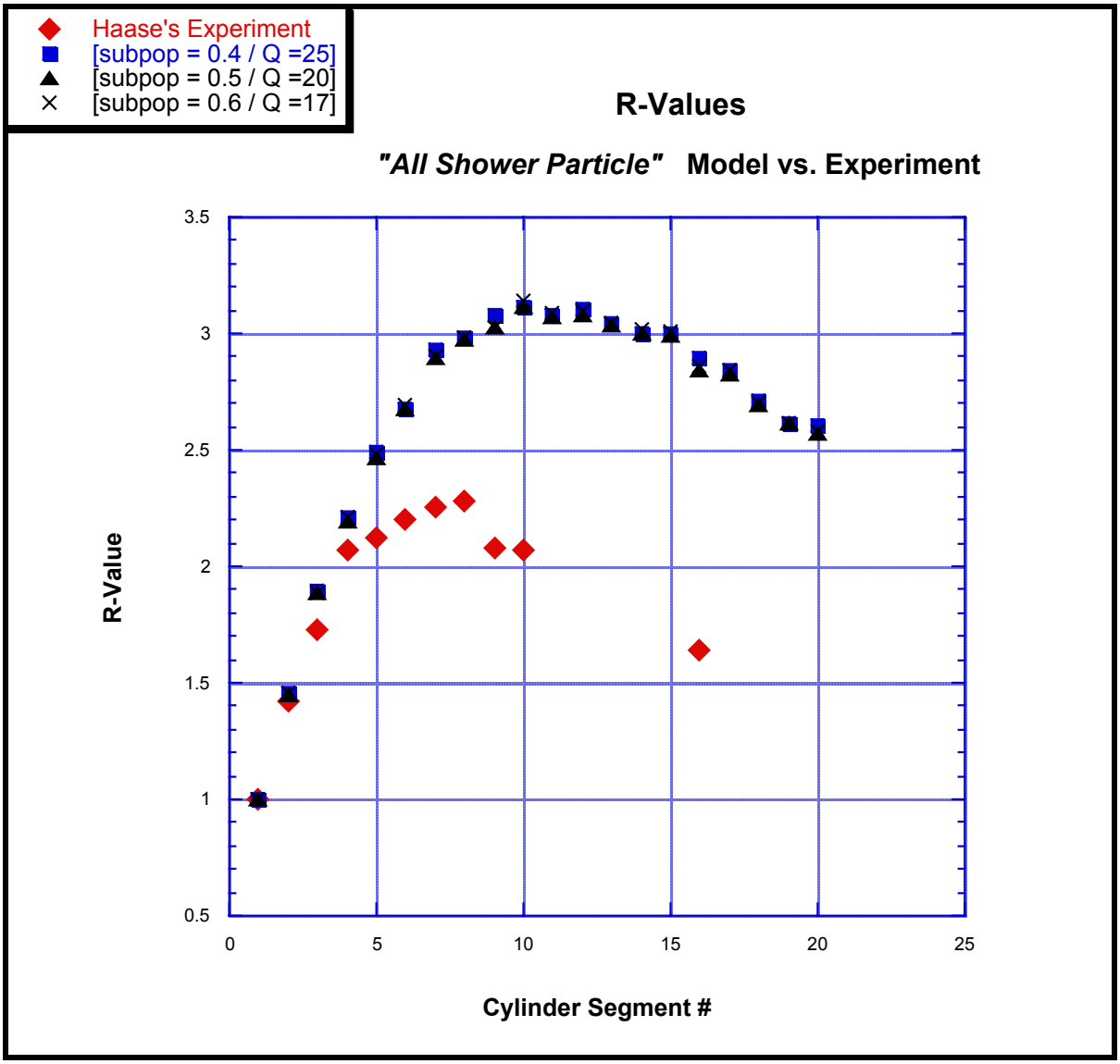

11.3 Discussion of Shower Particle Models

The *All Shower Particle* model which gave an enhanced production cross-section to every shower particle "sort of" fits the two-block experiment but it doesn't fit the cylinder. The *Wide-Angle Only* model DID NOT fit the two-block experiment, insofar as R_{20} was incapable of being reproduced, nor does it fit the cylinder experimental data.
By itself this might be enough to eliminate from consideration the shower particle enhanced production cross-section models.

But it must be pointed out that in the current set of simulations the secondary particles (fragments and shower particles) do not lose energy as they propagate through the target. This is a reasonable approximation for the fragments since they lose only a few hundred MeV in any collisions. But this is not so for the wide-angle shower particles which lose their initial energy within a few collisions and hence fall below the energy threshold required to make ^{24}Na.

Still operating in the fairy tale land of phenomenology we must ask if a quenching of ^{24}Na. production due to the energy dissipation of the shower particles might bring the shower models into the possibility of a fit? Could the energy loss of the shower particles offer a functional equivalent to the hypothesized 10^{-9} second decay introduced in the heavy ions enhanced production cross-section model? The next incarnation of the simulation programs is already being designed to take these possibilities into account, modelling both the energy dissipation of colliding shower particles as well as the time-decay of hypothetical cross-sectional properties. Stay tuned for more.

But the overall shape of the curves we see in this second class of potential solutions (the shower particle models) may be immediately useful in a more fundamental way. Recall from Figure 10.12 that 'ordinary' 1.8A GeV shower particles in a cylinder geometry generate a monotonically decreasing curve of R-values. It is conceptually striking that any and all of the models attributing to shower particles an enhanced production cross-section transforms their R-value curves into ones qualitatively similar to those seen experimentally (Figure 11.8).

This qualitative transformation seems to buttress the likelihood that some form of production cross-section enhancement is involved. But for now the evidence seems to support the principal role of heavy ions in whatever is going on.

Figure 11.8 Experimental Results vs. Enhanced σ_p Model Classes

(1.8 A GeV ^{40}Ar on a Copper Cylinder)

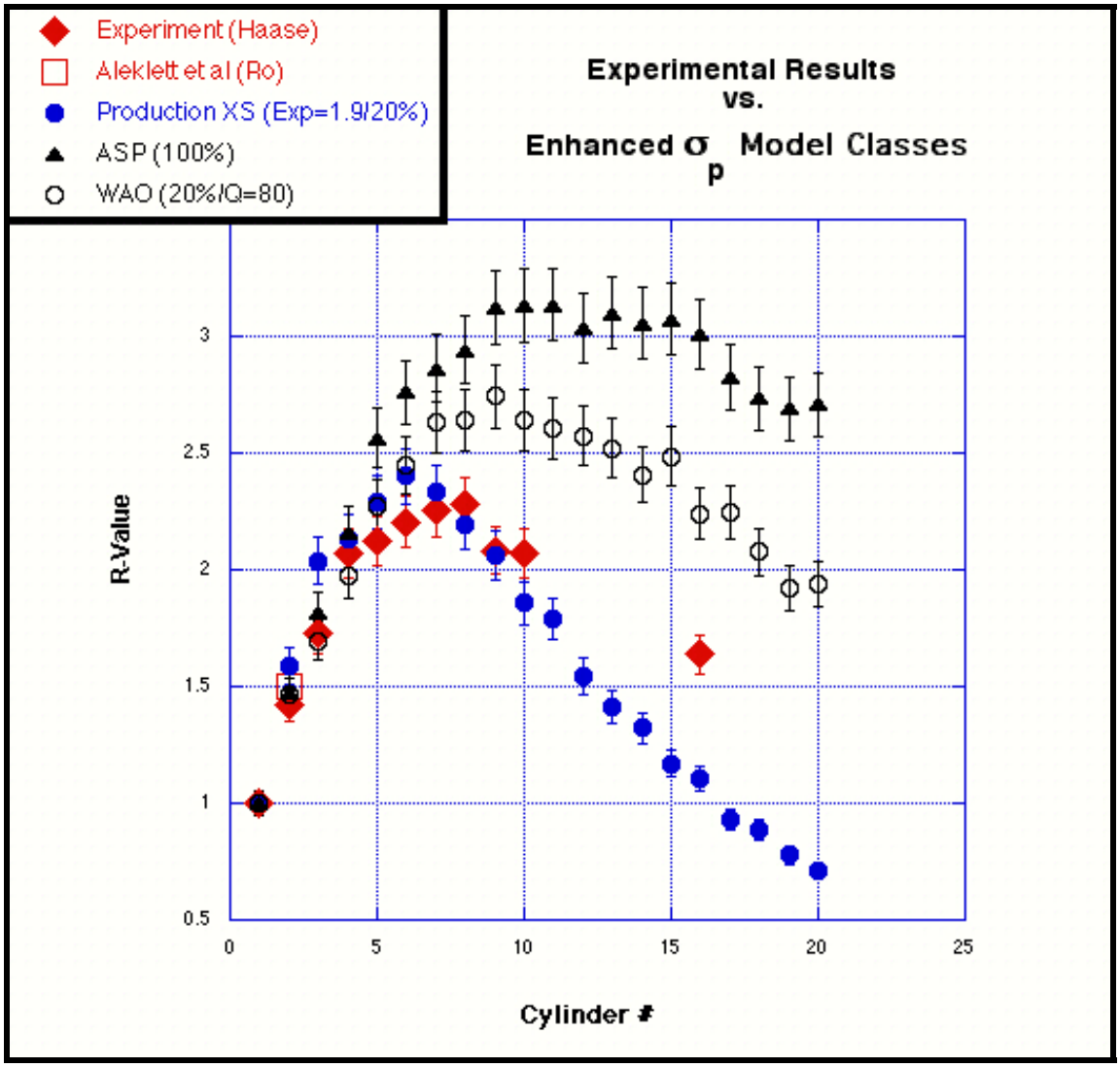

It must be emphasized that we are dealing here with partial cross-sections. Standard conservation principles are assumed to apply. By baryon conservation, for example, an enhancement in one set of production cross-sections must be compensated for by a decrease in those of other channels. An example: looking at the spectrum of R_0 values for the target residues involved[1], perhaps what is being manifested is an increase in the probability for symmetric fission (give or take a few alphas and shower particles). A commensurate decrease in other channels would then be expected. In summary then,

Figure 11.9 Comparison of R-values between Model Classes and Experiment

(1.8 A GeV ^{40}Ar on a Copper Cylinder)

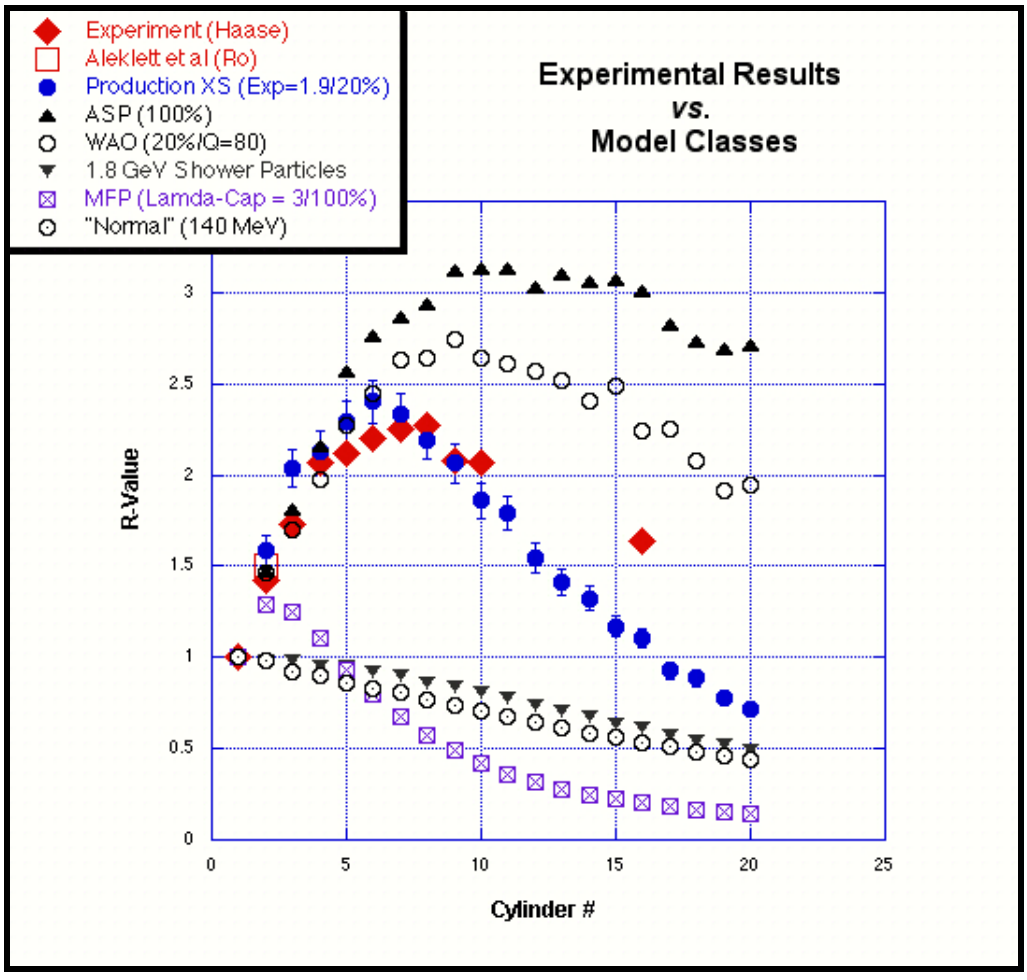

[1] Aleklett et al. (1987, 1988a,b)

Whatever is happening and whomever it is happening to, in the context of our basic experimental, theoretical, and phenomenological approach: **in the Copper Calorimetry Experiments performed, the symmetry of identity of nuclear interactions appears to be broken between the primary and secondary populations; and/or there are non-linear collective effects in these interactions that are doing by conventional standards some rather unusual things.**

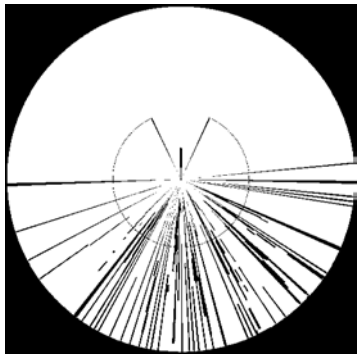

Appendix A

Mean Characteristics of Events
(Graphical Analyses & Statistics)

Scanning and measurements performed by the

High Energy Astrophysics Group

of the

Institute of Space Research (Bucharest, Romania)

Dr. Maria Haiduc

Group Head and Scanning Supervisor

High Energy Astrophysics Group

of the

Institute of Space Research (Bucharest, Romania)

Dr. Dumitru Hasegan: Director of the Institute of Space Research

Dr. Maria Haiduc: Group Head and Scanning Supervisor

Physicists

Andrei Gheata: Charge measurements including the design and implementation of the methodology for the photometer.

Mihaela Gheata: Management of the data. Also transformed data from the computer on-line with the microscope to formats usable by the programs.

Hardware

Mircea Ciobanu: Built the electronics for the semi-automatic system for geometry measurements under the KSM microscope.

Octav Anghelescu: Maintenance and improvements of the semiautomatic system, including the optics.

Igor Marin (DUBNA): Kept the KSM microscopes in repair.

Scanners

Mariana Boca: Scanning and drawing events.

Veronica Catrina: Scanning, delta ray counting, geometry measurements.

Aurelia Cristescu: Scanning and back scanning. Measurements on ionization for almost all the data (on light nuclei – gap length measurements as well as blob counting; on relativistic particles – grain and blob counting).

Anica Georgescu: Scanning, geometry, multiple scattering.

Ana Golea: Manager of handling the emulsions, planning the operations, keeping the reference book on events. Data integrity and quality control checks on the computer. Scanning and back scanning.

Sabina Herisanu: Drew almost every events. Also geometry.

Valeria Mocanu: Data entry for geometry (until the semi-automatic system was brought into function – about 2 years); then data entry for gap counting.

Ala Neagu: Scanning and geometry measurements.

Lidmila Sava: Scanning and charge measurements by delta ray counting and photometer.

Cristina Savu: Scanning and charge measurements by delta ray counting and photometer. Back scanning and gap counting on light fragments.

Diaconescu Tereza: Scanning.

Mean Characteristics of Events

1.8 A GeV ^{40}Ar Projectiles in Nuclear Emulsion

	All events **(Lerman)**	***$N_h \leq 8$*** ***(Lerman)***	***$N_h \leq 9$*** ***(Lerman)***
$\langle N_h \rangle$	***8.9 ± 0.3***	***2.9±0.1***	***21.79 ± 0.5***
$\langle n_s \rangle$	***9.8±0.3***	***6.0±0.2***	***17.8±0.6***
$\langle n_\alpha \rangle$	***1.19 ± 0.04***	***1.17 ± 0.05***	***1.2 ± 0.05***
$\langle \theta_s^o \rangle$	***19.8 ± 0.19***	***14.5 ± 0.25***	***23.6 ± 0.26***
$\langle \theta_\alpha^o \rangle$	***1.9 ± 0.04***	***1.8 ± 0.05***	***2.1 ± 0.08***
$\langle Z_{F,Z>2} \rangle$	***11.49 ± 0.18***	**12.0±0.2**	***8.7 ± 0.36***

As in Chapter 4

$\mathbf{N_h} = N_{black} + N_{grey}$

$\mathbf{N_s} = N_{shower}$

$N_\alpha = N_{alpha}$

and from Aleklett et al (1988) θ_s^o and θ_α^o are the critical angles for shower particles and alphas respectively; while $\mathbf{Z_{F,Z>2}}$ is the charge of projectile fragments with $Z > 2$.

Bibliography

Aleklett, K., et al. "Au Target Fragmentation at Intermediate Energies." In *6th High Energy Heavy Ion Study and 2nd Workshop on Anomalons:* LBL-16281, (1983): p. 337

———. "Unusual Behavior of Projectile Fragments Produced by the Interactions of Relativistic Ar Ions with Copper." preprint LBL-22422, (1987).

———. "Unusual Behavior of Projectile Fragments Produced by the Interactions of Relativistic Ar Ions with Copper." *Physical Review C* vol. 38, no. 4 (1988a): p. 1658

———. "Investigation of the Unusual Behavior of Projectile Fragments Using Nuclear Chemistry Techniques." *Journal of Radioanalytical and Nuclear Chemistry* vol. 122, no. 2 (1988b): p. 355

Bánó, M., et al. "Further Evidence for the Anomalous Interaction of ^{3}He Secondary Nuclei with Protons." *Physics Letters B* (1987).

Barkas, W. *Nuclear Research Emulsions*. vol. 1, New York, (1963).

Barr, Lawrence Berkeley Laboratory, UCRL-3793, (1957).

Bass, S.A. et al. "Microscopic Models for Ultrarelativistic Heavy Ion Collisions." Prog. Part. Nucl. Phys. 41 (1998): 225.

Bayman, B.F., and Tang, Y.C. "Anomalons in Relativistic Heavy-Ion Collisions." Minneapolis, Minnesota: School of Physics, Universtiy of Minnesota, (1987).

Beckmann, R. "Untersuchungen Von Schwerionenreaktionen Bei Hohen Energien Im Rahmen Des Hot Spot Modells Und Mit Hilfe Der Simulation Eines Kernchemischen Experimentes Zum Anomalonenproblem." Dissertation, Philipps University, (1984).

Becquerel, A.H. "On the Rays Emitted by Phosphorescence." *Comptes Rendus* 122 (1896a): p. 420

Becquerel, A.H. "On the Invisible Rays Emitted by Phosphorescent Bodies." *Comptes Rendus* 122 (1896b): p. 501

Beri, S. B., et al. "The Mean Free Path of Relativistic Fragments from Heavy Ion Reactions Induced by 1.8 A Gev ^{40}Ar in Low Sensitive Nuclear Emulsion." In *6th High Energy Heavy Ion Study and 2nd Workshop on Anomalons:* LBL, (1983): p. 27

Bisplinghoff, B. "Neutron Generation in an Extended Cu Target Irradiated with 22 and 44 GeV Carbon Ions (Preliminary Results)." *Istopenpraxis Enviornmental Health Studies* vol. 30 (1994): p. 29

Bohr, N. “Neutron Capture and Nuclear Constitution.” Nature 137 (1936): p. 344

Bowman, C. D. "Resolution of Nuclear Energy Issues Using Accelerator-Driven Technology." Los Alamos National Laboratory, (1994).

Bradt, H.L., and Peters, B. "The Heavy Nuclei of the Primary Cosmic Radiation." *Physical Review* 77 (1950): p. 54

Brandt, R., et al. "Search for New Phenomena in High-Energy Heavy Ion Interaction." *Nuclear Tracks Radiation Measurements* vol. 15 (1988): p. 382

———. "Recent Advances in the Investigation of Cu-Targets with Relativistic Heavy Ions, Also Using SSNTD." *Nuclear Tracks Radiation Measurements* vol. 17, no. 1 (1989): p. 9

———. "Wide Angle Emission of Heavy Fragments in Relativistic Heavy Ion Collisions and Some Open Problems." Paper presented at the *16th International Conference on Nuclear Tracks in Solids*, Beijing, China, September 7-11, 1992 (1992a).

———. "Enhanced Production of ^{24}Na by Wide-Angle Secondaries Produced in the Interaction of Relativistic Carbon Ions with Copper." *Physics Review C* vol. 45, no. 3 (1992b): p. 1194

Brandt, R., et al. *Nuclear Tracks and Radiation Measurements* 22 (1993): p. 537

———. "Transmutation of Radioactive Waste with the Help of Relativistic Heavy Ions." *Kerntechnik* (1997).

———. "Measurements of Neutron Yields and Radioactive Isotope Transmutation in Collisions of Relativistic Ions with Heavy Nuclei." Dubna, Russia: 85th Session of the JINR Scientific Council, (1999).

Carminati, F., et al. "An Energy Amplifier for Cleaner and Inexhaustible Nuclear Energy Production Driven by a Particle Beam Accelerator." CERN: European Organization for Nuclear Research, (1993).

Cetnar, J., Wallenius, J., and Gudowski, W. "MCB: A Continuous Energy Monte Carlo Burnup Simulation Code." Royal Institute of Technology, (2000).

Cole, A. J. *Statistical Model for Nuclear Decay (from Evaporation to Vaporization)*, (2000).

Cole, G. D., and Porile, N. T. "Enhanced Fragment Emission in the Interaction of ^{12}C Ions with Complex Nuclei." *Physical Review C* 24 (1981): p. 2038

———. "Recoil Properties of Fragments Emitted in the Interaction of Complex Nuclei with Relativistic ^{12}C Ions and Protons." *Physical Review C* 25 (1982): p. 244

Cui, H.H., et al. "Angular Distribution of Heavy Fragments in 72 GeV Ar Interactions with Cu." *Nuclear Tracks Radiation Measurements* vol. 16, no. 4 (1989): p. 225

Cui, H. H., et al. "Study of High Energy Heavy Fragments from the Interaction of 3.65 GeV/N ^{19}F and Cu." Paper presented at the *16th International Conference on Nuclear Tracks in Solids*, Beijing, China, September 7-11, 1992 (1992).

Cumming, J.B., et al. "Spallation of Cu by 3.9-GeV ^{14}N Ions and 3.9 GeV Protons." *Physical Review C* 10 (1974): p. 739

———. "Spallation of Copper by 25-GeV ^{12}C Ions and 28-GeV Protons." *Physical Review C* vol. 14, no. 4 (1976): p. 1554

———. "Spallation of Copper by 80-Gev ^{40}Ar Ions." *Physics Review C* vol. 17, no. 5 (1978): p. 1632

Curie-Sklodowska, M. "Rays Emitted by Compounds of Uranium and of Thorium." *Comptes Rendus* 126 (1898): p. 1101

Demers, J. *Ionographie*: Montreal, (1958).

Dersch, G., et al. "Unusual Behavior of Projectile Fragments from the Interaction of Copper with Relativistic Ar Ions." *Physical Review Letters* vol. 55, no. 11 (1985): p. 1176

Dersch, G. "Kernchemisce Studien zum Anomalenphänomen bei Kernreactionen mit Relativisticschen Schwerionen." Dissertation, Philipps University, (1986).

El-Nadi, M., et al. "Anomalous Mean Free Path for Z=2 Relativistic Projectile Fragments in Emulsion." In *6th High Energy Heavy Ion Study and 2nd Workshop on Anomalons*: LBL-16281, (1983): p. 43

Feshbach, H. and Huang, K. "Fragmentation of Relativistic Heavy Ions." *Physics Letters* 47B (1973): p. 300

Feynman, R. "Very High Energy Collisions of Hadrons." *Physical Review Letters* 23 (1969): p. 1417

Frauenfelder, H., and Henley, E. *Subatomic Physics*: Prentice-Hall, (1974).

Freier, P., et al. "Evidence for Heavy Nuclei in the Heavy Primary Radiation." *Physical Review* 74 (1948): p. 213

Friedlander, E.M., et al. "Evidence for Anomalous Nuclei among Relativistic Projectile Fragments from Heavy-Ion Collisions at 2 GeV/Nucleon. " *Physical Review Letters* vol. 45, no. 13 (1980): p. 1084

Friedlander, E.M., et al. "Anomalous Reaction Mean Free Paths of Nuclear Projectile Fragments from Heavy Ion Collisions at 2*A* GeV." *The American Physical Society* vol. 27, no. 4 (1983): p. 1489

Friedlander, E.M., and Heckman, H.H. "Relativistic Heavy Ion Collisions: Experiment." In *Heavy Ion Science*, edited by D. Allan Bromley: Plenum Press, (1982).

Friedlander, G., et al. "Nuclear Reactions of Copper with 22 BeV Protons." *Physical Review* 94 (1954): p. 727

Fuchs, C. "Probing the Nuclear Equation of State by K^+ Production in Heavy Ion Collisions Near Threshold." Invited talk at the *6th International Conference on Strange Quarks in Matter 2001 (SQM2001)*, Frankfurt, Germany 25-29 Sep 2001 (to be published in J of Physics G)

Gaisser, T. *Cosmic Rays and Particle Physics*: Cambridge University Press, (1990).

Galison, P. *How Experiments End*: University of Chicago Press, (1987).

———. *Image and Logic*: University of Chicago Press, (1997).

Gerland, L. "Hypermatter and Antimatter-Properties and Formation in Relativistic Nuclear Collisions", http://www.th.physik.uni-frankfurt.de/~gerland/stoecker/ger/ger.html, (1996).

Goldhaber, A., and Heckman, H.H. "High Energy Interactions of Nuclei." Submitted to Annual Review of Nuclear Science, preprint LBL-6570, (1978).

Goshal, S.N. "An Experimental Verification of the Theory of Compound Nucleus." *Physical Review* 80 (1950): p. 939

Greiner, C. "Physics of Strange Matter." Paper presented at the *IV International Conference on Strangeness in Quark Matter*, Padova, Italy, 1998.

———. "Strangeness in Strongly Interacting Matter." Invited opening talk at the *6th International Conference on Strange Quarks in Matter 2001 (SQM2001)*, Frankfurt, Germany 25-29 Sep 2001 (to be published in J of Physics G)

Greiner, C., and Schaffner-Bielich, J. "Physics of Strange Matter." In *Heavy Elements and Related Phenomena*, Vol. I, edited by W. Greiner and R. K. Gupta, 1074-146: World Scientific, Singapore, 1999.

Haase, G. "Kernchische Studien zum Ungewöhnlichen Weitwinkelverhalten von Sekundärteilchen in Relativistischen Schwerionenreaktionen." Dissertation, Philipps University, (1990).

Heck, M. "Weitwinkelemission Energiereicher Sekundärteilchen bei der Wechselwirkung Relativistischer Schwerionen mit Kupfer-Targets." Dissertation, Philipps University, (1992).

Heck, M., and Sosnin. A.N. "On the Interpretation of Recent Experiments Using ^{12}C-Ions on Various Cu-Target Experiments." Paper presented at the *11th International Seminar on High Energy Physics Problems*, Dubna, Russia, September 7-12, 1992, (1992)

Heckman, H.H., et al. "Fragmentation of ^{4}He, ^{12}C, ^{14}N, and ^{16}O Nuclei in Nuclear Emulsion at 2.1 GeV/Nucleon." *Physical Review C* vol. 17, no. 5 (1978): p. 1735

Hudis, J., et al. "Energy Dependence of Product Yields in Copper Spallation by Protons between 3 and 30 GeV. " *Physical Review* 129 (1962): p. 434

Hudis, J. "High Energy Nuclear Reactions." In *Nuclear Chemistry*, edited by L. Yaffe, (1968).

Karant, Y.J., et al. "First Results from a Repeat Experiment on the Mean Free Path of Projectile Fragments from 1.88 A Gev ^{56}Fe-Emulsion Interactions." In *6th High Energy Heavy Ion Study and 2nd Workshop on Anomalons*: LBL-16281, (1983): p. 23

Karol, P. J. "Nucleus-Nucleus Reaction Cross Sections at High Energies: Soft-Spheres Model." *Physical Review C* vol. 11, no. 4 (1975): p. 1203

Killinger, F., et al. "About a Possible Energy Dependence of the Anomalon Effect at Charge Two." In *6th High Energy Heavy Ion Study and 2nd Workshop on Anomalons*: LBL-16281, (1983): p. 23

Kinoshita, S. "Photographic Action." *Proc. Roy. Soc. (A)* 83 (1910): p. 432

Kinoshita, S. "The Tracks of the ą Particles in Sensitve Photographic Films." *Phil. Mag.* 28 (1915): p. 420

Klein, N., et al. "Are There Anomalons at Charge Two?" in *6th High Energy Heavy Ion Study and 2nd Workshop on Anomalons*: LBL-16281, (1983): p. 47

Lattes, C. M. G., et al. "Processes Involving Charged Mesons." *Nature* 159 (1947): p. 694

LBL. *5th High Energy Heavy Ion Study:* LBL-12652 (1981).

LBL. *6th High Energy Heavy Ion Study and 2nd Workshop on Anomalons*: LBL-16281, (1983).

Lock, O. "The Pion Pioneers." *CERN Courier* 37 (1997): p. 2

Lord, J. J. "Physics 552 Class Notes."

Lund, T., et al. "Charge and Mass Distribution of Products from the Nuclear Interaction between Copper and 1 GeV ^{12}C." *Physics Letters B* 102B (1981): p. 239

Maddox, R. L. "An Experiment with Gelatino-Bromide" *British Journal of Photography* 18 (1871): p. 422

Mugge, O. *Central. Mineral.* 71 (1909): p. 114, 42

Myssowsky, L , and P. Tschishow. *Z. Phys.* 44 (1927): p. 408

Nilsen, B.S., et al. "Fragmentation Cross Sections of Relativistic ^{84}Kr and ^{109}Ag Nuclei in Targets from Hydrogen to Lead." *Physical Review C* 52 (1995): p. 3277

Otterlund, I., et al. "Nuclear Interactions of 200 GeV and 300 GeV Protons in Emulsion." Paper presented at the *VI International Conference on High Energy Physics and Nuclear Structure*, Santa Fe and Los Alamos (9-14 June) 1975, (1975).

Particle-Data-Group. 1978.

———. "Review of Particle Physics." *Physical Review D* 54 (1996): p. 132

Perkins, D. H. *Introduction to High Energy Physics*: Addison-Wesley, (1982)

Pille, F., "Untersuchungen zum Verhalten leichter Relativistischer Projectilfragment" Dissertation (A) der Technischen Hochschule Leipzig, (1990)

Powell, C.F., Fowler, P.H., and Perkins, D.H. *The Study of Elementary Particles by the Photographic Method*: Pergamon Press, (1959).

Rudstam, G. "Spallation of Copper with 24 GeV Protons.", *Physical Review* 162 (1962): p. 1852

Rutherford, E. "Uranium Radiation and the Electrical Conduction Produced by It." *Philosophical Magazine* xlvii (1899): p. 109

Schaffner-Bielich, J. "Strangelets and Strange Quark Matter." Nuclear Physics A639 (1998): p. 443

———. "The Role of Strangeness in Astrophysics - an Odyssey through Strange Phases." Invited talk at the *6th International Conference on Strange Quarks in Matter 2001 (SQM2001)*, Frankfurt, Germany 25-29 Sep 2001 (to be published in J of Physics G)

Scott, D. K. "Critical Phenomena at Low Temperature." In *6th High Energy Heavy Ion Study and 2nd Workshop on Anomalons*: LBL-16281, (1983): p. 263

Shakespeare, W. "Measure for Measure" in *Mr. William Shakespeares comedies, histories, & tragedies. Published according to the true original copies.* Printed by Isaac Iaggard, and Ed. Blount, London, 1623 (originally produced 1604).

Shapiro, M. "Nuclear Emulsions." In *Handbuch Der Physik*, edited by S. Flügge, p. 342: Springer-Verlag, (1958).

Sobol, I.M. *The Monte Carlo Method*: Translated by V.I. Kisin, *Little Mathematics Library*. Moscow: Mir Publishers, (1984).

Sturm, C. et al. " Evidence for a Soft Nuclear Equation-of-State from Kaon Production in Heavy-Ion Collisions." *Physical Review Letters* vol. 86, (2001): p. 39

Taylor, E. F., and Wheeler, J.A. *Spacetime Physics*: W.H. Freeman and Company, (1966).

Tincknell, M.L. "Study of Anomalous Nuclear Projectile Fragments in CR-39 Etched Track Detectors." Thesis, University of California at Berkeley, (1984).

Wilkes, R. J. "Experimental Particle Astrophysics Notes." http://www.phys.washington.edu/~jeff/courses/ph576/notes7.html: University of Washington, (1997).

Williams, W.S.C. *Nuclear and Particle Physics*: Clarendon Press, (1991).

Yagoda, H. *Radioactive Measurements with Nuclear Emulsions*: Wiley, (1949).

Zhdanov, A.P. "Traces Des Particules." *J. de Phys. et Rad.* 6 (1935): p. 233

Appendix A

Mean Characteristics of Events
(Graphical Analyses & Statistics)

Scanning and measurements performed by the

High Energy Astrophysics Group

of the

Institute of Space Research (Bucharest, Romania)

Dr. Maria Haiduc

Group Head and Scanning Supervisor

High Energy Astrophysics Group

of the

Institute of Space Research (Bucharest, Romania)

Dr. Dumitru Hasegan: Director of the Institute of Space Research

Dr. Maria Haiduc: Group Head and Scanning Supervisor

Physicists

Andrei Gheata: Charge measurements including the design and implementation of the methodology for the photometer.

Mihaela Gheata: Management of the data. Also transformed data from the computer on-line with the microscope to formats usable by the programs.

Hardware

Mircea Ciobanu: Built the electronics for the semi-automatic system for geometry measurements under the KSM microscope.

Octav Anghelescu: Maintenance and improvements of the semiautomatic system, including the optics.

Igor Marin (DUBNA): Kept the KSM microscopes in repair.

Scanners

Mariana Boca: Scanning and drawing events.

Veronica Catrina: Scanning, delta ray counting, geometry measurements.

Aurelia Cristescu: Scanning and back scanning. Measurements on ionization for almost all the data (on light nuclei – gap length measurements as well as blob counting; on relativistic particles – grain and blob counting).

Anica Georgescu: Scanning, geometry, multiple scattering.

Ana Golea: Manager of handling the emulsions, planning the operations, keeping the reference book on events. Data integrity and quality control checks on the computer. Scanning and back scanning.

Sabina Herisanu: Drew almost every events. Also geometry.

Valeria Mocanu: Data entry for geometry (until the semi-automatic system was brought into function – about 2 years); then data entry for gap counting.

Ala Neagu: Scanning and geometry measurements.

Lidmila Sava: Scanning and charge measurements by delta ray counting and photometer.

Cristina Savu: Scanning and charge measurements by delta ray counting and photometer. Back scanning and gap counting on light fragments.

Diaconescu Tereza: Scanning.

Mean Characteristics of Events

1.8 A GeV ^{40}Ar Projectiles in Nuclear Emulsion

	All events **(Lerman)**	***$N_h \leq 8$*** ***(Lerman)***	***$N_h \leq 9$*** ***(Lerman)***
$\langle N_h \rangle$	***8.9 ± 0.3***	***2.9±0.1***	***21.79 ± 0.5***
$\langle n_s \rangle$	***9.8±0.3***	***6.0±0.2***	***17.8±0.6***
$\langle n_\alpha \rangle$	***1.19 ± 0.04***	***1.17 ± 0.05***	***1.2 ± 0.05***
$\langle \theta_s^o \rangle$	***19.8 ± 0.19***	***14.5 ± 0.25***	***23.6 ± 0.26***
$\langle \theta_\alpha^o \rangle$	***1.9 ± 0.04***	***1.8 ± 0.05***	***2.1 ± 0.08***
$\langle Z_{F,Z>2} \rangle$	***11.49 ± 0.18***	**12.0±0.2**	***8.7 ± 0.36***

As in Chapter 4

$\mathbf{N_h} = N_{black} + N_{grey}$

$\mathbf{N_s} = N_{shower}$

$N_\alpha = N_{alpha}$

and from Aleklett et al (1988) θ_s^o and θ_α^o are the critical angles for shower particles and alphas respectively; while $\mathbf{Z_{F,Z>2}}$ is the charge of projectile fragments with $Z > 2$.

$<N_h>$ *All Events*

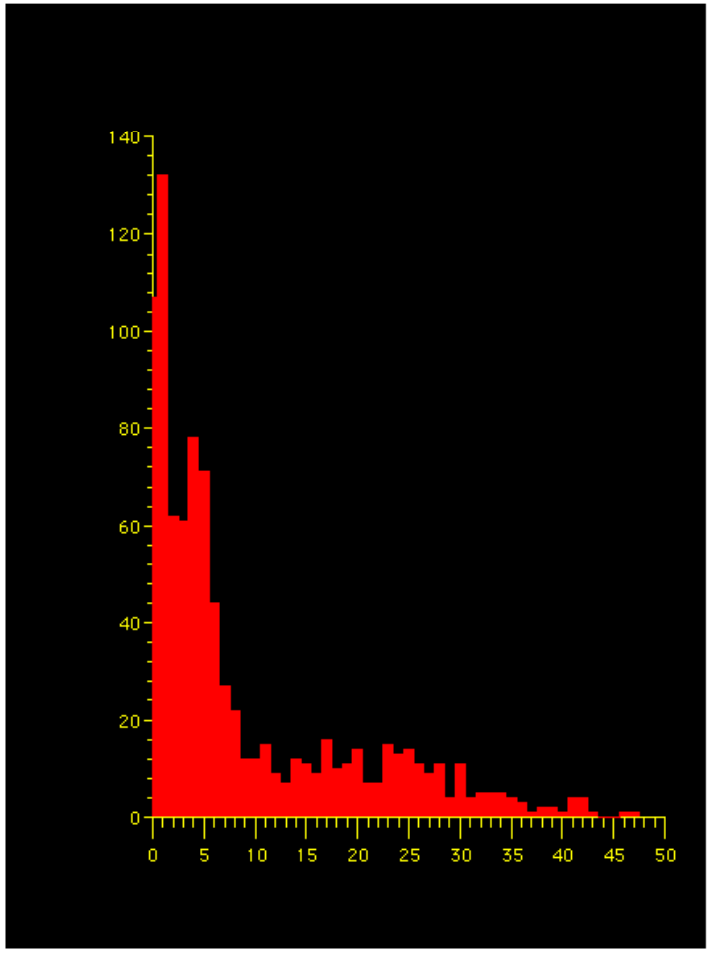

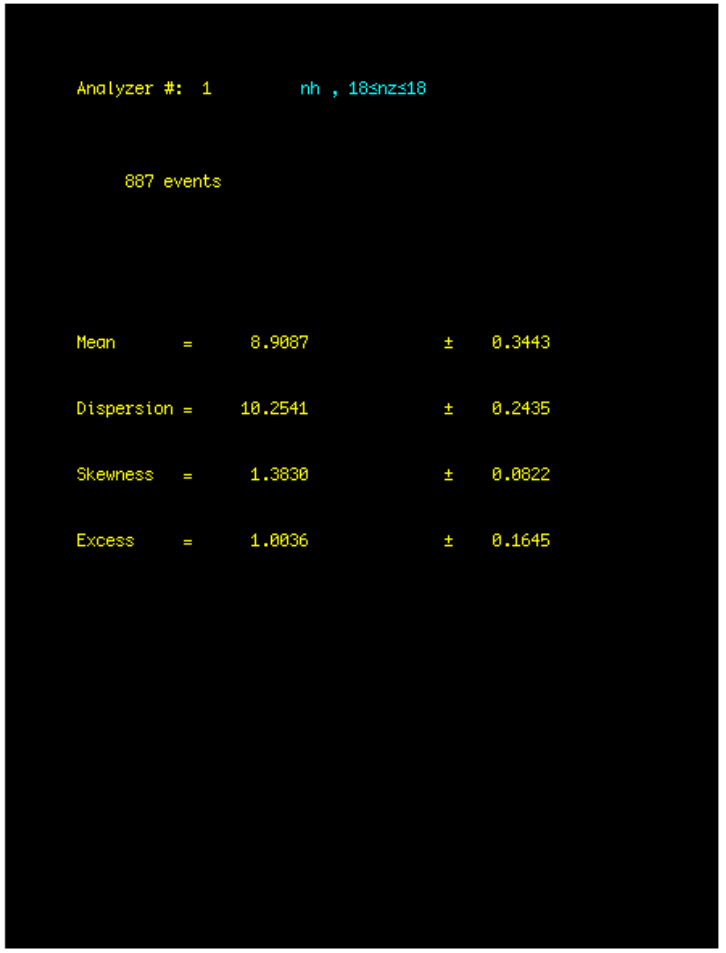

$\langle N_h \rangle$ *Central Region* ($N_h \geq 9$)

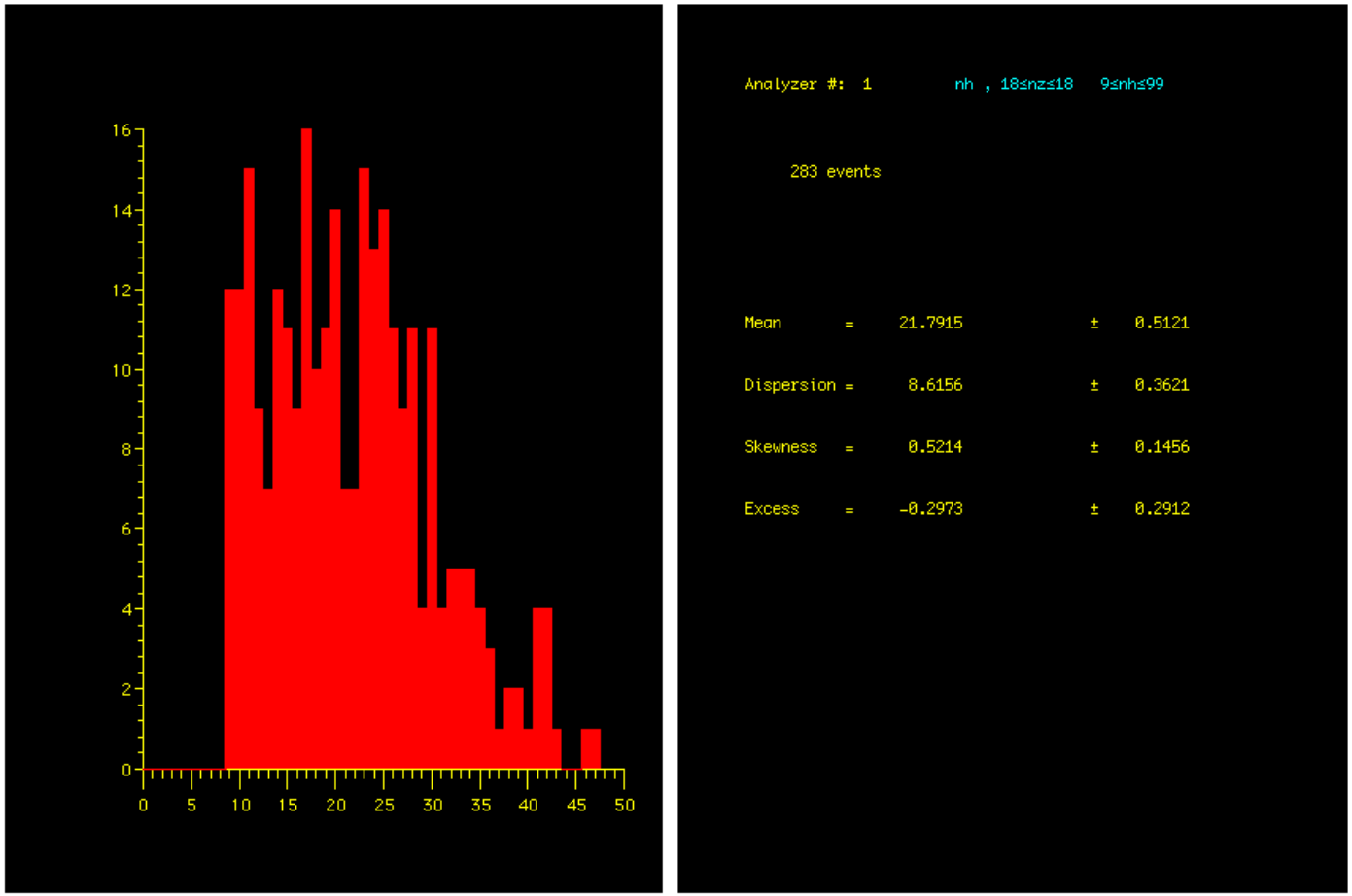

$<n_\alpha>$ *All Events*

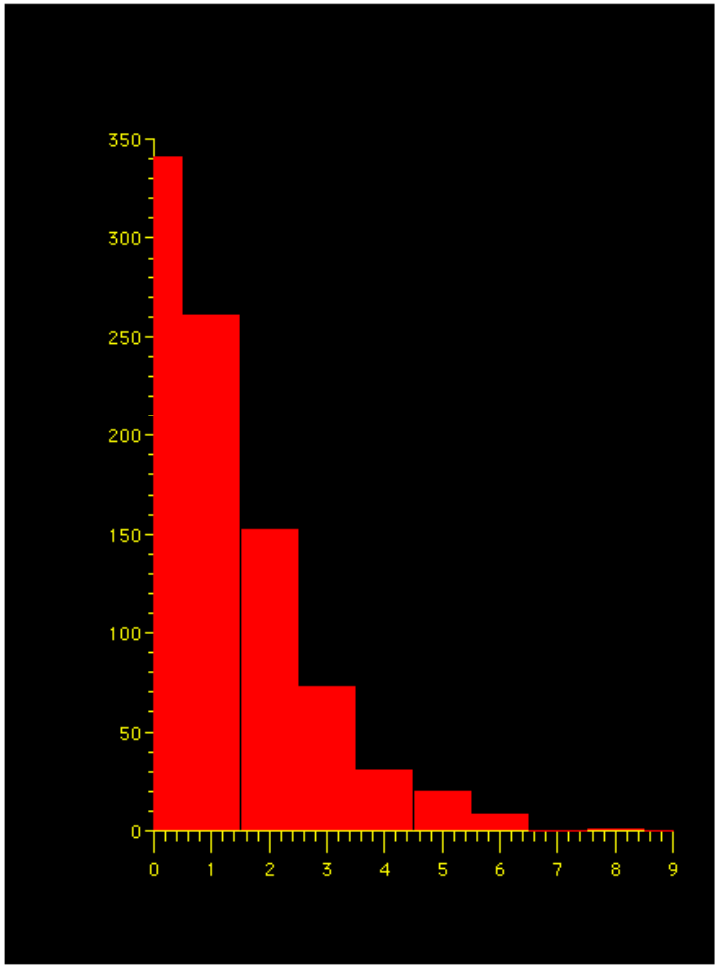

Analyzer #: 1 nalf, 18≤nz≤18

887 events

Mean	=	1.1995	±	0.0451
Dispersion	=	1.3421	±	0.0319
Skewness	=	1.3485	±	0.0822
Excess	=	1.8655	±	0.1645

$\langle n_\alpha \rangle$ Central Region ($N_h \geq 9$)

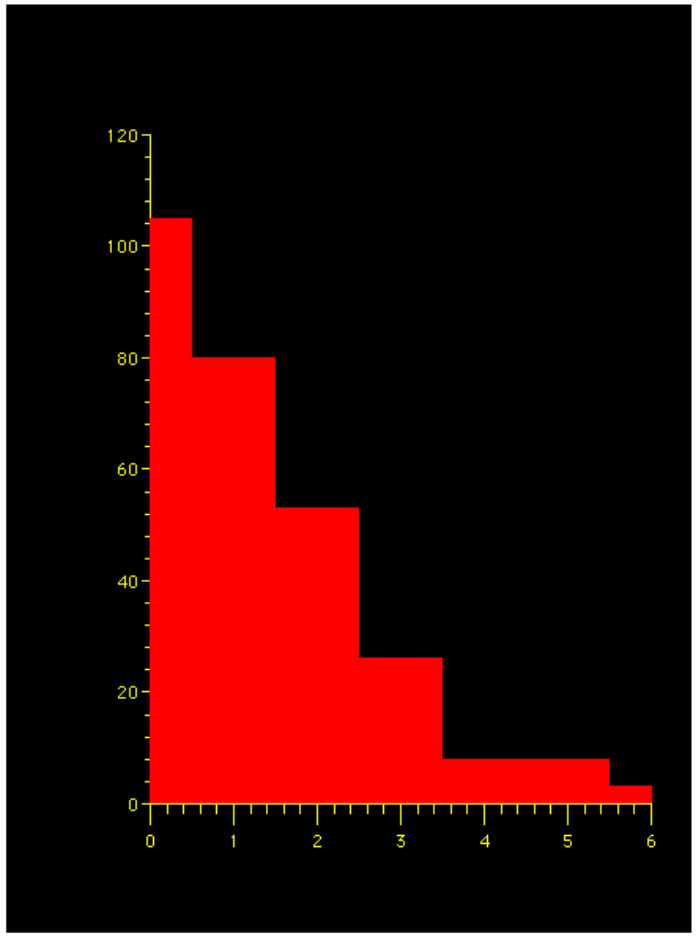

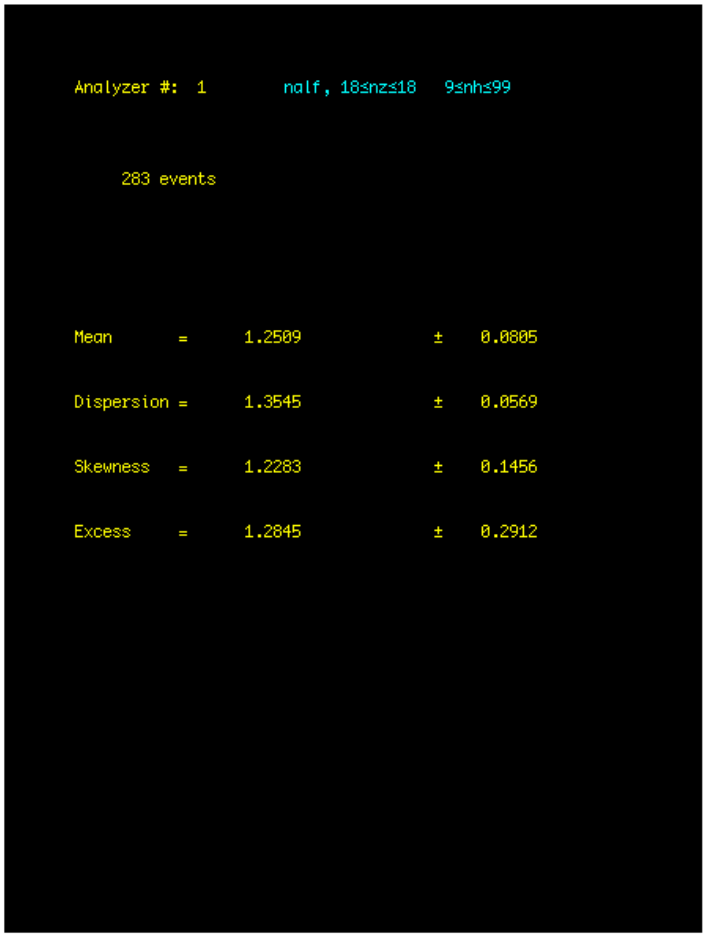

$\langle n_\alpha \rangle \quad (N_h \leq 8)$

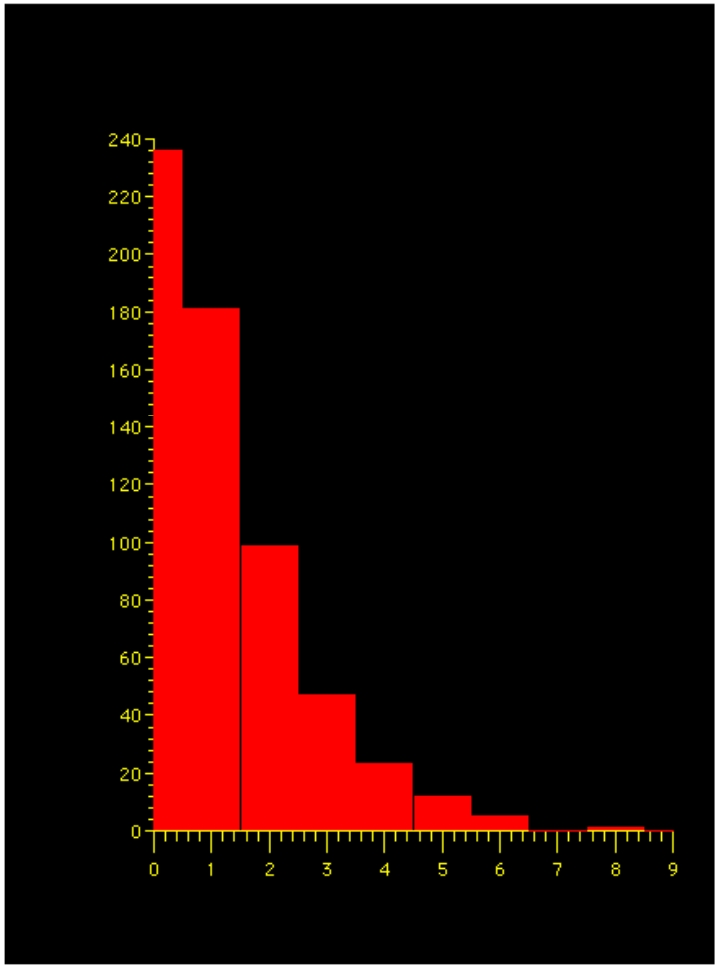

Analyzer #: 1 nalf, 18≤nz≤18 0≤nh≤ 8

604 events

Mean	=	1.1755	±	0.0543
Dispersion	=	1.3356	±	0.0384
Skewness	=	1.4076	±	0.0997
Excess	=	2.1651	±	0.1993

$<\theta_\alpha^\circ>$ *All Events*

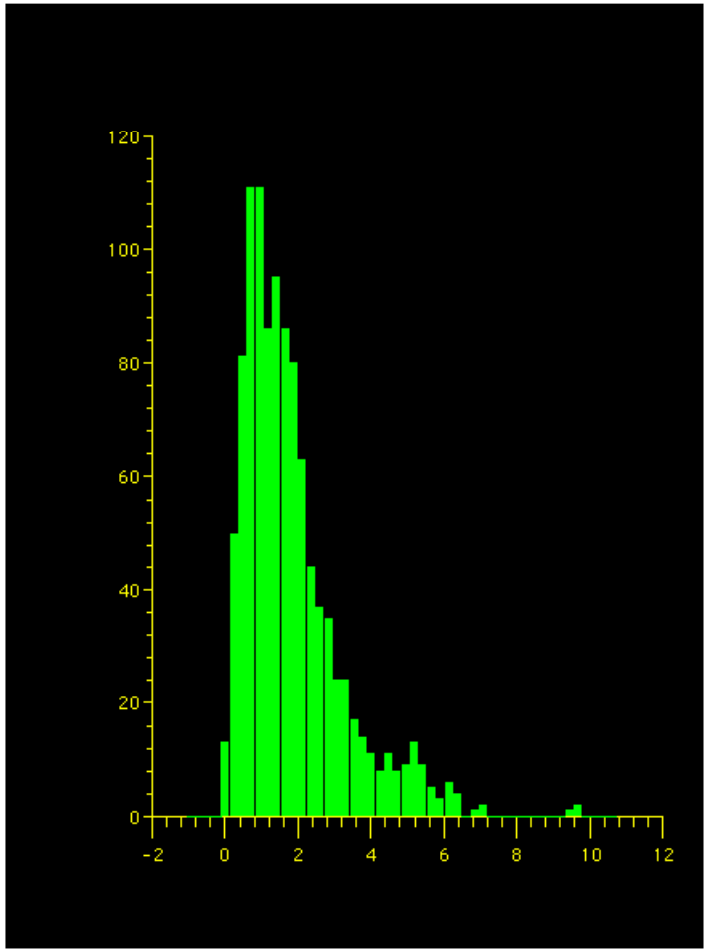

Analyzer #: 1 thet, 18≤nz≤18 4≤ty≤ 4

1064 events

Mean	=	1.9393	±	0.0424
Dispersion	=	1.3846	±	0.0300
Skewness	=	1.4372	±	0.0751
Excess	=	3.6152	±	0.1502

$<\theta_\alpha^o>$ Central Region ($N_h \geq 9$)

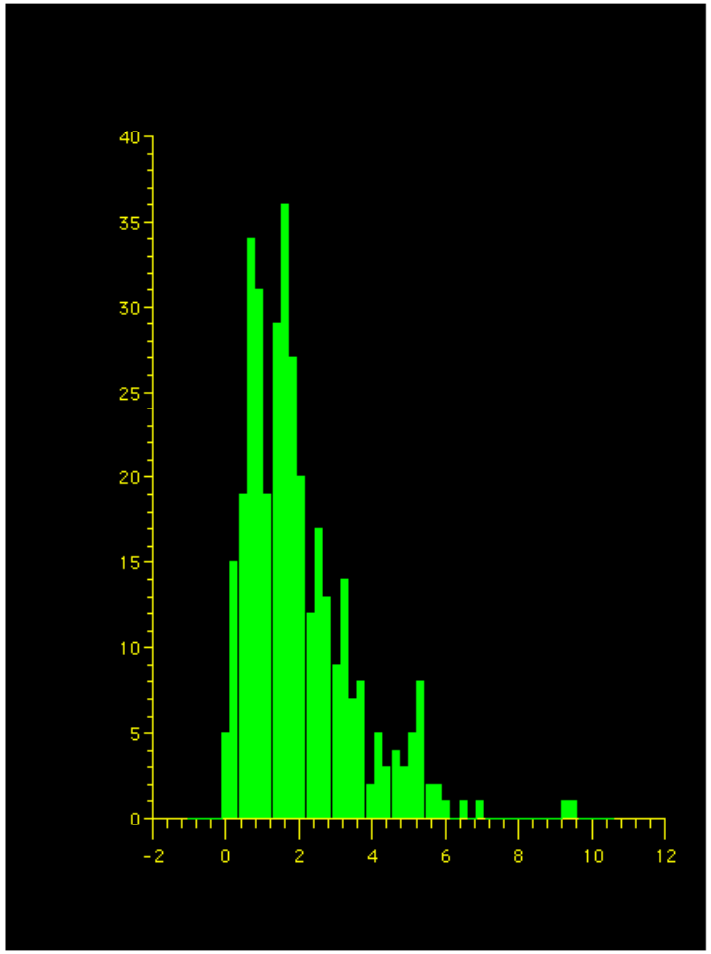

Analyzer #: 1 thet, 18≤nz≤18 9≤nh≤99

354 events

Mean	=	2.1196	±	0.0791
Dispersion	=	1.4878	±	0.0559
Skewness	=	1.6231	±	0.1302
Excess	=	3.2524	±	0.2604

$<\theta_\alpha^{\circ}>$ $(N_h \leq 8)$

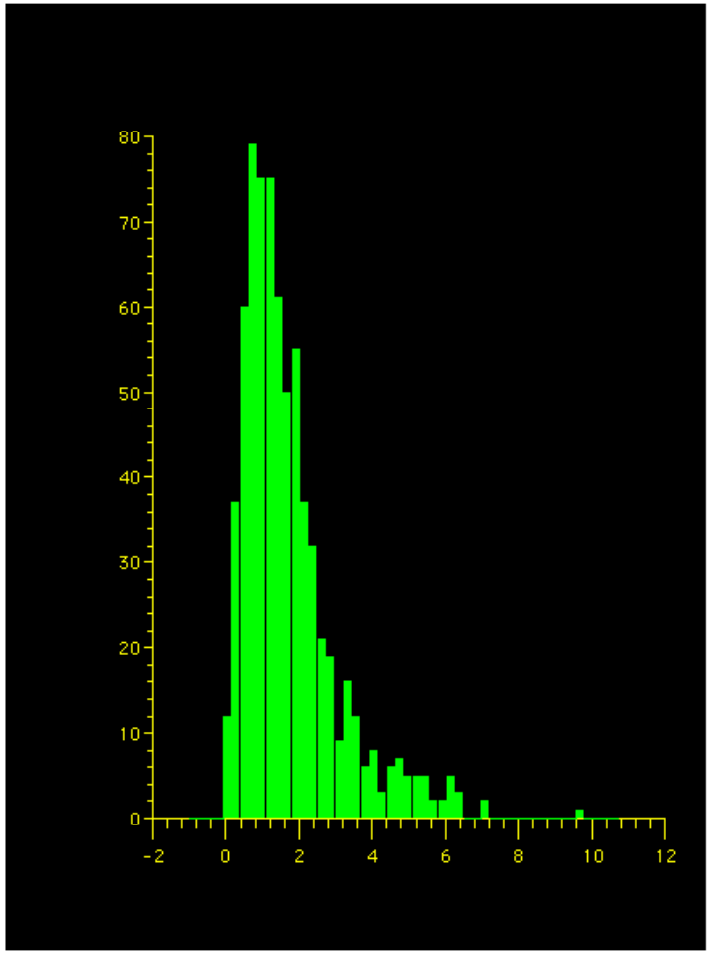

Analyzer #: 1 thet, 18≤nz≤18 0≤nh≤ 8

710 events

Mean	=	1.8494	±	0.0496
Dispersion	=	1.3221	±	0.0351
Skewness	=	1.2963	±	0.0919
Excess	=	3.7337	±	0.1839

$<\theta_s^o>$ *Relativistic Shower Particles (All Events)*

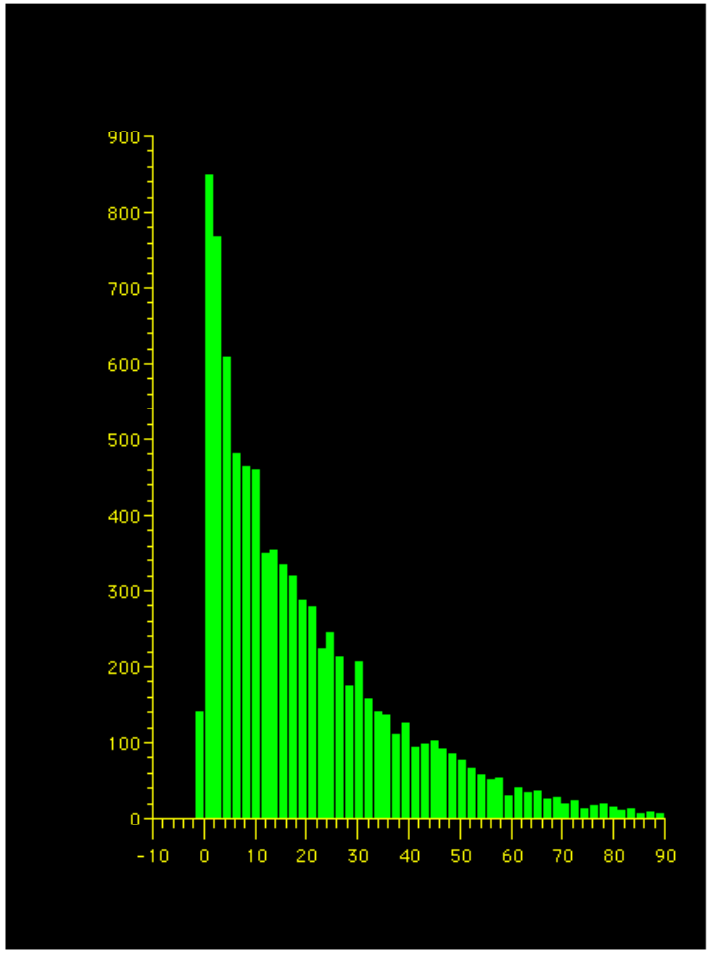

Analyzer #: 1 thet, 18≤nz≤18 3≤ty≤ 3

8543 events

Mean	=	19.8220	±	0.1932
Dispersion	=	17.8562	±	0.1366
Skewness	=	2422.3635	±	0.0265
Excess	=	1.2735	±	0.0530

$<\theta_s^o>$ *Relativistic Shower Particles in the Central Region* ($N_h \geq 9$)

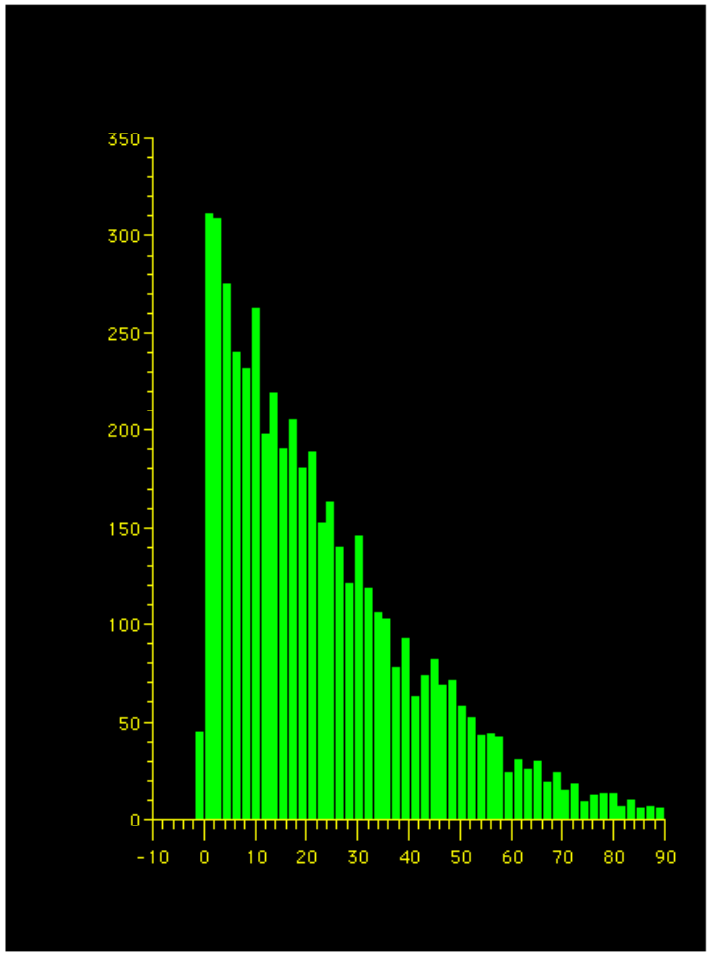

Analyzer #: 1 thet, 18≤nz≤18 9≤nh≤99

4943 events

Mean	=	23.6513	±	0.2666
Dispersion	=	18.7416	±	0.1885
Skewness	=	2243.6050	±	0.0348
Excess	=	0.5629	±	0.0697

$<\theta_s^o>$ *Relativistic Shower Particles* $(N_h \leq 8)$

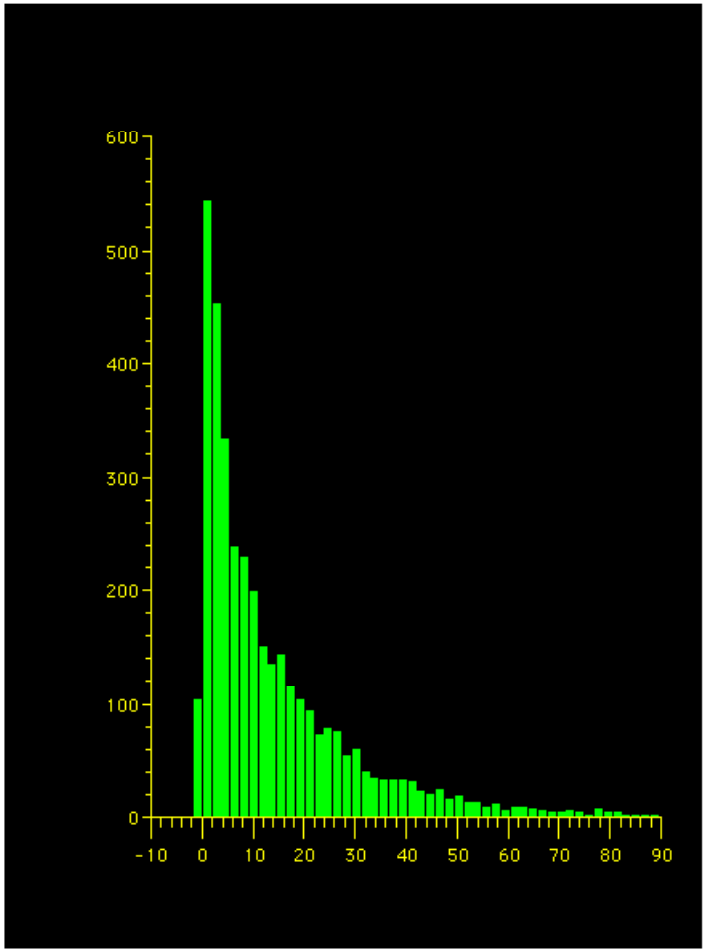

Analyzer #: 1 thet, 18≤nz≤18 0≤nh≤ 8

3600 events

Mean	=	14.5642	±	0.2509
Dispersion	=	15.0548	±	0.1774
Skewness	=	2034.1368	±	0.0408
Excess	=	3.4880	±	0.0816

$< Z_{F,Z>2} >$ *Fragmentation Charges (All Events)*

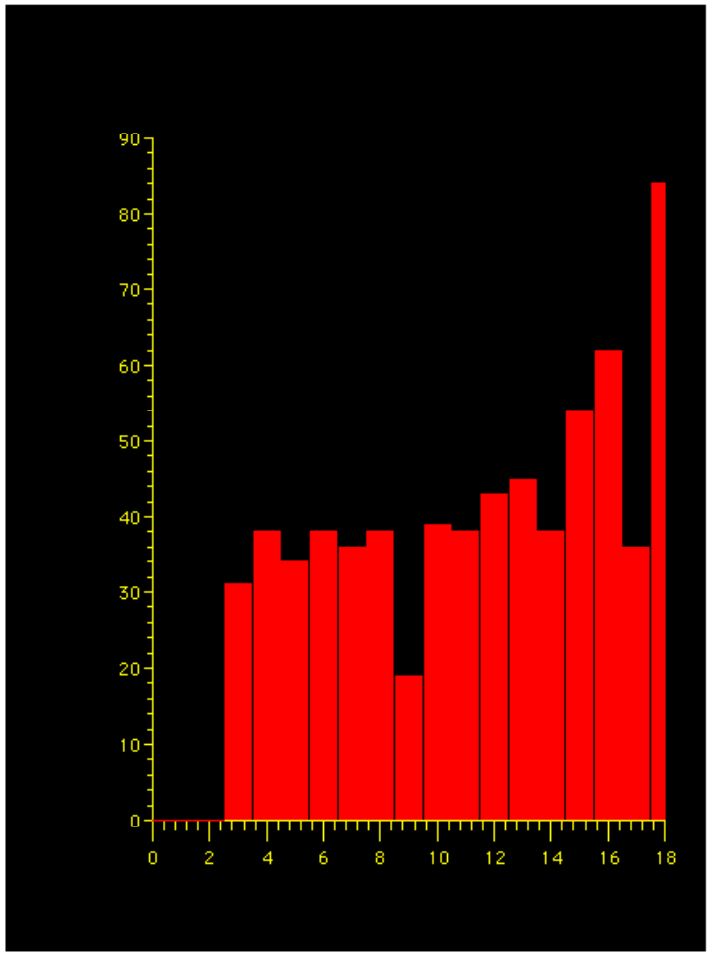

Analyzer #: 1 kz , 18≤nz≤18 5≤ty≤ 5

673 events

Mean	=	11.4963	±	0.1837
Dispersion	=	4.7646	±	0.1299
Skewness	=	-0.2490	±	0.0944
Excess	=	-1.2219	±	0.1888

$< Z_{F,Z>2} >$ *Fragmentation Charges in the Central Region* ($N_h \geq 9$)

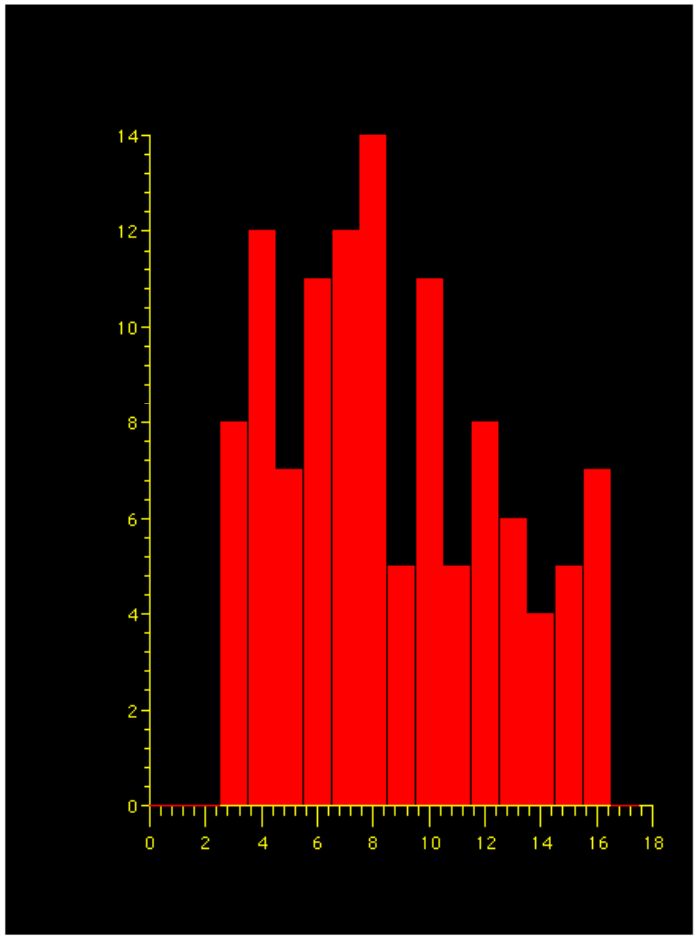

Analyzer #: 1 kz , 18≤nz≤18 9≤nh≤99

116 events

Mean	=	8.7414	±	0.3613
Dispersion	=	3.8910	±	0.2555
Skewness	=	0.3867	±	0.2274
Excess	=	-0.8409	±	0.4549

Appendix B

Simulation and Programming Details of of the Monte Carlo code BFHL[1]

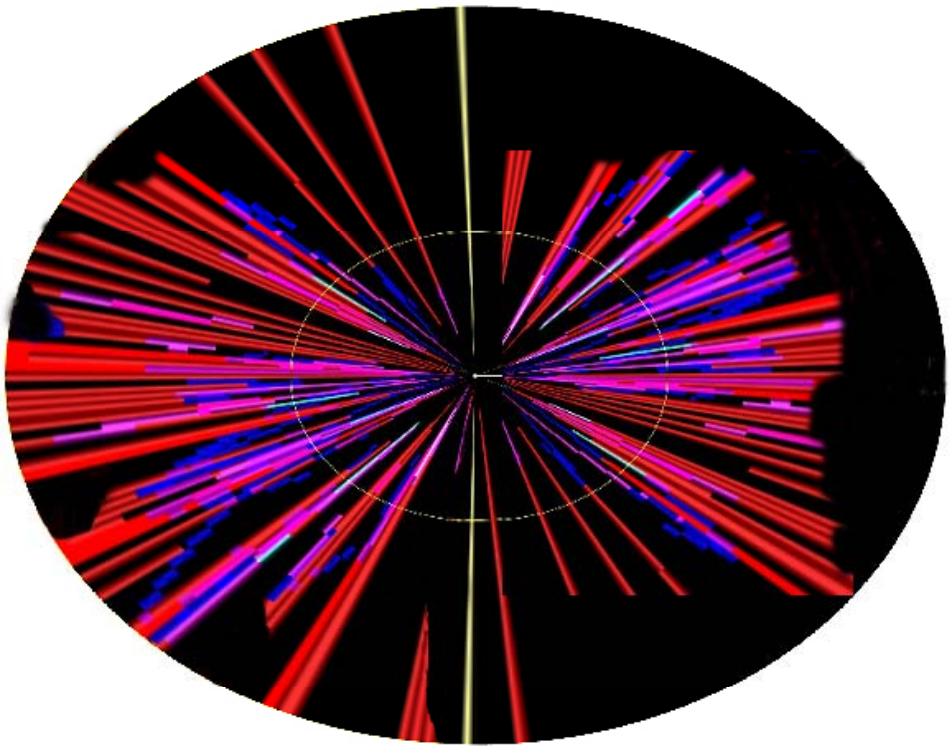

1. **Classes of variables found in all versions of *BFHL***
2. **Samples of visualizations of simulated beam trajectories**
3. **Flowcharts of BFHL**
4. **Variable List**
5. **Subroutine List**
6. **Matrices List**

[1] BFHL = Berkeley Friedlander Haiduc Lerman and pronounced 'baffle'.

B.1 Classes of Variables Found in All Versions of *BFHL*

Overall Target Geometries

1) Radius and height of cylindrical sectors
2) Full cylinder made up of sequential cylindrical sectors
3) Two cylindrical sectors, touching (R_0 in figure 6-1 below, scale in cm)
4) Two cylindrical sectors, apart (R-20 in figure 6-1 below, scale in cm)

Beam Variables

1) Number of particles in a pulse
2) Number of pulses in a 'run'
3) Central coordinates of the beam's interaction with the face of the target
4) The dispersion of the Gaussian beam distribution (see Figures 6-1, 6-2, 6-3)
5) Polar and azimuthal angles of beam's interaction with target face

Kinematic Variables

The total energy E_p and the transverse momentum P_t of shower particles

Interaction Variables

1) Mean Free Path (absolute values or fitting parameters)
2) Fragmentation (limited control)
3) Production Cross-section

Computational Variables

Random number generating functions, modulos, seeds, and subsets

Baryon Conservation

1) Twinned protons (i.e. twinning the shower particles found in each star)
2) Missing Mass (mass balancing to the atomic number A of each local primary)

Subpopulations

1) Λ, E_p , σ_p , fragmentation, and other variables of the nucleus
2) Percentage of subpopulation

B.2

Visualizations (simulated) of 1.8 A GeV ^{40}Ar on Cu Disks

Figure B.2a **Experimental set-up and beam propagation for $\sigma_{beam} = 0.1$**

Figure B.2b **Experimental set-up and beam propagation for $\sigma_{beam} = 1.0$**

Figure B.2c **Simulation of beam propagation for $\sigma_{beam} = 0.1$ (close-up)**

Figure B.2d **Simulation of beam propagation for $\sigma_{beam} = 1.0$ (close-up)**

Figure B.2e **Beam Distribution on Faceplate of Front Disk $\sigma_{beam} = 0.1$**

Figure B2f **Beam Distribution on Faceplate of Front Disk $\sigma_{beam} = 2.0$**

Figure B.2a **Experimental set-up and beam propagation for beam profile $\sigma_{beam} = 0.1$**

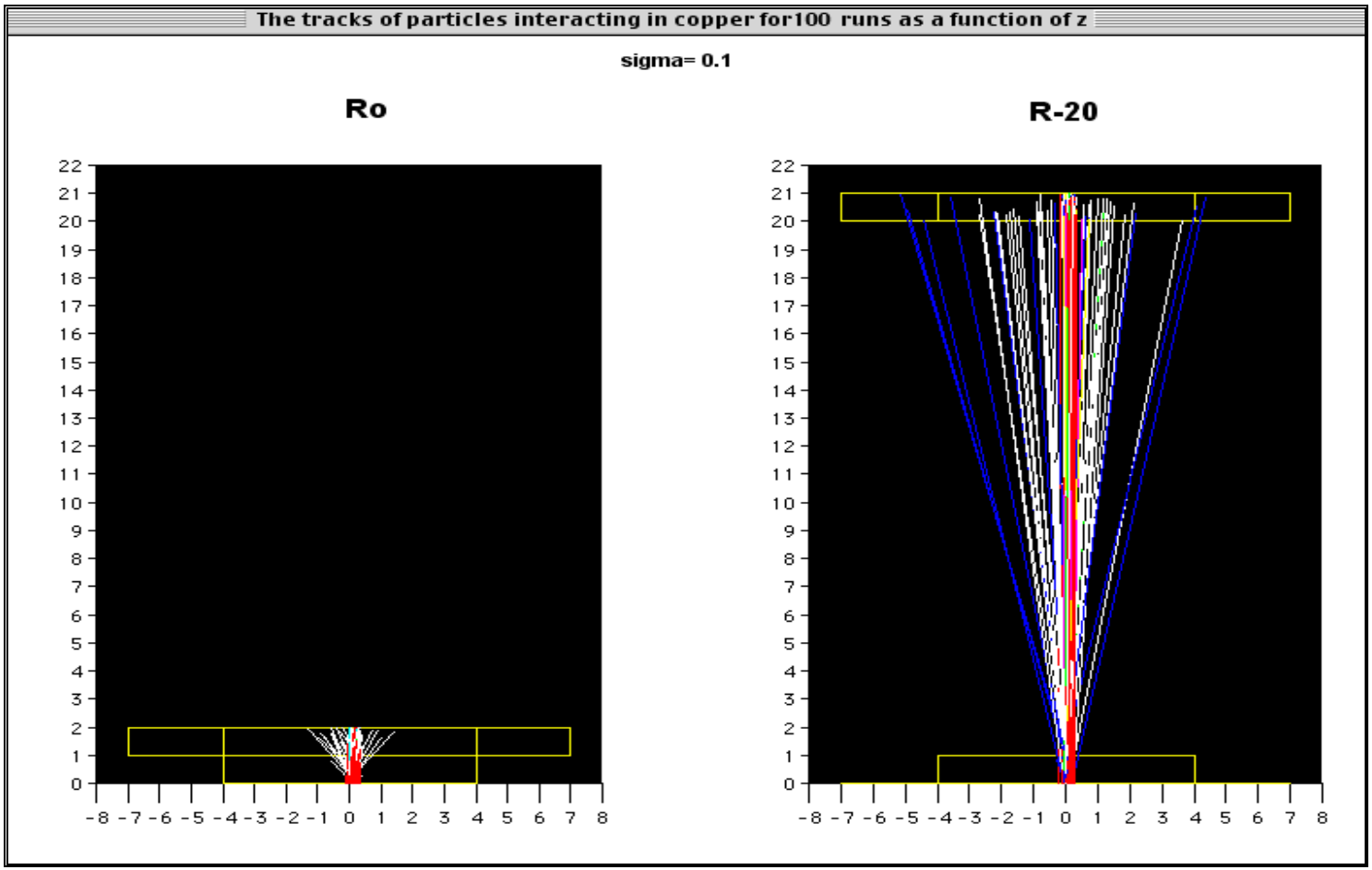

Figure B.2b **Experimental set-up and beam propagation for beam profile σ_{beam} = 1.0**

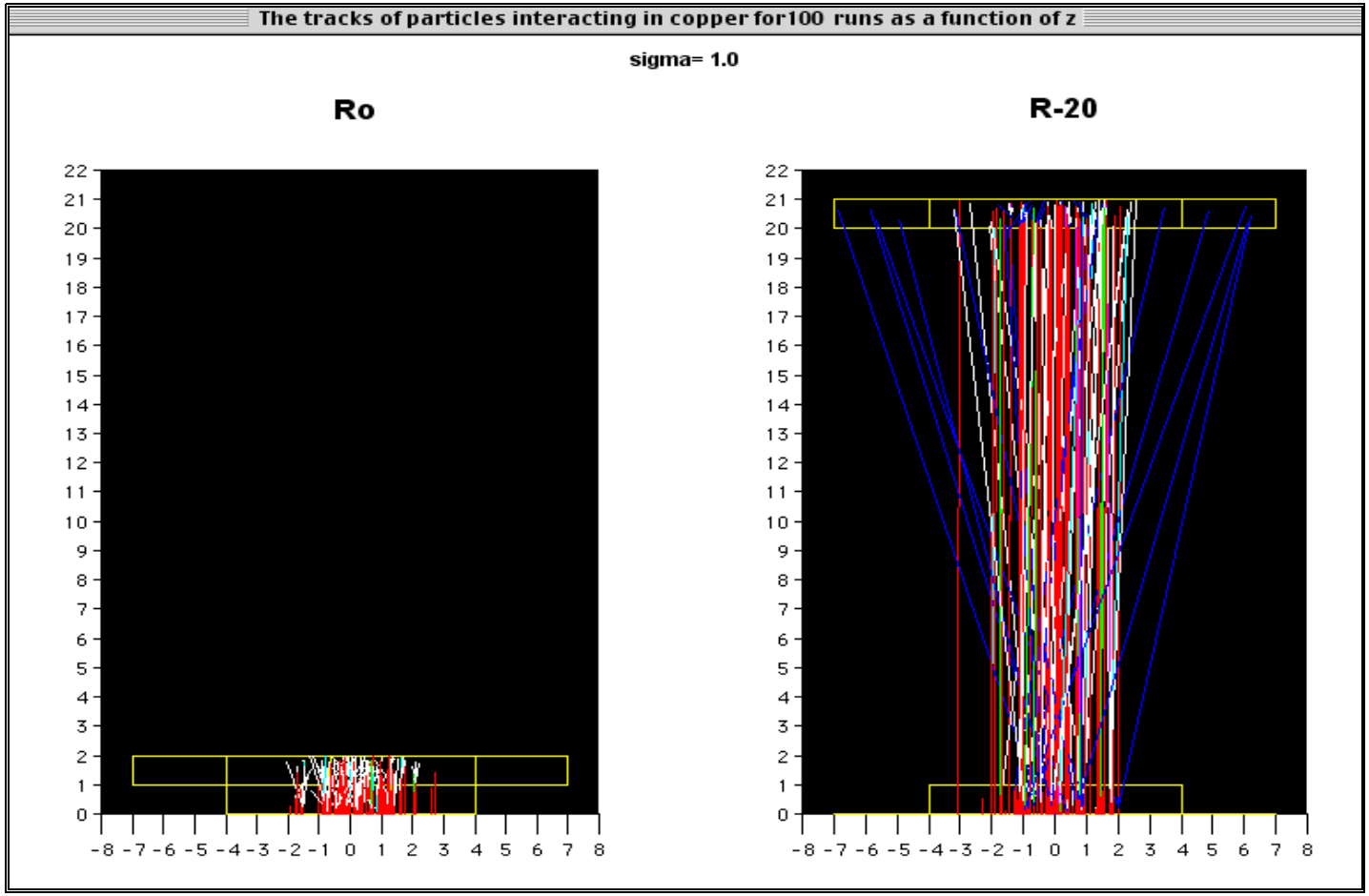

Figure B.2c Simulations of Argon Beam on Copper Disks (close-up)

Beam Profile Variance σ_{beam}= 0.1

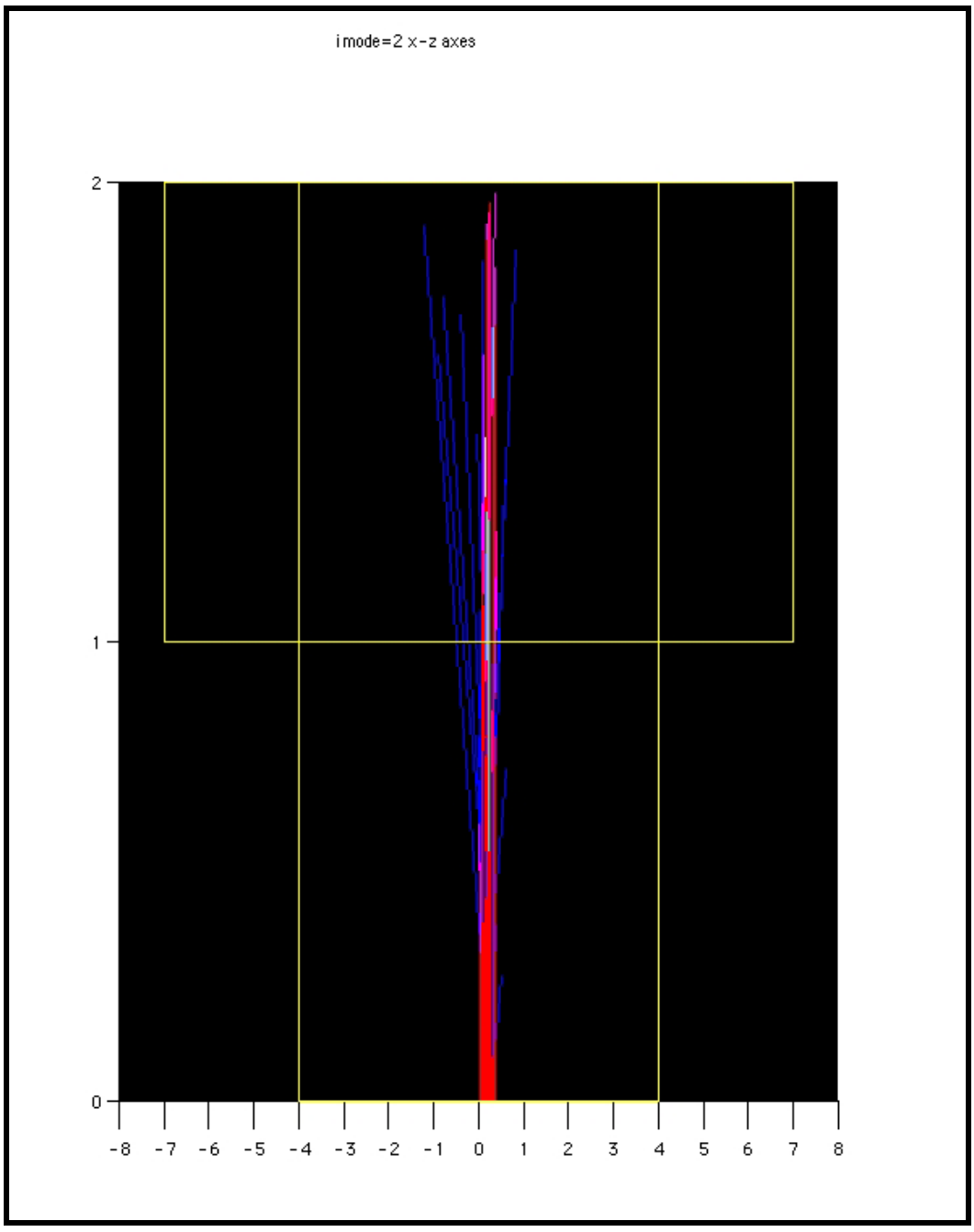

The different charges, or charge classes, are color-coded (red = primary, for example).

Figure B.2d Simulations of Argon Beam on Copper Disks (close-up)

Beam Profile Variance $\sigma_{beam}=2$

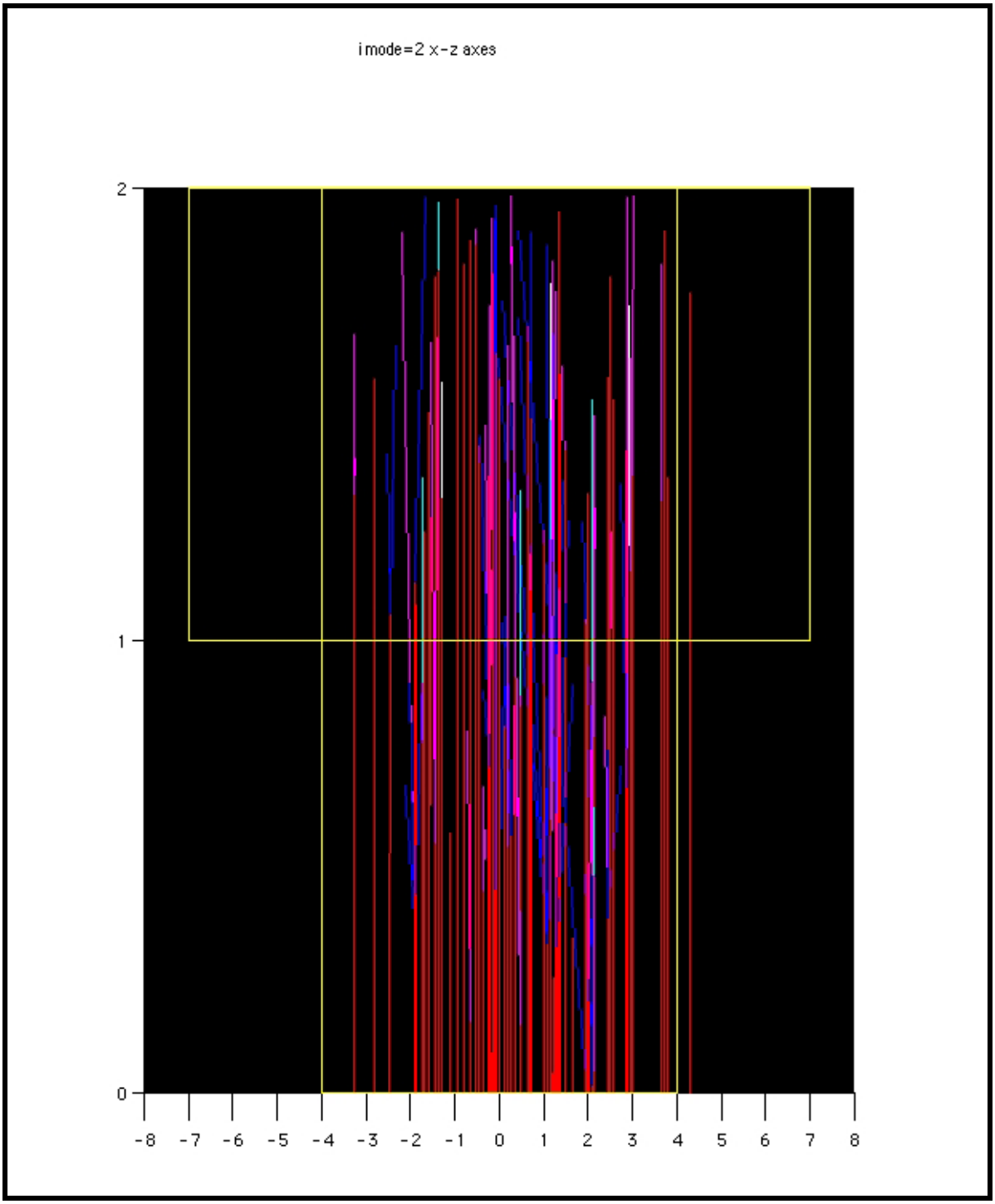

Figure B.2e Simulations of Argon Beam on Faceplate of Copper Disk

$$X=Y=\theta=\phi=0.0001 \qquad \sigma_{beam}=0.1$$

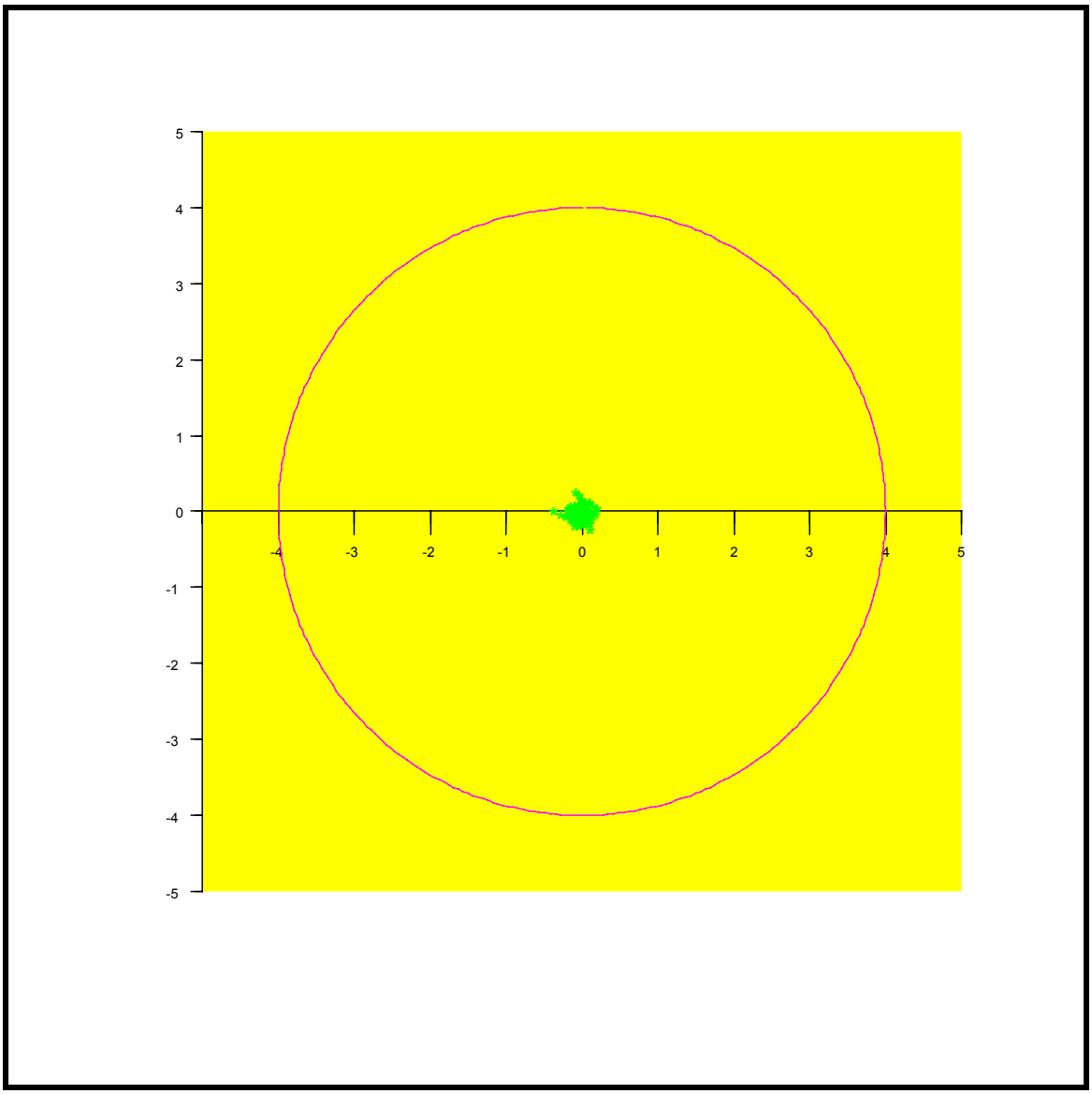

Figure B.2f Simulations of Argon Beam on Faceplate of Copper Disk

$$X=Y=\theta=\phi=0.0001 \qquad \sigma_{beam}=2.0$$

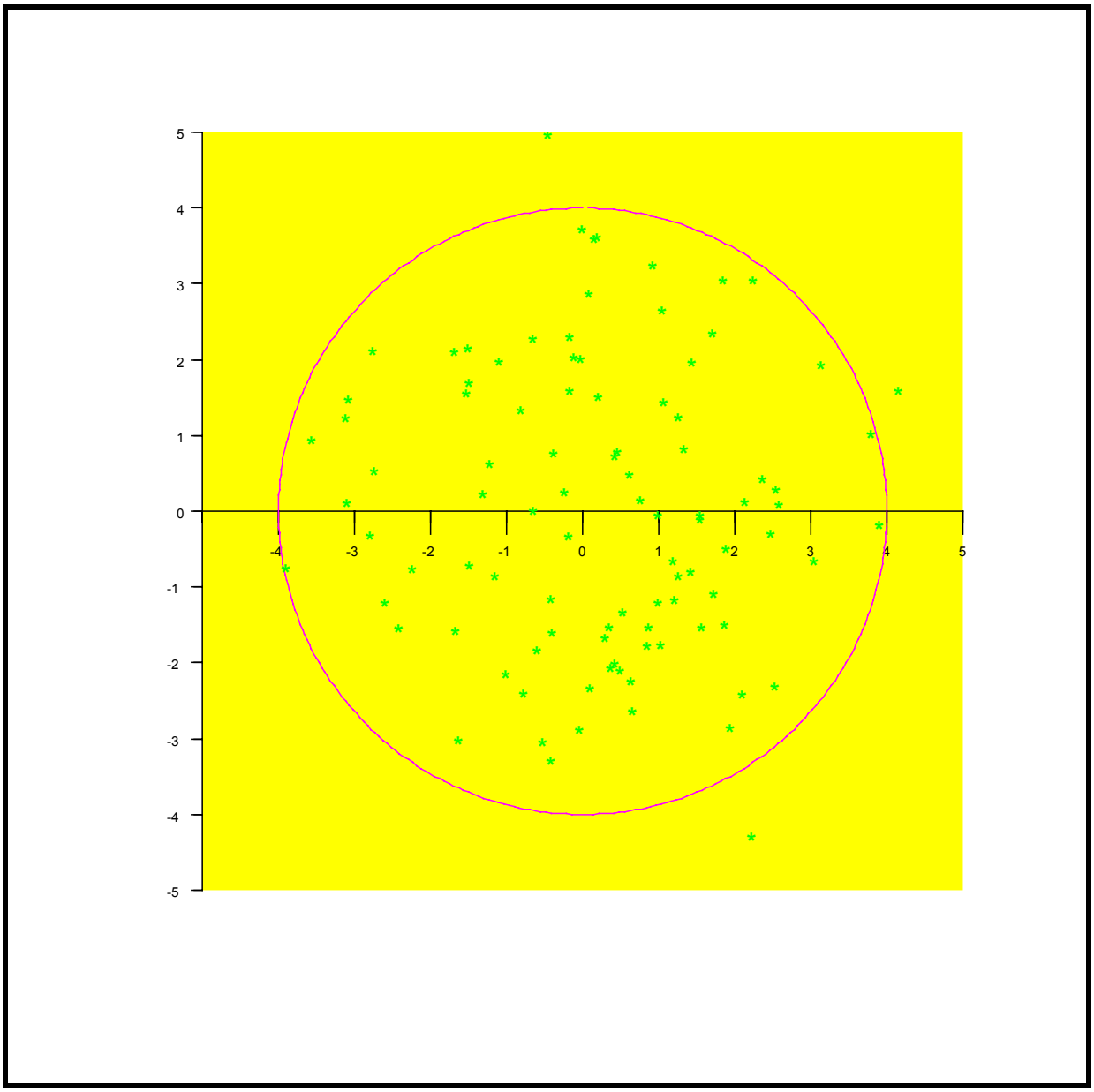

B.3 Variables

In more detail, those variables able to be set in a given run include:

Particle Variables

p0 = mean value of $\bar{P}$ used to extract P

p = $P_T / \sin\theta$

sect = cross-section of Na for a given track/particle (Z,E)

e = kinetic energy of a particle

d = interaction length of a given particle under consideration

Nuclear Interaction Variables

norm = normalization of ^{24}Na production cross-section

caplam = capital lamda (Λ)

caplam1 = capital lamda-1 (Λ_1) of the subpopulation

XXX = percentage of subpopulation

b = exponent of Z-dependent mean free path relationship

Beam Run Variables

***nerr* =** number of beam runs (also the number from which to extract errors)

Target Geometry

imode, kmode = target configuration

jmax = maximum number of sectors

j = number of sector [1,2,3…]

Beam-Target Interaction Geometry

$\mathbf{X_0}$ = X coordinate of the beam (distribution) center at the face of the target

$\mathbf{Y_0}$ = Y coordinate of the beam (distribution) center at the face of the target

sigma = Standard deviation of beam distribution at the face of the target

tbdeg = polar (theta) angle of beam as whole

abdeg = azimuthal (phi) angle of beam as whole

Database Constants

allstars ≡ number of stars in database

nch = number of different charges (equal to 20)

nig = max number of generations in database (usually cut at 3)

z1 ≡ mean free path of charge 1

Computational Variables

DS = number of random numbers extracted before one is selected for use (delayed spin)

Important variables internal to the workings of *BFHL* include:

Target Variables

nnjj = maximum number of stars of a given primary (run dependant and used to fix the dimensions of matrices)

nnst = maximum number of stars in a family (in a given run)

npr = max number of prongs (relativistic) in a star

zp ≡ 'LOCAL' primary charge {18-1)
(neutrons also have zp=1 in order to have the same history as proton)

nnk = total number of primary collisions throughout entire TARGET

nk = counter (running number of "nnK"… nK=0 → nnK)

ni = counter in DO loop in number of relativistic prongs for a given star (ordinal)

Star Variables

1 = current star under investigation

nst = running identification for which star's in a family (1^{st}, 2^{nd}, 3^{rd}…)

ig = generation of a star

jj = ordinal position of a star with a given charge in the DB as a whole

rint, rcrt = radius variables when extracting beam components in BeamStar ??

lp = projected length of a given vector (x,y components) in a given ???

vnonr ***(3)*** = vector components of a track potentially producing an interaction (star frame)

vo ***(3)*** = vector components of the origin of star in the lab frame

vr ***(3)*** = vector components of the track potentially producing interaction in the lab frame centered at the origin of the star

xc ***(3)*** = vector component of the new interaction in lab-frame

B.4 Flowcharts

Computationally, the data flow is outlined below.

(The numbers in the red boxes are flowcharts that successively follow.)

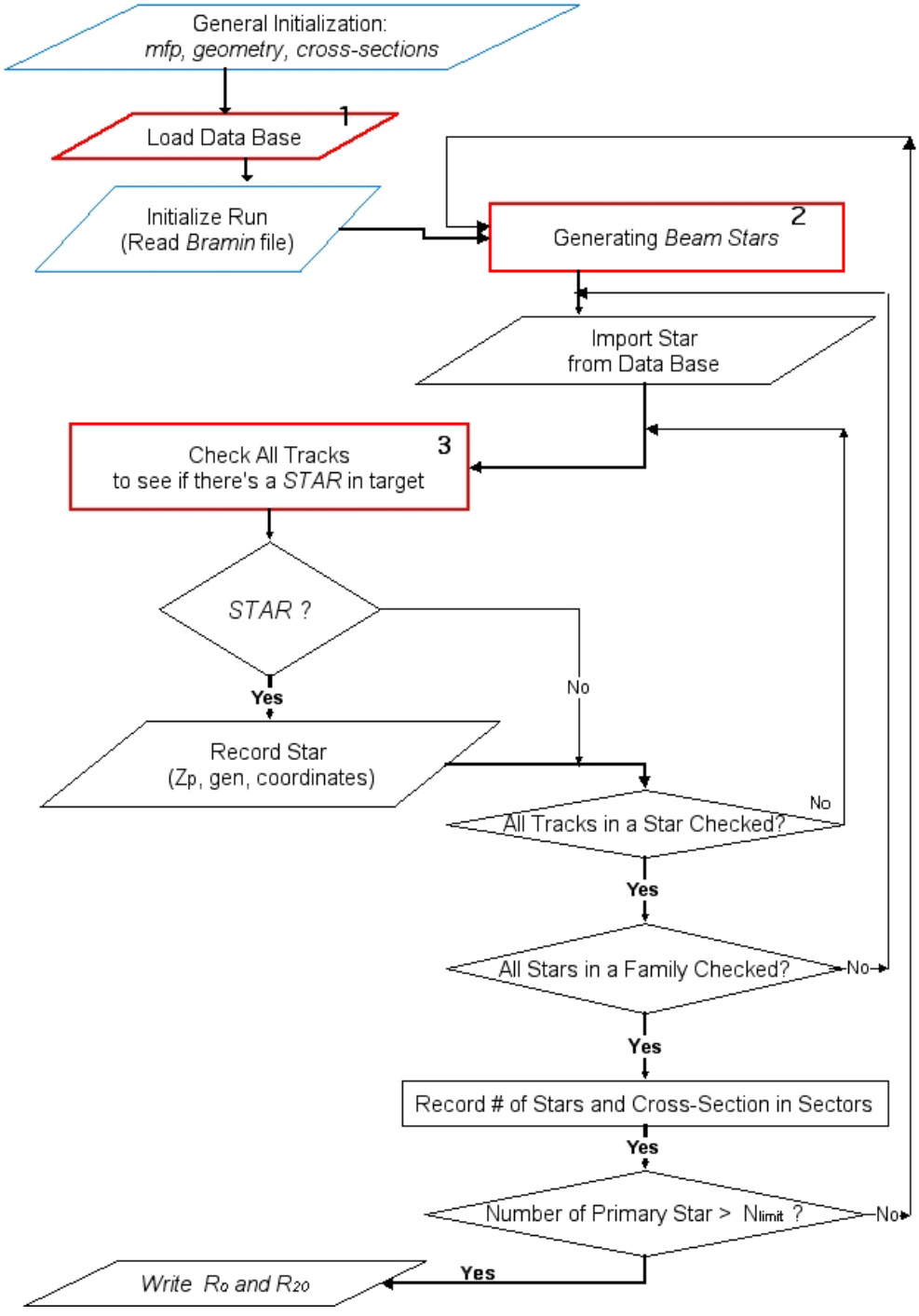

FLOWCHART #1

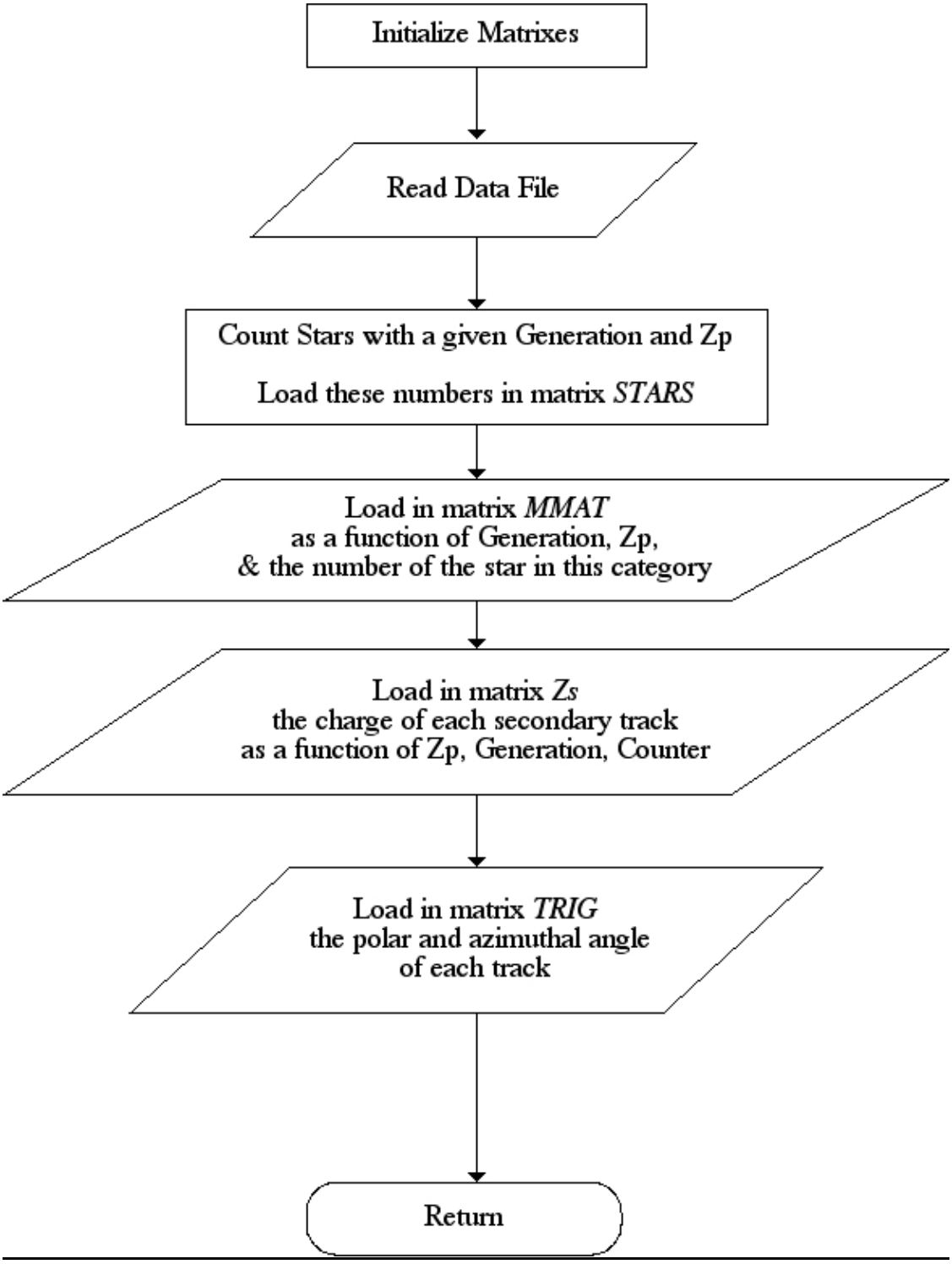
Initialize Matrixes
Read Data File
Count Stars with a given Generation and Zp
Load these numbers in matrix STARS
Load in matrix MMAT
as a function of Generation, Zp,
& the number of the star in this category
Load in matrix Zs
the charge of each secondary track
as a function of Zp, Generation, Counter
Load in matrix TRIG
the polar and azimuthal angle
of each track
Return

FLOWCHART #2

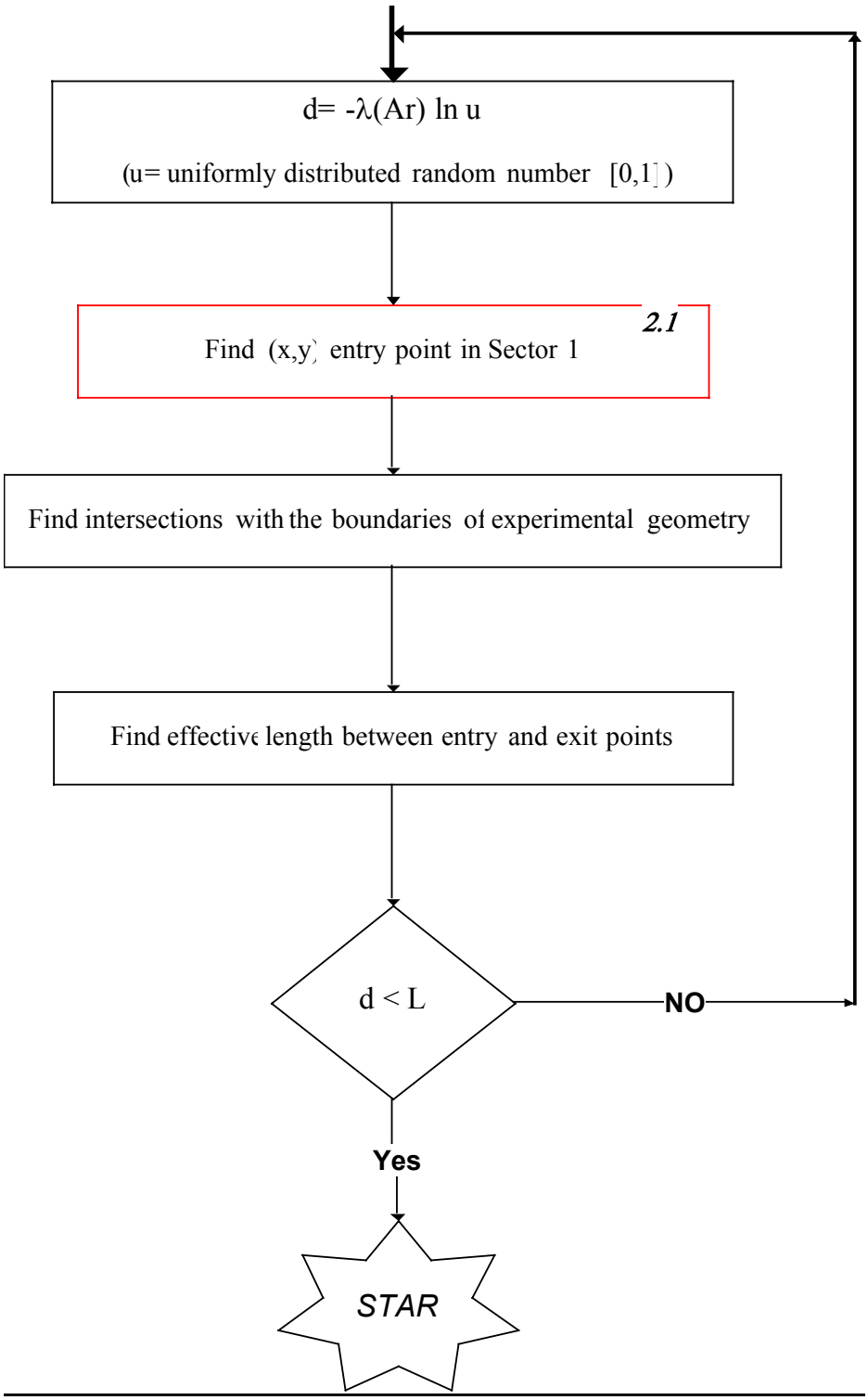
d= -λ(Ar) ln u
(u= uniformly distributed random number [0,1])
2.1
Find (x,y) entry point in Sector 1
Find intersections with the boundaries of experimental geometry
Find effective length between entry and exit points
d < L
NO
Yes
STAR

FLOWCHART #2.1

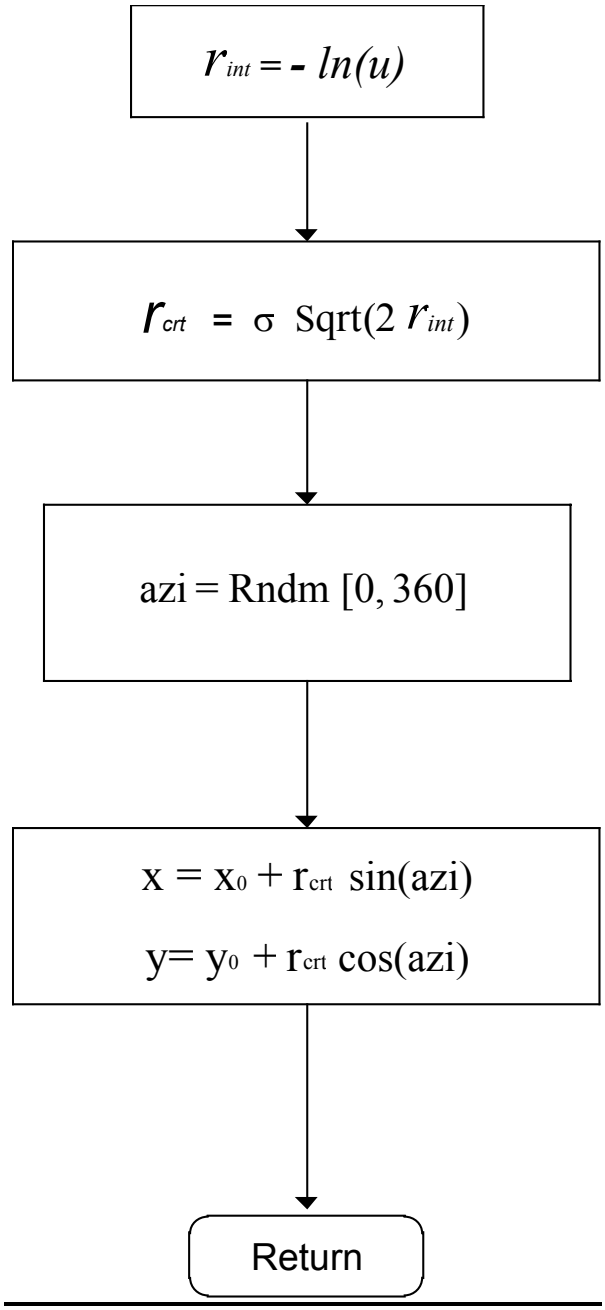

FLOWCHART #3

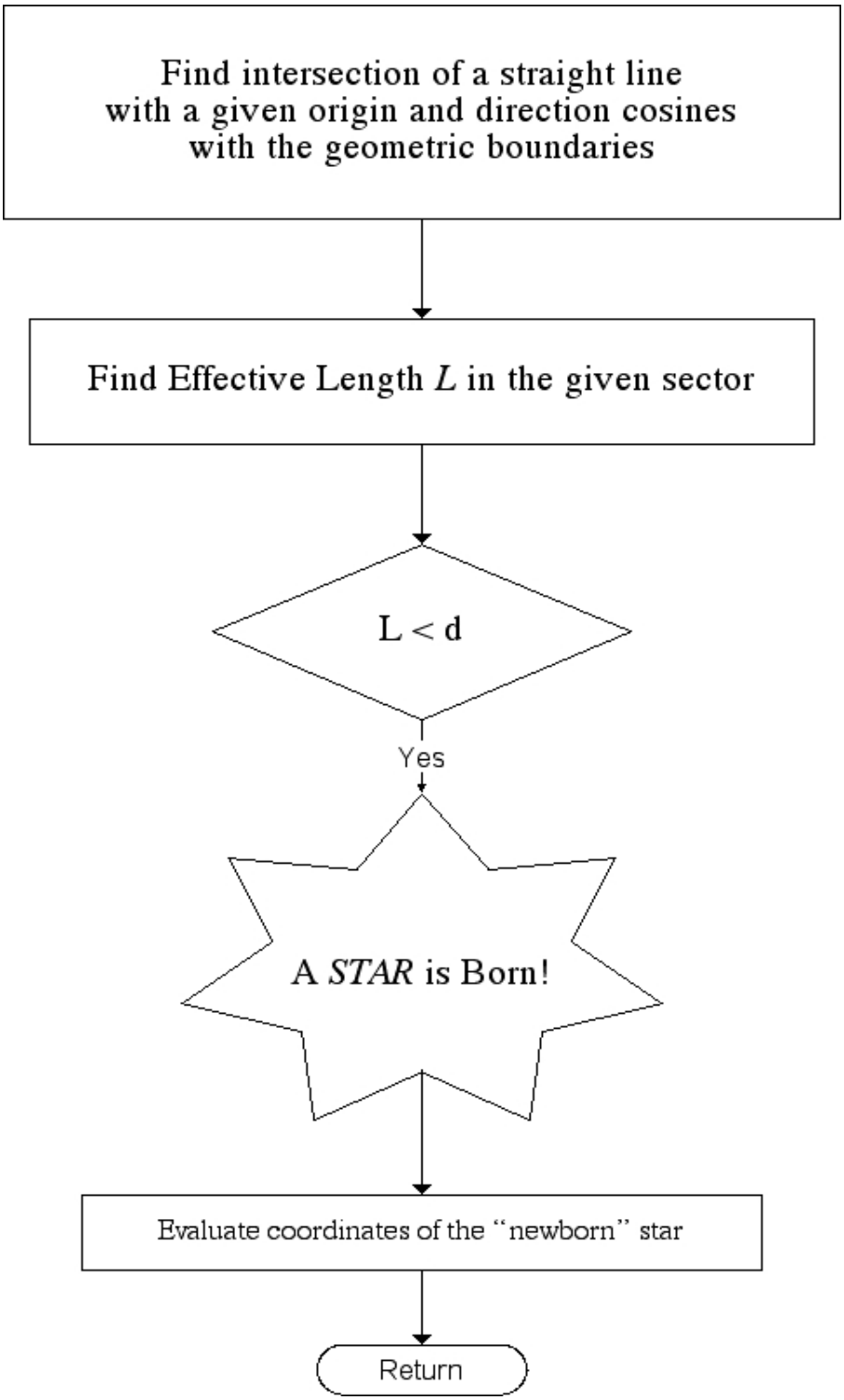
Find intersection of a straight line
with a given origin and direction cosines
with the geometric boundaries
Find Effective Length L in the given sector
L < d
Yes
A STAR is Born!
Evaluate coordinates of the "newborn" star
Return

B.5 Subroutines

An examination of the subroutines shows how these variables come into play:

calc(ig,zp,jj,l,nst,k)

Establishes existence of "actual" stars (collisions) from all possible virtual stars due to trajectories of primary and secondary particles

rec_charge (ig,nst,zp,jj)

Correlates secondary charges with local (nst) to become local primaries for stars

beam2(coef,xc,k)

Sets up primary ^{40}Ar collision with Cu target, initiating a new impact point for a beam primary in the z-direction

beam3(x,y)

Generates for a primary beam particle a Gaussian distribution generated (X,Y) point on the face of the target

cos_dir(coef,d)

Calculates direction cosines to improve computational ease and accuracy (cartesian coordinates are transformed into polar coordinates)

coords(ig,zp,jj,v,vnonr,st)

Finds the coordinates of a vector which is the track under investigation

rotation(l,r)

Transforms from local coordinate system to lab frame

vmult(r,vnonr)

Applies Rotation Matrix

crossing(cr1,cr2,kc,index)

Finds the crossing points for the target geometry for a given vector

plane(i,vz)

Sets intersection points for the faces of the next sector

cil(v1,v2,k)

Finds virtual exit points on next sector
(Called only if doesn't cross flat faces inside, then must cross side)

e(v1,v2)

General equivalence statement

load_mfp(clam)

Loads and calculates mean free paths

init_run()

All Monte-Carlos use 2 vectors and a matrix, initialized here

mark_up(ig,zin,n)

Short-term memory of which star's been loaded

translation(v1,xc)

Frame of reference translation of coordinates

translation1(xc)

Frame of reference translation of coordinates

translation2(v1,v2,xc)

Frame of reference translation of coordinates

rec_xyz(i1,xc)

Recording coordinates of a star in a more general matrix

test_extb(d,coef,k,xc)

Finds the coordinates of the crossing point coming from outside the sectors for beam tracks

vnew(d,coef,v)

Reconstructs a vector from direction cosines and distance

test_ext(d,coef,k,xc)

Another exterior test

test_int(d,k,xc)

Finds the coordinates of the crossing point coming from inside the sectors

rec_angle(nst)

Records angle under the (local) number of the (local) star

ini_geom(kmode)

Sets up geometry of different target configurations

cos_beam(coef)

Sets direction cosines and other angles used in Rotation Matrix

cross_sect(ist,gamma,sect,p0)

Finds cross-section for Na, part I

na(p,iz,sect)

Finds cross-section for Na, part II

calcsect

Internal check

LoadStar()

Loads and counts total number of stars

ClearStore()

Initializes all matrices which will load with stars

B.6 Matrices

While the matrices include:

zs ***(nig,nch,nnjj,npr)*** = charge of a secondary track *(ig, Zp, jj, ni)*

stars ***(nig,nch)*** = charge and generation distribution of total database

mmat ***(nig,nch,nnjj)*** = multiplicity of all relativistic particles in a given star

nhmat ***(nig,nch,nnjj)*** = multiplicity of slow fragments in a given star

mark ***(nig,nch)*** = keeps a count of where in the database you have already been
(which stars have already been imported)

tang ***(nig,nch,nnjj,npr,2)*** = angle (_ _ _ _, 1) = theta and angle (_ _ _ _, 2) = azimuthal

anglab ***(nnst,4)*** = angles transformed back into the lab-frame
(stored cos sin that are needed for rotations)

xyz ***(nnst,3)*** = X,Y,Z coordinates of stars

axaz ***(2,2)*** = geometry of target

mat ***(imode,3)*** = resulting number of stars in each sector

sodium ***(imode,3)*** = resulting amount of ^{24}Na in each sector

t ***(i,k,n)*** = matrix containing total number of stars

ts ***(i,k)*** = matrix for ^{24}Na

sodiu ***(imat, jmat)*** = used for internal check…should be equal to matrix **ts**

Appendix C

Simulations of a Cylindrical Target Geometry

with

Enhanced Production Cross-Section

for

Shower Particles

Models

'All Shower-Particle'

"Wide-Angle Only"

'All Shower-Particle' Models

Figure C.1 *'All Shower-Particle'* Models

(Composite Results)

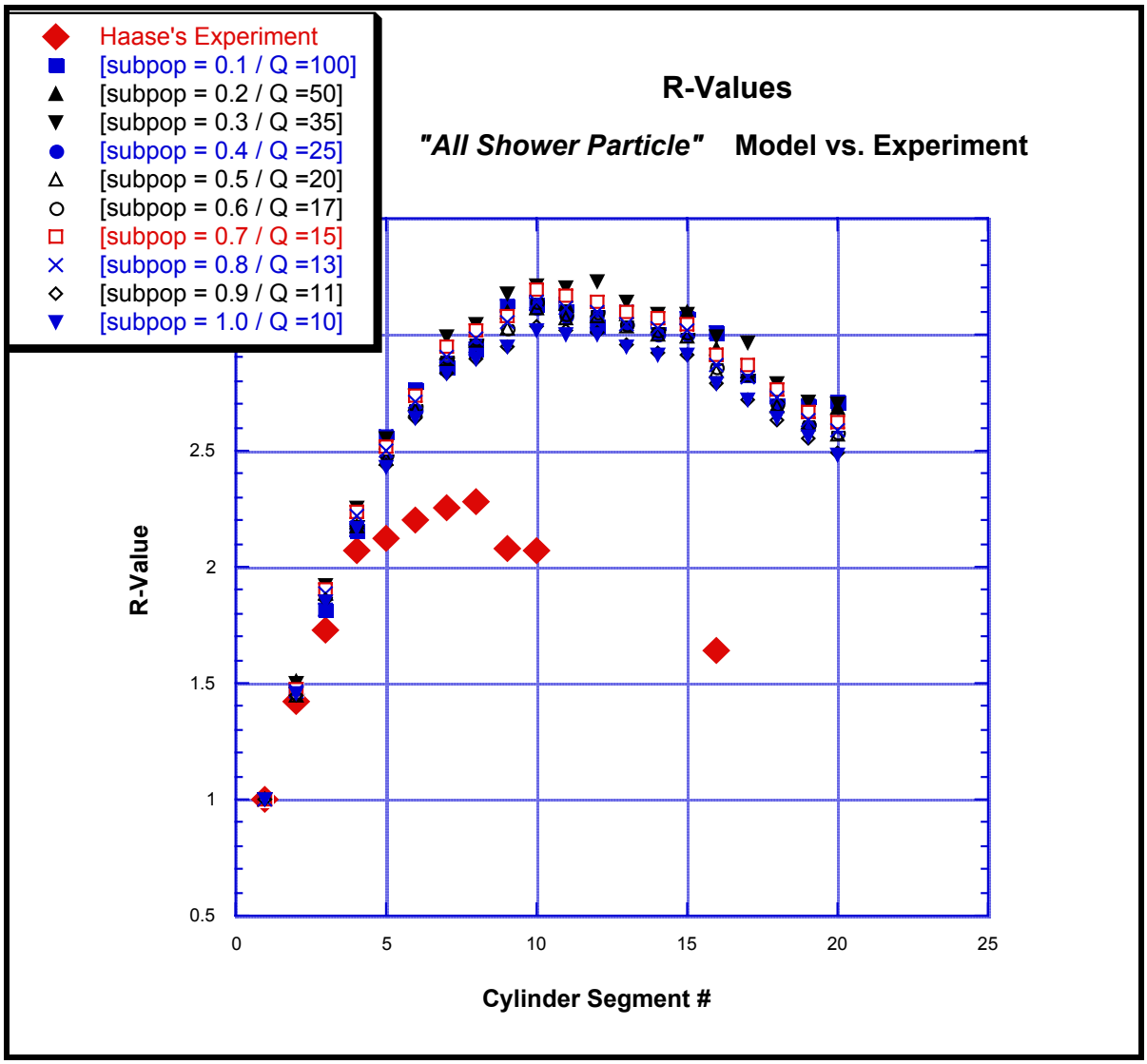

Figure C.2 *'All Shower-Particle'* Model

(Subpopulation = 10%; Enhancement Factor Q = 100)

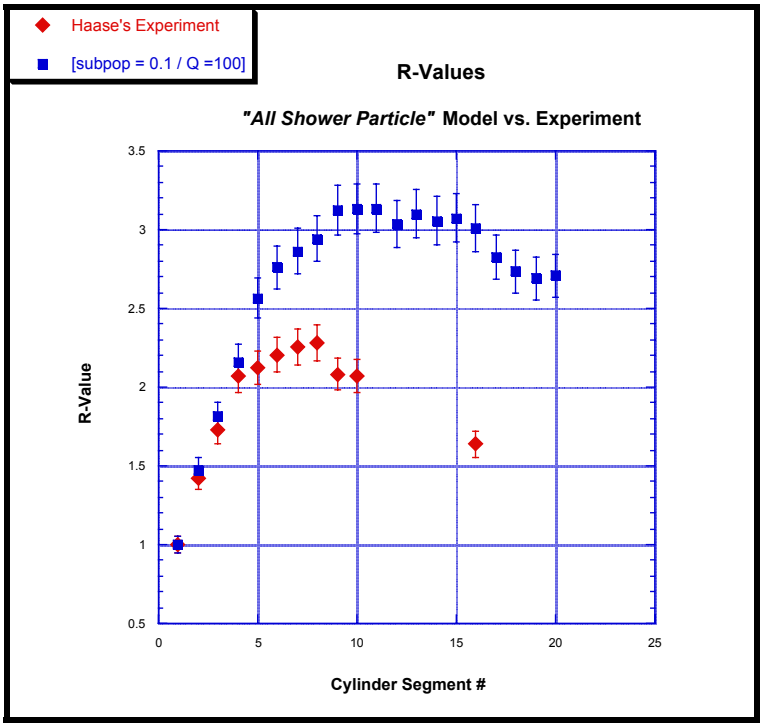

Figure C.3 *'All Shower-Particle'* Model

(Subpopulations = 10, 20, 30%)

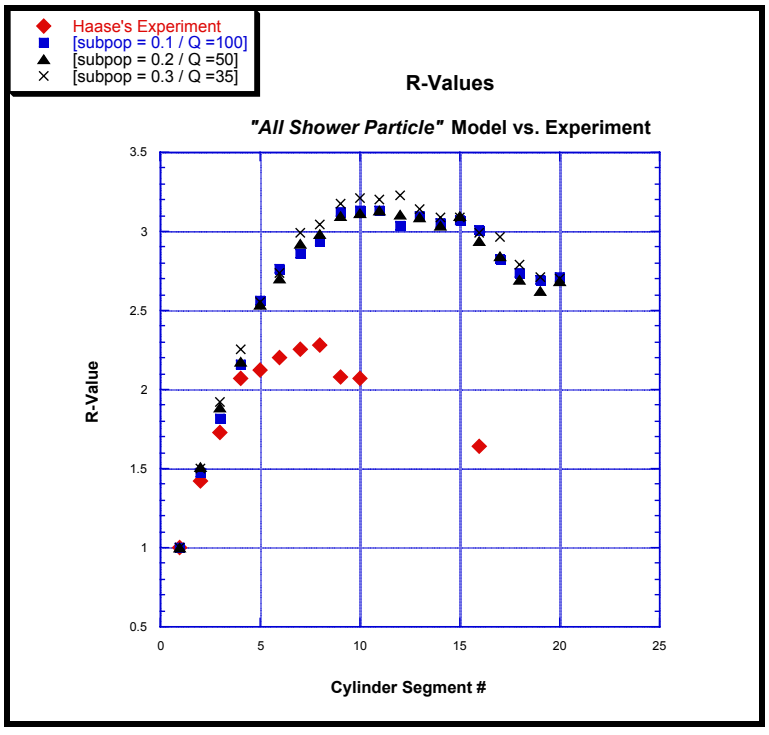

Figure C.4 *'All Shower-Particle'* Model

(Subpopulations = 40, 50, 60%)

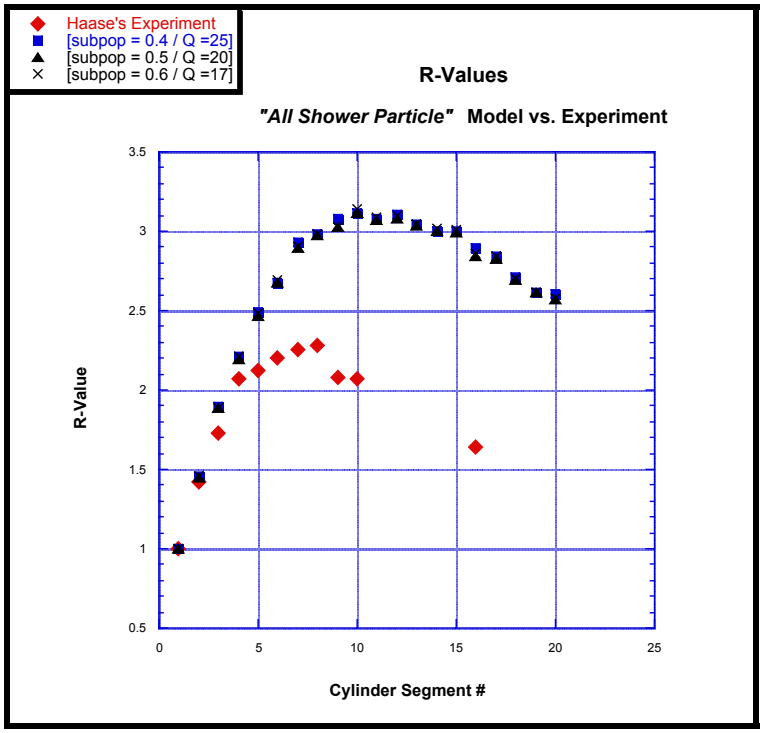

Figure C.5 *'All Shower-Particle'* Model

(Subpopulation = 70, 80, 90%)

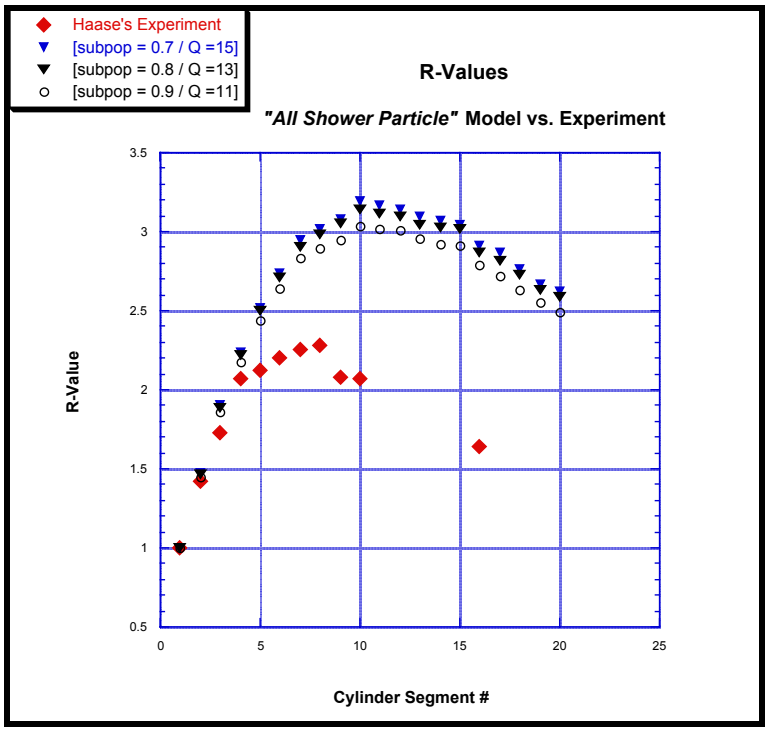

Figure C.6 *'All Shower-Particle'* Model

(Subpopulation = 100%)

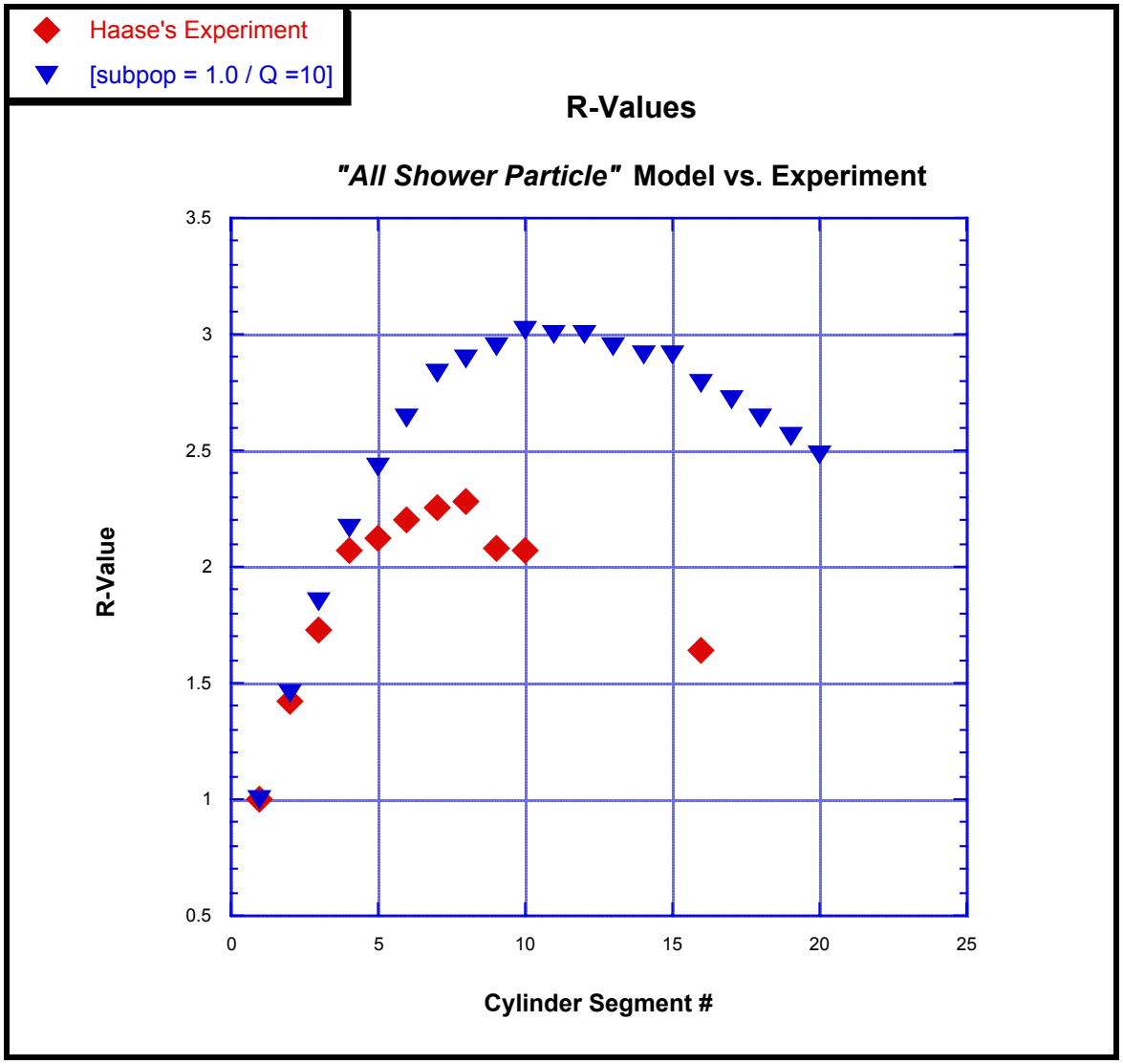

"Wide-Angle Only" Models

Figure C.7 *'Wide Angle Only'* Model

(Subpopulation = 10%)

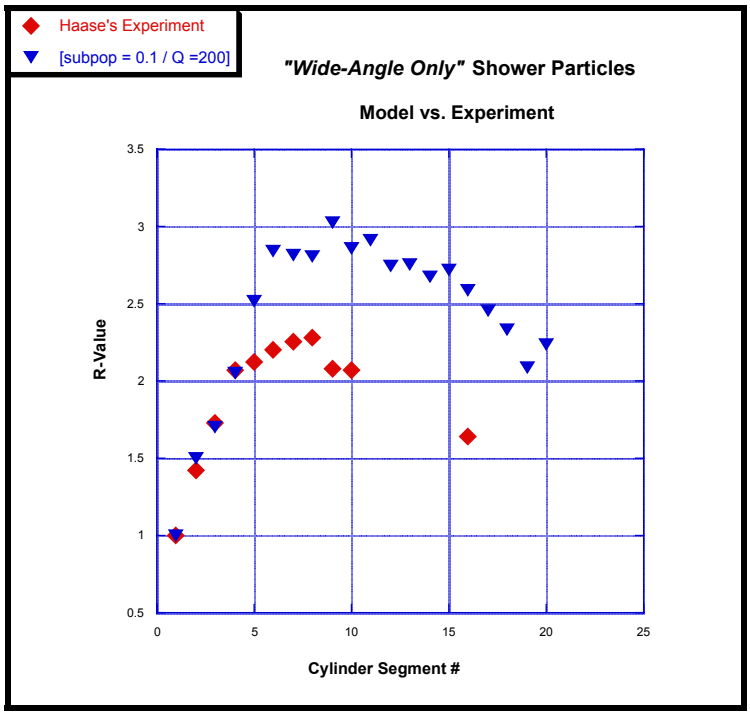

Figure C.8 *'Wide Angle Only'* Model

(Subpopulation = 20% at 2 different enhancement factors)

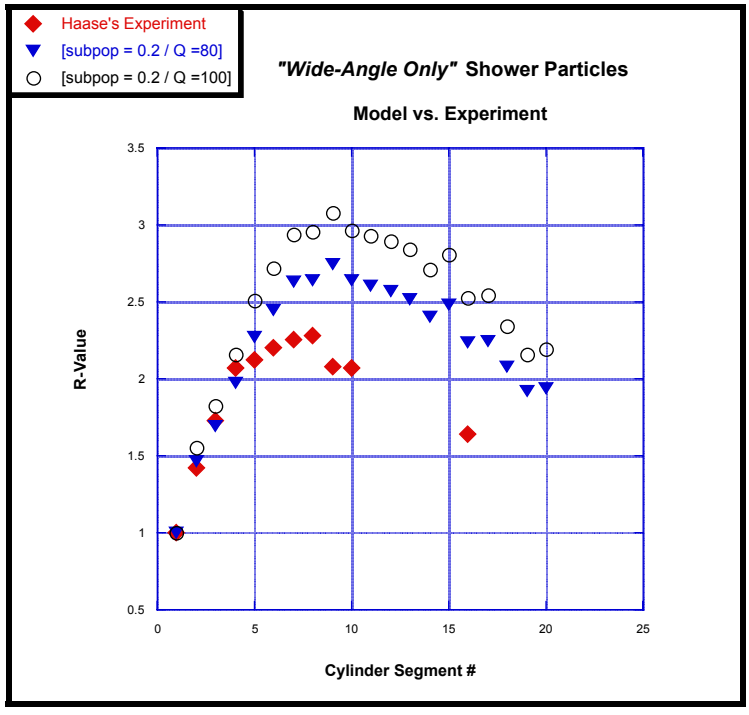

Figure C.9 *'Wide Angle Only'* Model

(*Subpopulation = 30%)*

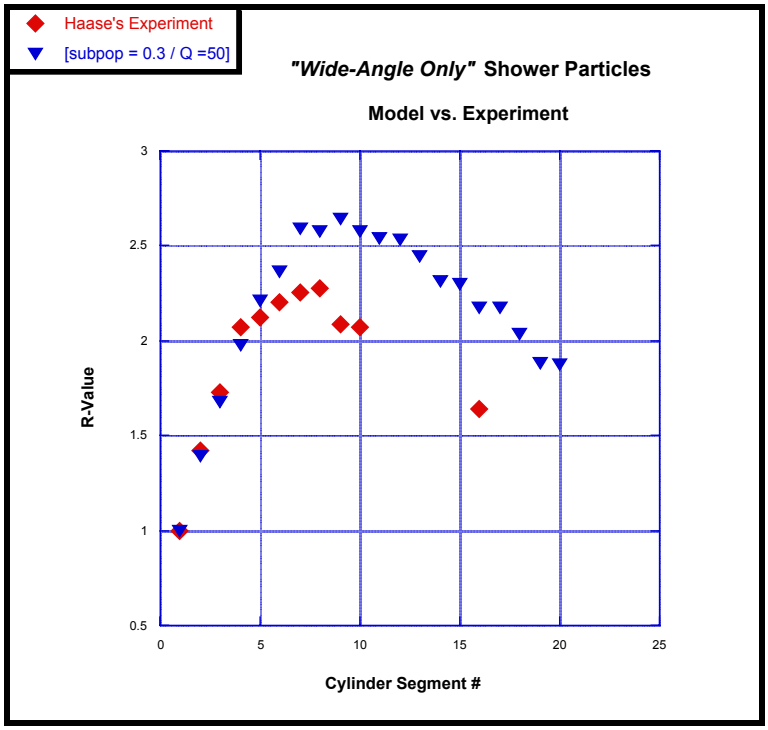

Figure C.10 *'Wide Angle Only'* Model

(*Subpopulation = 40%)*

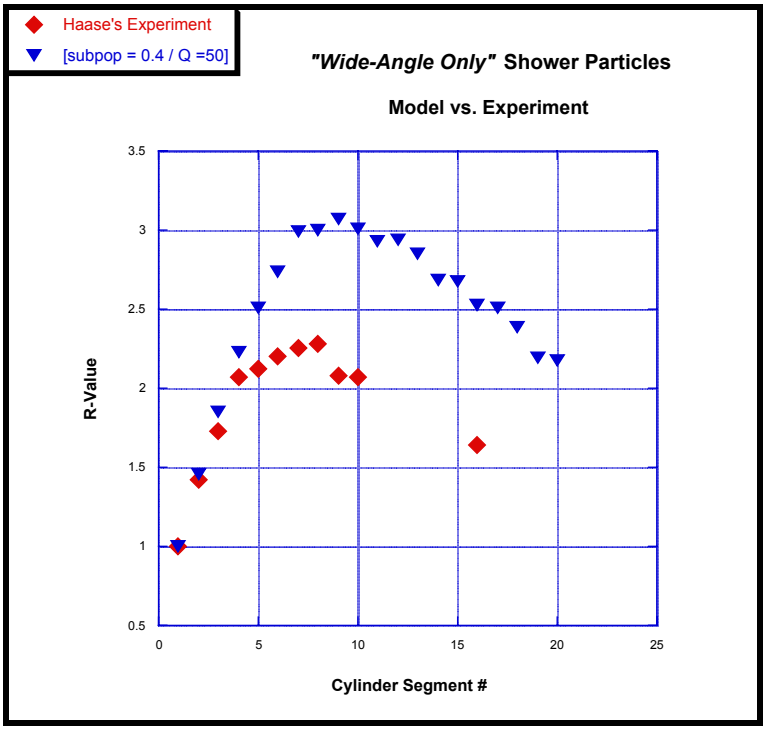

Figure C.11 *'Wide Angle Only'* Model

(*Subpopulation = 50%)*

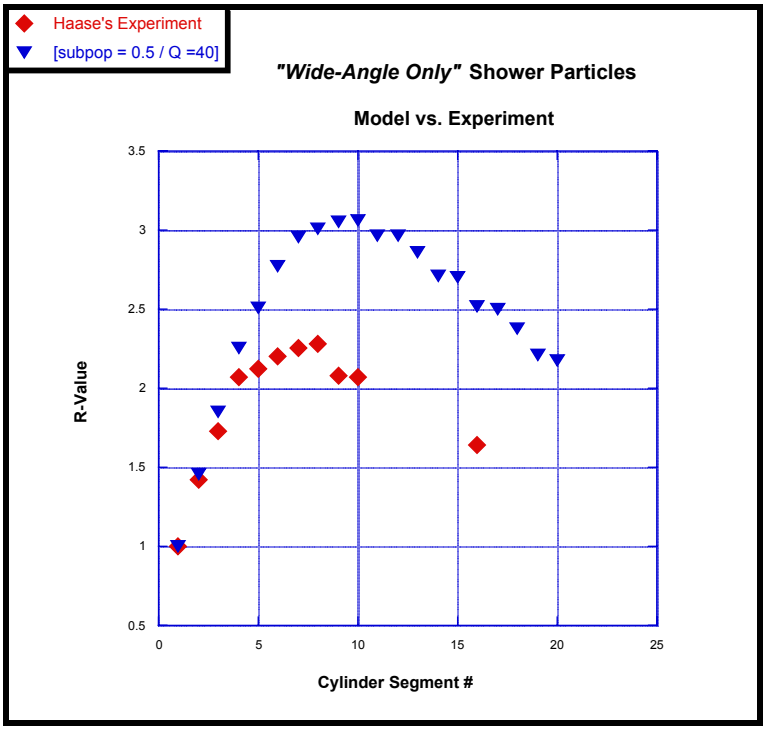

Figure C.12 *'Wide Angle Only'* Model

(Subpopulation = 60, 70%)

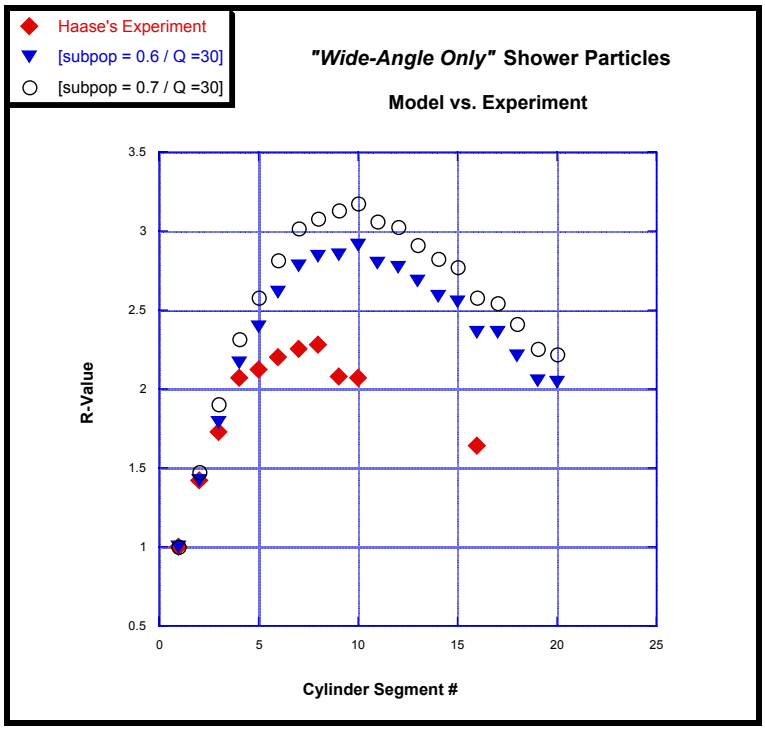

Figure C.13 *'Wide Angle Only'* Model

(Subpopulation = 80, 90%)

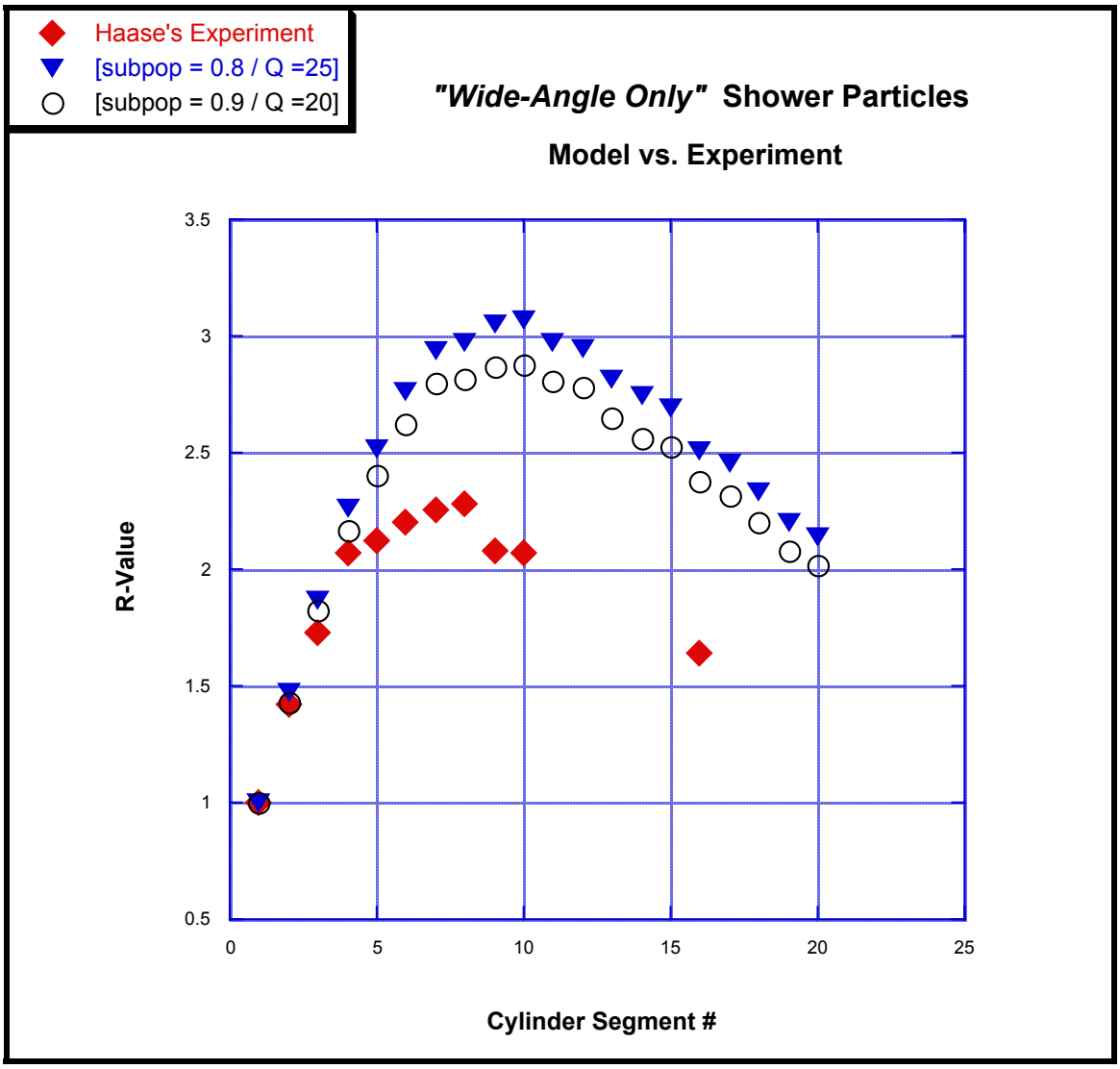

Figure C.14 *'Wide Angle Only'* Model

Computational Convergence Test

(Subpopulation = 100%)

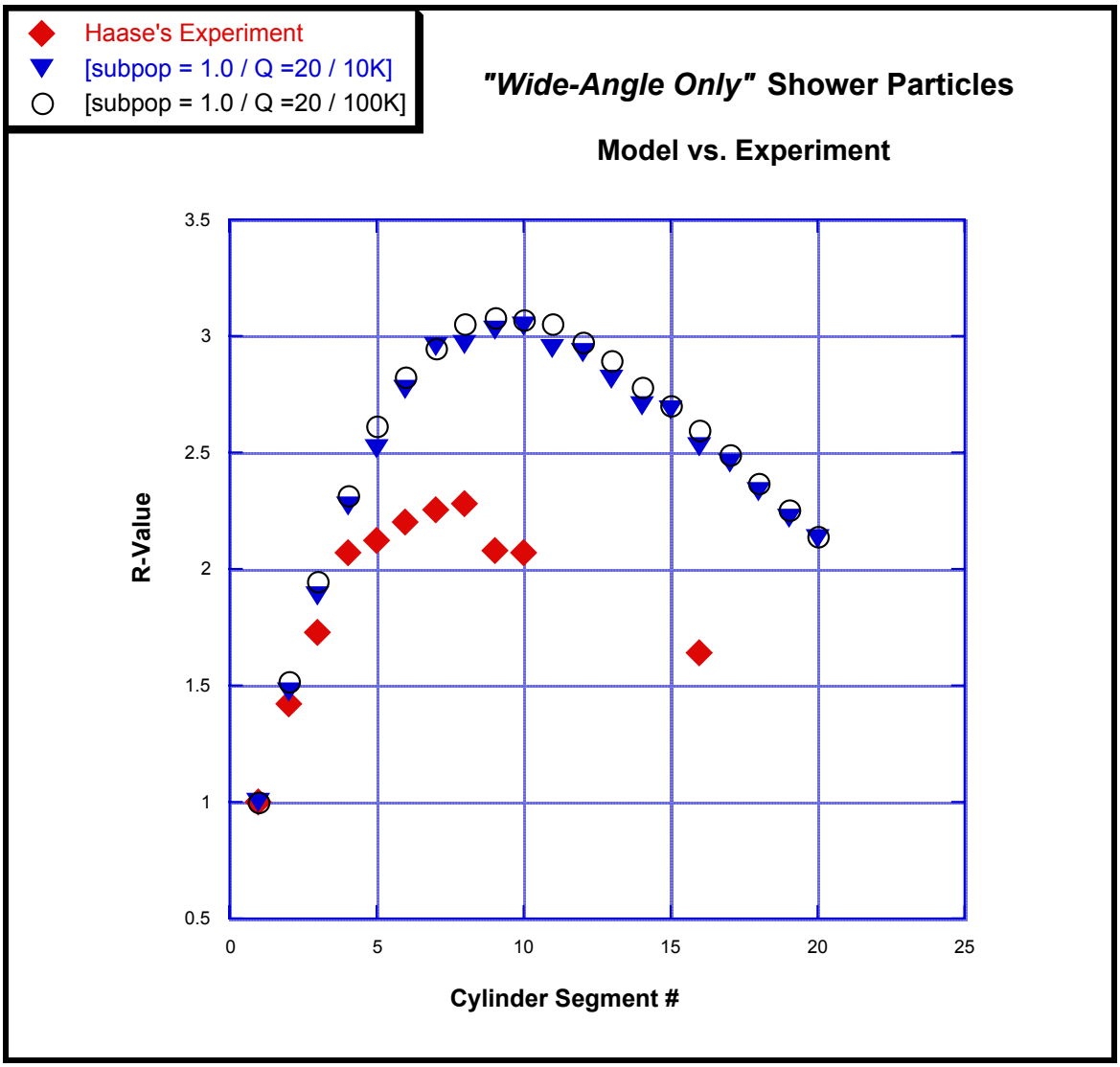

Figure C.15 Experimental Results vs. Enhanced σ_p Model Classes

(1.8 A GeV ^{40}Ar on a Copper Cylinder)

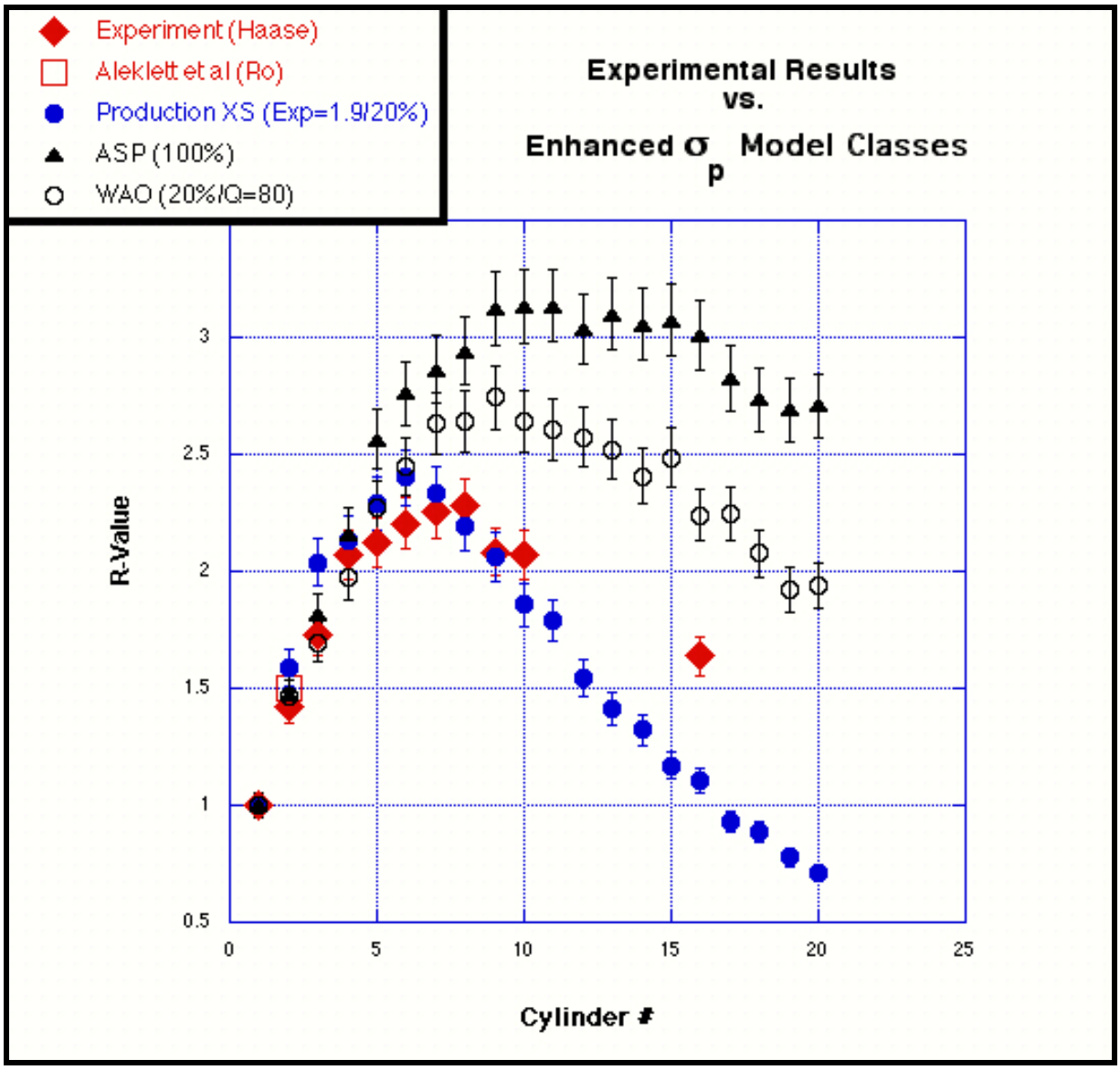

Figure C.16 Experimental Results vs Model Classes

(1.8 A GeV ^{40}Ar on a Copper Cylinder)

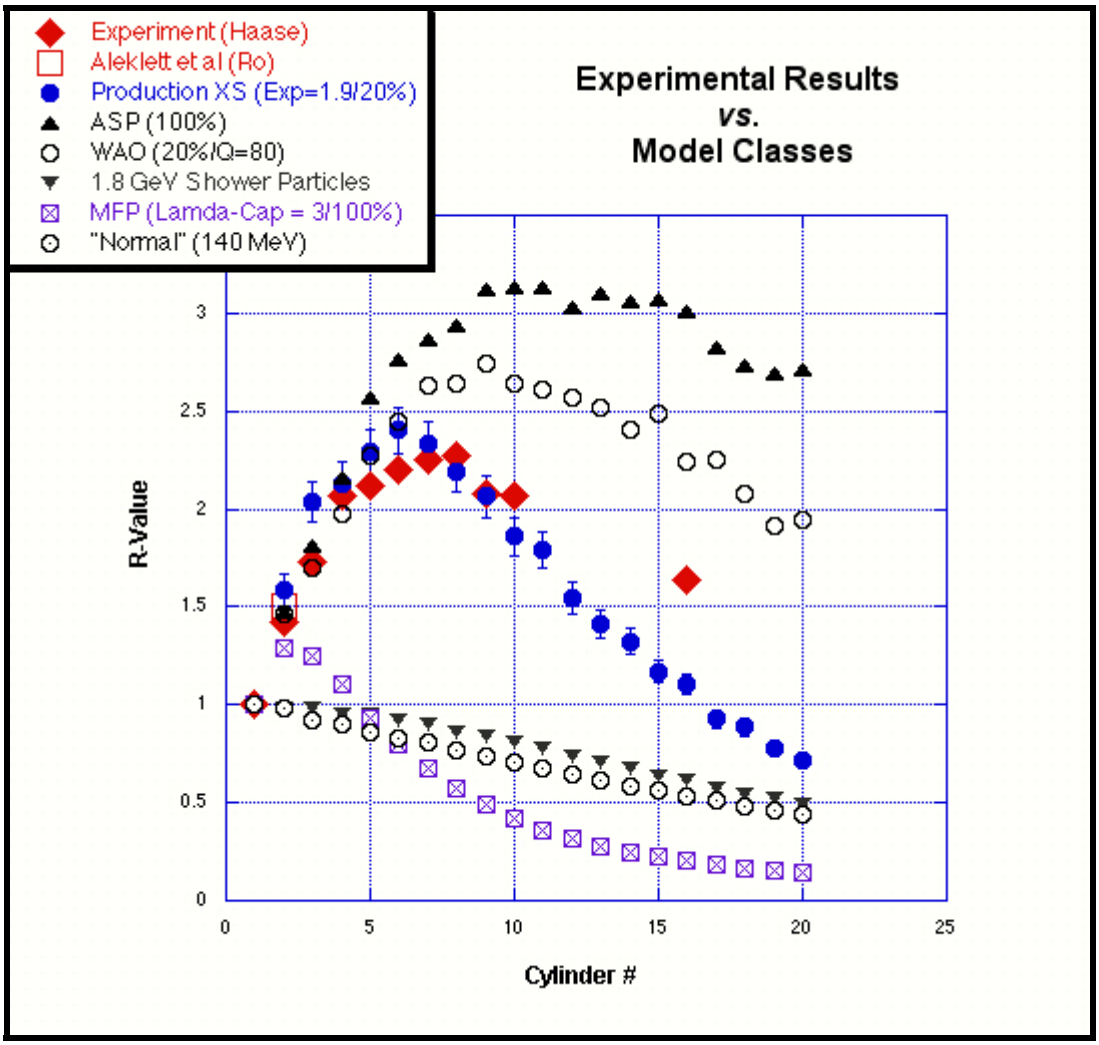

Acknowledgements

This is the fun part. For it is fun (after the fact) to recall how *impossible* problems in every sphere of science and life were eventually solved with the unbelievable generosity of time, effort, and materiél from others.. This has been a big project, representing about 100 man-years of composite work. If an accurate log and presentation of all those who have helped were to be presented here, it would be longer than the scientific report itself. But there is no way to explicitly characterize the open-ended nature of such generous and devoted friendships. The whole of a friendship is definitely greater than the sum of its parts; and the generosity of all constitutes an ever-expanding universe of continuing contributions and commensurately deserved thanks.

My family is first among equals to be thanked. Not only have they provided all the support commonly (and uncommonly) associated with families, but I have more than once taken advantage of the physics backgrounds of both my father and brother to 'run things by them'. My father's lifelong professional interests in high-energy radiation protection made him particularly susceptable to such requests. And it is gladly acknowledged that the personal loyalty and devotion of a number of others led them to become family members in all but biology.

Erwin Friedlander was amongst the founders of the Copper Calorimetry Approach and hosted the LBL component of Project Cascade in its early years. During this period he was the scientific leader of the overall project and in conjunction with Dr. Maria Haiduc provided invaluable scientific leadership in the setting up of the emulsion-scanning part of the overall project. In addition he offered a unique and much appreciated hospitality to me in his laboratory for the early years of this project. During this period he taught me many things, in particular the experimental nature of a Monte Carlo simulation and the importance of a rigorous approach to the statistics of interpretation. Most unfortunately health reasons forced his withdrawl from the project four years ago; and we have sorely missed his intellectual leadership, his broad and insightful views on physics, and his seemingly endless collection of inappropriate but always entertaining stories and jokes from half a dozen different cultures and languages.

To an extraordinary accuracy Maria Haiduc demonstrates the scale-invariant nature of grandmotherhood. Anyone who comes within her orbit risks the wonderful fate of being adopted by her and constantly being plied with the results of her justly-famous cooking. Even more generously shared is her extraordinary musicianship, whose embodiment in the Coon Quartet has entertained *all* of us with the most exhilirating of musical experiences. Her scientific contributions are no less appreciated. As Head of the Laboratory of Space Research at the Institute for Space Sciences she has been the organizer and manager of the Bucharest component of this project. As on-site head of the emulsion scanning and measurement team Dr. Haiduc led the *first* full-stack analysis of emulsions ever done. Her team has worked for almost seven years to create a truly unique database which will have many other uses besides the ones embodied in this report. Dr. Haiduc's contributions to the programming of the transport codes, linking it to the core of this extraordinary database, are also fundamental. Subsequently Dr. Haiduc will be the long-term "Keeper of the Code" for the transport codes *RHIP* and *BFHL* in their intended uses to both the nuclear physics and space science communities.

No words can express my thanks to the entire emulsion group at the Laboratory of Space Research (Bucharest, Romania). Each of them, along with their principal contribution, is listed in Appendix A. Through an extraordinarily difficult time of national and economic turmoil the entire team performed the extraordinary scanning and emulsion feats which made the rest of our work possible. Two historical "events" were involved in their efforts. They performed the first full-stack scan ever done and the stack itself was the very last beam ever run at Lawrence Berkeley Laboratory's Bevatron. It was in fact the last beam directly descended from Lawrence's first (tabletop) design.

Steven Sliwa, the president of Embry-Riddle Aeronautical University during most of this work, was the nexus of that institution's support and efforts. He claimed to be interested in the long-term benefits of our work to NASA's problem of better protecting astronauts for space flights to Mars. But through his extraordinary amalgam of spirit and time and efforts we know better; he just likes like to help. And help he and his staff did!

ERAU provided the infrastructure whereby Project Cascade was born and matured. All involved are thanked for doing the years of stuff that had to be done, and to have done it with efficiency and grace. Speaking of grace, Joan Sullivan managed and coordinated it all with transparency and ease. Thanks all!

James Symons, througout his tenure as Director of Nuclear Science at LBL, offered me a hospitality which was exceptional under any circumstances. But under the particular circumstances of the early days of this project his support went 5 sigma beyond the norm. His professional faith, embodied in his personal encouragement, was of critical support during those challenging times. James, you're a mensch.

Although such things have no quantitiative measure, Prof. Dr. Reinhard Brandt of Philipps University, has demonstrated an even greater faith in myself and all concerned. Being absent from the primary work sites of the collaboration I do not know how he sustained the faith that he did through the necessarily long periods of slow progress and (too) minimal communication. But have faith he did, and his faith was strong enough to convince his colleagues to similarly believe and support. Words alone cannot convey my appreciation of this, for Prof. Brandt did not have with me the history of past relationships as did all the folk above. Hence an instance of human-scale *factorization* (see section 1.4 :) whereby his trust and goodness of heart are cleanly demonstrated to be intrinsic to his own fine soul. Danke schön. Of more mundane practice, but equally appreciated, Prof. Brandt hosted me in Marburg for bi-annual visits of laboratory work. Scientifically, Prof. Brandt is one of the co-founders of the original LBL-based copper calorimetry experiments; and as seen in Chapter 10, the key for ultimately deciphering the phenomenology of this class of experiments was the later experiment done by him and his student G. Haase.

Prof. Dr. Wendorff is thanked for his long-standing role as 'godfather' in the formal degree process. As befits such an eminénce grisé, I was completely unaware of his active participation and now apparent support. Perhaps it is not surprising that faith and trust continue to be well represented in Luther's spiritual home in Hessen, but it is hardly taken for granted. Vielen Dank!

And to the others on my committee Professor Drs. Ganssauge, Junglas, and Hafner a sincere appreciation for their participation in the overall process. Additionally, their feedback on the early drafts of this manuscript was most useful. If it now communicates the subject more intelligibly, it is in part due to these fine gentlemen.

In my early visits to Marburg and the Kernchemie, Drs. Gerhard Haase, Mattias Heck, and Thorsten Schmidt introduced me to their particular experimental work on the nuclear chemistry of the copper block experiments. As seen in Chapter 10 Dr. Haase's work was of critical use to us. In subsequent stays in Marburg it was Dr. Eva Kalinowski who helped me to make (literal) sense of a host of nuclear chemistry techniques. And it was Dr. Peter Vater's knowledge of the true craft of nuclear experimentation which later helped me understand a truer meaning of what experiments are all about. I must admit to having forgotten much of what I was taught in all of those laboratory sessions. But what I've learned from all of them about the town and culture of Marburg remains fresh and lively in my memories.

Central to the success of our approach was a highly interactive investigation of the phase space to be explored. The computational requirements of the simulations presented here catalyzed the design and building from scratch of a 20-node 5 gigaflop distributed supercomputer. Many persons from many companies were critical in providing us with equipment (often commercially unavailable) and advice. Amongst the companies who so lavishly helped us out were UMAX, Newer Technology, Seagate, Adaptec, and IBM. Curtis Kim and Roger Kasten must be particularly mentioned. Their participation and involvement in the building of HOMER ((HOME supercomputeR) and their continuing fascination and interest in the motivating scientific problems makes them true collaborators.

In the finest traditions of cooperation between laboratories we traded Victor Decyk and Dean Dauger of the UCLA physics department our hardware expertise for their marvelous software tools for the implementation of parallel processing on the Mac.

It deserves to be stated that the experimental design and evolution of our ‘baby super’ could *only* have been so ‘easily’ implemented on IBM’s PowerPC chip coupled to the Macintosh’s sterling integration of hardware and software. In Marburg, vital equipment needed (invariably!) at the last minute was consistently provided by a fellow Mac afficionado, Prof. Dr. Greiner. And Heinz Eifert and all the volk at Eifert Datensysteme were of inestimable value in making this final document “final”.

And the most special thanks to all of you not explicitly mentioned here. Allow me instead to offer each one of you in private the thanks that you so richly deserve. Persons close to me know that this work represents the successful conclusion of a different experiment, one that has taken place in a regime far from the scales of particle and nuclear physics. To my friends and collaborators in this other endeavor my thanks extends far beyond words; and is coupled to the hope that someday I can reciprocate in ways of equal value.

As always my appreciation goes to the Bach and Koon clans. They’ve so eloquently taught me about the drive to survive and the forces to succeed that lie within each one of us; waiting only to be recognized and tapped.

Louis